FABRICATION OF 3D PHOTONIC CRYSTALS WITH SELF-ASSEMBLED COLLOIDAL SPHERES AS THE TEMPLATE

WANG LIKUI

NATIONAL UNIVERSITY OF SINGAPORE

2008

FABRICATION OF 3D PHOTONIC CRYSTALS WITH SELF-ASSEMBLED COLLOIDAL SPHERES AS THE TEMPLATE

WANG LIKUI

(PhD, NUS)

DEPARTMENT OF CHEMICAL AND BIOMOLECULAR ENGINEERING

NATIONAL UNIVERSITY OF SINGAPORE

2008

Acknowledgement

I would like to take this chance to express my gratefulness to all the people kindly offering help during my thesis work. First, I would like to sincerely and greatly thank my supervisor, Prof Zhao X. S. George, for his invaluable guidance, constant encouragement, and kindly understanding.

I would also like to thank all the colleagues in our group, a gathering of dynamic and warm-hearted people. Dr Zhou Zuocheng, Dr Yan Qingfeng, Dr Lv Lu, Dr Su Fabing, Mr Bao Xiaoying, Ms Lee Fang Yin, Ms Liu Jiajia, Ms Tian Xiaoning, Dr Zhou Jinkai, Dr Li Gang, Dr Bai Peng, Ms Wu Pingping, Ms Zhang Lili, Mr Cai Zhongyu, Mr Dou Haiqing, Ms Han Su Mar, all of them are greatly helpful during my thesis work and they made the last years colorful.

Particular acknowledgement goes to the technical team members of our department, Mr Shang Zhenhua, Mr Chia Phai Ann, Mr Yuan Zeliang, Ms Jamie Siew, Ms Sylvia Wan, for their kindly help guaranteeing the smooth progress of my project.

In addition, special thanks should also be given to Dr Li Qin, Prof Serge Ravaine, for their kindly guidance and supporting.

Furthermore, I am deeply grateful to my family and my wife for their love, encouragement and supporting.

Table of Contents

Chapter 8 Fabrication of Binary Colloidal Crystals and Inverse Opals

Chapter 9 Engineering Planar Defects in Colloidal Photonic Crystals

Chapter 10 Patterning Microsphere Surfaces and Fabrication of Nonspherical Particles

Summary

Photonic crystals are a type of materials with periodically varying refractive index, which results in the presence of a photonic bandgap. Analogous to semiconductors for controlling electrons, photonic crystals open an opportunity of controlling the behavior of photons by the photonic bandgap. According to the dimensionality that the photonic bandgap works, photonic crystals are classified into three categories, namely one-dimensional, two-dimensional, and three-dimensional photonic crystals. Due to the high cost and difficulty of fabricating three-dimensional photonic crystals using traditional lithography method, the self-assembly method that utilizes colloidal microspheres as the primary building units has been considered as an alternative cost-effective approach. This thesis work focuses on the fabrication of photonic crystals using the self-assembly method.

First, various monodisperse microspheres and core-shell structures were synthesized, which were used as the building blocks of colloidal crystals (artificial opals). The control over the particle size and size uniformity was attempted.

Second, an approach to the fabrication of crack-free colloidal crystals was designed and demonstrated for the first time. The addition of a silica precursor into a colloidal suspension containing microspheres was found effective in eliminating the defects formed in the crystal drying process. The precursor hydrolyzed during the drying process and took the place of solvent layer, leading to the formation of crack-free colloidal crystals in large domains.

Third, the fabrication of non-close packed opal was achieved through the combination of chemical vapor deposition and templating methods. Chemical vapor deposition was used to deposit a layer of silica on silica inverse opal. Upon infiltration of a polymer and removal of the silica template, a free-standing non-close packed opal was obtained with a mechanically tunable optical property.

Fourth, binary colloidal crystals were also synthesized using a horizontal deposition method. This provides a convenient method of producing complex structure of colloidal crystals.

Fifth, the incorporation of engineered defects into photonic colloidal crystals is still a challenge. A general route of introducing planar defects into colloidal photonic crystals without involving lithography was designed and demonstrated. A combination of spin-coating and horizontal deposition techniques allowed an effective control over the structure and thickness of the defect layer in a colloidal photonic crystal.

Finally, a colloidal crystal templating method was proposed and demonstrated for patterning the surface of microspheres. The patterning was achieved by controlling the contact areas between the adjacent spheres of a colloidal crystal. Using the surface-patterned spheres as seeds, uniform nonspherical particles were obtained. Colloidal spheres with nanoholes were also fabricated by selectively etching of a colloidal monolayer partially embedded in an electrochemically deposited metal layer. Since these surface-patterned spheres and nonspherical particles have well-defined surface pattern and shapes determined by the uniform structure of colloidal crystals, they hold a great promise in assembly of photonic crystal devices and other functional devices.

Nomenclature

1D	One-dimensional
2D	Two-dimensional
3D	Three-dimensional
Å	Angstrom
^{o}C	Degree Celsius
CC	Colloidal Crystal
d	Diameter
f	Volume fraction in colloidal crystal
φ	Particle volume fraction in colloidal suspension
j_e	Evaporation rate of the solvent
J_{evap}	Integral of water evaporation flux
L	Evaporation length
n	Refractive index
λ	Wavelength
bcc	Body centered cubic
BET	Brunauer-Emmett-Teller
BJH	Barrett-Joyner-Halenda
BTEE	1,2-bis(triethoxysilyl)ethane
BTEM	1,2-bis(triethoxysilyl)methylene
BTEEY	1,2-bis(triethoxysilyl)ethenylene
CP	Cross polarization
CVD	Chemical vapor deposition
DA	Dubinin-Astakhov
EDX	Energy dispersive X-ray spectroscopy
EM	Electromagnetic
FE-SEM	Field-emission scanning electron microscopy
fcc	Face-centered cubic
FCVD	Flow-controlled vertical deposition
FTIR	Fourier transform infrared

HCP	Hexagonal close packed
KPS	Potassium persulfate
LB	Langmuir-Blodgett
MAS	Magic angle spinning
NMR	Nuclear magnetic resonance
OMOS	Ordered macroporous organosilica
PAH	Poly(allylamine hydrochloride)
PBG	Photonic bandgap
PhC	Photonic crystal
PDMS	Poly(dimethylsiloxane)
PS	Polystyrene
PSS	Poly(sodium styrenesulfonate)
PMMA	poly(methyl methacrylate)
RI	Refractive index
SEM	Scanning electron microscopy
FESEM	Field Emission Scanning electron microscopy
TEM	Transmission electron microscopy
TGA	Thermogravimetric analysis
UV-Vis-NIR	Ultra-Violet visible near-infrared
XRD	X-ray diffraction

List of Tables

Chapter 3

Chapter 4

Chapter 7

Chapter 8

Chapter 10

List of Figures

Chapter 1

Chapter 2

Chapter 3

Chapter 4

Chapter 5

Chapter 6

Chapter 7

Chapter 8

Chapter 9

Chapter 10

Chapter 1

Introduction

Photonic crystals (PhCs) (John, 1987; Yablonovitch, 1987), also known as photonic band gap (PBG) materials, are a class of optical materials having a periodic alternation of dielectric medium with different refractive indexes (RIs) on an optical-length scale. This structure induces a photonic band gap – a range of forbidden frequencies, for which light with a frequency falling in this range cannot propagate through the structure. It is known that an energy range between the valence and conduction bands in semiconductors is called electronic band gap, through which electrons cannot transit. This property produces the possibility of processing electron flow. Similarly, the existence of a PBG allows the control of the behavior of photons.

The concept of PBG materials was first proposed independently by Yablonovitch (1987) and John (1987). Since these materials, especially the three-dimensional PhCs, have the potential of controlling the behavior of photons, they provide a promising future in photonics (Arsenault et al., 2004). Photonics, an analogy of electronics, deals with light and other forms of radiant energy whose quantum unit is photon. Photons have many advantages in information processing when compared to electrons. First, photons travel through a dielectric medium in a much faster speed than the electrons do. In addition, photons do not interact strongly with the medium, leading to a less energy loss. Furthermore, photons can carry larger amount of information than electrons. Thus it is believed that photonics will replace the electronics in the future as the heart of the information technology, with the increasingly rapid demand for high-speed computing and information transferring. Because of the promising properties of these PhCs, the past few years have seen a dramatic increase in the number of publications in terms of modeling, fabrication, characterization, property evaluation, and application of PhCs (Busch and John, 1998; John and Busch, 1999; Xia et al., 2001; Koenderink et al., 2002; Lopez, 2003).

1.1 PBG and PBG materials

According to the arrangement of the dielectric media, the PhCs can be classified mainly into one-dimensional (1D), two-dimensional (2D) and three-dimensional (3D) PhCs (see Figure 1.1). Accordingly, light with a frequency in PBG cannot propagate in one, two or all three dimensions respectively. However, the propagation behavior of electromagnetic (EM) waves in the PhCs is the same except the difference of the dimension. Thus the basic principle of the formation of PBGs can be explained simply by the model of 1D PhC as shown in Figure 1.2 (Yablonovitch, 2001). It can be seen that the 1D PhC has alternation of layers of different dielectric constants (Figure 1.2A). When an incident EM wave enters the PhC, it is partially reflected at each boundary of the dielectric layers (Figure 1.2B). The reflected waves are in phase and reinforce one another. They combine with the incident wave to produce a standing wave that does not travel through the material (Figure 1.2C). The range of wavelengths in which incident waves are reflected is the PBG of the PhC.

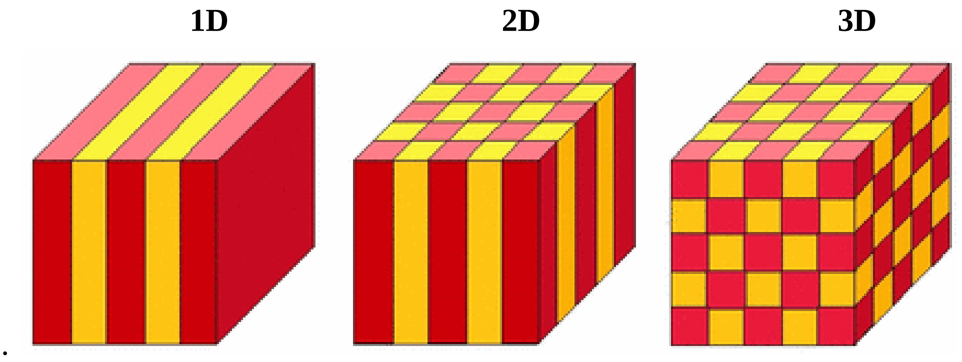

Figure 1.1 Schematic illustration of 1D, 2D and 3D PhCs. The different colors represent the difference of dielectric constants of the materials.

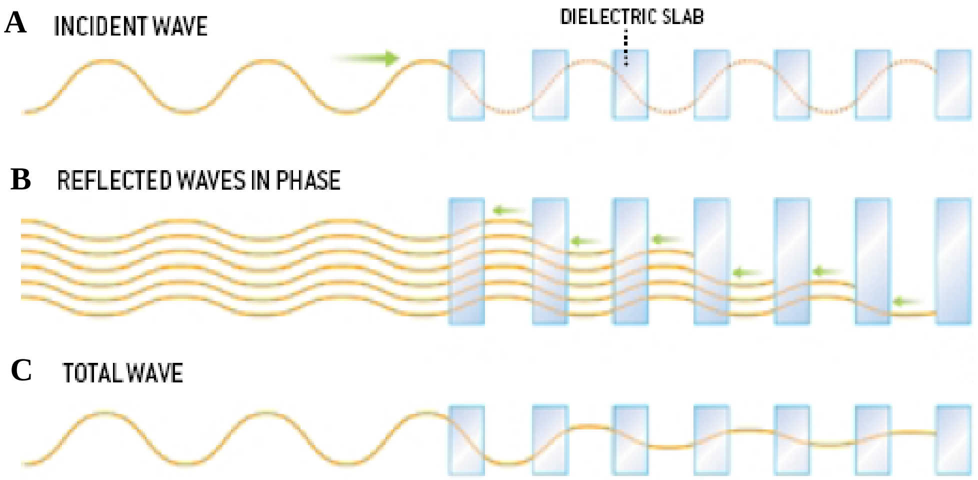

Figure 1.2 The propagation of EM waves in 1D PhCs. The wavelength of the incident wave is in the PBG (Yablonovitch, 2001).

There are two main factors influencing the structure of the PBGs, the RI contrast and average RI. The former governs the gap width and the greater the contrast the wider the gap, while the latter governs the gap positions (Yablonovitch, 1987). Among them, 3D PhCs obtain considerable attention recently because they can possess a full bandgap, which can stop the propagation of EM waves in all directions. Therefore, by fabricating waveguides in the PhCs the propagation direction of the EM waves can be controlled. As a result, 3D PhCs provide a foundation for the development of novel optical devices and integration of such devices into a microchip (Joannopoulos et al., 1997). However, the science and technology of PhCs are still in the early phase of development. The main challenges that are facing materials scientists are how to fabricate 3D PhCs in large domains and of high quality with acceptable cost.

1.2 Fabrication of 3D PBG materials

There are two general methods of fabricating photonic crystals, namely the traditional “top-down” method and the “bottom-up” method. The strategy of the “top-down” method is to work out the required shapes out of a bulk material using conventional micromachining and lithography techniques (Birner et al., 2001). Normally, in this method, a predefined pattern is employed to selectively remove unwanted parts or grow extra materials (Figure 1.3). It provides precisely control over the structure because of the use of advanced devices and the exact copy from the patterns. However, the cost of lithography is normally high and it’s difficult to build 3D structures using this method.

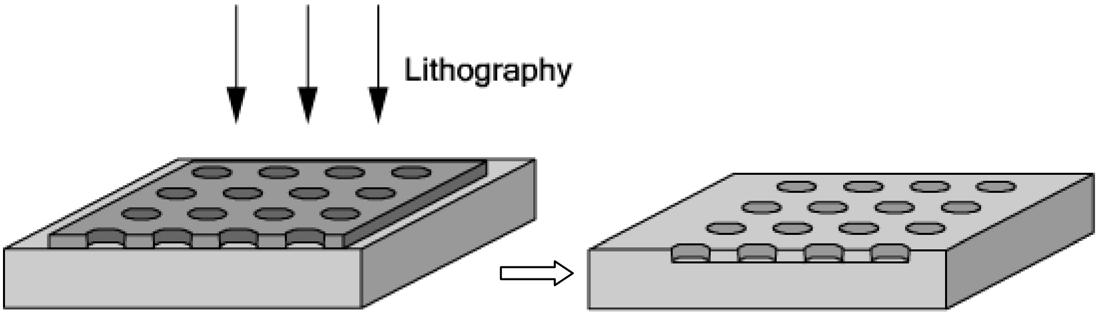

Figure 1.3 The strategy of the “top-down” methods.

In the recent years, the bottom-up method, involving self-assembly, has been explored and demonstrated as a simple and cost-effective route to fabricate 3D PhCs(Stein, 2001; Xia et al., 2001; Yablonovitch, 2001). The underling principle is that uniform microspheres in a colloid tend to self-organize in to an ordered crystal structure (normally face-centered cubic structure) under certain conditions. After infiltration of a secondary material with a high RI into the void between the spheres, followed by the removal of the colloidal spheres, an inverse opal with a complete PBG can be obtained (Blanco et al., 2000; Vlasov et al., 2001) (see figure 1.4). Because that the regularity of the structure need to be extremely high to open a complete PBG, it is essential to form a highly ordered colloidal crystal (CC), a template for fabricating inverse opal. Various methods, sedimentation, evaporation, electrophoresis, etc. have been explored for self-assembly of colloidal microspheres (Stein, 2001; Lopez, 2003). In addition, to infiltrate the template with a high RI material, several techniques have been developed, such as liquid infilling, chemical vapor deposition (CVD), and electrodeposition, etc. The inverse opal can be metals, metal oxides, semiconductors, carbons, etc. (Lopez, 2003).

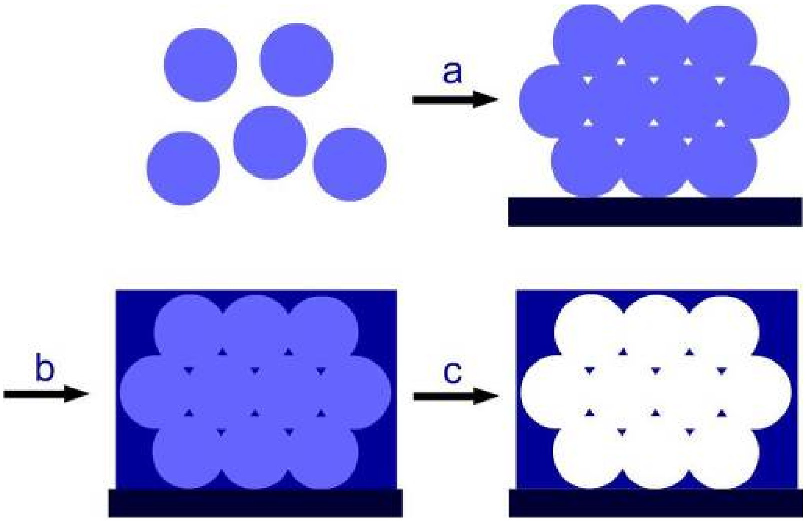

Figure 1.4 Scheme of fabricating inverse opal. (a) Self-assembly of microspheres into a CC; (b) Infiltration of the voids of the CC with a dielectric material; (3) Removal of the colloidal spheres to obtain an inverse opal.

1.3 Defect Engineering in Photonic Crystals

Given a photonic crystal with an omnidirectional band gap, its full potential can be harnessed only after the introduction of engineered defects, like the doping of semiconductors. A defect is anything that breaks the usual periodicity of dielectric constant. According to dimension of the defects, the defects can be classified into three types, namely, planar defects, line defects and point defects. All the three kinds of defects can introduce modes that lie inside the band gap of the bulk crystal, namely, localized states in the vicinity of the defect (Johnson and Joannopoulos, 2002).

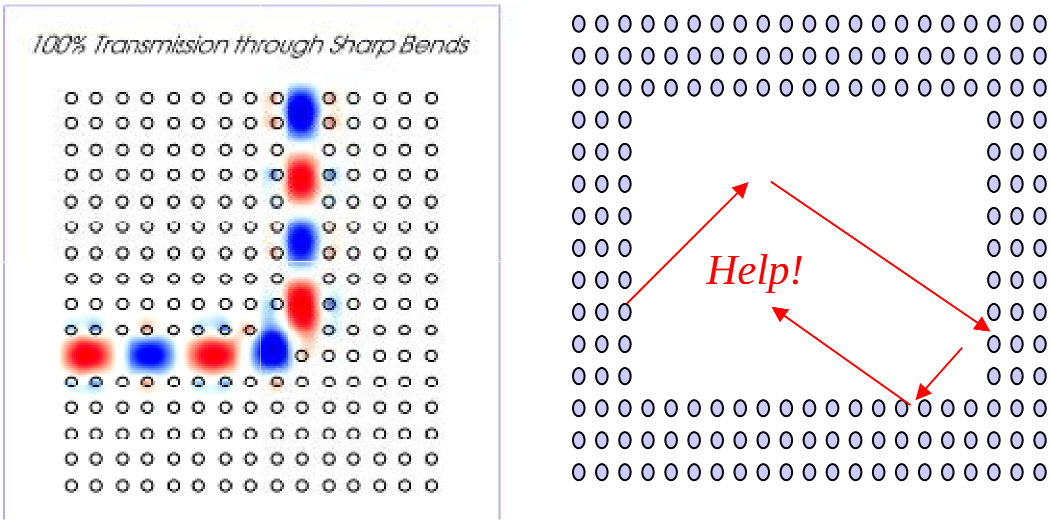

(a) (b)

Figure 1.5. An illustration of (a) line defect as a wave guide and (b) point defect as a photon trap (http://ab-initio.mit.edu/photons/tutorial/L2-defects.ppt).

For example, the point defect embedded can trap or localize photons and act as a micro-cavity with a high quality factor (Q) (John, 1987; Joannopoulos et al., 1997). A line defect introduced can direct the propagation path of photons, acting as an ultra-compact and low-loss optical waveguide (John, 1987). A planar defect on the other hand can be used a slab waveguide or a cavity depending on the direction of the incident optical field(Xia et al., 2001). Many photonic applications, such as optical waveguides, splitters, couplers, switches, micro-lasers, and others, exploit these properties(Norris and Vlasov, 2001) Thus, an important issue for the practical application of 3D PhCs is how to introduce artificial defects within the structure in a controllable manner, no matter which kind of fabrication method is used.

1.4 Objectives

Although the self-assembly method has many advantages for the fabrication of 3D PhCs, there are still a lot of problems limiting the application of the method. This PhD thesis work aimed at addressing some of the problems and was targeted to:

- synthesize various monodisperse microspheres to be used as the building blocks of colloidal crystals,
- overcome the formation of cracks during the drying process in the present self-assembly method,
- control the structure of colloidal crystals and fabricate non-close-packed structures, and
- engineer designed defects in colloidal photonic crystals using simple chemical methods.

Chapter 2

Literature Review

Two theoretical works on photonic crystals (PhCs) were independently published by Yablonovitch (1987) and John (1987) in 1987. Yablonovitch theoretically proposed a three-dimensional (3D) periodic structure as a means to control the emission of photons. The motivation was to create a photonic bandgap, in analogy with the bandgap in semiconductors. With this concept, the performance of lasers, solar cells and heterojunction transistors would be improved greatly. John found that a strong Anderson localization of photons could exist in an intricate dielectric superlattice and a photonic bandgap could be produced by ordered 3D periodic dielectric structures. These two pioneer works founded the basis of the PBG theory.

For PhCs there are only two parameters that determine the creation of a bandgap, namely the crystal structure and the dielectric constant contrast. Thus, PhC is scalable and can be designed to produce band gap in different wave region. The same crystal structure can work in wave regions of microwave, optical range and X-rays by changing its lattice constants to scales of centimeters, micrometers and angstroms. Thus, the design of 3D PhCs can be simplified into two steps. First, an appropriate crystal structure should be proposed, which might exhibit a certain width of complete bandgap. Subsequently, the lattice constant should be scaled up or down corresponding to the wavelength of the targeted light. Although it has been found that diamond (Maldovan and Thomas, 2004), woodpile and face-centered cubic (fcc) structures

(Doosje et al., 2000) could possess complete band gaps through theoretical simulation, the fabrication of these structures on an optical scale with high dielectric constants is still challenging. In the past decade, various methods were proposed to fabricate PhCs, most of which can be classified into two categories: traditional “top-down” method in which a desired structure is carved out a bulk material and the “bottom-up” method, which utilizes the self-assembly of colloidal particles (microspheres) into a colloidal crystal (CC) structure (opal).

2.1 Fabrication of photonic crystals

2.1.1 The “top-down” approaches to 3D photonic crystals

In 1991, Yablonovitch et al. first fabricated successfully photonic bandgap crystal, namely yablonovite. It was a fcc structure formed by drilling holes at a slab of semiconductor with 35 degree off normal incidence and 120^{o} on the azimuth (Yablonovitch et al., 1991) (See Figure 2.1).

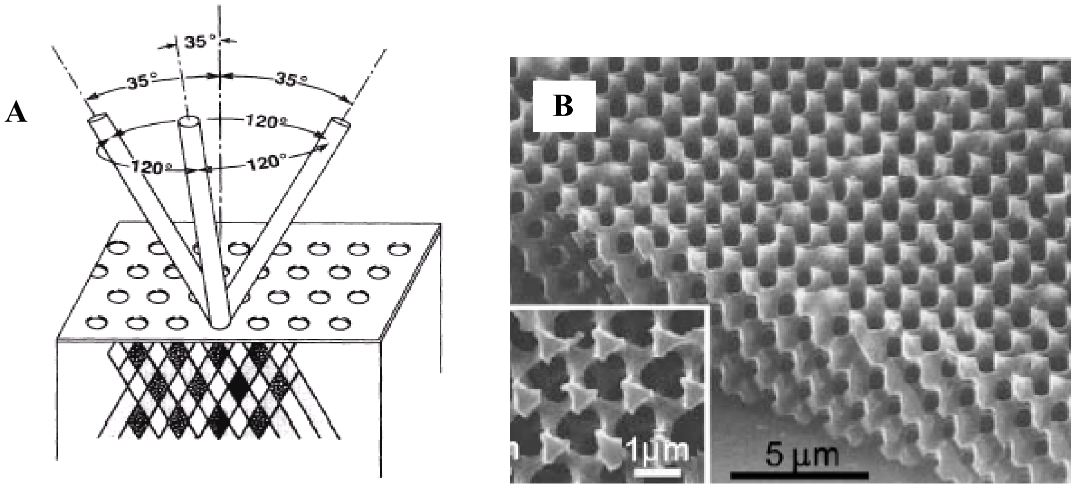

Figure 2.1 (A) Schematic illustration of the fabrication of yablonovite (Yablonovitch et al., 1991) and (B) SEM of the 6.2 µm PMMA yablonovite fabricated using X-ray beam (Cuisin et al., 2002).

A full band gap was created, but it was at the microwave range and not practical. The scale of Yablonovite is limited by the fabricating technique, micromachining. New fabrication techniques are required to decrease the scale of the PhC. Deep X-ray lithography (Feiertag et al., 1997) allows an extra degree of precision and an extremely high depth of focus due to the reduced wavelength of the radiation used. In this method, a pattern is drawn on a resist and transferred to a metal sheet. This metal is then used as a mask, whose shade can be projected in different directions, tilted with respect to the normal, to produce rod structures. Simple methods may be used to replicate yablonovite structures in other materials (Feiertag et al., 1997). The pattern can then be transferred to a metal (by electro deposition) or high refractive index materials (by a sol-gel technique). Glancing angle deposition (Robbie and Brett, 1997; Robbie et al., 1998), focused ion beam micromachining (Chelnokov et al., 2000), e-beam were also used to fabricate yablonovite structures .

Holographic lithography (Campbell et al., 2000) is a technique developed recently, carving the structures by using the interfering beams. When four laser beams were used together (Figure 2.2), the interference of them leads to a distribution of laser intensity with 3D translational symmetry. Thus, if an appropriate photoresist is exposed to these beams, a solubility pattern can be formed in the bulk photoresist. A 3D periodic structure can be formed after the development of the exposed structure (Figure 2.3). In this method, the period of the structure and its symmetry are dictated by the laser wavelength, the relative phases and the incidence directions of the interfering beams while the shape of the repeated feature in the lattice results from the beams' polarizations. Although this technique can produce complex 3D structure in a short period time, it can only apply to photosensitive polymers, which low RIs limit their application as PhCs. To improve the RIs of the structures, silica-methacrylate composites was used as photoresist to carve out desired structures (Saravanamuttu et al., 2003). Additionally, the holographic lithographic structure was used as template to produce PDMS (poly (dimethylsiloxane)) elastomeric structures, which optical property could be tuned by mechanical pressure (Jang et al., 2006). Through translation of a multi-beam interference pattern, two interference patterns could be aligned to produce diamond structure (Moon et al., 2005b).

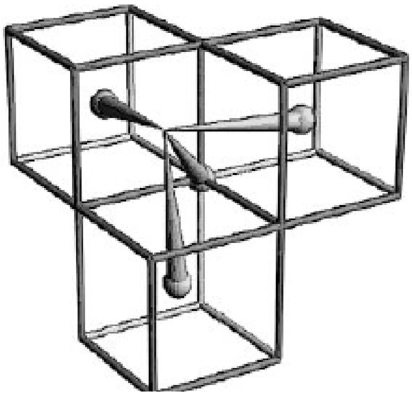

Figure 2.2 Beam geometry for an fcc interference pattern.

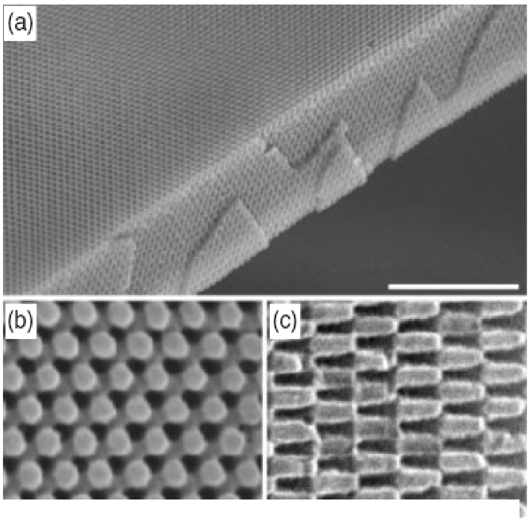

Figure 2.3 SEM images of different structures generated by holographic lithography (Campbell et al., 2000).

The woodpile structure, as shown in Figure 2.4, is another category of structure which has been proven exhibiting complete bandgaps. Ozbay et al. (1994a; 1994b) and Ho et al. (1994) first proposed this structure. Initially, woodpile structures were fabricated by layer-by-layer stacking of dielectric rods, which had bandgap only in the microwave region due to the large dimension of the rods. To develop woodpile materials with a bandgap in the optical region, wafer-bonding and selective etching (Noda et al., 1996), wafer fusion and alignment (Noda et al., 1999; 2000b), vapor deposition and direct holographic writing (Feigel et al., 2000) have used to fabricate structures with smaller critical dimensions. Additionally the packed metallic rods (see Figure 2.4D) were proven to have bandgap at infrared region. Through the combination of integrated circuit processing and micromanipulation, engineered defects could be incorporated at predetermined positions on a structure (Aoki et al., 2003).

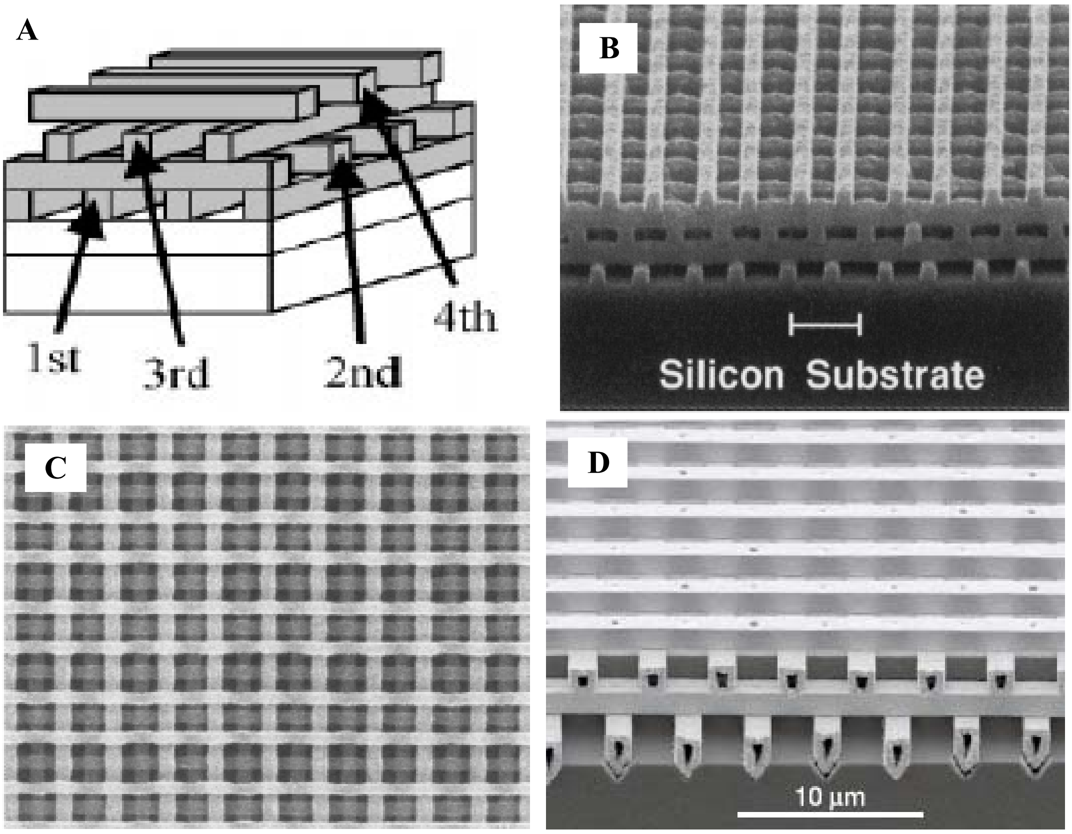

Figure 2.4 (A) Schematic illustration of one unit of woodpile-structure 3D PC (Noda et al., 2000b). (B) and (C) the side and top view of the woodpile-structure 3D PC (Lin and Fleming, 1999) and (D) SEM images of the metallic woodpile structure PCs (Fleming et al., 2002).

Direct laser writing of photoresist by multiphoton polymerization (Kawata et al., 2001) has also emerged as a promising technique for the rapid, cheap and flexible fabrication of photonic structures (Kawata et al., 2001). In 2002, two-photon photopolymerization was used to write a 3D structure with a fundamental pseudo bandgap at 1.9μm in a liquid resin (Straub and Gu, 2002). Direct writing of high quality large-scale fcc layer-by-layer structures was demonstrated by Deubel et al. (2004). Through silicon double inversion (Figure 2.5) a complex 3D photonic crystals of silicon with a complete PBG was obtained (Tétreault et al., 2006b). This combination of techniques offers great potential of producing PhCs with complete bandgaps in optical wavelength region.

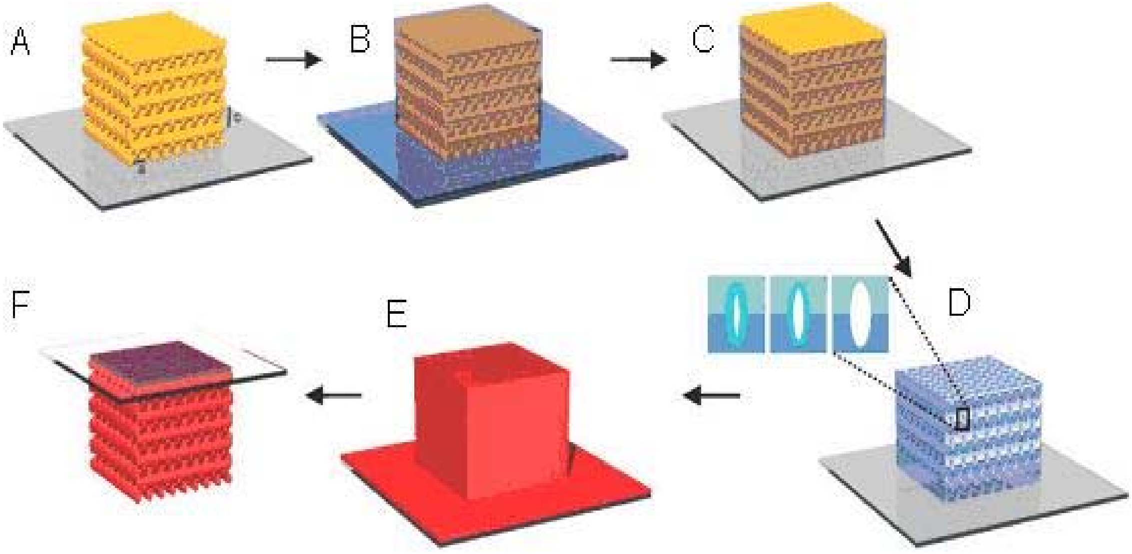

Figure 2.5. Schematic representation of the silicon double inversion method. a) The photoresist template fabricated by DLW. b) Full SiO2 infiltration by way of layer-by-layer chemical vapor deposition (CVD). c) Anisotropic reactive-ion etching of the top SiO2 overlayer to uncover the SU-8. d) Removal of the photoresist template by O2 plasma etching or calcination in air to obtain the SiO2 inverse woodpile; inset: re-infiltration of the SiO2 inverse woodpile by SiO2 CVD to fine-tune the rod filling fraction. e) Si infiltration of the inverse woodpile by low-pressure CVD. f) Attachment to an HF-resistant substrate with a polymer adhesive and removal of SiO2 inverse woodpile and substrate by chemical etching in an aqueous HF solution to obtain the Si woodpile replica (Tétreault et al., 2006b).

In 2002, García-Santamaría et al. (2002) fabricated a diamond structure consisting of colloidal microspheres by means of micro-robot manipulation, as shown in Figure 2.6B. In their fabrication process, the latex and silica nanospheres were arranged into body-centered cubic (bcc) structure and then the latex spheres were selectively removed with plasma etching. Consequently, the non-closed packed diamond structure was obtained. García-Santamaría et al. (2001) predicted that the silicon inverse structure templated from this diamond structure had a complete band gap of 12%.

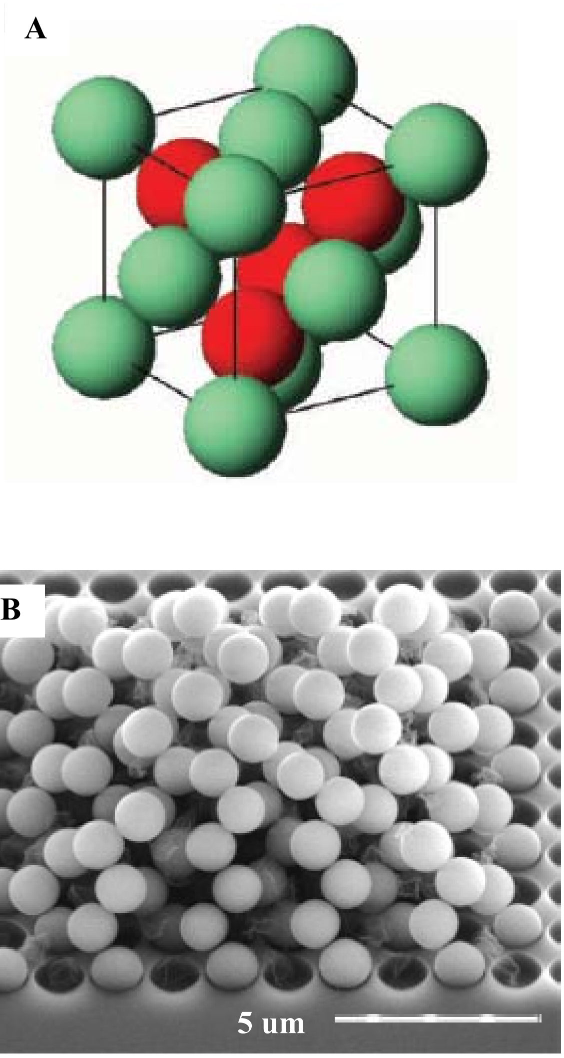

Figure 2.6 (A) PhC model with diamond structure (Maldovan and Thomas, 2004) and (B) Diamond array of silicon spheres (Garcia-Santamaria et al., 2002).

2.1.2 Colloidal self-assembly approaches to photonic crystals

Although the top-down method has already been proved applicable in fabrication of PhCs with precise structure control ability, its complexity and high cost limit its potential applications. By contrast, colloidal self-assembly approaches have recently been explored and demonstrated as a simple and inexpensive route to fabricate 3D PhCs. Self-assembly mostly result in close packed fcc arrangement of microspheres. Despite of the limitation of fcc structures and the low refractive index of colloidal beads, it is possible to take further steps to fabricate PhCs with a complete band gap using CC as templates. Normally a material with a high refractive index is infiltrated into the voids of CC and then the spheres are removed to obtain an inverse opal structure. In this step, not only is the refractive index contrast increased, but also the connectivity and topology of dielectric medium are improved.

2.1.2.1 Fabrication of colloidal crystals

A variety of methods are employed to organize monodispersed microspheres into highly ordered 3D arrays. Great efforts have been paid on reducing the unwanted defects formed in the process of crystal growth. The fundamental mechanism of self-assembly was also studied extensively.

Sedimentation and centrifuge. Sedimentation (Hunter, 1993) and centrifuge (Holland et al., 1999; Yan et al., 2000) seem to be the simplest methods to obtain crystalline arrangement of microbeads. In these processes microspheres move slowly under gravitational force (in sedimentation) or centrifugal force (in centrifuge) and form a 3D crystalline structure at the bottom of the container (Figure 2.7). Although it looks simple, this process involves a coupling of several complex processes including gravitational settling, translational diffusion and crystallization. Three parameters, namely the size and density of colloidal spheres and the rate of sedimentation, should be controlled carefully to allow the crystal growth.

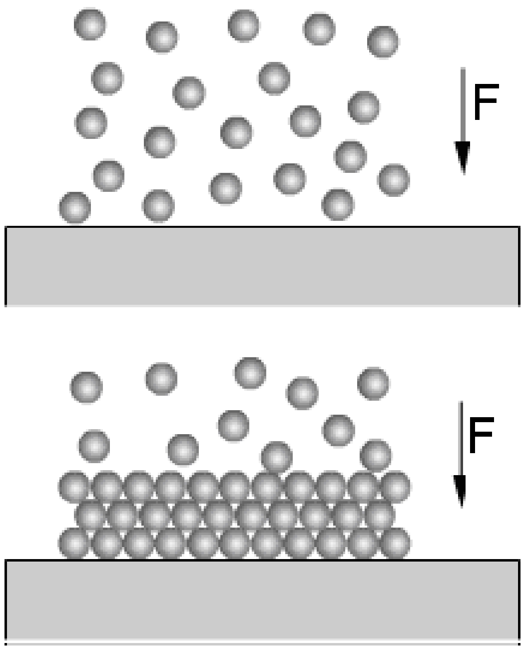

Figure 2.7 Schematic illustration of sedimentation and centrifuge method. In sedimentation method the force is gravitational force while it is centrifugal force in centrifuge process.

Thermodynamically, atoms or molecules tend to adopt the structure with the lowest Gibbs free energy. Self-assembly of spheres tends to form closely packed crystalline structures, such as fcc and hcp lattices. It has been demonstrated that the fcc structure has a slightly lower Gibbs free energy than the hcp structure with a difference of about 0.005 RT (Woodcock, 1997). Because this difference is so small that the structure obtained from sedimentation is normally a mixture of different crystalline phases. However, careful control over particle sedimentation velocity can allow one to obtain a single crystalline phase. To control the sedimentation velocity, two methods were applied. One is to use a proper solvent. Although both silica and polymer spheres can disperse in water, water is sometimes not a suitable solvent for sedimentation. For small particles, ethanol, which has a lower density and viscosity than water, has been found to be a good solvent. With large particles, a mixture of water and ethyl glycol or ethanol is a good choice (Blanco et al., 2000; Velev et al., 2000; Stachowiak et al., 2005). The other method is to use extra forces. The surface charge of the colloidal spheres can respond to a macroscopical electric field, thus the velocity of the sedimentation can be controlled by using an electric field parallel to gravity direction (Holgado et al., 1999; Rogach et al., 2000).

Although sedimentation and centrifuge are simple and easy to implement, a large quantity of defects and the large possibility of forming a mixture of colloidal crystal phase reduce its application in fabrication of PhCs.

Self-assembly under physical confinement. A simple device was designed to fabricate CCs by Xia's group (Park and Xia, 1998; Gates et al., 1999; Xia et al., 1999). In this method, colloidal spheres were assembled into a highly ordered structure in a specially designed packing cell (see Figure 2.8) under continuous sonication. Only under sonication was each colloidal sphere placed at the lattice site represented as a thermodynamic minimum. In this method the number of the layers was controllable because it is solely determined by the distance between the two substrates and the diameter of the spheres.

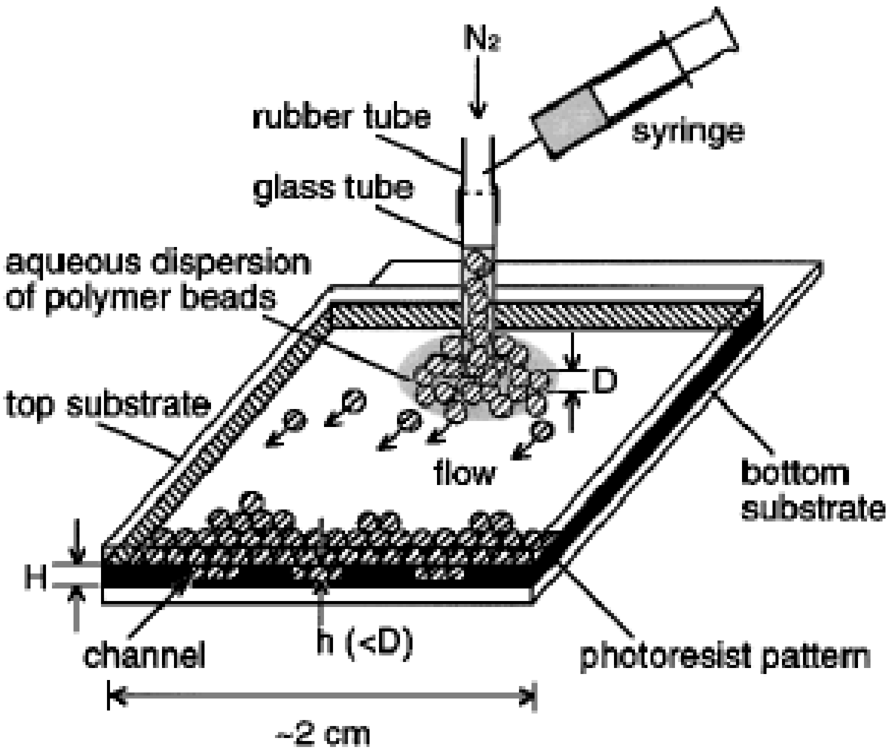

Figure 2.8 crystallization through physical confinement and hydrodynamic flow (Xia et al., 1999).

Vertical deposition method. In this method, a substrate such as a flat glass or silicon wafer is placed vertically in a colloidal suspension (Jiang et al., 1999a; Jiang et al., 1999b). The withdrawal of substrate or the evaporation of solvent causes the meniscus to wipe off the substrate surface vertically downward (see Figure 2.9). Under the combinational influence of convection flow and capillary force, colloidal particles accumulate to and organize at the edge of meniscus. CC grows along the direction in that meniscus wipe off the substrate. This method works well for silica and latex particles of diameter below 500 and 700 nm, respectively. However, it has two limitations: first, the long time of evaporation and second, more crucially, deposition is limited to smaller colloidal spheres that sediment slower than the solvent evaporates.

The typical evaporation rate used by Jiang et al. (1999a) was ca. 10^{-3} cm^3/min, and sedimentation of dense (ca. 2.0 g/cm^3) silica effectively precludes formation of continuous large-area colloidal crystal films out of silica spheres larger than ca. 500 nm. Sedimenting colloidal spheres depart from the meniscus, and the deposition process is terminated.

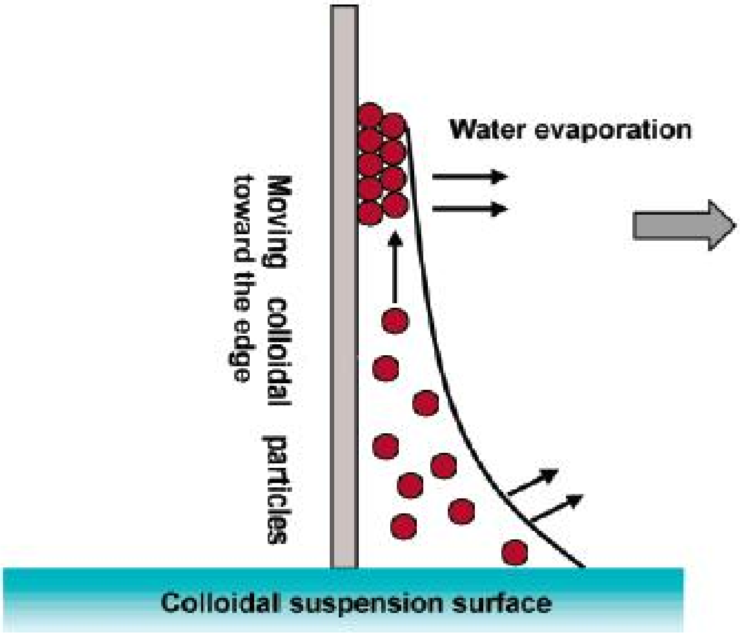

Figure 2.9 Scheme of vertical deposition

Two improvements were proposed to counteract the effect of sedimentation, namely, mechanical agitation (Yang et al., 2002) and convection induced by a temperature gradient (Vlasov et al., 2001). Vlasov et al. (2001) reported the successful application of heating from the bottom of a vial containing silica spheres dispersed in ethanol to induce convective flows and produce colloidal crystal films from 855 nm spheres. Mechanical agitation utilizing controlled gentle stirring was utilized successfully by Ozin and co-workers (Yang et al., 2002) for confined crystallization of large silica spheres within controlled geometry surface relief patterns in optical microchips. Mechanical agitation did not work well for the preparation of continuous colloidal crystal films. It seems that the swirl created by stirring disturbs the meniscus and impedes successful growth of continuous colloidal arrays. Low pressure was also used to accelerate ethanol evaporation and to counteract sedimentation (Kitaev and Ozin, 2003). This method proves to be very successful for self-assembling large (up to 1.5 μm) polystyrene (PS) latex spheres, and while it extends the self-assembly range for the silica spheres up to ca. 800 nm diameter, counteracting the sedimentation rate of faster sedimenting silica colloids of ca. 1 μm in size seems to be quite challenging. An isothermal heating evaporation-induced self-assembly method was demonstrated to further reduce the limitations on silica sphere size (Wong et al., 2003). By heating the solvent (ethanol) very close to the boiling point, the spheres were kept suspended in the dispersion by convection flows, and the time of growth was shortened considerably to about 1 h for centimeter extents of the film. A flow-controlled vertical deposition method was proposed to counter the effect of the sedimentation of the sphere in our group (Zhou and Zhao, 2004).

Horizontal Deposition. Zental' group (Muller et al., 2000) has successfully prepared CCs by drying drops of emulsion spread on a microscope placed horizontally. This method was further developed and the underlying mechanism was studied by Zhao's group (Yan et al., 2005d). In the latter work, concentrated colloids were spread on various substrates and allowed to dry in room temperature. In this method the growth of CCs proceeded from the edge to the center of the substrates, and voids were left at the center. This was because that water evaporation caused meniscus shifting from periphery to the center and the convection flow and capillary force caused the particles moving to the meniscus, reducing the concentration of particles in central area, as illustrated in Figure 2.10.

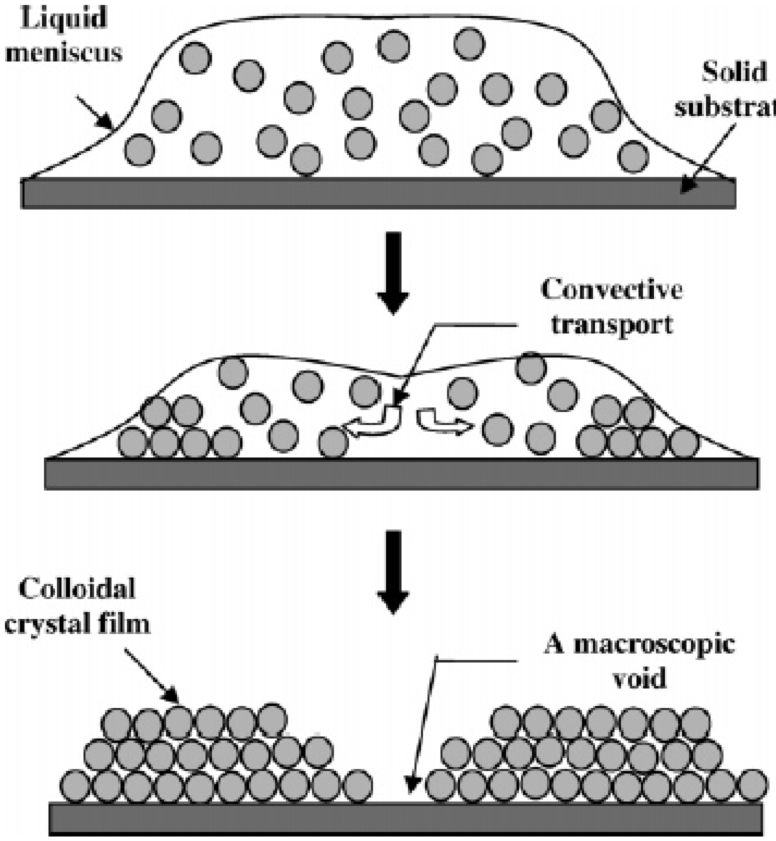

Figure 2.10. A scheme showing the inward self-assembly mechanism for colloidal crystal films deposited on a horizontal solid substrate (Yan et al., 2005d).

Other methods. Self-assembly of particles can not only happen on the solid substrates, but also on the surface of liquids. This leads to the method of floating self-assembly. The surface of mercury and gallium were used as substrates to allow the growth of CCs (Griesebock et al., 2002). PS microspheres were found also self-organizing at the surface of water (Im et al., 2002; Im and Park, 2002; Zeng et al., 2002; Im et al., 2003). Electrohydrodynamic deposition method was employed by Trau et al. (1996; 1997) to fabricate CCs of both silica spheres (0.9 μm in diameter) and PS spheres (2 μm in diameter).

2.1.2.2 Infiltration of the colloidal crystals

To obtain a PhC with a complete band gap, it is necessary to infiltrate the interstices among the spheres in CCs with a material of high RI, followed by removal of the colloidal spheres. The infiltration process influences the morphology and the optical property of the inverse opal greatly. Because incomplete infiltration may lead to the collapse of the inverse opal structure, complete and uniform infiltration is important. Many infiltration techniques have been developed to precisely control the infiltration process.

S**oaking method**. Soaking method is a simple and effective method. Through soaking CCs in a precursor, followed by further reactions (e.g. polymerization, carbonization, hydrolysis, etc.) a desired material can be obtained and occupy the voids between the microspheres (Gates et al., 1999; Xia et al., 1999; Deutsch et al., 2000; Miguez et al., 2001b). This is termed precursor infiltration. Also, the CCs can be infiltrated directly with colloid containing metal or semiconductor nanoparticles (Vlasov et al., 2001).

Electrodeposition. An artificial opal was placed on the cathode and a semiconductor was electrodeposited directly in the voids of the opal (Braun and Wiltzius, 1999). The most obvious advantage is that the deposition grows from the bottom to the top of the template, leading to a complete filling. Additionally electrodeposition can be used for making II-VI, III-V and IV group semiconductors such as CdS and ZnO, etc. and metallic materials such as Pt (Bartlett et al., 2000; Luo et al., 2001), Pd (Bartlett et al., 2000), Ni (Xu et al., 2000; Luo et al., 2001), Ag (Lellig et al., 2002), Au (Wijnhoven et al., 2000; Xu et al., 2000).

Chemical Vapor deposition (CVD). CVD, a widely used materials-processing technique has been used for fabricating PhCs of high dielectric constants (Yates et al., 1998; Dag et al., 1999; Blanco et al., 2000; Chomski and Ozin, 2000; Vlasov et al., 2001). Because silicon and gallium can be easily be implemented in the present photonic technology, it can be easily integrated in the optical devices. PhCs of silicon with a RI of 3.5 (Blanco et al., 2000) and gallium with a RI of 4 (Miguez et al., 2001a) have been fabricated, which guarantee a sizeable full bandgp (Sozuer et al., 1992).

2.1.2.3 Removal of colloidal particles

To get inverse opals, the final step is to remove the colloidal particles. Calcination and dissolving method were normally used to remove polymer particles. Due to the contraction induced by high temperature, calcination could have an enormous impact on the optical properties of the inverse opal (Yan et al., 1999; Yan et al., 2000; Yang et al., 2001). Silica is often removed by chemical etching with a low-concentration hydrofluoric acid solution. The main problem of HF-etching is that HF is extremely toxic and corrosive.

2.2 The Incorporation of Engineered Defects in Photonic Crystals

Although it is a primary desire to fabricate perfect PhCs without intrinsic defects, engineering of artificial defects (point, line, and planar defects) in 3D PhCs is also of paramount importance especially for practical device applications (Joannopoulos et al., 1995; Joannopoulos et al., 1997). Like impurity atoms doped in semiconductors, artificial defects in PhCs act as photonic dopants. Depending on their structure, they can offer PhCs different functions. For example, the point defect embedded can trap or localize photons and act as a micro-cavity with a high quality factor (the measure of energy loss, the higher the quality factor, the lower the energy loss) (John, 1987; Yablonovitch, 1987; Joannopoulos et al., 1997). A line defect introduced can direct the propagation path of photons, acting as an ultra-compact and low-loss optical waveguide (John, 1987; Yablonovitch, 1987; Joannopoulos et al., 1997). A planar defect on the other hand can be used a slab waveguide or a cavity depending on the direction of the incident optical field (Istrate and Sargent, 2002). Many photonic applications, such as optical waveguides, splitters, couplers, switches, micro-lasers, and others, exploit these properties (Joannopoulos et al., 1995). Thus, an important issue for the practical application of 3D PhCs is how to introduce artificial defects within the structure in a controllable manner, no matter which kind of fabrication method is used.

Unfortunately, artificial defect engineering in self-assembled 3D PhCs has been a great challenge for a long time. It is only very recently that some exciting advancements have been achieved. There are mainly two reasons behind this delay. The first reason is that artificial engineering in self-assembled 3D PhCs is not as straightforward as that in 3D PhCs fabricated using the “top-down” method (Noda et al., 2000b; Ogawa et al., 2004; Qi et al., 2004; Imada et al., 2006) or the laser direct-writing technique (Deubel et al., 2004; Moon et al., 2005a; Seet et al., 2005; Tétreault et al., 2006a). In a self-assembly process, the natural tendency of colloidal spheres is to form a “perfect” crystal, which makes the insertion of artificial defects challengeable. Techniques other than self-assembly have to be introduced to introduce engineered defects. The second reason lies on the high density of intrinsic defects (e.g. cracks, vacancies, dislocations, and grain boundaries) present in the early PhCs made by using the self-assembly method (Zhu et al., 1997; Holgado et al., 1999). Thus, many of the previous efforts were placed on obtaining a perfect self-assembled colloidal PhC without the presence of intrinsic defects rather than on how to introduce artificial defects (Miguez et al., 1998; Park et al., 1999; Muller et al., 2000). At the same time, the existence of intrinsic defects presents difficulties for the characterization of artificially induced defects. Since the availability of the vertical deposition method described by Colvin’s group (Jiang et al., 1999a), together with that of other improved methods developed afterwards (Gu et al., 2001; Wong et al., 2003; Jin et al., 2005b; Yan et al., 2005d), the research progress has dramatically advanced. Nowadays, planarized colloidal crystals with a high optical quality can be grown on a wide variety of substrates.

Over the past years, great efforts have been put on introduction of artificial defects within a colloidal PhC by using a combination of self-assembly methods and micromachining techniques.

2.2.1. Line Defect Engineering

A line defect constructed inside an otherwise perfect 3D PhC constitutes a PhC waveguide. Such a device represents a new kind of optical waveguides whose functional principle completely differs from that of the conventional waveguides. In the conventional waveguides, e.g. optical fibers or semiconductor ridge waveguides, light is confined by using the total internal reflection, thus suffering large bend loss. In a PhC waveguide, light is confined by the PBG. Once a light with a frequency within the band gap of the 3D PhC is coupled into the waveguide, it can only propagate along the path of the line defect introduced since the guided mode is prohibited to escape into the surrounding PhC. Thus PhCs with line defects in principle can serve as a lossless waveguide with ultra-compact size, even can guide light around tight corners. Achieving lossless optical waveguides with a sharp bend has been of great interest since they might lead to the miniaturization of optical components and eventually realize the high-density photonic integrated circuits.

Up to now, various approaches have been employed to incorporate line defects in colloidal crystals. Generally, underling these approaches there are two different methodologies: a) modifying the structures of the colloidal crystals through direct writing by confocal microscopy or high-energy beam after self-assembly, b) templating the growth of colloidal crystals.

2.2.1.1 Line defect engineering by directly modifying the structure of the colloidal PhCs

As a significant first step, Braun and coworkers developed a multi-photon photopolymerization method for introducing micron-scale line defects into a monomer-infiltrated silica colloidal PhC (Lee et al., 2002; Pruzinsky and Braun, 2005). The process can be schematically illustrated in Figure 2.11 (Taton and Norris, 2002). After colloidal self assembly, the voids between the silica spheres were filled with a photosensitive monomer (Figure 2.11a). A focused laser beam was used to scan and polymerize small volumes of the infiltrated monomer, thus writing a line defect within the structure (Figure 2.11b). After the unexposed monomers have been removed, the engineered defect can be visualized by staining the structure with a fluorescent dye (Figure 2.11c). Figure 2.11d schematically illustrates a 3D PhC with a full PBG (inverse opal) and an artificial line defect in its interior. By using the similar strategy, Zental and coworkers reported the incorporation of both emitters and defects in an inverted polymer opal (Lange et al., 2006). A photo-polymerizable resin in which a fluorescent dye was dissolved was first filling into the voids in an inverse opal PhC. Two-photo polymerization was then performed to polymerize the resin at the focus. The unexposured monomer can be removed after development, leaving artificial defects created inside the inverse opal.

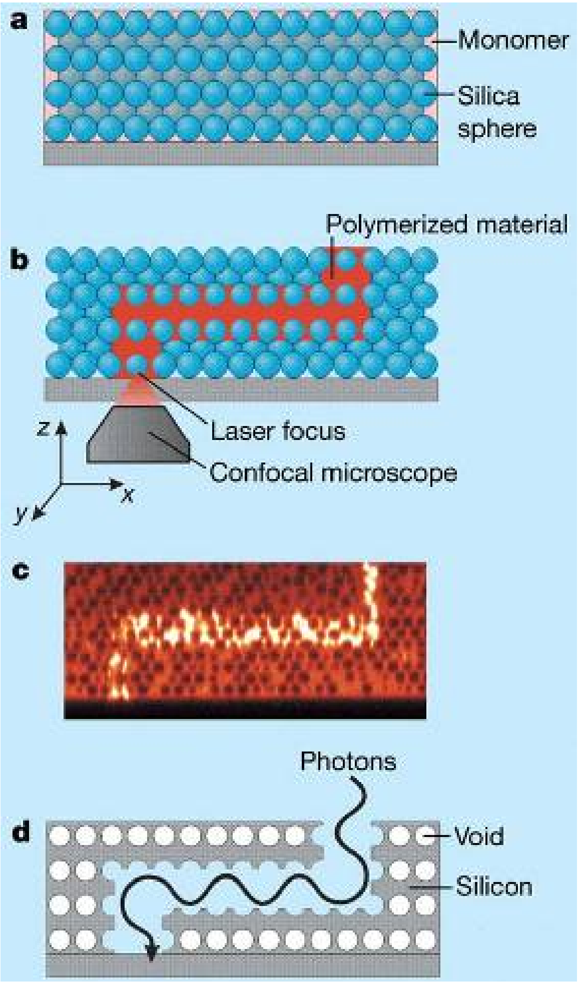

Figure 2.11. Schematic illustration of introducing micron-scale line defects into a self-assembled 3D PC by using the multi-photon photopolymerization method (Taton and Norris, 2002). (a) infiltration of a photosensitive monomer into a silica colloidal crystal, (b) polymerization with a focused laser beam, (c) the engineered line defect within the 3D structure, (d) a silicon inverse opal with an artificial line defect in its interior (Taton and Norris, 2002).

Direct electron-beam writing technique has been employed to construct deterministic defects in self-assembled poly (methyl methacrylate) (PMMA) opals (Ferrand et al., 2003; Romanov et al., 2003; Ferrand et al., 2004). PMMA is in nature a resist material typically used in electron beam lithography. Once PMMA colloidal spheres are self-assembled into an opal film, EBL can be directly implemented on the film, forming intentional defects on the surface of the PMMA opal film. After repeating growth of the PMMA opal film on the patterned one, a buried line defect in a self-assembled 3D PhC can be achieved (Romanov et al., 2003). With the similar method, López and coworkers (Juarez et al., 2004) reported the formation of micron-scale defects in a silica-infiltrated PMMA opal. As the Figure 2.12 shows, after growth of the PMMA colloidal crystal, silica was infiltrated into the opal by using chemical vapor deposition (CVD) method. Then EBL was used to pattern the silica-PMMA composite. After dissolution of the exposed PMMA, an area of inverted opal was selectively formed within a silica infiltrated PMMA opal as an artificial defect. However, the applicability of the multi-photon polymerization is limited to the polymer materials. The direct electron-beam writing method to non-PMMA colloidal crystals is also challengeable.

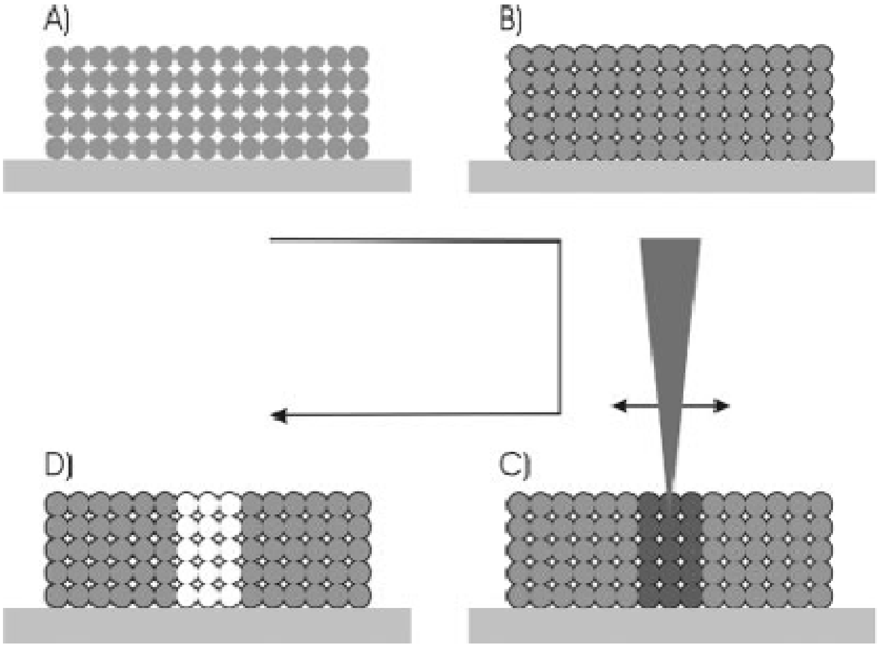

Figure 2.12. A process shows the selective formation of an inverted-opal area in an opal by using electron beam lithography. A) Growth of PMMA opal film on a substrate. B) Infiltration of silica into the PMMA opal by using CVD technique. C) Patterning of the silica-infiltrated PMMA opal by using electron beam lithography. D) Selective formation of inverted-opal area in the PMMA opal by dissolution of the exposed PMMA (Juarez et al., 2004).

Micron-scale line defects on the surface of an inverse silicon PhC have been obtained by modification of the local refractive index using laser micro-annealing techniques (Tetreault et al., 2003). In this method, a spatially resolved laser was used to selectively anneal amorphous silicon to be nanocrystalline silicon. Because of the difference of the refractive index of the amorphous and nanocrystalline silicon, refractive index patterns can be obtained in an amorphous silicon inverse opal. Thus the method enables the creation of micrometer-sized extrinsic defects on the surface of a 3D PhC. Although the inverse silicon PhC possess a full PBG, it will be interesting to show whether the small refractive index contrast between the nanocrystalline silicon line defect and the surrounding amorphous silicon can realize an optically confined waveguide. With the similar method, laser direct writing by using a pulsed deep-ultraviolet F_2 laser has been employed to form extrinsic line defects on the surface of silica colloidal crystals (Li et al., 2005).

Norris and co-workers (Jun et al., 2005) have demonstrated the fabrication of 1-µm air-core line defects embedded in a silicon PhC by means of colloidal-crystal-templating and multiphoton polymerization techniques. In this method, a silica opal was first infiltrated with a hybrid photoresist containing organosilica precursor. A laser-scanning confocal microscope was then used to construct patterns inside the silica opal via multiphoton polymerization. After development and annealing process, a silica defect pattern can be created inside the silica opal. Silicon was then infiltrated into the silica opal by using low-pressure CVD method. The silica opal template together with the silica line defects were finally removed by chemical etching, resulting in a silicon inverse opal with embedded (Akahane et al., 2003) line defects.

The performance of the PhC-based photonic device has proved to be closely related to the dimension of the line defects introduced (Akahane et al., 2003; Galli et al., 2005; Tanaka et al., 2005). In conventional 2D PhC-based waveguide devices, the dimension of the line defects is typically comparable with the lattice constant of the 2D PhC (Akahane et al., 2003; Galli et al., 2005; Tanaka et al., 2005). For self-assembled 3D PhCs working within the visible and near-infrared wavelength scope, the lattice constant or the sphere size are typically of submicron scale (Miguez et al., 1998; Blanco et al., 2000; Vlasov et al., 2001). Thus, line defects with submicron dimensions are desired for light-waveguiding applications. However, the smallest feature size of the line defect achieved is limited to about 1 μm because of the resolution of the confocal microscope (see Figure 2.13).

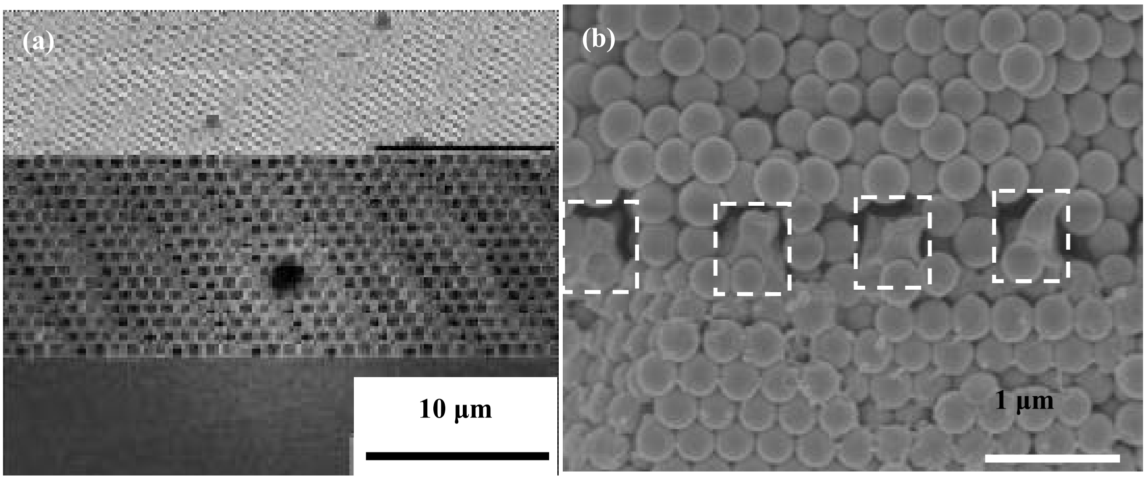

Figure 2.13 (a) Silicon inverse opal with an air-core line defect, of which the size is around 1 μm (Jun et al., 2005). (b) Silica opal (sphere size 450 nm) with sub-micron line defects. The white rectangular highlights the presence of the line defect (550 nm × 480 nm PMMA strips) embedded.

2.2.1.2 Line defect engineering by templated growth of colloidal crystals

The combination of colloidal self-assembly and conventional optical lithography provides an alternative approach to building line defects within self-assembled colloidal PhCs. Ye et al. (2002) have described the fabrication of air-core micron-scale line defects within a silica inverse opal using this strategy. Micron-scale photoresist line patterns were constructed on a silicon or glass substrate by using typical optical lithography. PS colloidal spheres were self-assembled into an opal film on the pattered substrate. After removal of the photoresist strips and inverting the structure with silica, air-core line defects confined between a silica inverse opal and a dielectric substrate were obtained (Figure 2.14a). A similar structure, i.e. a rib-type Si_3N_4 waveguide surrounded by a silica opal (Figure 2.14b), has also been reported by Baek and Gopinath (2005), in which the ridge waveguide can be regarded as a line defect within the silica opal. However, a line defect constructed in the bottom or on the surface of a 3D PhC (as constructed by using E-beam direct writing noted above) can not act as an ideal light-waveguiding structure because the line defect was not fully embedded in a 3D PhC, which may lead to the leakage of guided modes from the surrounding dielectric.

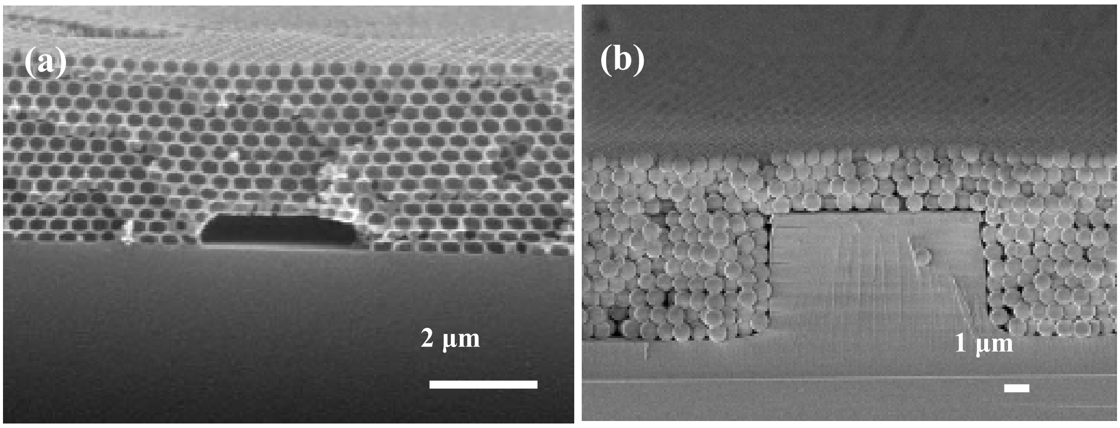

Figure 2.14 (a) An air-core line defect on the bottom of a silica inverse opal (Ye et al., 2002). (b) A Si_3N_4 ridge-type waveguide on the bottom of a silica opal to form a line defect within the opal (Baek and Gopinath, 2005).

Very recently, Ozin's group (Vekris et al., 2005) and our group (Yan et al., 2005c) have independently demonstrated a straightforward method to embed micron-scale line defects within the interior of a self-assembled 3D PhC. The fabrication method was based on a multi-step process. A silica colloidal crystal film was first deposited on a Si substrate with the typical vertical deposition method (Jiang et al., 1999a). A layer of photoresist (AZ P4620, Clariant) was then spin-coated on the opal film. Conventional optical photolithography was employed to pattern photoresist lines on the surface of the silica opal film. After that, silica opal film was re-grown on the patterned one, resulting in a silica colloidal crystal with photoresist line defects embedded in its interior. The photoresist can be removed simply by chemical etching, leaving a silica colloidal crystal with an air-core line defect (Figure 2.15a). Consequently, a high-refractive-index material like silicon can be infiltrated in the voids of the silica colloidal crystal by using a CVD method. Removal of the silica spheres template may yield an air-core line defect embedded in the 3D PhC with complete PBG (e.g. silicon inverse opal). The feature size of the line defects can be easily controlled by manipulating the photolithographic parameters like photoresist type, spin-coating time and speed, and so on. It was demonstrated that line defects with complex patterns, such as ring, Y-branch, X-cross, and S-band, can be introduced into the silica colloidal crystal in a similar way to meet the requirements of various photonic devices (e.g. optical coupler, switch, Machn-Zehnder interferometer) (Yan et al., 2005c). In addition, the air-core line defect can be filled with colloidal spheres with different size or material (Figure 2.15b), resulting in a heterogeneous colloidal PhC or a colloidal crystal with a three-dimensional line defect (Yan et al., 2005b).

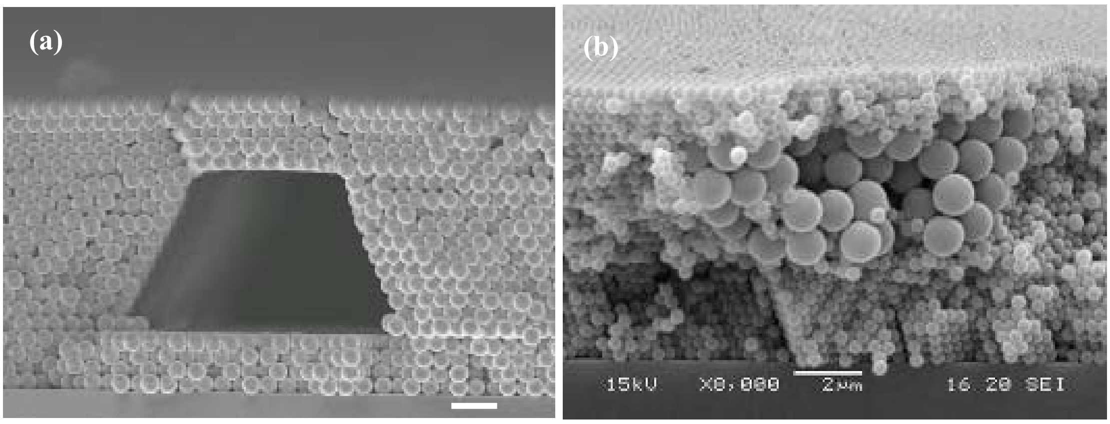

Figure 2.15 (a) A micron-scale air-core line defect embedded in a silica colloidal crystal opal (sphere size 0.39 μm) (Yan et al., 2005c). (b) A three-dimensional micron-scale line defect embedded in a silica colloidal crystal opal (sphere size 0.39 μm). The 3D line defect is composed of a colloidal strip of PS spheres (1.1 μm) (Yan et al., 2005b).

2.2.2. Planar Defect Engineering

Planar defects in PhCs can introduce allowed photon states within the otherwise forbidden bandgap frequencies. If a light of the allowed frequency is launched into the PhC perpendicularly to the planar defect, a minimum will appear within the reflection peak associated with the PBG. In this case, the planar defect acts as an optical cavity

(Istrate and Sargent, 2002). On the other hand, if the light is launched into the PhC and coupled with the planar defect in a parallel manner, the light will be confined and propagate along the planar defect. In this case, the planar defect serves as a slab optical waveguide (Istrate and Sargent, 2002).

Generally, the fabrication and the optical characterization of planar defects are relatively easier than those of linear defects and point defects. A variety of planar defects in self-assembled 3D PhC has been achieved by using a layer-by-layer deposition strategy. In general, a colloidal crystal film was first deposited on a substrate, followed by the deposition of a defect layer. The sequential growth of another layer of colloidal crystal resulting in a planar defect sandwiched in the self-assembled 3D PhC (Egen et al., 2003; Wostyn et al., 2003; Zhao et al., 2003; Masse et al., 2006). The planar defects can be a layer of colloidal spheres with different sizes or different refractive indexes from the host opal (Figure 2.16a), dielectric materials (Figure 2.16d), polyelectrolyte multilayers (Figure 2.16b), or even nanocrystalline materials (Figure 2.16c).

A monolayer of spheres with different sizes or different refractive indexes can be sandwiched into two opal films by using the Langmuir-Blodgett method (Wostyn et al., 2003; Zhao et al., 2003; Masse et al., 2006), withdrawing technique (Egen et al., 2003), or spin-coating (Wang et al., 2006). For the incorporation of polyelectrolyte multilayers, either a layer-by-layer deposition of oppositely charged electrolytes directly on the bottom opal film or a transfer-printing of the as-formed polyelectrolyte multilayer can be used (Figure 2.17) (Fleischhaker et al., 2005a; Fleischhaker et al., 2005b; Tetreault et al., 2005; Fleischhaker et al., 2006).

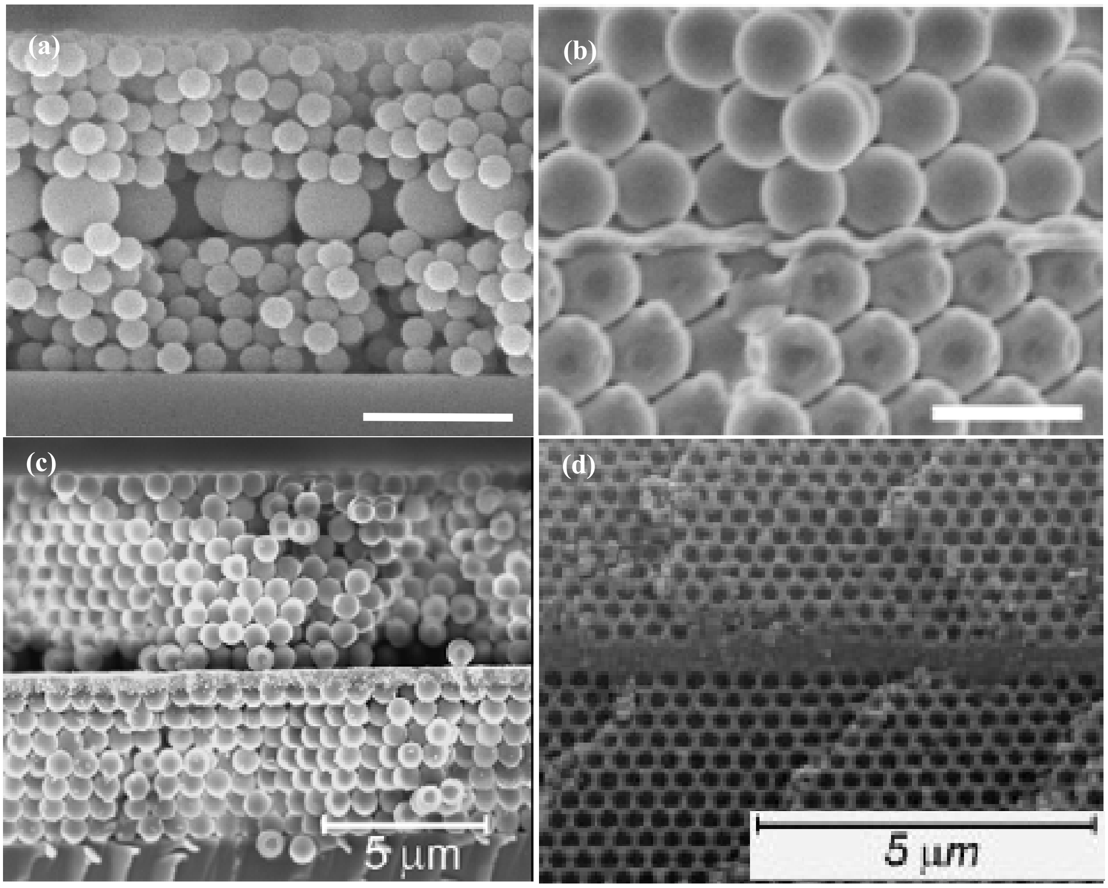

Figure 2.16 (a) A monolayer of large colloidal spheres (980 nm silica spheres) embedded in a colloidal crystal (390 nm silica spheres) as a planar defect (Masse et al., 2006). (b) A polyelectrolyte multilayer sandwiched in a silica colloidal crystal (280 nm colloidal spheres) as a planar defect (Fleischhaker et al., 2005b). (c) A layer of nanocrystalline TiO_2 embedded in a PS colloidal crystal (700 nm colloidal spheres) as a planar defect (Pozas et al., 2006). (d) A silica dielectric layer sandwiched in a silica inverse opal (from 375 nm PS colloidal spheres) as a planar defect (Tetreault et al., 2004).

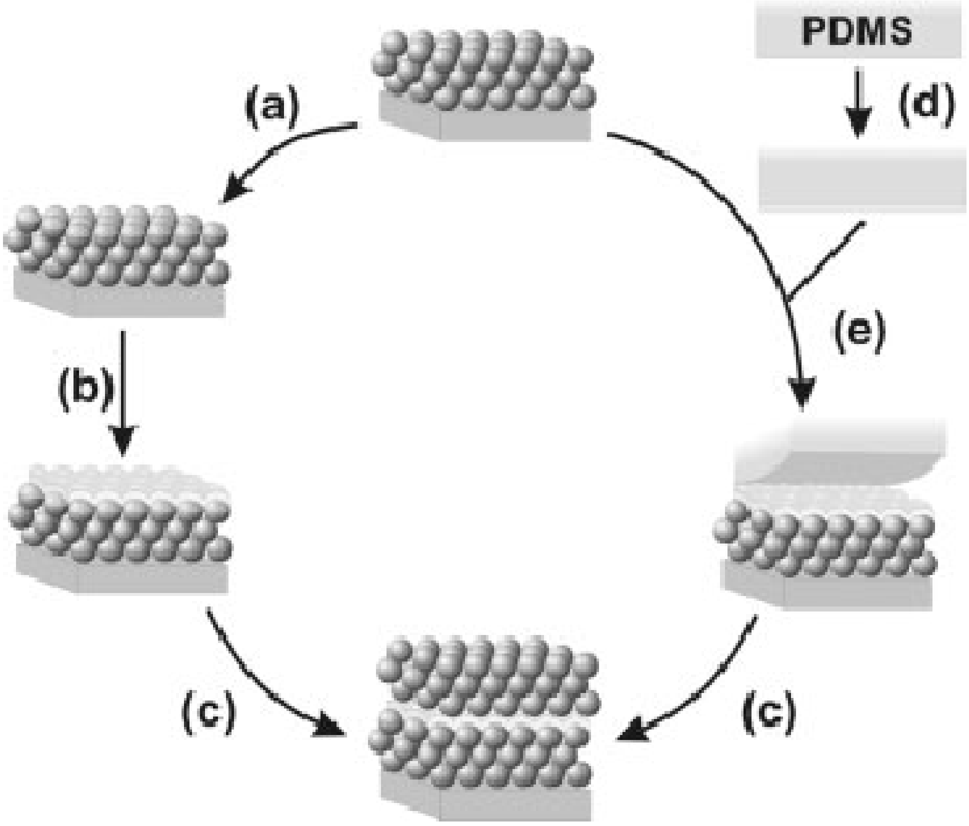

Figure 2.17 Two different methods used to introduce polyeletrolyte multilayers into a colloidal crystal as planar defects. Both methods start with the growth a planar opal film on a substrate. (a) The top of the colloidal crystal is sputter-coated with a thin layer of gold (~5 nm), which was then chemically treated to be negatively charged. (b) The polyelectrolyte multilayers were deposited on the gold-coated silica colloidal crystal in a layer-by-layer manner by alternate immersion in a solution of polycation and one of polyanion. (c) A second silica colloidal crystal film was grown on top the planar defect. (d) In another transfer-printing route, the polyelectrolyte multilayers were first grown on a flat poly (dimethylsiloxane) (PDMS) substrate. (e) The PDMS was then contacted with the opal film surface to transfer the whole polyelectrolyte multilayers to the surface of the as-formed silica colloidal crystal. A sequential growth of the second silica opal film resulted in a planar defect sandwiched in the silica colloidal crystal (Tetreault et al., 2005).

By using the spin-coating method, Miguez and coworkers (Pozas et al., 2006) reported the insertion of a layer of nanocrystalline TiO_2 into a silica colloidal crystal as a planar defect. A universal method to place dielectric planar defects within 3D PhC involves the CVD technique (Palacios-Lidon et al., 2004; Tetreault et al., 2004). In the method concurrently developed by Lopez’s group (Palacios-Lidon et al., 2004) and Ozin’s group (Tetreault et al., 2004), a PS colloidal crystal film was over-infiltrated with silica by using CVD technique, resulting in a homogeneous silica surface layer on the top of the infiltrated PS opal. Then the second PS colloidal crystal film was grown on the silica layer. The top-layer PS opal was infiltrated with silica with the same technique. Removal of the PS spheres template yielded a silica inverse opal with a dielectric silica layer as a planar defect. The method allows precise control over the thickness of the planar defects introduced, thus making the tuning of the optical property of the system possible (Palacios-Lidon et al., 2004; Tetreault et al., 2004).

The optical properties of the colloidal PhCs with planar defects were widely studied (Wostyn et al., 2003; Zhao et al., 2003; Palacios-Lidon et al., 2004; Tetreault et al., 2004). The introduction of a planar defect produces localized states for photons in the bandgap. The position of the states depends not only on the property and the thickness of the defect, but also on the characteristics of the PhCs sandwiching the defect. A defect layer with a higher effective refractive index arouses increased-index defect, which originates from the conduction band, while a defect with a lower effective refractive index produces decreased-index defect, originating from the valence band. The spectral position of the defect state oscillates periodically between the low-wavelength edge and the high-wavelength edge of the gap with the increase of the defect thickness/lattice parameter ratio (see Figure 2.18) (Palacios-Lidon et al., 2004; Tetreault et al., 2004).

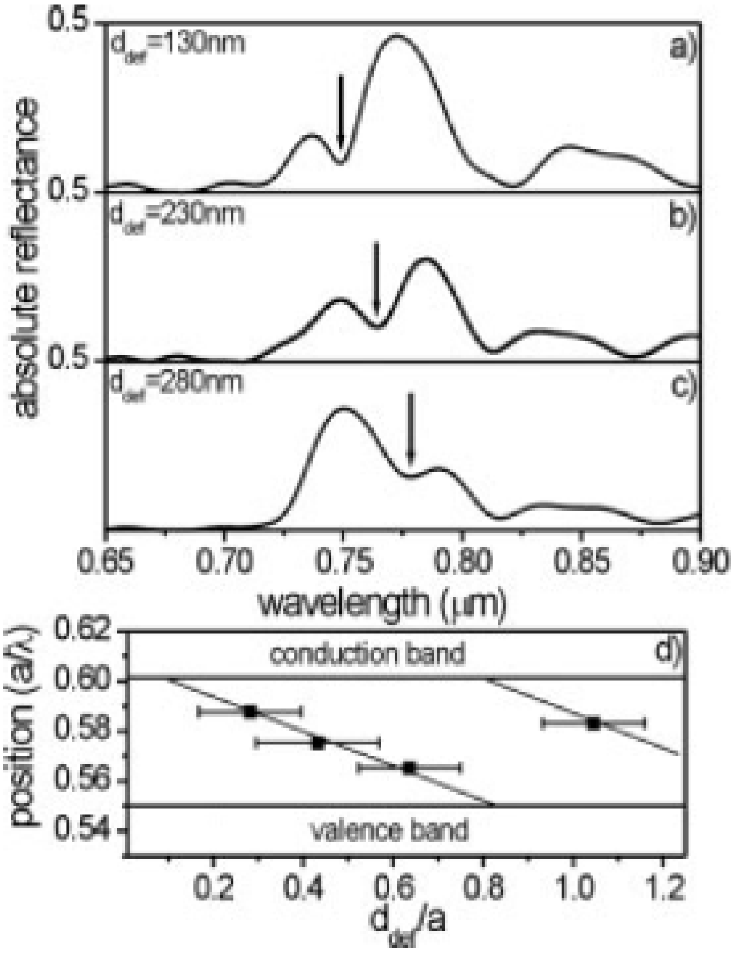

Figure 2.18 Reflectance spectra of engineered defects in 311 nm SiO2/PS opals. Silica film planar defects of a) 130 nm, b) 230 nm, and c) 280 nm are embedded in the photonic crystal. Depending on the defect thickness the dip position shifts through the gap, starting at low wavelengths (high energies). d) Spectral position as a function of defect thickness. The straight lines are guides to the eye (Palacios-Lidon et al., 2004).

Recently, noteworthy efforts in planar defect engineering have been made to offer the introduced planar defects with multiple functionalities. Ozin and coworkers (Fleischhaker et al., 2005b; Tetreault et al., 2005) have demonstrated the fabrication of a series of planar defects in colloidal PhCs based on polyelectrolyte multilayers (PEMs). Various functional materials can be incorporated in these layers without loss of function, thus opening an opportunity of tuning the defect states of the colloidal PhCs by external stimulations. Two approaches of incorporating the PEMs were proposed (Tetreault et al., 2005). The first one involves the modification of the surface of the colloidal crystal, which producing a wettability difference between the surface and the bulk. Then oppositely charged polyelectrolyte layers are deposited alternatively directly on the surface. The second one starts with the deposition of a PEM onto a flat piece of poly (dimethylsiloxane) (PDMS), followed by transfer-printing the PEM onto the surface of the colloidal crystal. The PEM defect formed by deposition of poly (sodium styrenesulfonate) (PSS) and poly (allylamine hydrochloride) (PAH) can be accurately adjusted by the pressure-controlled vapor absorption (Tetreault et al., 2005). An azo polyelectrolyte was employed to fabricate a PEM defect layer sensitive to photochemical and thermal stimuli (Fleischhaker et al., 2005b). Redox swithchable planar defect was achieved through incorporating a polyferrocenylsilane (PFS) metallopolymer PEM (Fleischhaker et al., 2005a). More recently, it was demonstrated that DNA-based polyelectrolyte (Fleischhaker et al., 2006) can be used to fabricate biologically sensitive planar defect structures. These functional PEM defects provides the structures many potential applications such as sensors, electrochemically tunable microcavities, and electrochemically tunable PhC-based laser sources (Fleischhaker et al., 2005a).

2.2.3 Point Defect Engineering

Point defect in an otherwise perfect 3D PhC can trap or localize the photons of certain frequencies in a very small volume (λ^3), form so-called micro-cavity. Such a micro-cavity has a very high quality factor (Q), which is of great importance to achieve low-threshold micro-lasers. Introducing point defects into 3D PhCs has proven quite difficult, with only a few examples reported (Pradhan et al., 1996; Gates and Xia, 2001; Matthias et al., 2004; Ogawa et al., 2004; Qi et al., 2004; Lai et al., 2005; Palacios-Lidon et al., 2005). By using a top-down lithographic method, 3D GaAs (Ogawa et al., 2004) and silicon (Qi et al., 2004) PhCs with designed point defects have recently been fabricated. Matthias *et al.* (2004) have shown the possibility of introduction of point defects into a 3D silicon PhC by using modified electrochemical etching and lithographic methods. Direct laser writing (Scrimgeour et al., 2006) and lithographic masks (Lai et al., 2005) have been used to produce point defects within polymer 3D PhCs fabricated by using holographic lithography.

Introduction of point defects into self-assembled 3D PhCs was first attempted by doping impurity colloidal spheres of different sizes or dielectric strengths during the self-assembly process (Pradhan et al., 1996; Gates and Xia, 2001; Vlasov et al., 2001; Palacios-Lidon et al., 2005). Waston and co-workers (Pradhan et al., 1996) reported the impurity modes in the optical stop bands of a intentionally doped PS colloidal crystal. They added a small volume of smaller spheres and larger spheres into the colloidal suspension as accepter dopants and donor dopants, respectively. Experimental results showed that both the accepter and donor dopants could introduce defect modes within the stop bands. At the same time, it was found that the presence of the impurities leaded to a significant widening of the optical stop band (Figure 2.19) (Pradhan et al., 1996). Xia's group (Gates and Xia, 2001) and Lopez's group (Palacios-Lidon et al., 2005) also reported the doping of impurities into a self-assembled PhC. Both of their study showed that with the increase of the impurity concentration the attenuation of transmittance within the optical stop band decreased while the defect modes associated with the impurities within the stop band were not observed. The reason lies in that such point defects introduced by doping are randomly distributed throughout the structure. For precisely manipulating the defect states within the stop band and for practical device applications, the position of the point defects should be controllable.

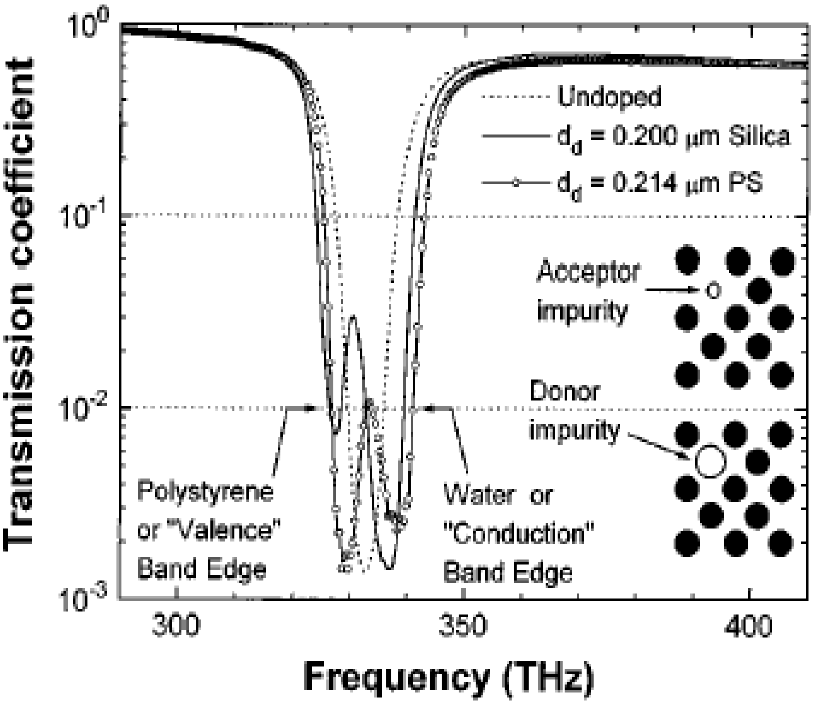

Figure 2.19 Near-infrared transmission spectra for PS colloidal crystals containing intentionally doped impurities. The dotted curve is a transmission spectrum for an undoped polystyrene colloidal crystal (sphere size 0.173 μm). The plain solid curve and the solid curve with open circles show the spectra for crystals doped with 0.200-μm silica (2% number fraction) and 0.214-μm polystyrene (10% number fraction), respectively. The polystyrene and the water band edges are also shown. The insets illustrate two different types of impurities. One is the acceptor impurity that caused by doping of small colloidal spheres and the other one is the donor impurity that caused by doping of large spheres (Pradhan et al., 1996).

For self-assembled polymer colloidal crystals from PMMA spheres, it is possible to introduce point defects precisely by using e-beam processing (Jonsson et al., 2005)˙

E-beam was employed to individually expose an array of spheres on the surface layer of a PMMA colloidal crystal. After development, an array of point defects can be defined on the surface of the colloidal crystal (Figure 2.20). If a second PMMA colloidal crystal can be deposited on the exposed one, followed by development to remove the exposed individual PMMA colloidal spheres, a colloidal crystal with embedded point defects can be obtained (Jonsson et al., 2005). Similarly, laser direct writing by using a pulsed deep-ultraviolet F_2 laser was employed to remove single microspheres of a silica colloidal crystal, forming extrinsic defects (point and line defects) on the surface of the silica colloidal crystal (Li et al., 2005). Scanning electron microscope with a variable pressure was also used to precisely create point defects on the surface of a self-assembled 3D PhC (Xie et al., 2006). However, the defects constructed via these techniques have to be written point by point, which is relatively time-consuming.

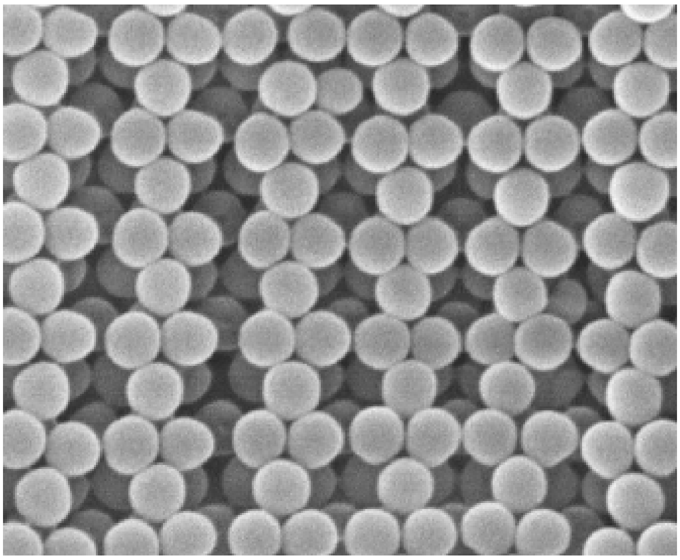

Figure 2.20 An array of point defects defined on the surface layer of a PMMA colloidal crystal (sphere size 498 nm) by using electron beam lithography (Jonsson et al., 2005).

Very recently, our group has developed a straightforward method to incorporate point defects within a self-assembled silica colloidal PhC in a controllable manner (Yan et al., 2005a). The fabrication method involved a couple of steps, including self assembly of colloidal spheres, nanoimprinting lithography, template-directed self assembly, and sequential growth of colloidal crystals (Figure 2.21a). By using the typical vertical deposition method (Jiang et al., 1999a), monodisperse silica colloidal microspheres were first assembled on a silicon substrate to form a planar opal film (host opal). Silica colloidal spheres were chosen because they are mechanically and thermally stable, allowing high-temperature processing such as infiltration of semiconductor materials using CVD technique to yield a 3D PhC with a full PBG (Blanco et al., 2000; Vlasov et al., 2001). After spin-coating a layer of PMMA polymer, nanoimprinting lithography was employed to produce a hole array on the surface of the PMMA layer. Further treatment by using mild oxygen plasma etching allowed the holes to penetrate the entire PMMA layer down to the surface of the underneath silica host opal. The resultant hole array was used as a template to direct the assembly of silica colloidal spheres of different sizes from the host silica spheres into the holes as point defects. After full removal the PMMA resist layer around the point defects by a second-time oxygen plasma etching, a point defect array of silica spheres was loaded on the surface of the host silica opal film (Figure 2.21b). Finally, vertical deposition was carried out again to re-grow the silica host opal. Thus, a silica colloidal crystal containing point defects within its interior was obtained. The eventual silica colloidal PhC (from 450 nm silica spheres) containing point defects within its interior can be seen from Figure 2.21c, where the arrows highlight the presence of point defects (390 nm silica spheres). One additional advantage of this method is that the point defects and line defects can be embedded into the colloidal PhC simultaneously, between which the distance can be easily controlled by properly designing the nanoimprinting mould. This property is of importance since in many cases the point defects need to be incorporated together with the line defects to realize a certain photonic functionality to meet the requirement of practical photonic devices (Fan et al., 1998; Noda et al., 2000a; Sugitatsu et al., 2005). Furthermore, both acceptor-type and donor-type point defects can be introduced by using this method.

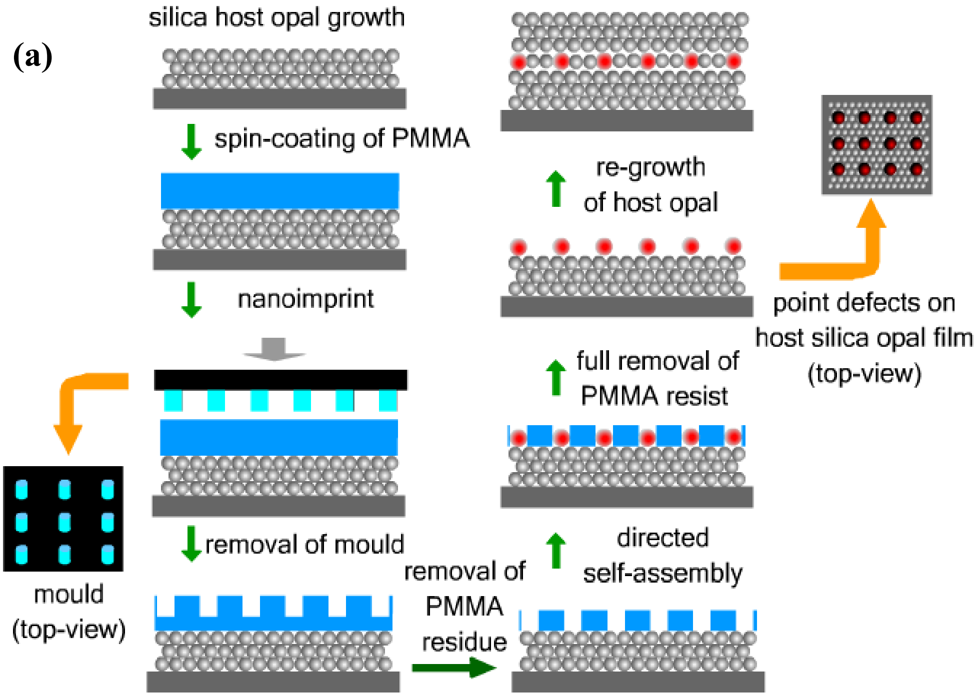

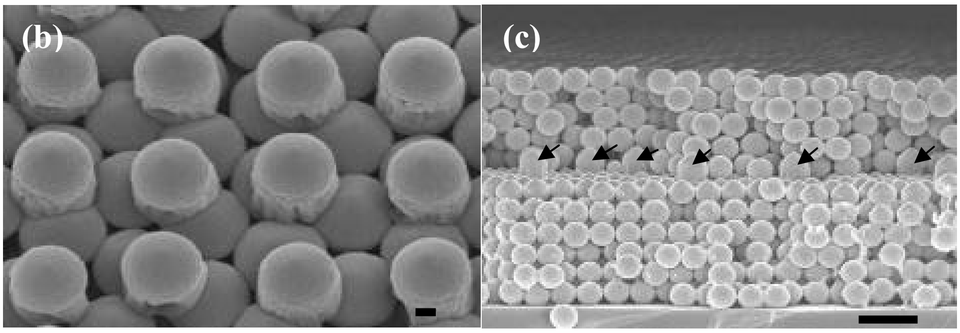

Figure 2.21 (a) Schematic illustration of introducing point defects into self-assembled 3D PCs (b) A top view of the point defect array loaded on the surface of the host silica opal film. (c) A cross-section view of the silica colloidal photonic crystal containing point defects within its interior. The arrows in (c) highlight the presence of the point defects (Yan et al., 2005a).

The past five years have witnessed the encouraging advancement on incorporation of artificial defects (point, line, and planar defects) into the interior of a self-assembled 3D PhC, which is of paramount importance for the practical device applications of these novel materials. Although the self assembly approach alone has proved to be difficult to introduce artificial defects into a 3D PhC, the combination with other techniques, such as optical lithography, nanoimprinting, spin-coating, and CVD, provide a straightforward way to producing artificial defects within the 3D PhC in a controllable manner. The latest advancement has proven that self-assembled 3D PhCs with a full PBG and artificial defects embedded are now available (Jun et al., 2005). These achievements represent a significant advancement towards functional optical devices from self-assembled PhCs.

In spite of these recent research progresses, a real photonic device based on a self-assembled 3D PhC has not been reported yet. For the artificial planar defects introduced into a self-assembled 3D PhC, optical study indeed confirmed the presence of the defect modes within the stop band. Detailed relation between the thickness of the planar defect, as well as the thickness and material characteristics of the surrounding PhC, and the position of the defect modes has been established (Zhao et al., 2003; Palacios-Lidon et al., 2004; Tetreault et al., 2004; Fleischhaker et al., 2006). For the point defects and line defect incorporated, however, optical characterizations are scarce (Jun et al., 2005; Vekris et al., 2005; Yan et al., 2005a; Yan et al., 2005b; Yan et al., 2005c; Xie et al., 2006). It seems that the structural perfection needs to be further improved to fulfill the technological requirements. The presence of unwanted intrinsic defects such as cracks, vacancies, dislocations, and grain boundaries in colloidal crystals degrades the optical quality of the colloidal crystal template, even eliminating the PBG behavior of the final 3D PhC (Li and Zhang, 2000; Li and Zhang, 2001). Fortunately, theoretical studies (Norris et al., 2004; Reyes and Duda, 2005; Tirumkudulu and Russel, 2005; Zhou et al., 2006) and recent experimental studies both indicate that using appropriate self-assembly techniques (Wong et al., 2003; Chabanov et al., 2004; Kuai et al., 2004; McLachlan et al., 2004; Jin et al., 2005a; McLachlan et al., 2005) and highly uniform colloidal spheres (Wong et al., 2003; Kuai et al., 2004; Jin et al., 2005a) can minimize or even eliminate the presence of the unwanted intrinsic defects.

At the same time, artificial defects introduced should be further tailored to meet the requirements of real photonic devices. On one hand, the size of the extrinsic defects should be optimized not to disturb the ordered host structure. On the other hand, the geometries and position of the extrinsic defects should be precisely controlled. For instances, how to remove an array of colloidal spheres to release an air-sphere line defect efficiently? How to locate the line defect along a certain direction to achieve a better waveguide property? A more challengeable problem is how to couple light between line-defect based waveguide and planar-defect based micro-cavity. The available planar defects are all oriented parallel with (111) crystalline faces, which are typically perpendicular with the supporting substrate. If a light from a PhC waveguide is expected to couple with the planar defect to initiate the micro-cavity modes, the orientation of the line defect should be perpendicular with the planar defect. This requires a three-dimensional configuration of the artificial defects introduced. The two-photon polymerization may be a leading method since it is able to create 3D embedded line patterns throughout the bulk of the PhC. It is expected that a further advancement in defect engineering in self-assembled 3D PhCs will lead to the eventual technological applications of these novel materials.

Chapter 3

Experimental Section

3.1 Chemicals and substrates

The chemicals used in this study include benzene (Merck), styrene (99%, Aldrich), divinylbenzene (DVB, Aldrich, 80%), potassium persulfate (KPS, 99%, Aldrich), hydrogen peroxide (30%, Ashland Chemical) sodium hydroxide pellet (99%, Merck), sulfuric acid (98%, Merck), fuming hydrochloric acid (HCl, 37%, Merck), tetraethyl orthosilicate (TEOS, 98%, Fisher), absolute ethanol (99.99%, Merck), toluene (99.5%, Merck), ammonia solution (NH_4OH, 28%, Fisher), hydrofluoric acid (HF, 49%, J.B. Beaker), sucrose (98%, Fluka), acetononitrile (TEDIA), silicon tetrachloride (SiCl4, 99.998%, Aldrich), 3-(trimethoxysilyl)propyl methacrylate (MPS), sodium dodecyl sulfate (SDS, >98%, Sigma), benzyl peroxide (BPO, 98%, Merk), poly(allylamine hydrochloride) (PAH, Aldrich, ave Mw~ 70000), ammonium hexafluorotitanate ($(NH_4)_2TiF_6$, 99.99%, Aldrich), boric acid (H_3BO_3, Lancaster), tera-n-octylammonium bromide solution ($[CH_3(CH_2)_7]_4NBr$, TOAB, Merck), H_2PtCl_6 (aldrich), dodecanethiol ($CH_3(CH_2)_{11}SH$, DDT, Aldrich), NaBH4 (Aldrich), 3-mercaptopropionic acid (MPA, Merck)

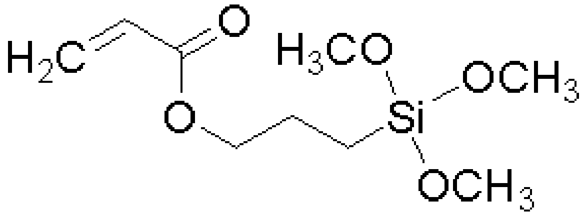

Figure 3.1 The molecular structure of 3-(trimethoxysilyl)propyl methacrylate(MPS)

All the chemicals were used as received without further purification. Glass substrates (microscope glass slide, 22 × 22 × 0.3 mm^3, Marienfeld, Germany) and silicon substrates (20 × 20 × 0.5 mm^3, HNS, Singapore) were pretreated by bathing in a piranha solution, the mixture of concentrated sulfuric acid and hydrogen peroxide with volume ratio of 3: 1 for 3 h (CAUTION: piranha solution reacts violently with organic material and should be handled with care). Subsequently, the substrates were washed with copious deionized water and dried in nitrogen flow before use.

3.2 Synthesis of colloidal spheres

3.2.1 Synthesis of silica microspheres

The synthesis of the SiO_2 microspheres was conducted in a 500 ml three-neck round-bottom flask. A teflon wedge connected with a teflon sprayed stick driven by an electric motor, was used as stirrer. A variable flow mini-pump (Fisher scientific) was used to control the feeding of the chemicals.

The first step is the synthesis of silica microspheres that are used as seeds in the following re-growth step. A mixture of 19g H_2O, 2.8ml ammonia and 40ml ethanol was poured into a three-neck flask and stirred for 10 min (stirring speed: 300 MPH). Then a mixture of TEOS 2.7ml and Ethanol 60ml is added into the flask and allowed to react for 4 h. Thus the seeds are successfully fabricated. There is no need to take out the seeds and wash them. Mixture of TEOS and ethanol can be dripped into the reaction flask to grow the silica seeds directly.

Subsequently, a mixture of certain amount of TEOS and 4 times amount of ethanol was dripped at a speed of 5.15ml/h using peristaltic pump. When the volume of the reaction medium doubled, the dripping was paused for 2 hours and ammonia and DI water were added to restore their concentrations to the original values before the dripping. After the restoration the reaction media was stirred for 1 hour before the dripping was resumed. Two hour after the completion of the dripping, monodisperse silica beads could be washed and collected. The washing process involved 3 times of washing by ethanol followed by 3 times of washing by DI water using centrifuge and redsipersion. In some rare cases, there are some second seeds formed during the re-growth process, thus a separation process was introduced to purify the silica beads. The separation process involved 8 times of centrifuge at an appropriate speed and redispersion.

3.2.2 Synthesis of polystyrene microbeads

The reaction was carried out in a 500 ml three-neck flask, which was immersed in a water bath to control the reaction temperature. A mechanical stirrer with a water seal device driven by an electric motor was used in the reaction. Pure nitrogen was bubbled into the flask throughout the experiment. At the outlet of nitrogen, a condenser was installed to condense the styrene vapor brought by the nitrogen, so as to reduce the styrene loss during the reaction.

An emulsion polymerization process was employed to synthesize polystyrene (PS) spheres. During this process, 200g DI water, certain amount of styrene monomer, some amount of sodium dodecyl sulfate (SDS) were added into the flask. The flask was then put in the water bath controlled at 60 ^{o}C. After installment of the mechanical stirrer and start of nitrogen flow, the mixture was stirred at 300 rpm. At the same time, an initiator solution was prepared by solving certain amount of potassium persulfate (KPS) in 50g DI water. After the mixture was stirred for 1h, the initiator was poured into the flask to start the polymerization. After 30h PS spheres were washed by centrifuge and redispersion of 4 times. Finally, the PS spheres were stored as colloid in water for subsequent experimental use. In the experiment, different amounts of styrene monomer were used to test the influence of it on the final PS bead size. Additionally, the effect of SDS, DVB was also examined by control the addition of SDS in the reaction system (see the recipe of the PS synthesis in Table 3.1).

Weight percentage and volume fraction measurement. The weight percentage of the silica and PS spheres was measured by drying 200 μL colloid on a piece of aluminum foil followed by weighting the remaining solid. The weight percentage and the volume fraction of the colloids were calculated with the following equations:

$$w = \frac{W_d - W_f}{W_w - W_f}$$

Where, w is the weight percentage of the colloid and W_d, W_f and W_w are the weight of dried colloid with the aluminum foil, the weight of the foil and the weight of colloid with the aluminum foil, respectively.

Table 3.1 Recipe of the PS bead synthesis

Sample	*Styrene Amount (g)*	*DVB (g)*	*KPS (g)*	*SDS (g)*
PS1	25		0.14	
PS2	25		0.14	
PS3	25		0.14	
PS4	20.89		0.14	
PS5	20		0.14	
PS6	20.2		0.14	
PS7	10		0.14	
PS8	8		0.3	
PS9	7.5		0.14	
PS10	5.4		0.14	
PS11	5		0.14	
PS12	3		0.14	
PS13	20		0.143	0.15
PS14	20	0.8	0.14	
PS15	17	3	0.14	
PS16	15.45	4.55	0.14	
PS17	5		0.35	

The volume fractions of PS and silica aqueous colloids were calculated according to the following equation, where the specific gravities of PS and silica beads were assumed as 1.08 and 2:

$$f_{PS} = \frac{w_{PS}}{1 - 0.08 w_{PS}}$$

$$f_{Silica} = \frac{w_{Silica}}{2 - w_{Silica}}$$

Preparation of colloids of different concentrations. Aqueous PS and silica colloids were prepared by diluting the concentrated mother colloids directly according to the weight percentage of the colloids. Alcoholic silica suspensions were prepared by diluting the concentrated silica colloids with ethanol.

3.3 Synthesis of composite microspheres and shells

3.3.1 Synthesis of SiO_2/TiO_2 and SiO_2/TiO_2-Pt core/shell nanostructures

Silica spheres of 650nm were synthesized by the method described previously. The surface of them was then functionalized by adsorption of a type of polyelectrolyte, poly allylamine hydrochloride using a layer-by-layer technique (Strohm and Lobmann, 2005). Briefly, about 20 mL of a PAH solution containing 1 g L^{-1} of PAH was added to 30 mL of a colloid containing 0.5 g silica spheres. After being magnetically stirred for 30 min, the spheres were collected by centrifugation, followed by three-time washing using deionized (DI) water to remove residual PAH. The PAH-coated silica spheres were dispersed in 40 mL of DI water. Then, a given amount of 0.6 M $(NH_4)_2TiF_6$ solution was added to the dispersion. The above dispersion was mixed in a conical flask placed in an ultrasonicator and sonicated for 1 h before the pH was adjusted to 2.85 using HCl (1M). Finally, a H_3BO_3 acid solution of 0.6 M was added to the system and sonicated for 9 h. The solid spheres were collected by centrifuge, washed with DI water, and finally dried at 60 ºC overnight.

SiO_2/TiO_2 core/shell structure with Pt nanoparticles incorporated in the titania shells were prepared according to the method of Li and Zeng (Li and Zeng, 2006). Briefly, 28 mL of tera-n-octylammonium bromide solution in toluene ($[CH_3(CH_2)_7]_4NBr$, TOAB, 27 g L^{-1}) and 10 mL of H_2PtCl_6 solution (0.05 M) were stirred vigorously for 5 min, followed by adding 4 mL of 0.22 M dodecanethiol in toluene. Subsequently, 20 mL of 0.24 M $NaBH_4$ aqueous solution was added to obtain a Pt nanoparticle suspension. Afterward, SiO_2/TiO_2 core/shell composite particles was added to 50 mL of a 3-mercaptopropionic acid (MPA) solution (0.22 M in toluene) and stirred for 10 min. Then the Pt suspension was added under stirring and kept stirred for another 3 h. Finally, the solid was washed with acetone, dried at 60 ºC overnight, and calcined at 500 ºC for 3 h to obtain a powder sample of gray color.

3.3.2 Synthesis of various hollow spheres

The synthesis of single shelled hollow carbon spheres (SHCSs). Monodisperse silica spheres with diameters of 460 nm, 650 nm, 730 nm, and 1600 nm were synthesized (Stöber et al., 1968). Subsequently, silica spheres were coated with carbon using a chemical vapor deposition (CVD) method, as shown in Figure 3.2. Briefly, the powder of silica spheres of a given diameter was placed in a quartz tube and were heated to 900 ºC or 1000 ºC with a heating rate of 5 ºC/min under N_2 flow (30 cm^3 min). Then, another N_2 flow of 30 cm^3 /min containing 10 wt% benzene vapor was passed through the silica spheres to allow deposition of carbon on the surface of the silica spheres. After a given period of time, composite carbon/silica spheres were obtained. Removal of the silica spheres using a 20 wt% HF solution yielded a carbon sample. The samples obtained at CVD temperatures of 900 ºC and 1000 ºC for 4 h are denoted as SHCS900 and SHCS1000, respectively.

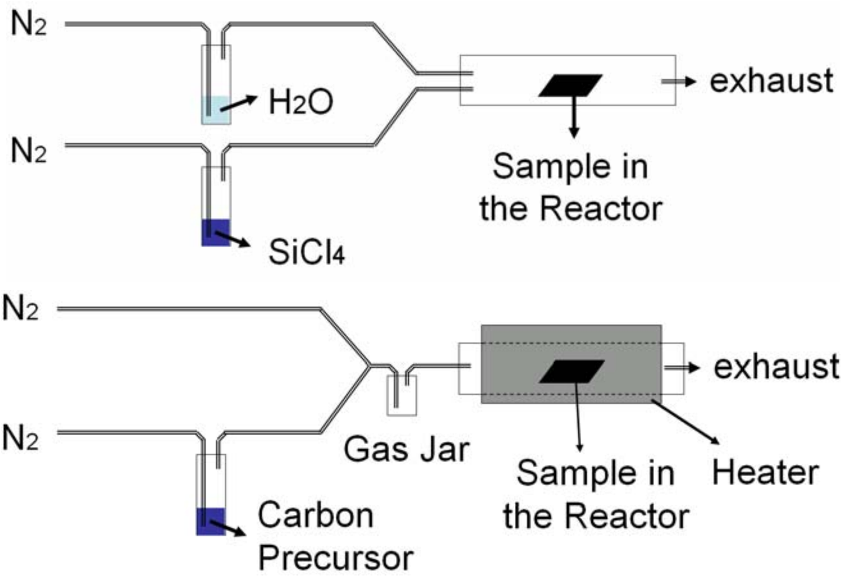

Figure 3.2 The setups of silica CVD (top) and carbon CVD (bottom)

The preparation of N-doped hollow carbon spheres (NHCSs). N-doped hollow carbon spheres (NHCSs) were prepared following a similar experimental procedure as described above. Briefly, nitrogen gas (30 cm^3/min) containing 5 wt% acetonitrile (CH_3CN, Tedia) vapor instead of benzene vapor was passed to the quartz tube to allow carbon deposition on the surface of the silica spheres. The sample obtained at a CVD temperature of 1000ºC for 4 h is denoted as NHCS1000.

The fabrication of double shelled hollow carbon spheres (DHCSs). First, silica spheres of 1600 nm were coated with a layer of carbon using the CVD at 1000 ºC for 1 h with benzene as precursor. Second, the silica/carbon core/shell structures were dispersed in ethanol and sonicated for 0.5 h. Third, deposition of a silica layer on the core/shell spheres was conducted by silica CVD according to the method described by Ozin and co-workers, as shown in Figure 3.2 (Miguez et al., 2002). Briefly, the samples were placed in a home-made glass tube reactor working at room temperature and atmospheric pressure. De-ionized (DI) water was bubbled into the reactor by a highly pure nitrogen flow, followed by bubbling silicon tetrachloride. Hydrolysis of SiCl4 formed a layer of silica on the interior surface of the silica-inverse opals to produce NCIOs. By controlling the bubbling time and nitrogen flow rate, the thickness of the deposited silica layer can be easily controlled. Fourth, the above silica/carbon/silica composite spheres were dispersed in ethanol and sonicated for 0.5 h. Fifth, silica/carbon/silica composite spheres was further deposited with carbon using the carbon CVD method. Finally, the silica component in the composite spheres was removed using a 20 wt% HF solution to obtain DHCSs.

The synthesis of hollow silica spheres. The SHCSs prepared above were used as templates here to prepare hollow silica spheres. After the SHCSs was coated with silica layer using silica, the sample was calcined in air at 700 ºC for 5 h to burn off the SHCSs, leaving behind hollow silica spheres.

3.4 Fabrication of colloidal crystals

3.4.1 Vertical deposition (VD) method

Colloidal spheres were diluted to a certain concentration before use (normally the volume fraction was lower than 1%). Then about 15 ml of the colloidal suspension was added into a polyethylene vial and a glass slide or silicon substrate was vertically immerged into the suspension and fixed to the wall of the vial. Then the vial was placed in an oven of different temperature overnight (Jiang et al., 1999a; Im et al., 2002; Im and Park, 2002).

3.4.2 Horizontal deposition (HD) Method

After being treated with piranha solution, the glass or silicon substrates were washed with copious deionized water and dried in nitrogen gas flow before use. A few drops of colloidal suspension of a given concentration were placed on a substrate and carefully spread to fully cover the substrate surface, as illustrated in Figure 3.3 The spread suspension was exposed to ambient conditions with a temperature around 23 °C.

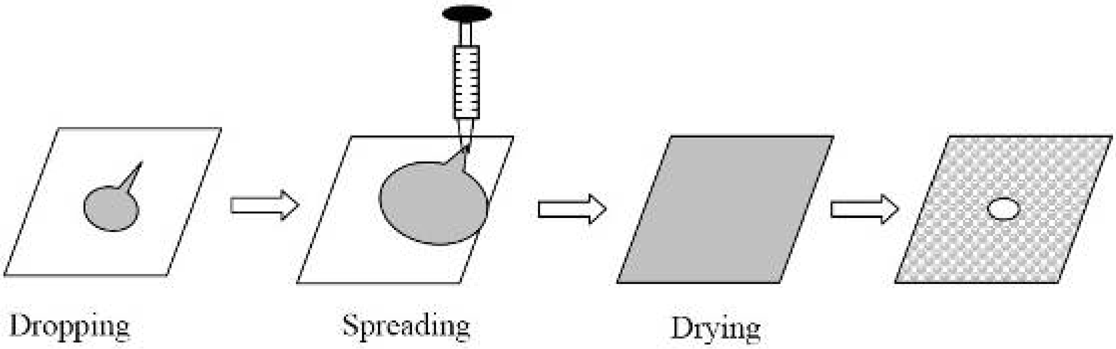

Figure 3.3 Schematic illustration of the procedure of horizontal deposition. The colloids of a given concentration were dropped on the substrate by using a finnpipette (Labsystems, J36207, 10~100 μl) which could control the drop volume precisely. Then a pipette tip was used to spread the suspension on the substrate. When one moved the tip along the surface of the substrate, the colloidal suspension will be guided to spread on the substrate and finally fully cover the substrate surface, as illustrated in the second panel. Subsequently, the spread suspension was exposed to ambient conditions with a temperature of around 23^{o}C and the colloidal crystallization took place (see the third panel). After 1~2 hours, a thin colloidal crystal film with a macroscopic void formed on its center was obtained, as illustrated in the fourth panel.

The annealing process is necessary to increase the mechanical strength of the colloidal crystals and form necks among the microspheres. For PS spheres the colloidal crystals were heated at 105 ^{o}C or 110 ^{o}C for a certain time (normally, 5 to 15 min according to different purpose), while the silica spheres were calcinated at 500^{o}C or 550^{o}C for a certain period of time (normally, 2 to 5 h).

3.4.3 Fabrication of crack-free colloidal crystals using vertical deposition (VD) method

Silica beads of 277 nm in diameter with a polydispersity lower than 3% were synthesized following a procedure (Giesche, 1994) based on the Stöber method (Stöber et al., 1968). Silicon wafer was treated in a piranha solution at 60 °C for 2 h before use (WARNING: the above solution reacts violently with organic materials. Handle with caution). A silica precursor solution was prepared by mixing TEOS, ethanol, and 0.1 M HCl (volume ratio = 1:10:1) under stirring for 4 h. Different amounts of the silica precursor solution was mixed with the colloid of silica spheres under ultrasonication before the VD method (Jiang et al., 1999a) was used to grow CC films on the silicon substrate. During the VD process, two silicon substrates were placed back to back in the center of a cylindrical vial containing 15 mL of silica sphere colloidal suspension. Self-assembly of the silica beads was completed after about 40 h at 30 °C. Then, the silica bead films were exposed to vapor for different periods of time depending upon the thicknesses of the films.

3.5 Fabrication of free-standing non-close-packed opal films

Fabrication of PS Opals. PS spheres of 569 and 687 nm in diameter with a polydispersity of < 3% were synthesized using an emulsifier-free emulsion polymerization method (Shim et al., 1999). The spheres were used to fabricate PS opals on a silicon substrate by using an inward-growing self-assembly technique as described in the previous section. The PS opals fabricated from the 569-nm and 687-nm beads were annealed at 110 °C for 20 and 30 min, respectively, before further processing.

Fabrication of Silica Inverse Opals. A silica precursor solution was prepared by mixing tetraethyl orthosilicate, ethanol, and 0.1 M HCl solution (volume ratio = 1:10:1) under stirring for 4 h. Then the solution was infiltrated into the voids of the opals fabricated above using a Laurell spin coater (WS-400B-6NPP/LITE) operating at 1200 RPM for 15 s, followed by drying at room temperature for 4 h (Matsuura et al., 2005). Three circles of infiltration and drying were performed to enhance the infiltration. Subsequently, the PS spheres were removed by immersing the samples in toluene at 60 °C for 4 h. This was repeated three times to ensure a complete removal of the PS beads.

Backfilling of the Inverse Opals to Obtain Non-Close-Packed Inverse Opals (NCIOs). A silica layer was deposited on the interior surface of the silica-inverse opals by using the CVD method as described by Ozin and co-workers (Miguez et al., 2002). Briefly, the samples were placed in a home made glass tube reactor (as illustrated in Figure 3.2) working at room temperature and atmospheric pressure.

De-ionized (DI) water was bubbled into the reactor by a highly pure nitrogen flow, followed by bubbling silicon tetrachloride. Hydrolysis of $SiCl_4$ formed a layer of silica on the interior surface of the silica-inverse opals to produce NCIOs. By controlling the bubbling time and nitrogen flow rate, the thickness of the deposited silica layer can be easily controlled.

Infiltration of the NCIOs with Styrene Monomer and Removal of the Silica NCIOs. According to the method described by Jiang et al. (1999b), styrene was infiltrated into the pores of the NCIOs followed by polymerization to allow the formation of PS in the pores of the NCIOs. In detail, styrene was washed with a 10% NaOH solution three times to remove the inhibitor, followed by three times of washing with DI water. Then, 1 wt% of benzyl peroxide (Fluka) was added to the styrene. Covered with a glass slide, the NCIOs was dipped in the monomer to allow full infiltration of the voids of the NCIOs by the styrene monomer. Polymerization of the monomer was conducted at 60 °C overnight. A 10 wt% HF solution was used to etch away the silica framework to obtain free-standing NCO films.

3.6 Fabrication of planar defects in opals and inverse opals

Synthesis of PS spheres and fabrication of first multilayer. PS spheres of 380, 560 and 655 nm in diameter (polydispersity < 3%) were synthesized and washed 4 times before redispersion in water to obtain a colloidal suspension having volume fractions of 6, 8 and 9 %, respectively. Horizontal deposition method was used to grow PS multilayer on a glass substrate

Spin coating of a silica layer as planar defect. Silica particles of 225 and 585 nm in diameter synthesized using the Stöber method were washed and redispersed in ethanol (99.95%, Aldrich) to form a colloidal suspension of 4 and 5.6 % volume fractions, respectively. The silica beads were spin-coated on the PS film obtained earlier at spinning speeds of 1000 RPM for the 225-nm beads and 1200 RPM for the 585-nm beads on a Laurell spin coater (WS-400B-6NPP/LITE). Then the sample was annealed at 100 °C for another 3 min before the subsequent treatment.

Growth of the second PS multilayer. Another 40 μL of the PS colloidal suspension were dropped and spread carefully on the surface of the sample obtained above. After the formation of the PS colloidal crystal, the sample was annealed at 100 °C for 15 min.

Infiltration with silica. A SiO_2 sol was prepared by mixing tetraethyl orthosilicate (TEOS, 98%, Acros Organics), ethanol and 0.1 M HCl solution (Merck) (volume ratio: 1:10:1) under stirring for 4 h. The samples were placed vertically and the sol was dropped on them to make them fully wetted. Then the wetted samples were allowed to dry at room temperature for 12 hours. This infiltration process was repeated for another 3 times to make the voids of opal fully infiltrated by silica. Finally the samples were calcined at 500°C for 6 hours to remove PS particles.

3.7 Patterning the surface of microspheres and fabrication of nonspherical particles

3.7.1 Patterning Microsphere Surface by 3D Colloidal Crystal Templating and

Fabrication of Nonspherical Particles

A CC self-assembled from 984-nm PS spheres was annealed at 110 °C for 15 min. Then 6g CC was grinded into small pieces and put in a conical flask. Concentrated H_2SO_4 (the weight ratio of CC over H_2SO_4 was around 1:20) into the flask. The flask was then placed in an oil bath at 40 °C. The mixture of CC and H_2SO_4 was mildly stirred for 2.5 h to allow sulphonation (Yang et al., 2003) of the CC. Subsequently, the CC was washed four times. Upon redispersion of the sulphonated CC in water using the ultrasoniction technique, 3.89g functionalized PS beads were obtained. In the following seeded regrowth process, 15 mL of surface-sulphonated PS sphere (containing 0.29 g of PS spheres) was mixed with 50 mL of H_2O and 0.28 mL of styrene monomer under stirring for 60 min at 60 °C under the protection of N_2 flow. Then, a solution containing 10 g of H_2O and 0.016 g of potassium persulfate was added to the above mixture. After polymerization for 24 h, non-spherical PS particles were obtained after centrifuging and washing.

A CC self-assembled from 400-nm PS spheres was annealed at 110 °C for 5 min. Then 6g CC was grinded into small pieces and put in a conical flask. Concentrated H2SO4 (the weight ratio of CC over H2SO4 was around 1:20) into the flask. The flask was then placed in an oil bath at 40 °C. The mixture of CC and H2SO4 was mildly stirred for 2.5 h to allow sulphonation (Yang et al., 2003) of the CC. Subsequently, the CC was washed four times using deionized water. Upon redispersion of the sulphonated CC in water using the ultrasoniction technique, 4.3g functionalized PS beads were obtained. Similarly, PS particles with protruding edges were also synthesized with 400 nm PS spheres. Briefly, first, 15 mL of surface-sulphonated PS sphere (containing 0.195 g of PS spheres) was mixed with 50 mL of H_2O and certain amount (0.1 mL, 0.2mL and 0.4mL for the samples shown in Figure 2b, c and d, respectively) of styrene monomer under stirring for 60 min at 60 °C under the protection of N_2 flow. Then, a solution containing 10 g of H_2O and 0.015 g of potassium persulfate was added to the above mixture. After polymerization for 24 h, non-spherical PS particles were obtained after centrifuging and washing.

Silica spheres of 415nm with a polydispersity of 3% were synthesized using a modified Stöber method (Giesche, 1994). A vial containing a 0.75 wt % colloid of the silica spheres, with a piece of cleaned silicon wafer placed vertically (Jiang et al., 1999a) near the vial wall was placed in a desiccator connected with a vacuum pump. The desiccator was put in a 50 °C oven and kept at a pressure of 115 mm Hg for 24 h to allow the formation of colloidal crystals (CCs) on the silicon substrate. CCs containing 0.05g silica spheres (the weight of the spheres were calculated by subtracting the weight of the bare substrates from that of the substrate with CCs) was first annealed at 750 °C for different periods of time. Subsequently, the CC films were placed in a solution containing 40 mL of ethanol, 1.5 g of H2O, 0.5 mL of 3-(trimethoxysilyl) propyl methacrylate (MPS), and 1 mL of ammonia solution (25%) for 24h. Then, the CC films were taken out and washed with ethanol five times to remove residual MPS. The washed films were dried at room temperature and their masses were measured. Finally, the CC films were redispersed in ethanol by ultrasonication. After drying it was found that 0.039 g patterned silica spheres was collected. 0.02 g of the surface-patterned silica spheres was added to a 40 mL mixture containing ethanol, 5 g of H2O, and 1 mL of ammonia solution (25%) under stirring for 30 min. Then, an ethanol solution containing 40 μL of tetraethyl orthosilicate (TEOS) and 40 mL of ethanol was dropped into the mixture containing silica spheres at a speed of 3.6 mL/h still under stirring. After completion, the system was stirred for another 2 h. The solid (non-spherical silica particles) was collected by centrifuging.

3.7.2 Drilling holes in colloidal spheres by selective etching

Monodisperse colloidal PS spheres of 450 nm in diameter were synthesized using previously described method and self-assembled into a monolayer on an glass substrate (1 × 2 cm) coated with indium-tin-oxide (ITO) using VD. A diluted PS colloidal suspension with a concentration of 10^{-4} (volume ratio) was used to obtain a hexagonally close-packed PS monolayer. After annealing at 110°C for 5 min, the above sample was dipped into a 0.1 M nickel sulfate solution containing 0.06 M boric acid and 0.01 M sodium dodecyl sulfate for electrochemical deposition of nickel at pH = 3, 50 °C, and - 1 V against Ag/AgCl (3 M KCl) for 30 min.

Inductively coupled plasma (ICP) etching was then carried out using a Plasma-Therm SLR-770 system with 2.0 MHz source configured with an electrode chuck in the chamber, which was biased separately at 13.56 MHz. The reactive gas was CF_4 with a flow rate of 20 sccm while the operation pressure was kept constant at 7 mTorr. The inductive power was kept at 400 W at a constant rf chuck power of 100 W.

3.8 Characterization

Scanning electron microscope (SEM). When a condensed, accelerated electron beam hits a specimen and secondary and backscattered electrons are produced. In SEM process, secondary electrons emitted from the sample are collected to create an area map of the secondary emissions. Since the intensity of secondary emission depends highly on the local morphology, the area map is a magnified image of the sample. In our experiment, a dilute solution of microparticles was prepared and this solution was dropped on a piece of clean smooth copper tape attached on a SEM copper holder. Dry samples were obtained after the complete drying of the solution. The samples of colloidal crystals and films were directly cut by diamond cutter or knife. The free-standing PS colloidal crystals films were break into small piece in liquid nitrogen to keep their microstructure from being destroyed. Then small pieces of samples were attached on the copper holder. Before measurement, the samples were coated with platinum with a sputter coater (JEOL JFC-1300 Auto fine coater). Finally, SEM images were obtained on a JEOL JSM-5600LV and a JEOL-7600F field emission scanning electron microscope (FESEM), which were operated at an acceleration voltage of 5, 10 and 15 kV and filament current of 60 mA. The sizes and deviations of the sphere diameter, shell thickness, feature lengths were obtained by measuring at least 50 samples on the SEM images.

Energy-Dispersive X-ray Analysis (EDX). EDX attached on the SEM was used to analyze the atomic composition of the samples. The energy of the electronic beam is typically in the range 10-20 kV. The energy of the X-rays emitted depends on the material under examination. The X-rays are generated in a region about 2000 nanometers in depth, and thus EDX is not a surface science technique.

Transmission electron microscope (TEM). Before measurement, the sample was dispersed in ethanol and then dripped and dried on copper grid. In the operation of TEM, an electron beam is focused on a specimen and part of the electron beam is transmitted. This transmitted portion is focused by objective lens into an image and the image is passed down through enlarge lenses and a projector lens, being enlarged all the way. In the experiment, the TEM was used to characterize the nonspherical particles and the TEM images were obtained on a JEOL 2010 transmission electron microscope, operated at an acceleration voltage of 200 kV.

UV-Visible-near-infrared Scanning Spectrophotometer. The reflectance and transmission spectra of the colloidal crystals and the PCs were characterized on a Shimadzu UV-3101PC UV-Visible-near-infrared Scanning Spectrophotometer. A home-made mask was used to constrain the incident light into 5 mm diameter circle.

Scanning spectrophotometers normally utilize diffraction gratings to scan across a spectral region, which can be used in the UV, visible, and NIR regions. The polychromatic light from the radiation source passes through lenses and filters and onto the sample. After being modified by the samples, the light is then collected and transferred to the monochromator where it is diffracted into individual wavelengths and measured by the detectors.

X-ray Photoelectron Spectroscopy (XPS). XPS was employed to measure the surface composition of the samples. The sample in colloid state was dropped on the surface of a small piece of glass. After complete drying, the glass piece was attached to a XPS holder, which was further place in the XPS cabinet to do the measurement. XPS can be used to measure the elemental composition, chemical state and electronic state of the elements that exist in the surface of a material. By irradiating a material with a beam of X-rays and simultaneously measuring the kinetic energy and number of electrons escaping from the surface, elemental information can be produced about the 10 nm depth of the surface of a sample. The XPS machine used is AXIS HSI 165 spectrometer, from Kratos Analytical.

X-ray diffraction (XRD). X-ray diffraction (XRD) takes advantages of the coherent scattering of x-rays by polycrystalline materials to obtain a wide range of structural information. The x-rays are scattered by each set of lattice planes at a characteristic angle, and the scattered intensity is a function of the atoms, which occupy those planes. The scattering from all the different sets of planes results in a pattern, which is unique to a given compound. In addition, distortions in the lattice planes due to stress, solid solution, or other effects can be measured. TiO2 samples in the thesis were also identified by using X-ray diffraction (XRD) on a Shimadzu XRD-6000 diffractometer (CuKα radiation) operated at 40 kV and 30 mA with a scanning speed of 0.02 ° s-1.

Chapter 4

Synthesis of Colloidal Microspheres

Various methods have been employed to fabricate colloidal crystals, which can be further used as template for producing photonic crystals. Almost all of these methods involve growth of colloidal crystals by the using of a colloid of microspheres. To produce a highly ordered colloidal crystal the colloid has to meet the following prerequisites. First, the monodispersity is highly important for the formation of ordered structure. Normally, to obtain an ordered colloidal crystal the polydispersity of the spheres should be less than 5% (Allard and Sargent, 2004). Moreover, the colloid should be relatively stable in a time period compared to the growth of colloidal crystals. Furthermore, the microspheres will be removed after infiltration of dielectric materials. Thus, the physicochemical properties of the spheres are also of high importance. The spheres need to exhibit a solvability, chemical properties or decomposition temperature that is different from the infiltrated materials. Thus they can be removed by dissolution, etching or by calcination. Additionally, the solvent should be volatile sot that it can be completely removed after the formation of colloidal crystals.

Various approaches have been employed to produce monodisperse colloidal spheres. Presently, the most commonly used methods are controlled precipitation for spheres of inorganic oxides and emulsion polymerization for polymer latex spheres. (Xia et al., 2000) In this chapter, the synthesis of monodisperse silica spheres and polystyrene (PS) spheres are discussed.

4.1 Synthesis of silica microspheres

Silica spheres are widely adopted to fabricate colloidal crystals as template of photonic crystals because of its several advantages. First, it can be easily dispersed in water or ethanol to form a stable colloid. Additionally, it can be easily removed by hydrofluoric acid after infiltration of dielectric materials. Furthermore, it is stable under high temperature so that the colloidal crystals maintain their structure during process such as chemical vapor deposition of silicon.

Stöber et al. (1968) first reported the synthesis of monodisperse silica spheres in 1968. Subsequently, the method has been improved by a number of research groups (Giesche, 1994a; 1994b; Yano and Fukushima, 2003). Generally, a dilute solution of tetraethylorthosilicate (TEOS) is allowed to hydrolyze in an ethanol media with the presence of ammonia solution. The hydrolysis and condensation processes produce initial nulei of silica and the growth of nuclei forms the final silica beads. The reaction mechanism is shown as following:

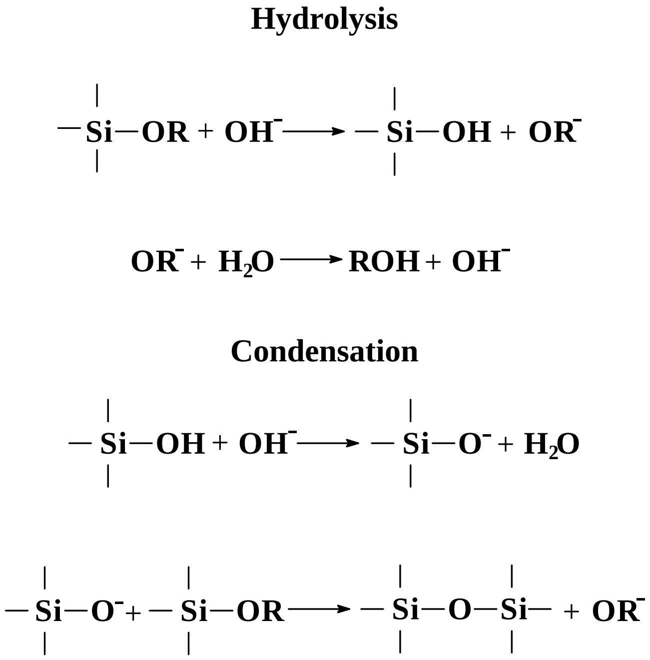

$$-\mathrm{Si}-\mathrm{OR} + \mathrm{OH}^- \longrightarrow -\mathrm{Si}-\mathrm{OH} + \mathrm{OR}^-$$

$$\mathrm{OR}^- + \mathrm{H_2O} \longrightarrow \mathrm{ROH} + \mathrm{OH}^-$$

$$-\mathrm{Si}-\mathrm{OH} + \mathrm{OH}^- \longrightarrow -\mathrm{Si}-\mathrm{O}^- + \mathrm{H_2O}$$

$$-\mathrm{Si}-\mathrm{O}^- + -\mathrm{Si}-\mathrm{OR} \longrightarrow -\mathrm{Si}-\mathrm{O}-\mathrm{Si}- + \mathrm{OR}^-$$

Figure 4.1 Schematic illustration of reaction mechanism of TEOS under basic conditions (Chang and Ring, 1992).

As a general rule, precise control of reaction conditions, for instance, the pH, the concentration of water and the concentration of reactants is necessary to generate monodisperse silica spheres. Since TEOS reacts strongly with water, high concentration of water should be avoided and water should be distributed in the reaction solution as homogeneously as possible. Alcohol is normally chosen as the reaction media because both organic reactant (TEOS) and inorganic catalyst (aqueous ammonia hydroxide) can be mixed homogeneously in it.

The choosing of catalysts is considered as the most important factor in determining the mechanisms of silica growth. It has been found that only when ammonia is used as catalyst, spherical silica particles can be obtained. Thus ammonia can be taken as a morphological catalyst.

In this work, a modified Stöber method was used to synthesize silica spheres, which involved a formation of seeds and regrowth of them. As the first step, the mixture of TEOS and ethanol was poured into a solution of ammonia and alcohol under stirring to allow the formation of silica spheres under 200nm. By dripping diluted TEOS into the reaction media after the formation of the seeds, larger silica beads can be obtained.

Table 4.1 The TEOS amounts used in the synthesis of seeds and the final beads and the sizes of them

Batch Number	***TEOS used for the synthesis of seeds (ml)***	***The size of the seeds (nm)***	***TEOS amount dripped to grow the seeds (ml)***	***The final bead size (nm)***
S1	3.38	122	20	211
S2	4.5	145	34	277
S3	2.7	174	24	378

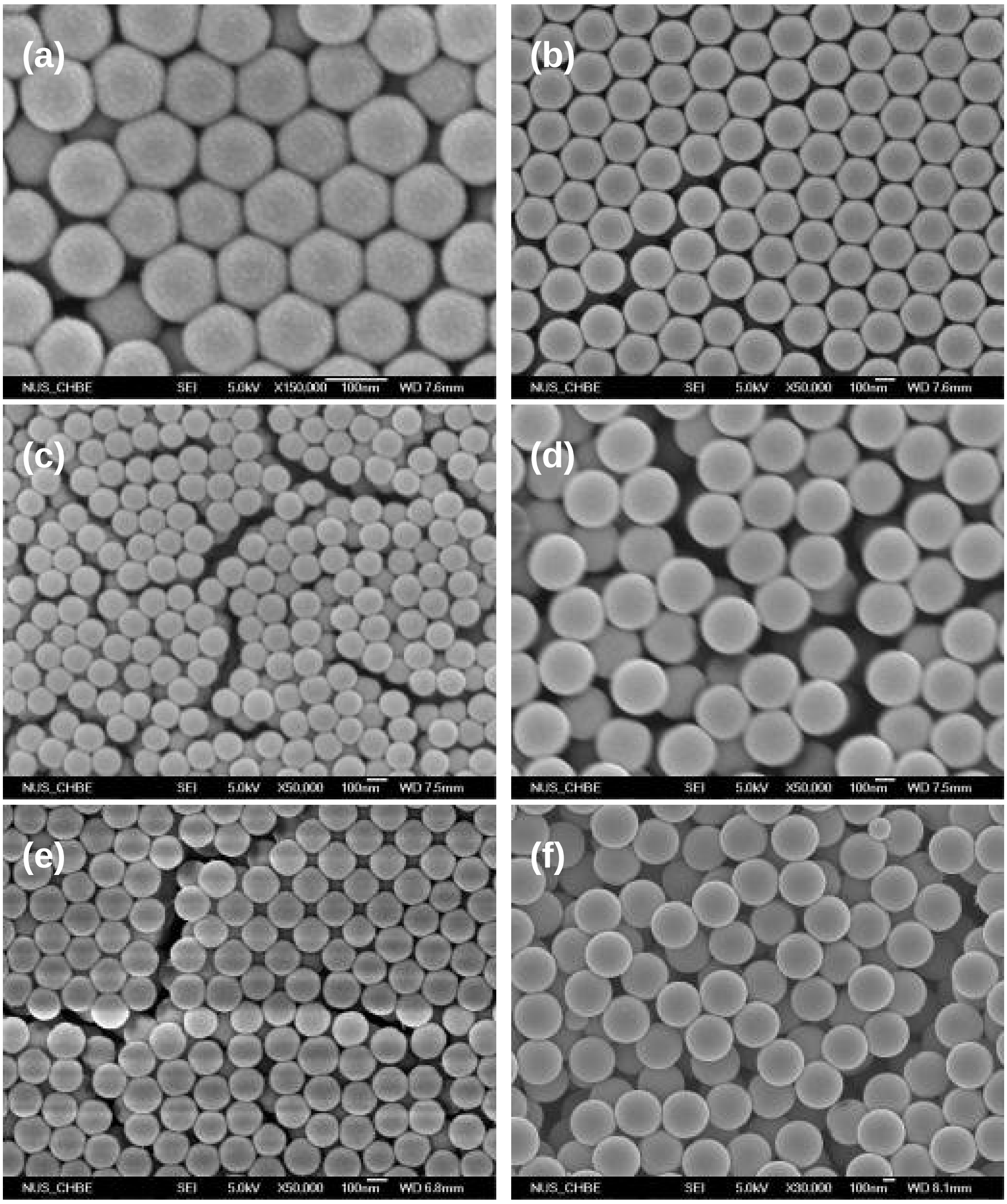

Figure 4.2 Images (a-f) are the FESEM images of samples S1, S1a, S2, S2a, S3 and S3a respectively.

During the seed-regrowth processes, a key issue to ensure the monodispersity of the final seeds is to prevent the formation of second seeds during the dripping of TEOS. Thus, assuming that the formation of second seeds is neglectable in all the three batches of synthesis, the final bead size $Ø_f$ could be calculated with the initial seed size $Ø_s$ and the amount of TEOS dripped into the reaction system according to the following equation:

$$\phi_f = \sqrt[3]{\frac{V_d + V_S}{V_S}} \times \phi_S$$

In the equation V_s and V_d are the amount of TEOS used for synthesis of the seeds and dripped to grow the seeds, respectively.

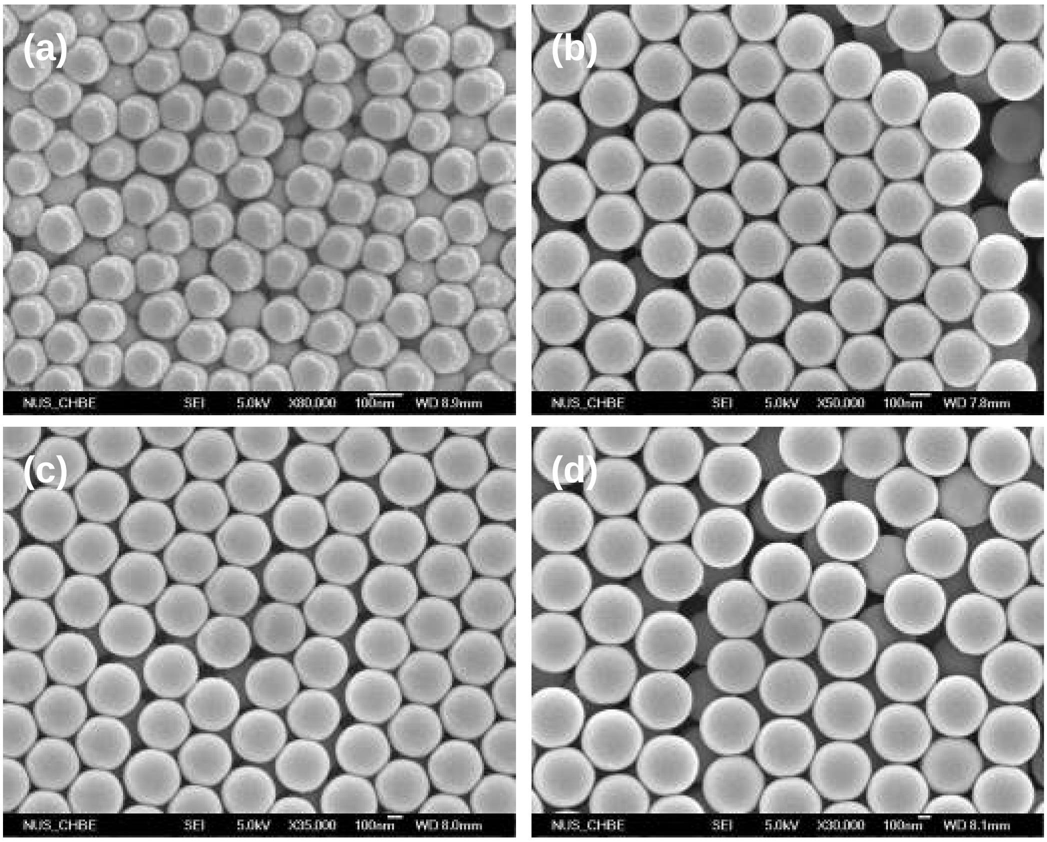

Figure 4.3 Images (a-d) are the FESEM images of samples S4, S4a, S4b and S4b respectively.

Thus, theoretically the sizes of the final beads of the three batch of synthesis should be 232 nm, 296 nm and 373 nm respectively. They are in well accordance with the experimental observation of the final bead sizes. The difference between the experimental and theoretical value might come from the formation of tiny second seeds, incomplete reaction of the dripped TEOS and the SEM observation error. It can be concluded that the final beads size can be controlled by the amount of TEOS dripped into the reaction system.

At the same time, it is possible to synthesize beads of different sizes in one batch by simply pausing the TEOS dripping and taking out a portion of the colloid at different stages of dripping. Figure 4.3 shows the images of the seeds and three final beads obtained in a single batch of synthesis. The sizes of them are 134nm, 266nm, 367nm and 480nm respectively. The sizes of them also can be predicted by the seed size and the relative dripped TEOS amount.

In some cases, as shown in Figure 4.4 (a, c), second seeds formed during the growth of beads, probably due to the speed variation of the perilistic pump. However, we found that the second seeds can be removed by centrifuge if the size of the second seeds is less than half of the beads. During the separation process, the rotation speed and time should be set properly so that the desired beads can be deposited completely while the second seeds are still in the colloid. In the sample shown as Figure 4.4a, the beads and the second seed sizes are 415nm and 140nm, respectively. Optimal centrifuge speeds were chosen to settle down the larger beads while leaving the smaller beads in the colloid bulk. Four times of centrifuge at 5000RPM for 3min were used to separate the seeds and obtain the sample shown as Figure 4.4b. The bead and the second seed sizes are 447nm and 220nm respectively. Four times of centrifuge at 4500RPM for 3min were taken to purify the beads.

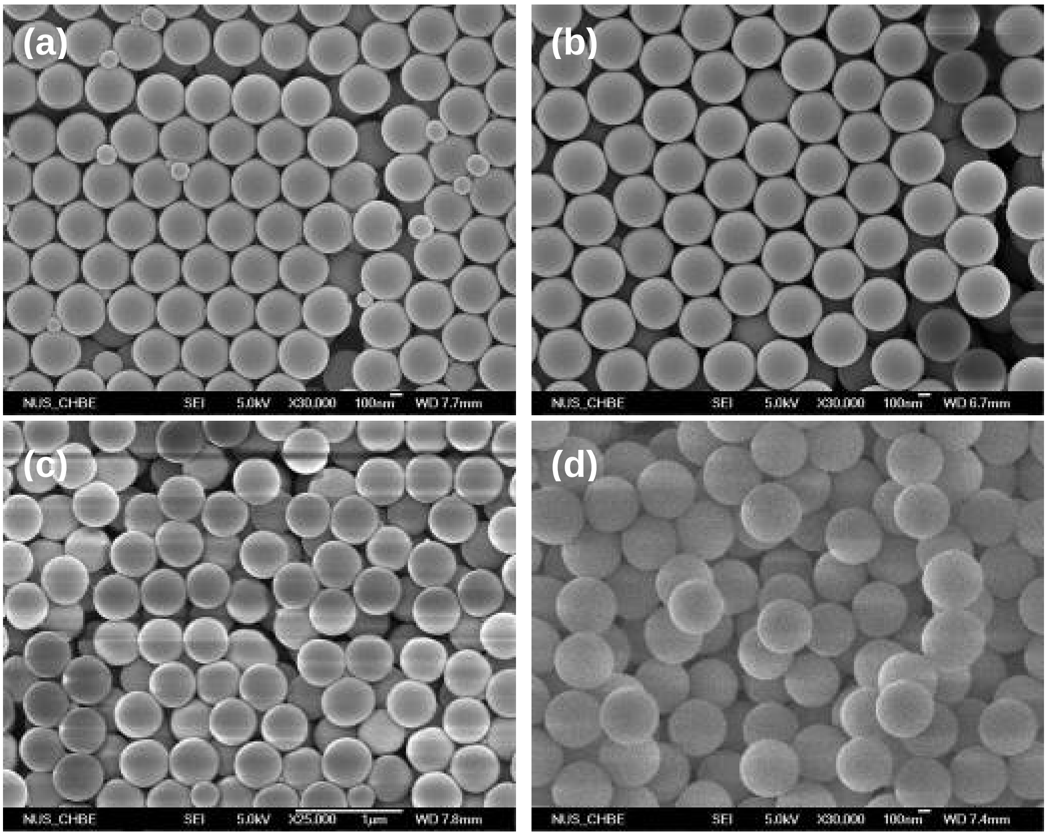

Figure 4.4 Images (a, b) and (c, d) shows the FESEM images of silica beads of 415nm and 445nm before and after separation.

4.2 Synthesis of PS beads by emulsion polymerization

PS spheres are widely employed in the self-assembly of colloidal crystals because of their low density and high ratio of surface charge to density. In some processes such as vertical deposition, typically half a day or several days are needed to allow the growth of the colloidal crystals. The surface charge and low density of PS spheres ensure the stability of the colloid under gravitation force during this period of time, subsequently allowing the self-assembly of larger PS beads.

The polymer microspheres are normally prepared with the techniques suspension polymerization, dispersion polymerization, emulsion polymerization, and seeded polymerization (Arshady, 1992). Among these methods, emulsion polymerization is a well-established method to synthesize monodisperse and submicron polymer microspheres.

In this work, emulsion polymerization was used to synthesize PS microspheres of different sizes. Emulsion polymerization, emulsifier-free emulsion polymerization were employed in the experiments. The experimental results of the different polymerization batches are listed in Table 4.2

Table 4.2 The sizes and the monodispersities of the PS beads

Sample	*Diameter (nm)*	*S.D. Acceptable Yes or No?*
PS1	1060	Y
PS2	970	Y
PS3	1033	Y
PS4	1330	Y
PS5	789	Y
PS6	820	Y
PS7	590	Y
PS8	538	Y
PS9	655	Y
PS10	485	Y
PS11	390	Y
PS12	150	Y
PS13	295	Y
PS14	414	Y
PS15	330	Y
PS16		N
PS17	175	Y

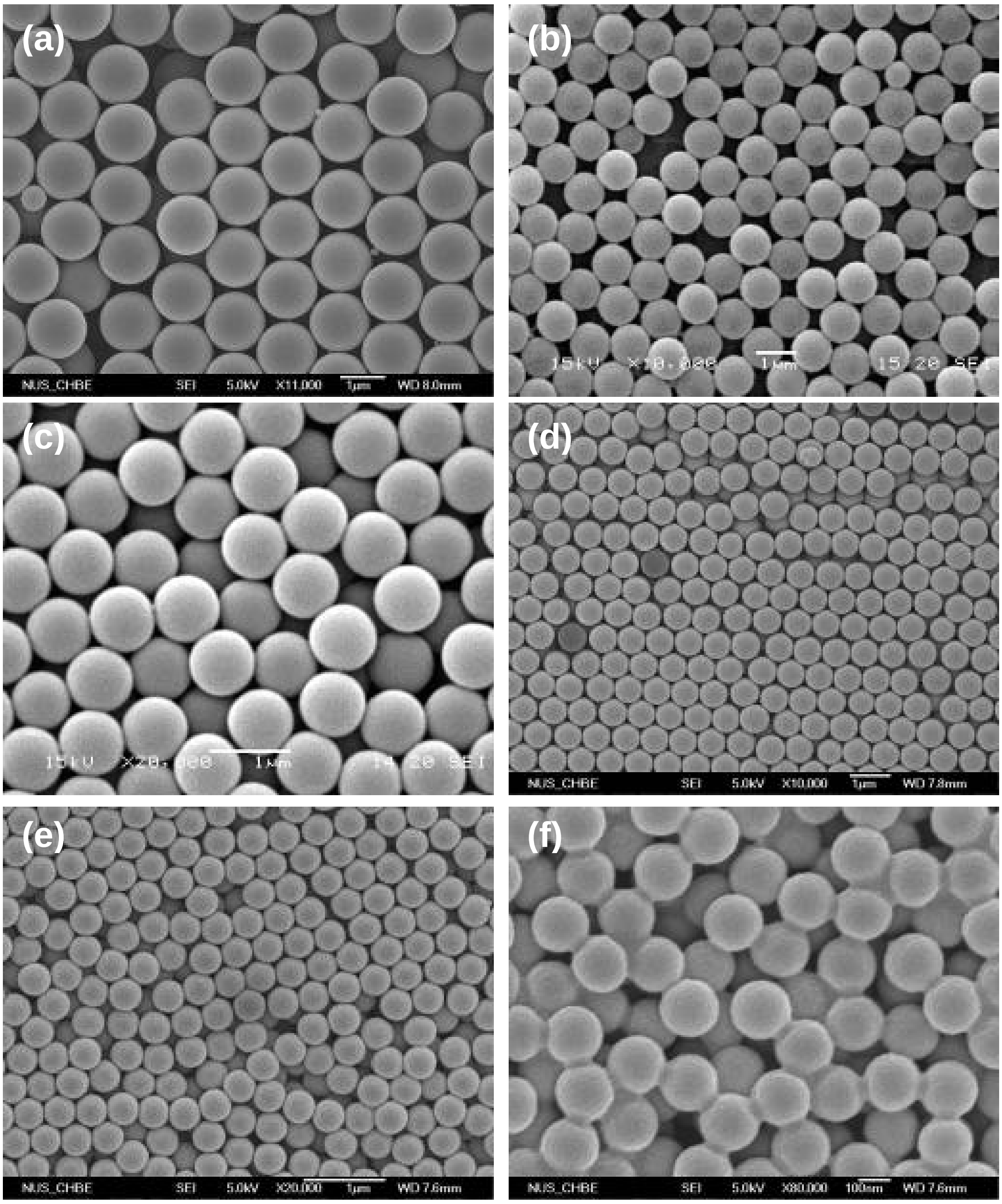

Figure 4.5 SEM of PS microspheres with a diameter of (a) 1330nm, (b) 970nm (c)820nm (d) 655nm, (e) 380nm and (f) 175nm.

The influence of the monomer amount. From the experimental results Figure 4.6, it can be concluded that the final bead size increase with the increase of the monomer amount when the other experimental conditions were fixed. It could be understood that at the initial stage, the number of nuclei formed was limited, so that with the addition of monomer the beads numbers did not increase proportionally, leading to the increase of the final bead sizes.

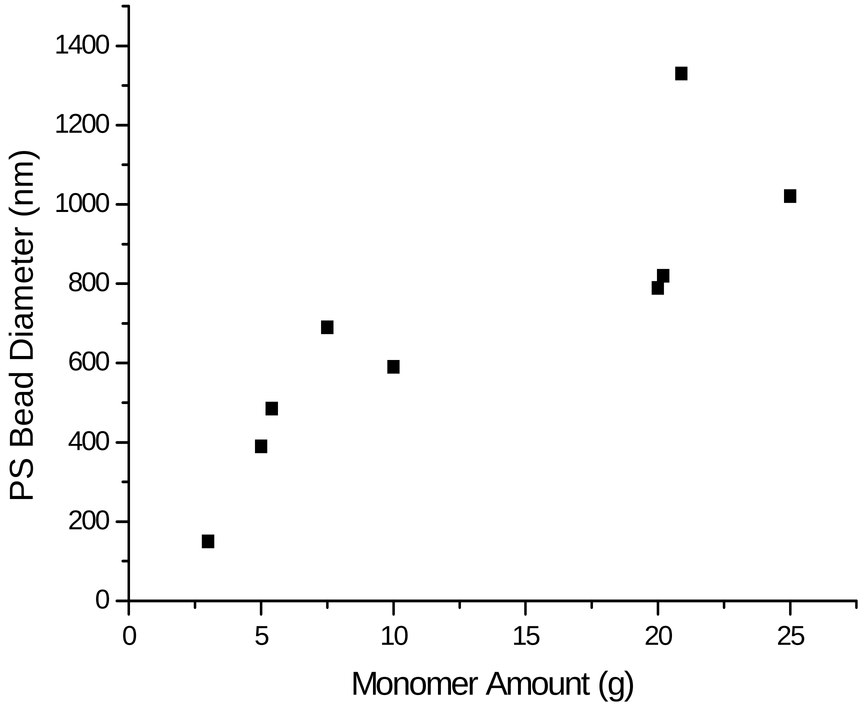

Figure 4.6 The relationship between the monomer amount and the final PS bead size when the initiator is 0.14g and no DVB and SDS were added.

The influence of surfactant. The different sizes of PS5 and PS13 illustrated that the addition of surfactant decreased the final bead size. During both emulsion polymerization processes with and without emulsifier, the polymerization mainly happens in the micelles. In an emulsion process with emulsifier, the micelles of monomer are stabilized by the surfactant. However, in emulsifier-free polymerization, the monomers dissolved in solvent are initiated by radicals of initiator to form water-soluble oligomers. When the chain length of the oligomers achieve to the critical length, they precipitate out and adsorb on the micelle surface and stabilize them. However, the density of the radicals on the surface is much lower than the surfactant on micelle surface in tradition emulsion polymerization. Consequently, during the growth of the oligomers, they are easier to coagulate together. As a result, the final particle size will be much larger than that of emulsion polymerization.

The influence crosslink agent divinylbenzene (DVB). It was found that the addition of DVB also decreased the PS bead sizes. It might be because that DVB is easier to polymerize than styrene, thus addition of DVB increase the speed of polymerization at the initial stage. Thus more seeds are formed and the final bead size decreases while the monomer amount is fixed. The glass transition temperature of the beads was increased from about 100 to 135°C with the addition of DVB (Cha and Choe, 1995). Thus crosslinked PS beads are desirable in some processes that require better thermal stability.

4.3 Summary

Silica spheres have been synthesized using a modified Stöber method. Small silica spheres were first synthesized and the solution of TEOS was dripped into the reaction solution to allow the growth of the silica spheres. Through seed-regrowth process, high uniformity of the size of the silica beads was achieved. The size of the final beads can be precisely controlled by the size of the seeds or the amount of the TEOS dripped into the reaction solution. During the synthesis, the dripping speed should be controlled carefully to avoid the formation of second seeds, which leads to wide distribution of the final bead sizes. Emulsifier-free polymerization has been employed to synthesize monodisperse polystyrene spheres. The control of the sphere size can be achieved by simply adjusting the amount of the monomer while other conditions are fixed. The final bead size increases with the increase of the monomer amount. On the other hand, bead size decrease with the addition of surfactant and divinylbenzene.

Chapter 5

Fabrication of Complex Microspheres

5.1 Synthesis of SiO2/TiO2 core/shell microspheres

Presently, the majority of spheres used in self-assembly approaches to photonic crystals are polystyrene, poly (methyl methacrylate) and silica spheres because of the ease of synthesizing and processing these spheres, as well as the good control of their surface morphology. However, the refractive indexes of these materials are relatively lower than those semiconductor materials. Among various semiconductor materials, titania has long been considered an ideal candidate for fabrication of photonic crystals because of its low absorption in the visible and near-infrared regions and its relatively high refractive index. Unfortunately, it is difficult to prepare titania as uniform colloidal spheres with polydispersity less than 5%. Therefore, employment of microspheres of core-shell structure is an interesting alternative method for the formation of novel photonic crystals, which are expected to exhibit unique optical properties (Breen et al., 2001; Kalinina and Kumacheva, 2001; Velikov and van Blaaderen, 2001; Graf and van Blaaderen, 2002)

Several methods have been applied to deposit TiO_2 films on SiO_2 materials, such as chemical vapor deposition (CVD) and liquid-phase deposition methods (Koumoto et al., 1999; Pizem and Sukenik, 2002; Strohm and Lobmann, 2005). The layer-by-layer deposition approaches are adopted to produce homogeneously coated particles, which utilize the electrostatic attraction between oppositely charged species deposited from solution onto microspheres (Caruso et al., 1998; Caruso, 2001; Caruso et al., 2001a; 2001c). This method allows precise control of the morphology of the microspheres as well as uniform layers of diverse composition. At the same time, the incorporation of metal nanoparticles in the colloidal crystals is of interest because of their influence on the photonic bandgap (Lin et al., 2006) as well as their surface plasmon response (Noguez, 2007). In present work, a novel ultrasonic-assisted liquid-phase deposition method is used to synthesize mono-dispersed SiO_2/TiO_2 core/shell nanostructures with a well-controlled composition. Pt particles were deposited on the SiO_2/TiO_2 core/shell structure.

The surface of the silica spheres were first coated with a layer of PAH (poly allylamine hydrochloride), a cationic polyelectrolyte. The charge on the surface could be determined by zeta potential measurement, as shown in Figure 5.1. We can see that the surface of the SiO_2 spheres was negatively charged in the pH range studied (see curve a) before PAH coating. After coating the surface of the SiO_2 spheres became positively charged as shown in curve d, which facilitated the subsequent deposition of TiO_2 through strong electrostatic attractions. It can be seen from curve b that the addition of $[TiF_6]^{2-}$ reversed the surface charge again. After the addition of H_3BO_3, the titanium species were converted to titania, coating on the silica sphere surface (see curve c).

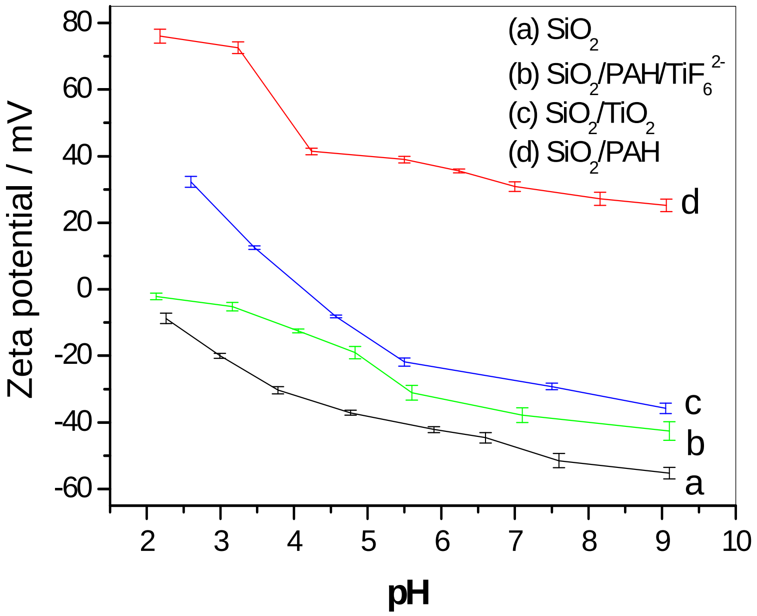

Figure 5.1 Zeta potential profiles of the silica particles at different stages of particle preparation.

The titania film was firstly deposited on the silica spheres surface due to electrostatic interactions. This interaction disappeared after the complete covering of titania. Subsequently, van der Waals force dominated and allowed the continuous deposition of titania on the surface of the silica spheres (Strohm and Lobmann, 2005).

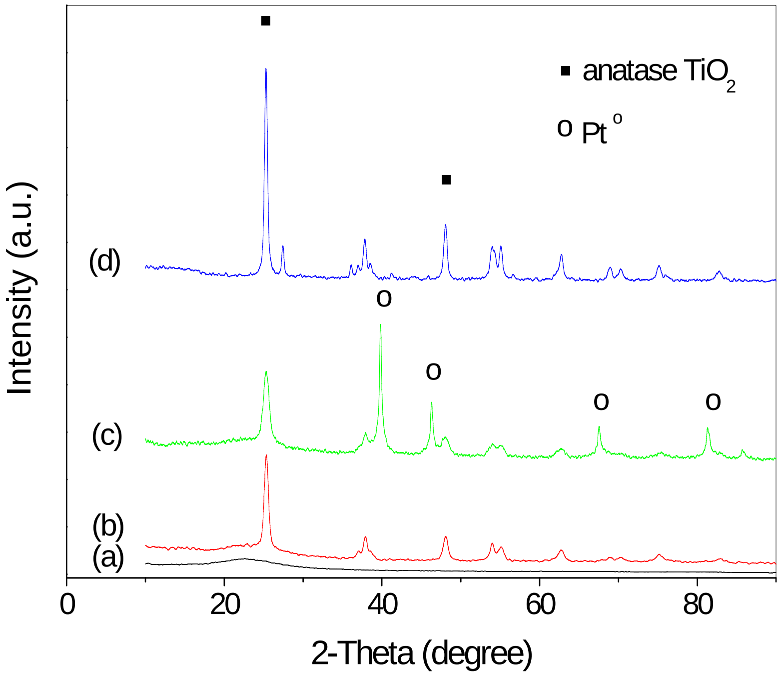

Figure 5.2 XRD patterns of (a) SiO_2 spheres, (b) SiO_2/TiO_2 core/shell structure, (c) SiO_2/TiO_2-Pt particles, and (d) Degussa P25.

The wide-angle XRD patterns of the silica spheres, SiO_2/TiO_2, SiO_2/TiO_2-Pt, and Degussa P25 are shown in Figure 5.2. The silica spheres exhibited a featureless XRD pattern due to its amorphous nature. Samples SiO_2/TiO_2, SiO_2/TiO_2-Pt, and P25 exhibited two characteristic peaks at $2\theta = 25.3$ and 48.1°, which signify titania of anatase phase.[27] The characteristic peaks of Pt^0 with 2θ of 39.7, 46.2, 67.5, and 81.3° were observed on sample SiO_2/TiO_2-Pt, confirming the presence of crystalline Pt^0 phase.

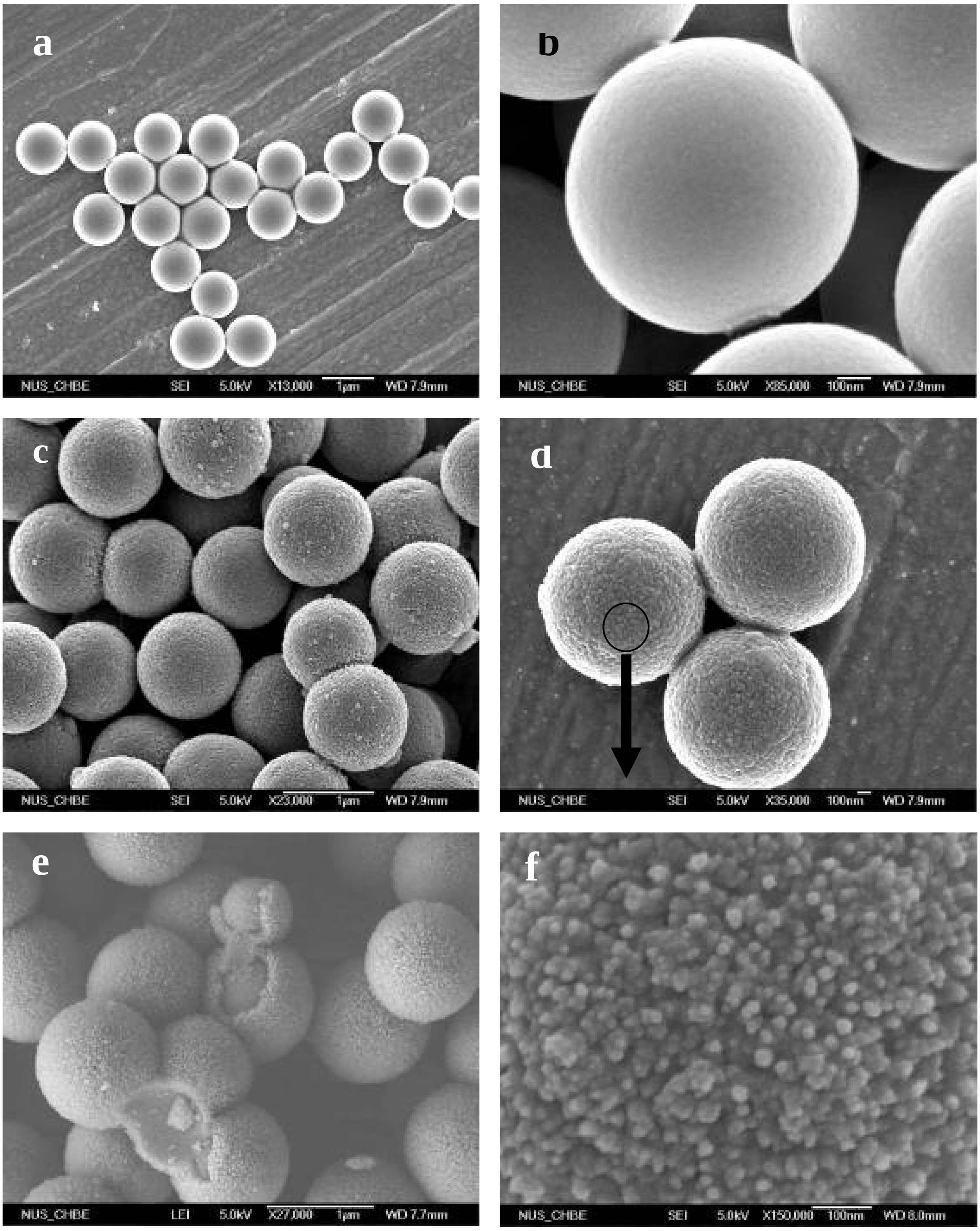
a
NUS_CHBE SEI 5.0kV X13,000 1µm WD 7.9mm
b
NUS_CHBE SEI 5.0kV X85,000 100nm WD 7.9mm
c
NUS_CHBE SEI 5.0kV X23,000 1µm WD 7.9mm
d
NUS_CHBE SEI 5.0kV X35,000 100nm WD 7.9mm
e
NUS_CHBE LEI 5.0kV X27,000 1µm WD 7.7mm
f
NUS_CHBE SEI 5.0kV X150,000 100nm WD 8.0mm

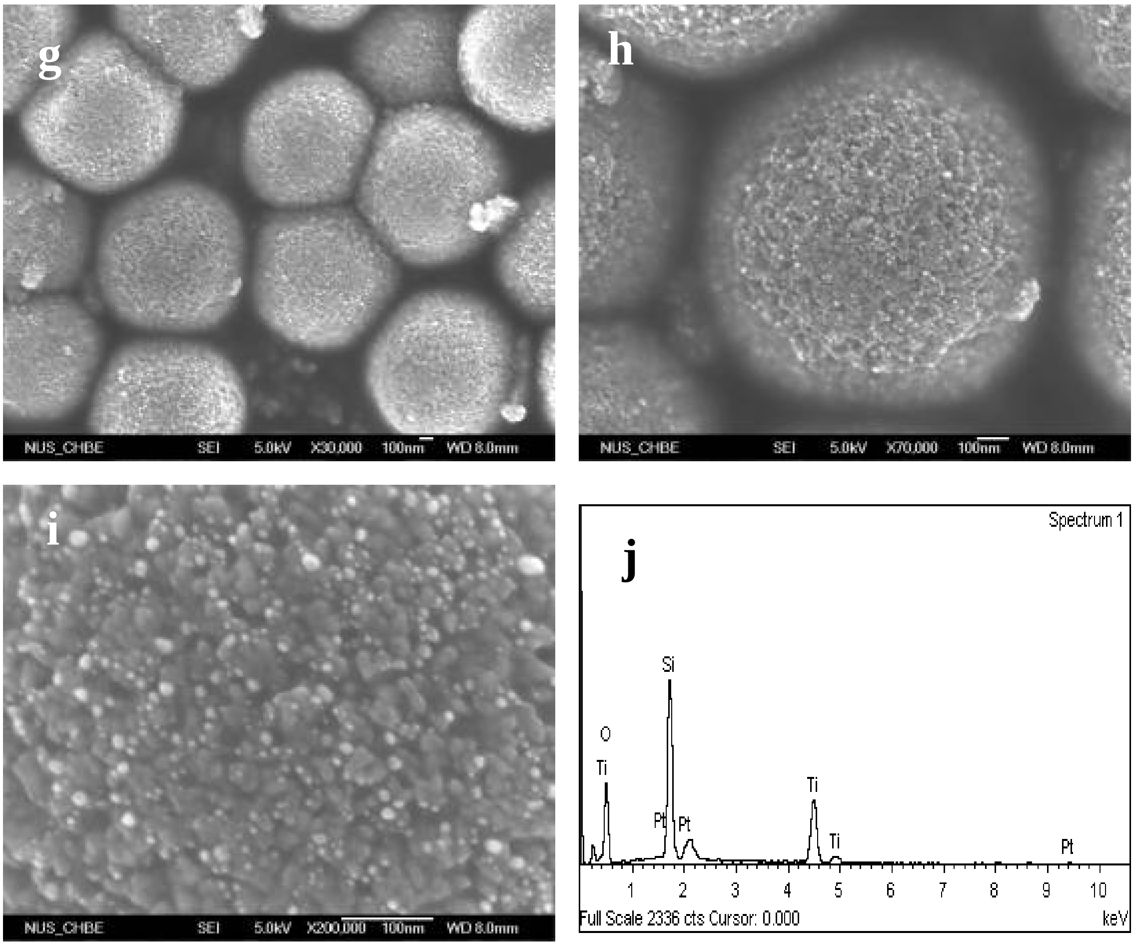

Figure 5.3 SEM images of synthesized silica spheres and core-shell particles: (a) and (b) SiO_2 spheres, (c)-(f) SiO_2/TiO_2, (g)-(i) SiO_2/TiO_2-Pt, (j) EDX analysis of SiO_2/TiO_2-Pt (Pt wt% = 5%), (k) 6th reused SiO_2/TiO_2-Pt and (l) EDX analysis of SiO_2/TiO_2-Pt after 6 runs of recycling.

Figure 5.3 shows the SEM images of silica and the core-shell spheres. It can be seen that the silica spheres is uniform in size with a smooth surface, as can be seen in Figures 5.3a and b. After coating a layer of tatania, the surface of the spheres become rough (Figures 5.3c-f), probably because that titania are deposited as nanoparticles on the silica sphere surface. As shown in Figure 5.3f, the titania film is composed of titania nanoparticles with the size of 10-20 nm. Additionally, the titania shell thickness is uniformly around 80 ± 15 nm. The control of the titania thickness could be achieved easily by adjusting the concentration of the titanium precursor in the preparation steps. Figures 5.3g-i show the SEM images of SiO_2/TiO_2-Pt particles prepared in this work. Pt nanoparticles with sizes of 5-10 nm can be observed uniformly coated on the surface of the TiO_2 shell. MPA molecules have two functional groups, with the carboxyl group adsorbed on titania surface and thiol groups attracted Pt nanoparticles. Thus the density of the Pt nanoparitcles on the shells can be controlled MPA group adhesion density or the Pt particle concentration during the preparation. Figure 5.3j, the EDX analysis confirmed the presence of Pt element.

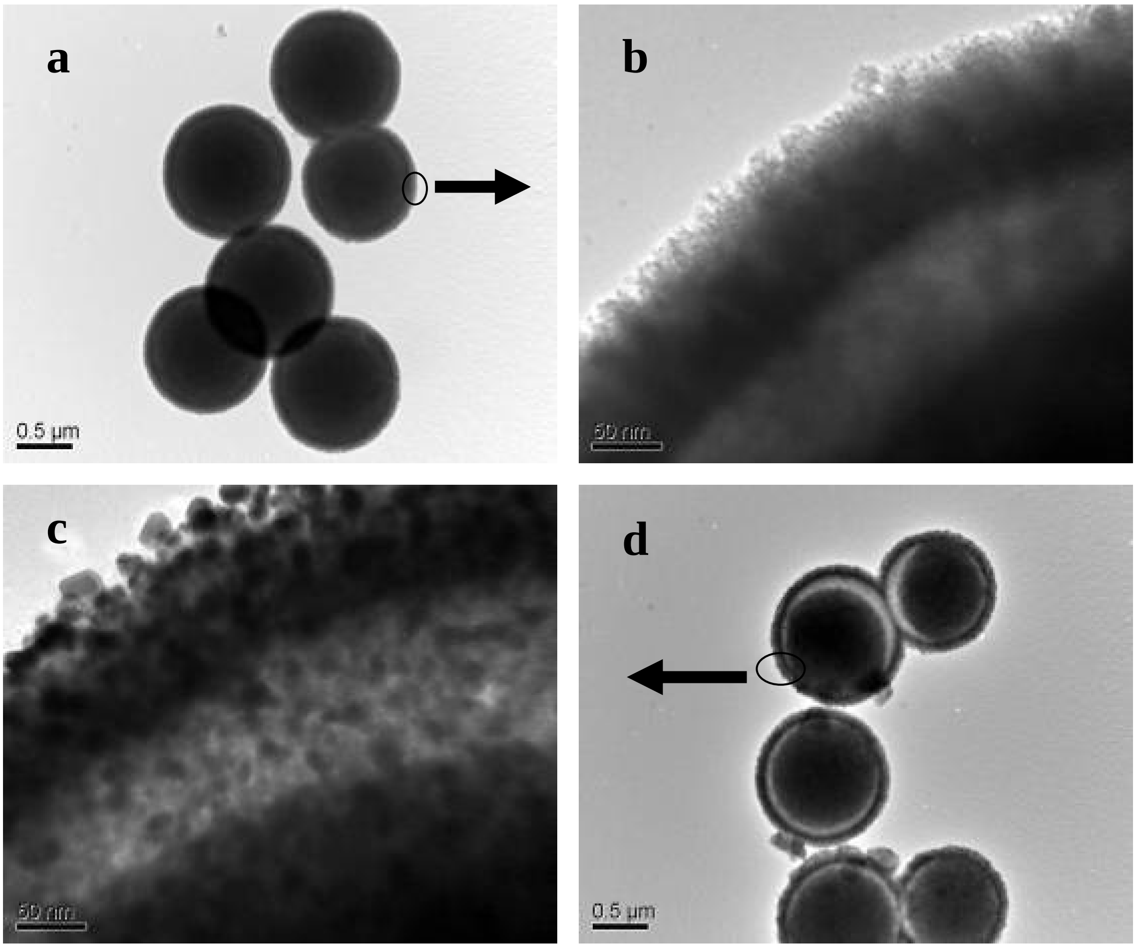

Figure 5.4 TEM images of SiO_2/TiO_2 (a and b) and SiO_2/TiO_2-Pt (c and d).

The TEM images of samples SiO_2/TiO_2 and SiO_2/TiO_2-Pt are shown in Figure 5.4. From Figures 5.4a and d the core-shell structures can be clearly observed. The average thickness of the TiO_2 shell was measured to be in the range of 75 – 90 nm, in accordance with the SEM data. The Pt nanoparticles are observed to have diameters in the range of 7 - 15 nm on the surface of the TiO_2 shell (see Figures 5.4b and c). The TEM images in Figures 5.4b and c were taken at the edge of spherical particles since electron could not penetrate the particles due to their size.

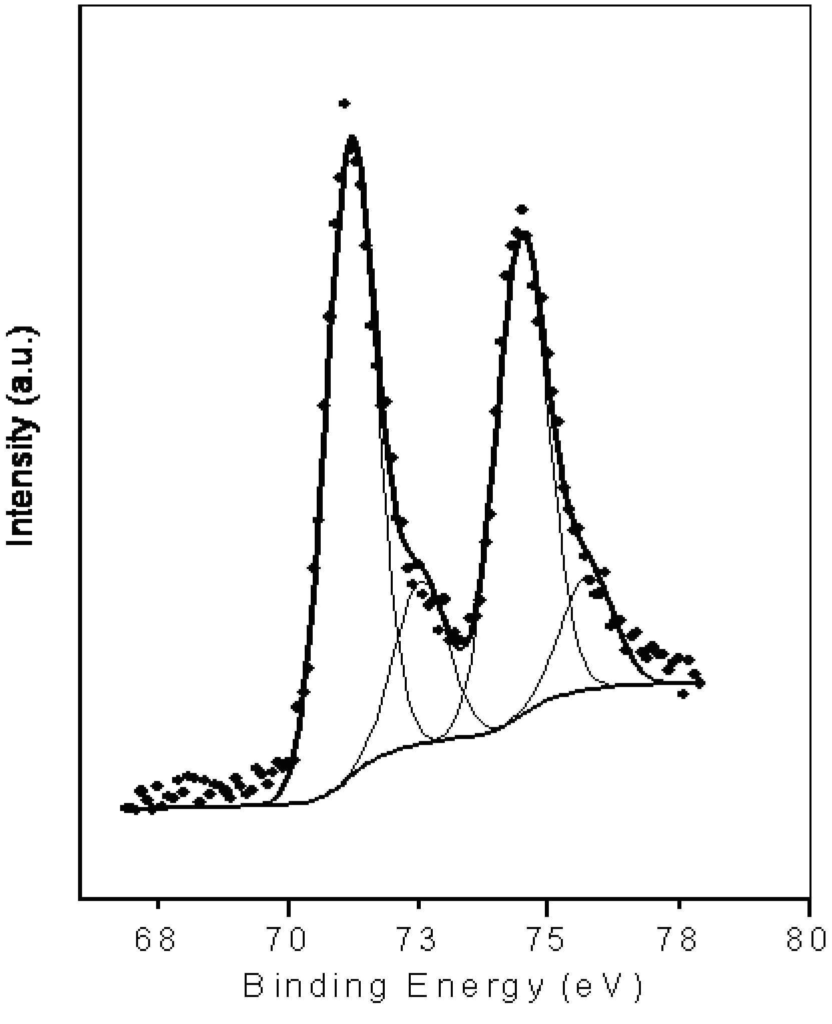

Figure 5.5. XPS spectra of TiO_2/SiO_2-Pt

XPS technique was used to characterize the surface of the particles containing Pt nanoparticles. Figure 5.5 shows the XPS spectra of the SiO_2/TiO_2-Pt samples. The Pt ($4f_{7/2,5/2}$) peaks in SiO_2/TiO_2-Pt could be decomposed into two sets of spin-orbit doublet. Therefore, the Pt ($4f_{7/2,5/2}$) peaks at 71.2, 74.5, and 72.6, 75.7 eV are respectively due to the presence of Pt meal and PtO. The smaple contained both Pt^0 and PtO because of the calcination of the particles during preparation.

5.2 The fabrication of carbon hollow spheres with a controllable shell structure

Monodisperse hollow microspheres have attracted intense attention because of their potential applications in drug delivery systems, catalysis, microreactors, chromatography, adsorption and energy. Over the past few years, template method (Liu and Zeng, 2005; Yang et al., 2005a) emulsion polymerization strategy (Rana et al., 2002) and self-assembly method have been utilized to fabricate hollow spheres of silica (Caruso et al., 1998; Lu et al., 1999; Caruso, 2001; Caruso et al., 2001b; Rana et al., 2002; Chen et al., 2006; Zoldesi et al., 2006), zeolite (Wang et al., 2000), polymer (Yu et al., 2005), metal and metal oxide (Caruso et al., 1998; Yang et al., 2003; Correa-Duarte et al., 2005; Yang et al., 2005a), semiconductor (Liu and Zeng, 2005), and hybrid composites (Tierno and Goedel, 2006). The template method involves coating or deposition of a desired material on the surface of microspheres to form core-shell structures, followed by removing the microspheres, template to obtain hollow structures.

Hollow carbon spheres (HCSs) have received a lot of research interest due to their excellent chemical inertness, electrical conductivity, and controllable surface properties. They might find application in photonic band gap materials, catalyst support, biomaterials, and electrode materials (Lee et al., 2003; Li et al., 2005; Xia and Mokaya, 2005b; Zhou et al., 2005; Wang et al., 2006). Therefore, various methods have been explored to prepare HCSs. Sucrose was used as a carbon precursor to fill in silica inverse opal to obtain HCSs (Zhou et al., 2005). A spherical core-shell structure was used as template to fabricate porous hollow carbon structures (Arnal et al., 2006). A sol-gel method was explored to synthesize HCSs encapsulating tin (Lee et al., 2003). The preparation of graphitic hollow carbon nanoshells was recently achieved by using cellulose chars (Herring et al., 2003) and polypyrrole (Jang et al., 2004). However, complex procedures and the difficulty of controlling the size and morphology of the HCSs in these methods might limit their potential applications.

We report the fabrication of various HCSs with a single shell, deformed shell, double shell, and N-doped shell by silica sphere templates, as illustrated in Figure 5.6. In our work, carbon was coated by CVD of benzene or acetonitrile vapor on the surface of silica spheres and silicon tetrachloride was used for silica coating. HF solution was used to remove the silica spheres or layers to obtain HCSs. Additionally, the use of obtained HCSs as templates was demonstrated to synthesize monodisperse hollow silica spheres.

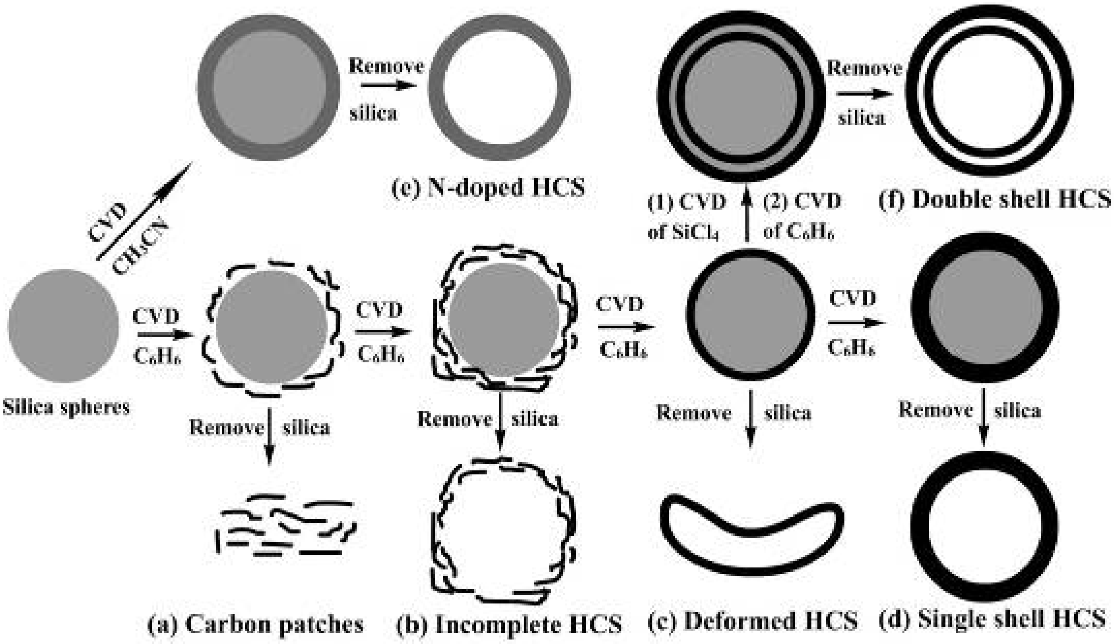

Figure 5.6 The strategy of synthesizing various HCSs. (a) carbon patches from incomplete ; (b) incomplete HCSs from the assembly of carbon patches; (c) deformed HCSs prepared using large silica spheres as templates with a short CVD duration; (d) complete single-shell HCSs prepared obtained after a long CVD period or a high CVD temperature; (e) N-doped HCSs prepared using acetonitrile as the carbon source; (f) double-shelled HCSs prepared using a three-step CVD, depositing layers of carbon, silica and carbon subsequently on a silica spheres, followed by removal of silica.

Single-shell hollow carbon spheres (SHCSs)

Figure 5.7 shows the SEM and TEM images of the silica particles, silica/carbon composite particles and the patches or shells obtained after removal of silica from the composite particles. Figure 5.7a is the image of the silica spheres of 650 nm with a smooth surface used as templates for the following samples. Figure 5.7b shows the silica/carbon composite particle obtained by depositing carbon on the silica spheres with a CVD temperature 900 °C and a deposition time of 0.5 h. It can be seen that carbon patches of different sizes sparsely deposit on the surface of silica spheres.

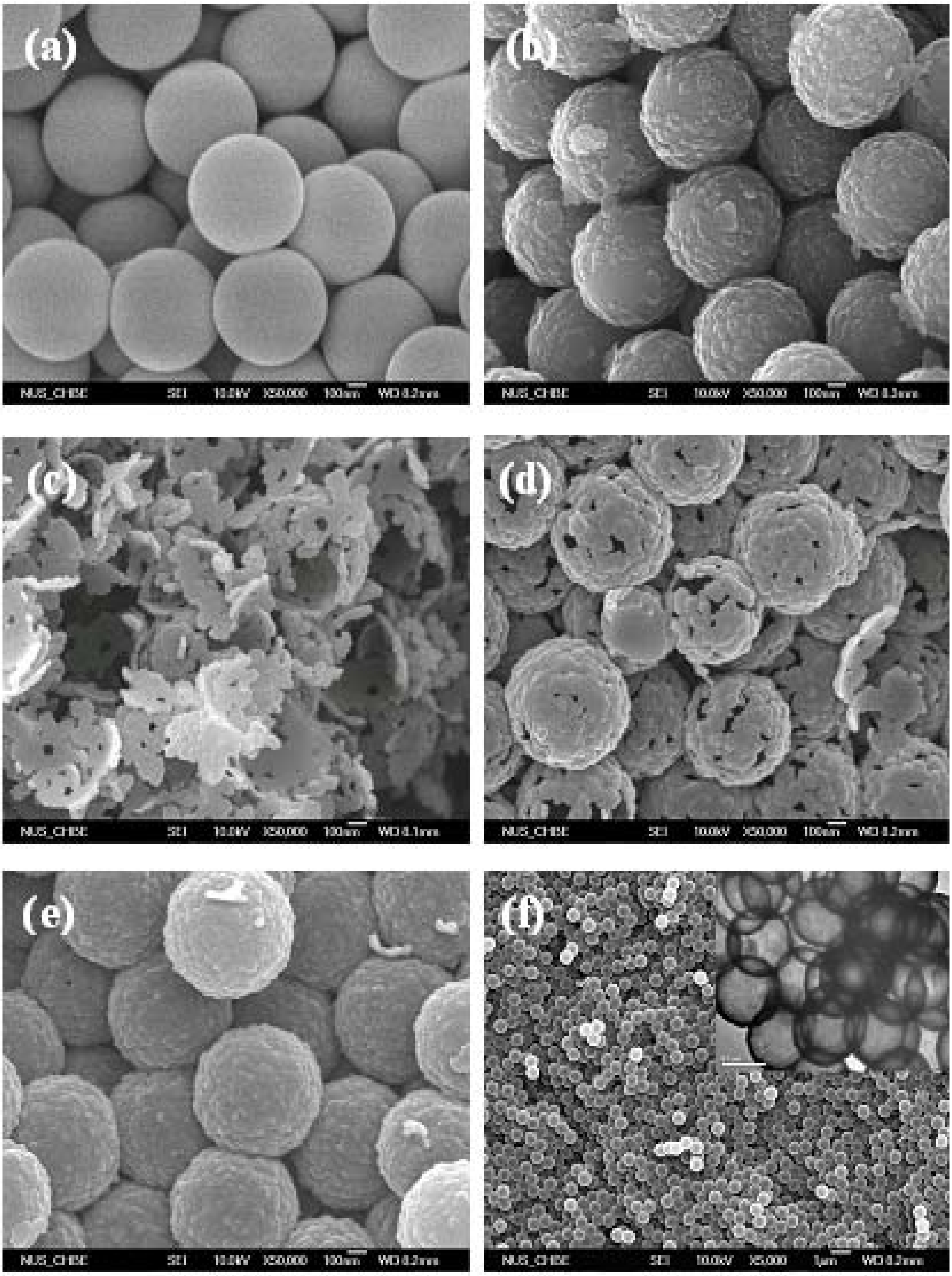

Figure 5.7 SEM and TEM (inset) images of (a) silica spheres of 650 nm in diameter, (b) silica/carbon core/shell after CVD of carbon for 0.5 h, (c, d) are carbon patches and incomplete SHCSs obtained after CVD of carbon for 1 h, 2.5 h, respectively, followed by removal of the silica spheres, (e) SHCSs obtained after CVD of carbon at for 4 h, (f) sample (e) after removal of the silica spheres (this sample is denoted as SHCS900). All the CVD are operated at 900°C.

The patches were formed by the polycyclic aromatic hydrocarbon species produced by dehydrogenation and pyrolysis of benzene molecules (Bokros, 1969). The carbon patches became larger when the CVD time was extended to 1 h at the same temperature, as can be seen from Figure 5.7c. An incomplete carbon shell were achieved by further extending CVD time to 3 h (Figure 5.7d). By prolonging CVD time to 5 h, intact SHCSs with an external diameter of about 730 nm, named as SHCS900, was obtained (Figure 5.7e and f). The shell thickness was measured to be around 50 nm from the inset of Figure 5.7f. The inner diameter of SHCS900, around 630 nm, is smaller than that of the original silica spheres (650 nm), probably due to the shrinkage of silica spheres at high temperatures. Additionally, increasing CVD temperature also gave rise to the speed of carbon depositing on silica spheres, evolving into larger carbon patches.

Figure 5.8 shows the images of the SHCSs prepared under different conditions. Compared with the SHCS900 sample (Figure 5.7e), the SHCSs prepared at 1000 ^{o}C for 4 h (Figure 5.8a) exhibit a smother surface, an external diameter of around 740 nm, a thicker shell of about 70 nm, and a smaller inner diameter of around 600 nm. This indicates that a higher CVD facilitates the formation of a smoother surface, accelerate the carbon deposition rate, and increase the extent of silica shrinkage. When smaller silica spheres (460 nm) were employed as templates, the morphology of HCSs (Figure 5.8b) synthesized under the same conditions was dramatically changed, probably due to the size effect of the silica template on the carbon patches, the building blocks for the formation of hollow structures.

Consequently, larger carbon patches caused a rougher surface and non-spherical morphology of HCSs in our work. The size effect was further confirmed by employing larger silica spheres (around 1600 nm) as templates, as seen in Figure 5.8c. We can see that the surface of SHCSs prepared at 1000 °C for 4 h (named as SHCS1000) is smoother. SHCS1000 has an external diameter of 1720 nm and a shell of 120 nm. Interestingly, when the CVD time was shortened to 1 h using the same silica spheres (1600 nm), a deformed carbon hollow shell was obtained with a shell thickness of around 30 nm (Figure 5.8d).

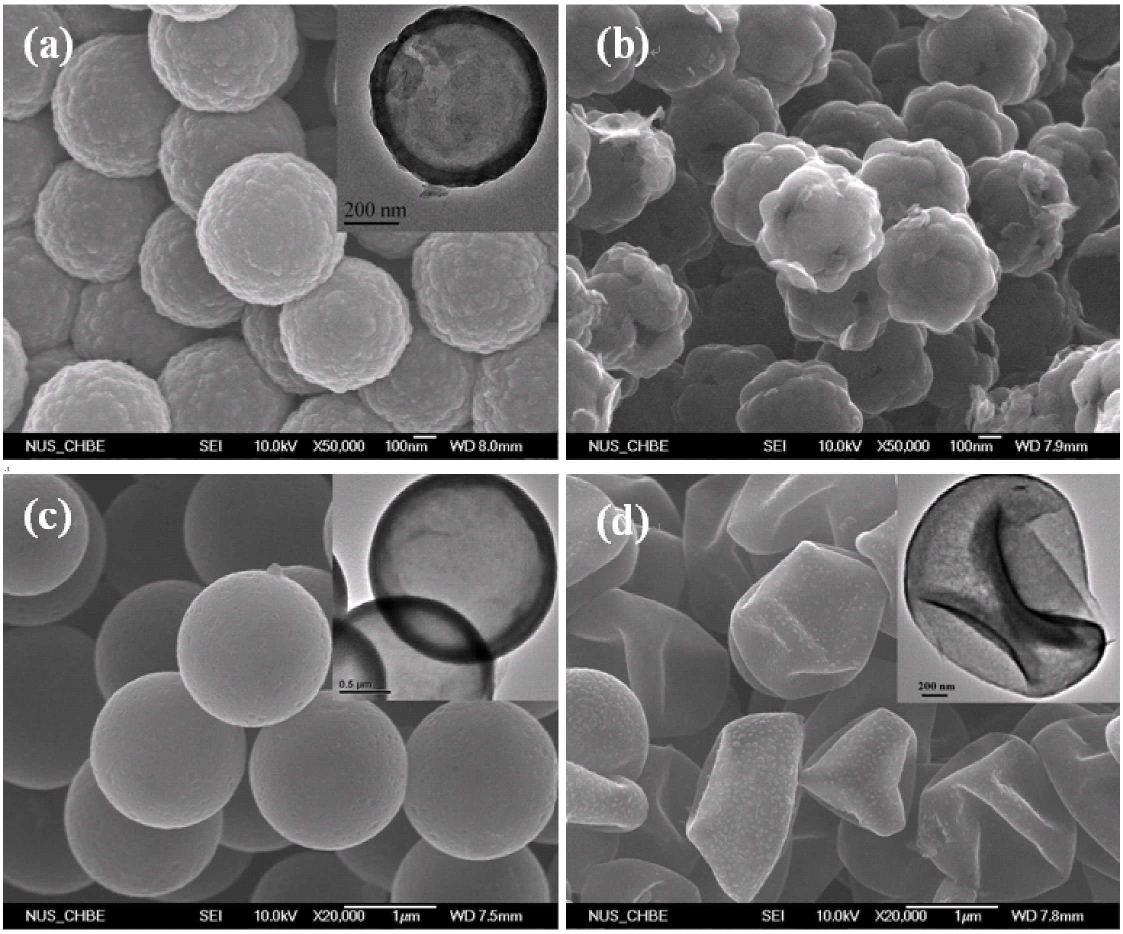

Figure 5.8 SEM and TEM image of SHCSs prepared under CVD temperature of 1000 °C: (a) SHCSs prepared with 650-nm silica sphere template, CVD 3 h; (b) SHCSs prepared with 460-nm silica sphere, CVD 3 h; (c) SHCSs prepared with 1600-nm silica sphere template, CVD 4 h (named SHCS1000); (d) deformed SHCSs prepared with 1600-nm silica spheres, CVD 1 h.

To the best of our knowledge, this is the first time to achieve the deformed graphitizable HCSs. Hollow silica spheres (Chen et al., 2006; Zoldesi et al., 2006), hollow polymer spheres (Yu et al., 2005), and nongraphitizable HCSs (Arnal et al., 2006) with similar deformable hollow structures have been synthesized so far. The deformable property of these structures are owed to the template deformation (Chen et al., 2006), or a high ratio of hollow sphere diameter over shell thickness (Zoldesi et al., 2006) or plastic property of materials (Yu et al., 2005). Probably in our case, the graphitizable thin carbon shells possess some extent of flexibility due to the formation of defects in the graphitic network for strain relief and mechanical relaxation after drying.

N-doped hollow carbon spheres (NHCSs)

By using acetonitrile as the precursor of carbon CVD, we also prepared NHCSs at 1000 ^{o}C (see Figure 5.9). With 730-nm silica spheres as template, monodisperse NHCSs with an external diameter of around 810 nm and a shell thickness of about 60 nm were obtained (Figure 5.9a). With 1600-nm silica spheres as templates, NHCSs (named as NHCS1000) with an external diameter of around 1760 nm and a shell thickness of around 120 nm were achieved (Figure 5.9b). Moreover, the smoother surface morphology of NHCS1000 further demonstrates that the lower curvature of the silica sphere surface leads to smoother carbon shell surface. The EDX spectrum of sample NHCS1000 (Figure 5.9c) shows that NHCS1000 is composed of 80.7 wt % C, 12.6 wt % O, 6.6 wt % N, and 0.1wt % Si, confirming the presence of nitrogen element and the removal of the silica spheres. The XPS spectrum of the sample depicted in Figure 5.9d also shows the presence of C (284.0 eV), O (532.0 eV), N (398.0 eV), and minor Si (99.5 eV). The mass percentages of the four elements were calculated to be 84.4 wt %, 9.5 wt %, 5.6 wt %, and 0.5 wt %, respectively, fairly consistent with the EDX result. The N_{1s} spectrum (inset, Figure 5.9d) can be fitted into two peaks labeled with 1 with a binding energy (BE) of 399.4 eV and 2 with a BE of 400.8 eV, corresponding to pyridine-type N atoms existing at the edge of the grapheme sheet, or quaternary N atoms incorporated in the matrix of the graphene sheets (Xia and Mokaya, 2005a), respectively. In general, C_{1s} spectrum characterized by a large peak at 284.5 eV is attributed to sp^2 carbon atoms and wider peak normally suggests less degree of graphitization (Yang et al., 2005b). It was found that the full width at half maximum (FWHM) of the C_{1s} XPS spectrum of sample NHCS1000 was larger than that of sample SHCS1000, indicating a higher crystallinity of the former.

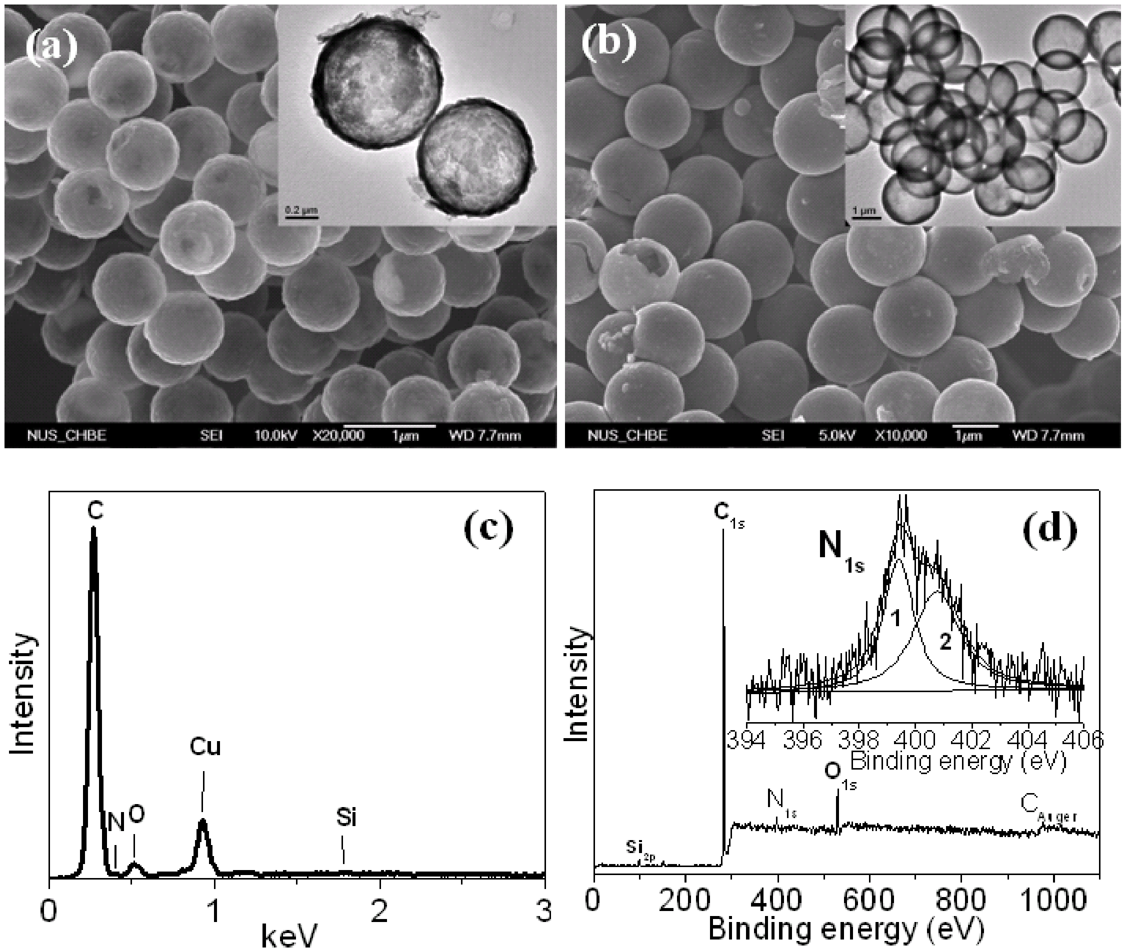

Figure 5.9 (a) Images of SEM and TEM (inset) of NHCSs (730 nm, 1000 °C for 3 h); (b) Images of SEM and TEM (inset) of NHCSs (1600 nm, 1000 °C for 4 h, designed as NHCS1000). (c) EDX and (d) XPS spectrum of NHCS1000.

Figure 5.10 presents the high-resolution TEM images of samples SHCS1000 and NHCS1000, together with their XRD patterns. It can be seen that graphene sheets of different sizes are arranged parallel to the carbon shell surface, indicating the graphitizable nature of the HCSs. However, the discrete and curved features of the graphene sheets indicate a low crystallinity. In addition, SHCS1000 seems to have a shorter graphene sheets and a larger distance between graphene sheets than NHCS1000, implying its lower crystallinity. The XRD patterns (Figure 5.10c) shows the presence of (002), (101), and (004) reflections, indicating the graphitic nature of the carbon materials. Compared with SHCS900, SHCS1000 has a smaller d_{002} value and a larger crystallite size L_c, suggesting that a higher CVD temperature promotes the formation of a higher graphitic carbon structure.

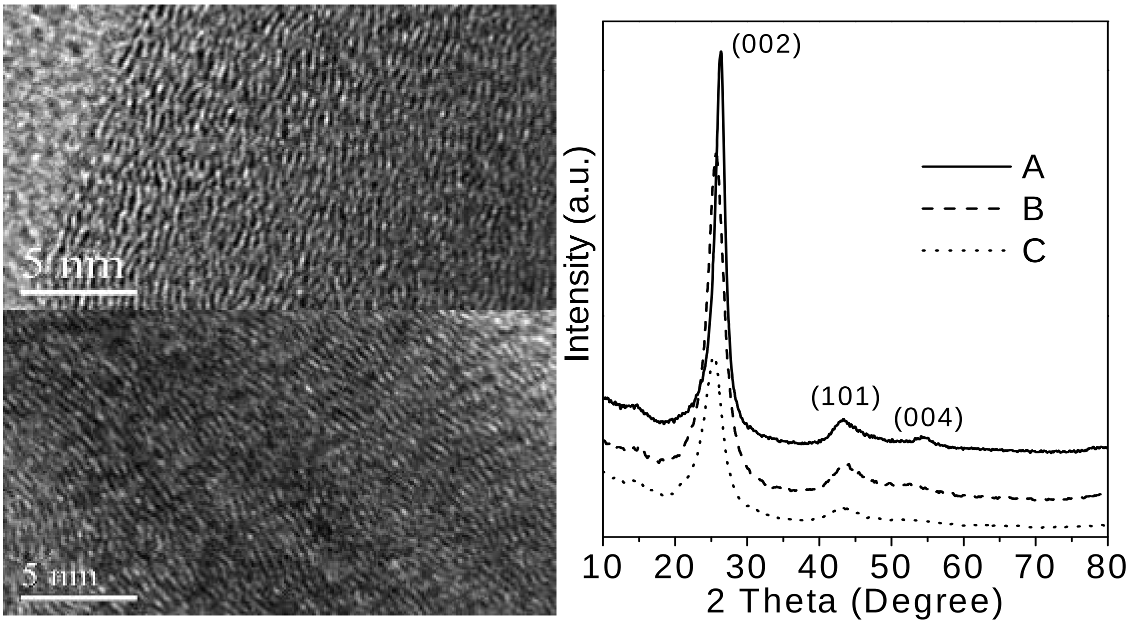

(a) top and (b) bottom (c)

Figure 5.10 TEM images of the carbon shell fringe lattice: (a) SHCS1000 and (b) NHCS1000, together with (c) XRD patterns: (A) NHCS1000, (B) SHCS1000, (C) SHCS900.

Double shelled hollow carbon spheres (DHCSs)

DHCSs were prepared using 1600-nm silica spheres as templates, as shown in Figure 5.11. The external diameter of the DHCSs was measured to be around 1750 nm. The double shell structure can be clearly observed from the broken area of the shells. The TEM image (Figure 5.11b) further confirmed the double shell structure, through which the thicknesses of the outer and inner shells were estimated to be about 35 and 55 nm, respectively. The distance between the two shells was measured to be around 70 nm. The difference between the thicknesses of the two shells might be due to the different surface chemistries of the original silica spheres and the silica layer formed by hydrolysis of $SiCl_4$ during the silica CVD (Miguez et al., 2002).

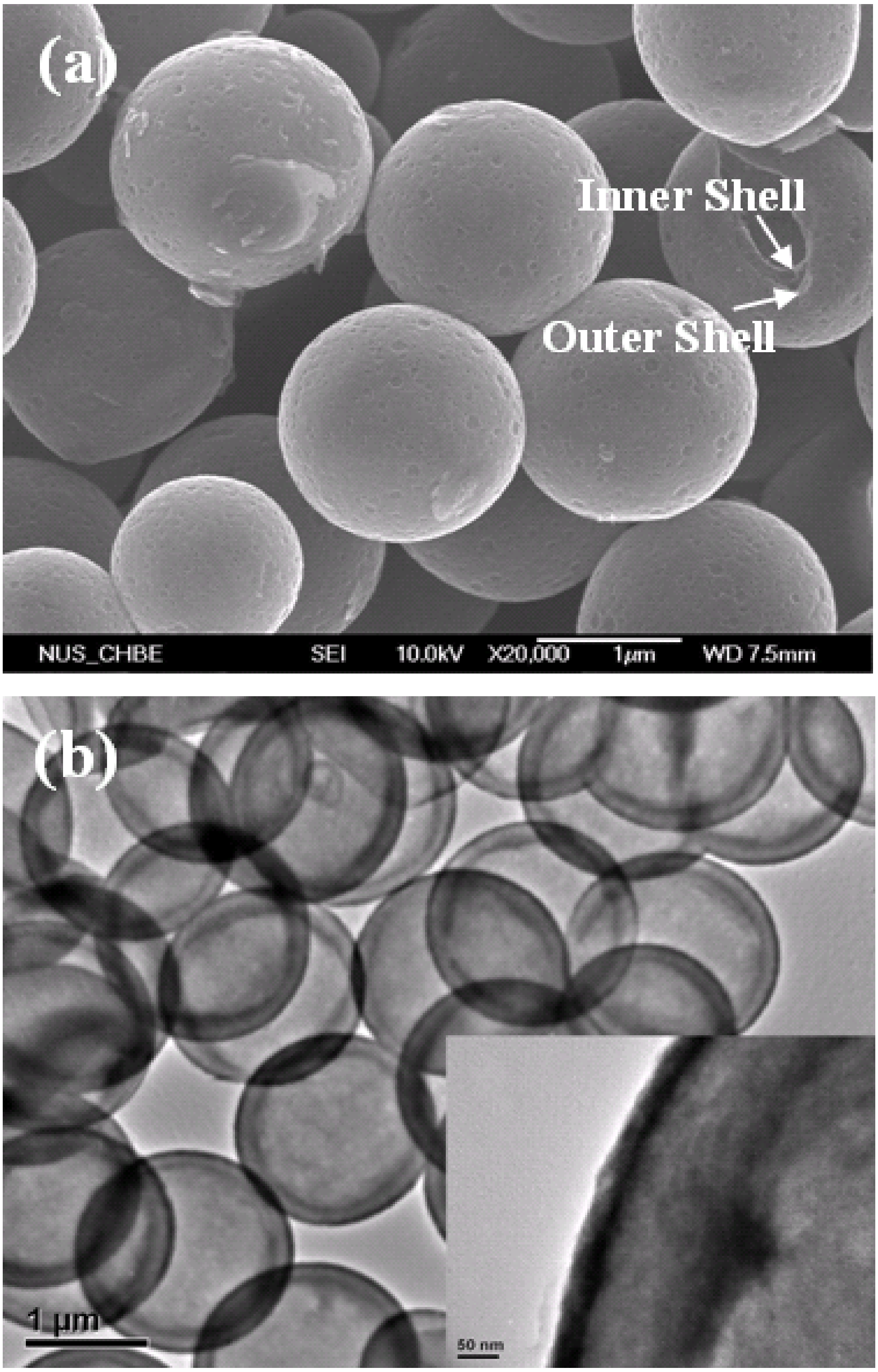

Figure 5.11 SEM (a) and TEM (b) images of DHCSs.

Hollow silica spheres

By using SHCS1000 as template we synthesized hollow silica spheres, as illustrated in Figure 5.12. The average diameter of the silica spheres was measured to be 1520 nm (Figure 5.12a), less than that of template SHCS1000 (1720 nm), probably due to the shrinkage during calcination at 700 ^{o}C for 4 h. From the TEM image, it can be observed that the hollow structure has a shell thickness of 150 nm. In the silica CVD process, water vapor and $SiCl_4$ vapor reacted to form silica depositing on the surface of template SHCS1000 (Miguez et al., 2002). Subsequently, removal of carbon yielded the hollow silica spheres. The thickness of the silica layer can be tuned by controlling the deposition time.

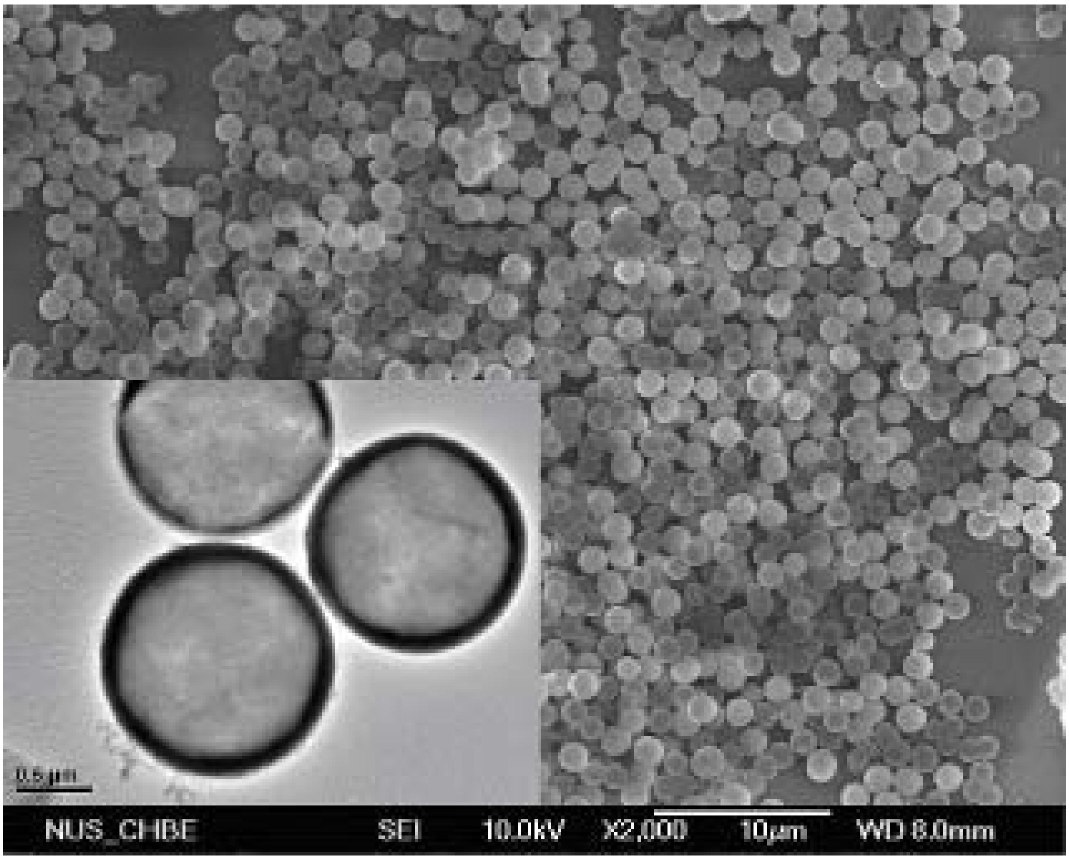

Figure 5.12 (a) SEM and TEM (inset) images of hollow silica spheres

5.3 Summary

SiO_2/TiO_2 core/shell structure and SiO_2/TiO_2-Pt core/shell structures with Pt nanoparticles well dispersed in the TiO_2 shell were syntheiszed and characterized with SEM, XRD and XPS.

The preparation of graphitizable hollow carbon spheres (HCSs) with a single shell, deformed shell, double shell, and N-doped shell were also demonstrated by using silica spheres as templates via chemical vapor deposition (CVD) of benzene or acetonitrile. The shells of carbon materials was found to be assembled from carbon patches (polycyclic aromatic hydrocarbon). The structure and thickness of the hollow carbon shells depended on the experimental conditions including silica sphere diameter, CVD temperature and duration. The syntheis of deformable graphitizable HCSs were first achieved. It was found that higher CVD temperature resulted in higher graphitic nature of HCSs and the N-doped HCSs is more crystallized than undoped HCSs under same CVD conditions. Monodisperse hollow silica spheres was also synthesized using HCSs as templates.

Chapter 6

Fabrication of Crack-free Colloidal Crystals

6.1 Introduction

Since Yabnolovitch (1987) and John (1987) independently proposed the concept of photonic crystals (PhCs) or photonic bandgap (PBG) materials in 1987, this family of optical materials has attracted a great deal of research interest because PhCs can be used to manipulate photons, offering a platform for future photonic and optoelectronic integrated circuits. Self-assembly of colloidal microspheres is an inexpensive approach to the fabrication of three-dimensional (3D) PhCs (Xia, 2001). While self-assembly of colloidal microspheres does not produce PhCs with a complete PBG, it yields colloidal crystals (CCs), which are excellent template for further processing to fabricate materials with a complete PBG (Busch and John, 1998; Blanco et al., 2000; Vlasov et al., 2001). Various methods of self-assembly have been developed to produce CCs, including gravitational sedimentation (Zhu et al., 1997; Miguez et al., 1998), vertical deposition (VD) (Jiang et al., 1999), horizontal deposition (Yan et al., 2005), electrophoretic deposition (Holgado et al., 1999), spin-coating (Jiang and McFarland, 2004; Mihi et al., 2006), confined cell method (Park et al., 1999), Langmuir-Blodgett technique (Reculusa and Ravaine, 2003) and floating self-assembly (Im and Park, 2002). These methods afford CCs in large domains with a desired thickness.

However, the resultant colloidal crystals fabricated using the above-mentioned self-assembly methods often contain unwanted defects, such as cracks, stacking faults, and dislocations. It has been a great challenge to experimentally avoid the formation of such intrinsic defects. Cracks occurring vertically with regard to a substrate, typically divide the colloidal crystal films into areas of several tens of micrometers, creating a major obstacle to the application of CCs as template. It has been observed that the formation of cracks is mainly caused by the decrease in the distance between two adjacent spheres due to the tensile stresses during the drying step (Jiang et al., 1999; Wong et al., 2003; Tirumkudulu and Russel, 2004). Although optimization of the conditions of self-assembly of colloidal spheres has been carried out to minimize the formation of cracks (Griesebock et al., 2002; Wong et al., 2003; Chabanov et al., 2004; McLachlan et al., 2004; Li et al., 2005; Chung et al., 2006), only very recently Jin and co-workers (Jin et al., 2005) reported a successful fabrication of crack-free CCs. In this method, a template with periodic pillars on a silicon substrate is used to direct the growth of CCs in a VD process. By scrupulous control over the experimental parameters, crack-free (100)-oriented CC films can be obtained. Wong et al. (2003) hypothesized that adding tetraethyl orthosilicate (TEOS) or tetramethyl orthosilicate to an alcoholic colloidal suspension of silica spheres may minimize the formation of cracks. However, no experimental results were presented to support this hypothesis.

6.2 The Fabrication of Crack-free Colloidal Crystals

In this thesis work, a method on the basis of the VD method was designed and demonstrated for the fabrication of crack-free CCs. How the method works is schematically illustrated in Figure 6.1. A given amount of a silica precursor solution containing TEOS, hydrochloric acid, and ethanol is added to an alcoholic colloidal suspension of silica spheres. The hydrolysis of TEOS produces coarse silica species, which fills the spaces between the silica spheres. The importance of the silica species is to counteract the shrinkage of the CCs during drying. By adjusting the amount of the silica precursor solution, crack-free colloidal films can be obtained. The films thus fabricated are composed of non-close packed silica spheres with the voids being filled with coarse silica. Interestingly, the silica species in the interstices can be easily etched away by HF vapor, (Marczewski and Goedel, 2005) leaving behind the silica spheres forming a crack-free CC film. Additionally, if an excessive amount of the silica precursor solution is used in the VD process of producing silica sphere bilayer, the resultant CC films curl and peel off from the substrate, resulting in the formation of ordered nanobowl arrays (Xu et al., 2004) on the substrate.

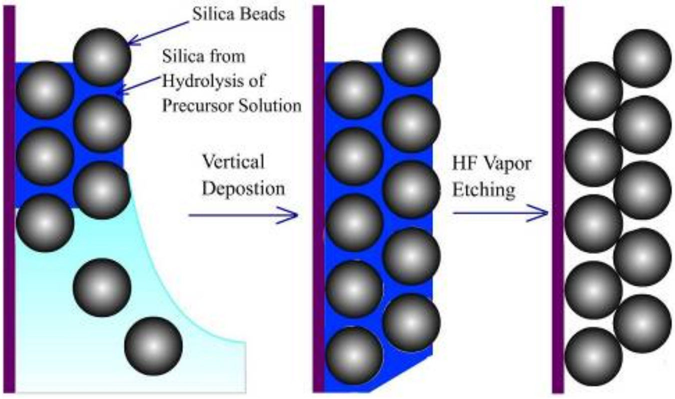

Figure 6.1 A scheme illustrating the steps of fabricating crack-free colloidal crystal films.

It was found that when pure TEOS was added to a silica sphere suspension in the VD process, little effect on the formation of cracks was observed. When 0, 200, 420, and 500 μL of the silica precursor solution containing TEOS, ethanol and HCl were respectively added to 15 mL of 1.7 wt% 277nm silica sphere suspension in the VD process, samples denoted as VD-1, VD-2, VD-3, and VD-4 were obtained, and their FESEM images are shown in Figure 6.1. It can be seen that the domain sizes of the CC films became larger and larger from samples VD-1 (Figure 6.2b) to VD-2 (Figure 6.2a), and sample VD-3 is a crack-free CC film (Figure 6.2c). The existence of HCl was essential for the fabrication of crack-free CC films because it catalyzed the hydrolysis of TEOS.

The cracks seen from sample VD-1, which was prepared in the absence of the silica precursor solution, arose from the decrease of the distance between the centers of the adjacent spheres in the CC film during drying, caused by shrinkage of the spheres and the evaporation of solvent (Jin et al., 2005). Because the spheres of the bottom layer were attached to the substrate, the trend of contraction of the film during drying was resisted by the substrate. Thus a tensile stress was produced and became stronger and stronger until it was released by cracking (Tirumkudulu and Russel, 2004). When some silica precursor solution was added into the colloidal suspension, the concentration of the silica species and HCl in the meniscus region was increasing with the evaporation of the solvent. The silica species filled in the voids between spheres and occupied the place of the solvent layers. Consequently, the force bringing silica spheres to become closer was balanced by the deposited silica layer. A crack-free CC film can be obtained when the concentration of silica precursor solution is appropriate. From the high magnification image of the CC film of sample VD-3 (Figure 6.2e) it can be seen that the voids between the spheres are completely filled with silica. It was measured that the average distances between the centers of the adjacent spheres were 283 and 289 nm respectively in the CC films of samples VD-2 and VD-3, both larger than the diameter of the silica spheres. This demonstrates that the introduction of the silica precursor solution increased the final distance between the adjacent silica spheres.

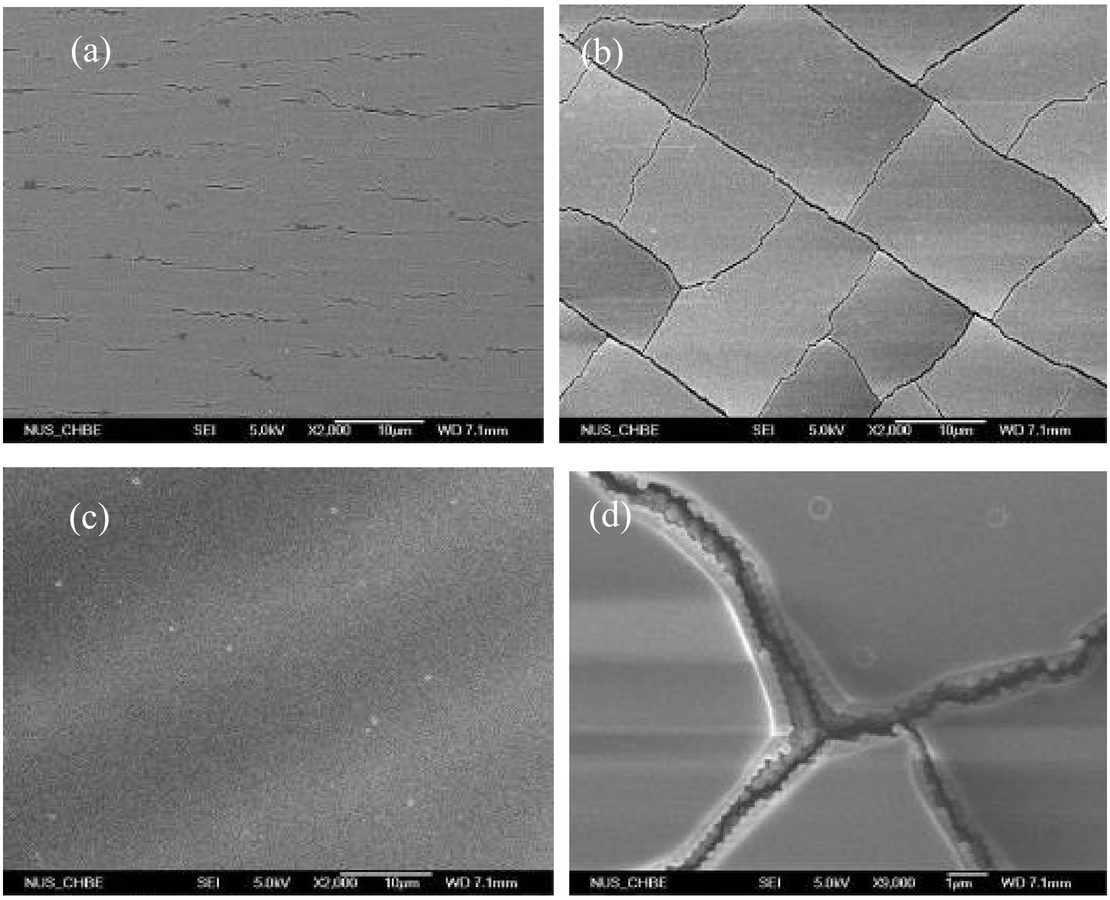

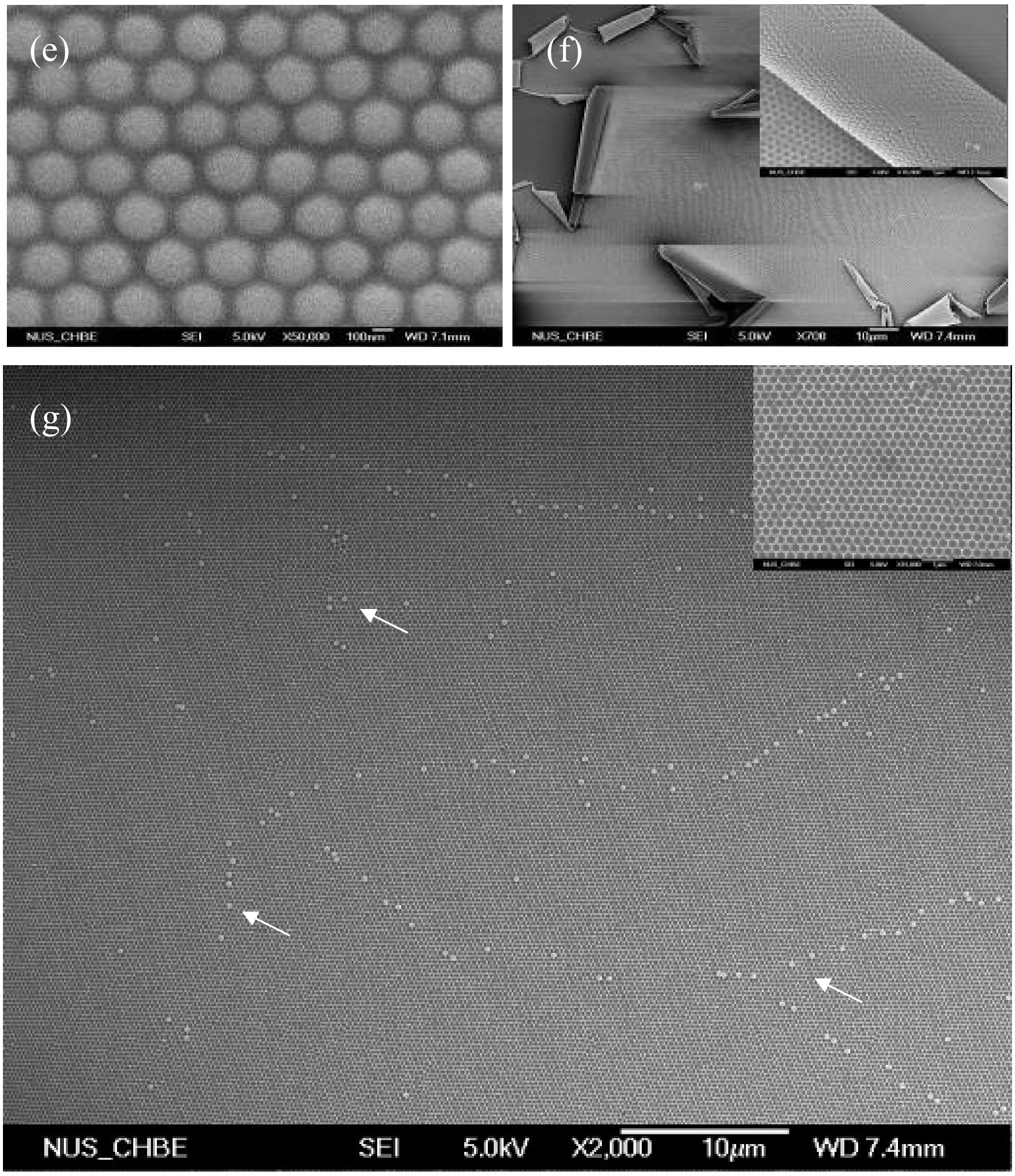

Figure 6.2 Top views of colloidal crystal films VD-1 (a), VD-2 (b), VD-3 (c and e), VD-4 (d), and VD-5 (f) (the inset image shows the magnified view of a CC roll). (g) is a SEM image of an exposed nanobowl array of sample VD-5 (the inset image is a magnified view, the scale bar in the inset is 1 μm).

When an excessive amount of the silica precursor solution was added to the colloid, the silica produced from hydrolysis not only filled up the voids of the silica beads, but also deposited an additional silica layer on the top of the CC film. This silica layer was dried ahead of the CC of silica spheres, causing the reappearance of cracks due to the contraction of the additional silica layer during drying. It can be clearly observed from Figure 6.2d that the first layer of silica beads near the cracks was dragged apart from the bottom layer by the additional top silica layer. When a 0.56 wt% silica sphere colloid with addition of 200μL of the silica precursor solution was used in our VD experiment (the sample thus obtained is denoted as VD-5), the resultant bilayer of silica spheres curled together with the top silica layer. Thus the whole CC film peeled off partially from the substrate (Figure 6.2f), forming a roll-like structure (the inset image of Figure 6.2f). A nanobowl array was left on the areas where the CC film peeled off from the substrate. It should be noted here that this observation can lead to a one-step method of fabrication of nanobowl arrays in large domains (Figure 6.2g). For the nanobowl arrays, some silica spheres that had not been pulled together by the curled CC film are still seen as indicated by the arrows.

From the cross-section view of the CC film of sample VD-3 (Figure 6.3a), it can be seen that a coarse silica layer occupies the voids between the silica spheres. Thus, when the CC film was exposed to HF acid, the interstice silica could be etched away rapidly while the silica spheres were not significantly affected because HF acid can diffuse much more easily into the coarse silica layer than into the dense silica spheres. When the film was exposed to a dilute HF solution, however, the etched film presented serious cracks. In this work, HF vapor was used to avoid the introduction of cracks during the etching process. Figure 6.3c is a top view of the CC film of sample VD-3 after being exposed to HF vapor for 85 s. From the high magnification view it can be observed that all interstice silica was removed while the average diameter of the silica spheres was reduced to 274 nm (the silica spheres deviated a little from their position because of exposure to the electron beam of SEM). In the same layer the silica spheres are no longer close packed, but a non-close-packed array. However, the adjacent layers are still closely packed. Point defects arising from smaller particles and doublets are indicated by the arrows. The domain areas are normally larger than 1mm^2 and most of them are divided because of stack faults rather than cracks. Images of different magnifications of the etched crack-free CC film are shown in Figures 3d and e.

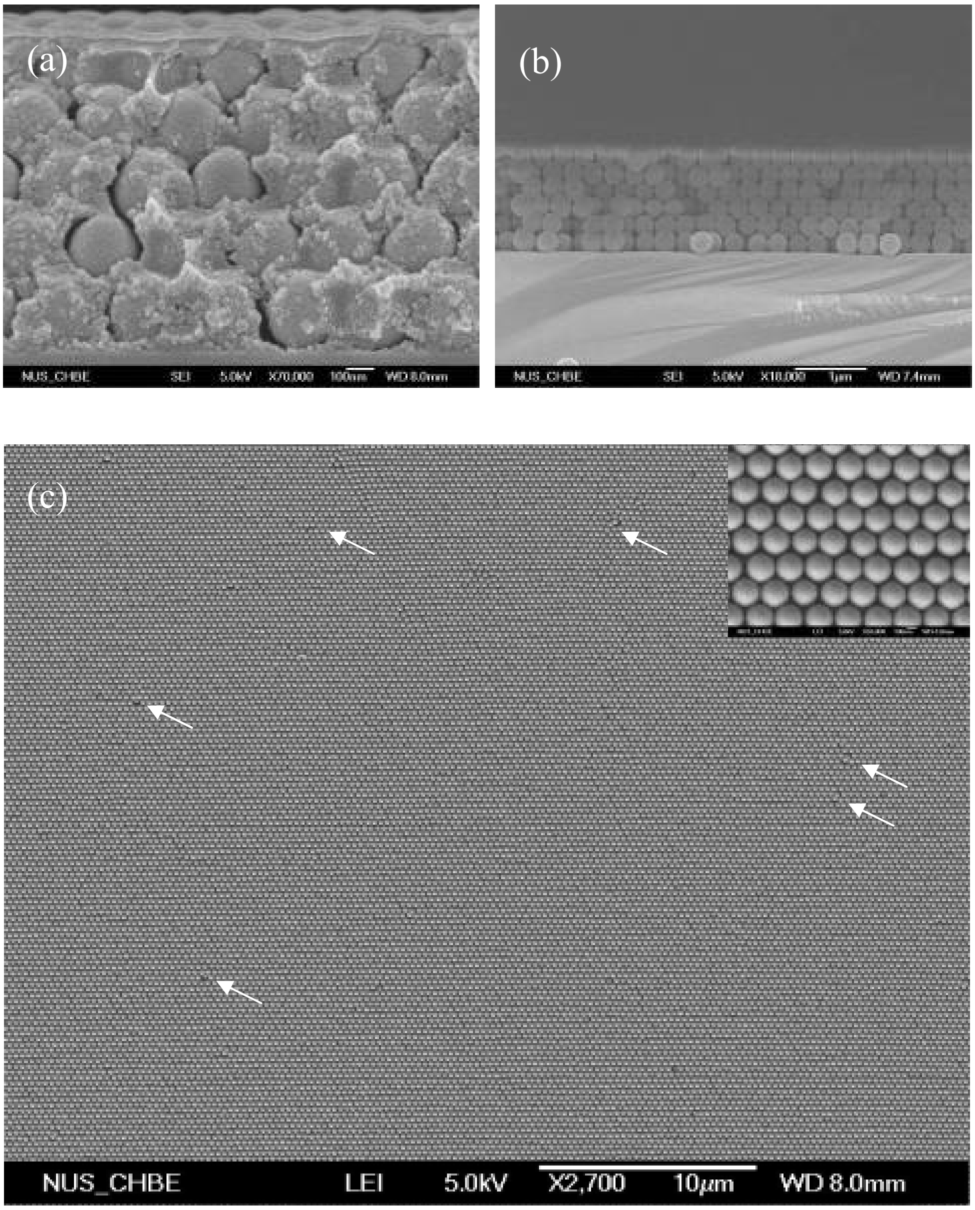

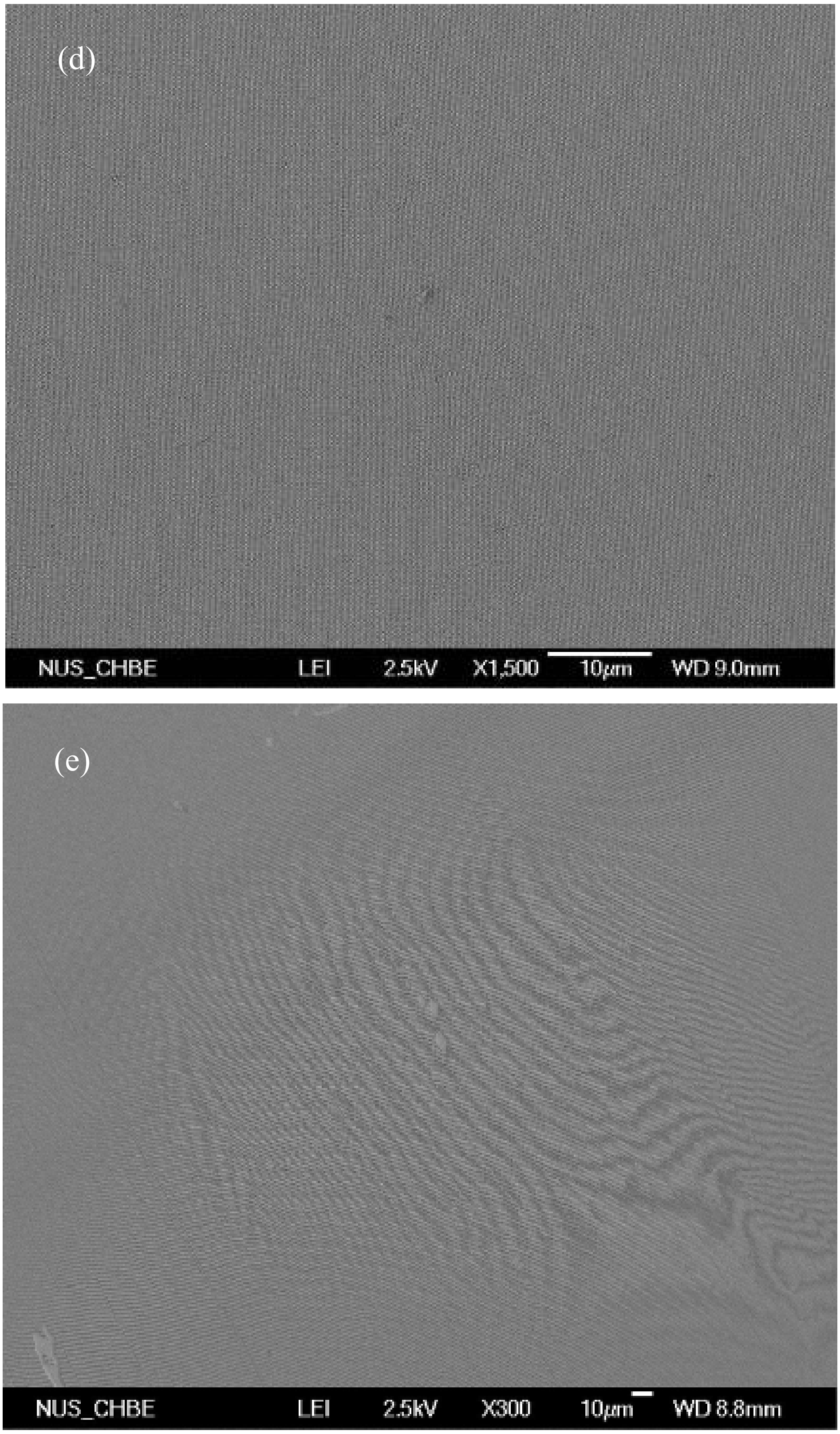

Figure 6.3. (a) and (b) are the FESEM cross section views of the sample VD-3 before and after HF vapor etching, respectively. (c) are the top view of the sample VD-3 after HF etching with an inset image of higher magnification (the scale bar is 100nm in the inset image). (d) and (e) are the top view of VD-3 after HF etching in smaller magnification.

Figure 6.4 shows the optical properties of the films obtained from the VD method and that of the CC film of sample VD-3 after being exposed to HF vapor. It can be seen that with the increase of the amount of the silica precursor solution added to the self-assembly system, the diffraction peak due to the pseudo-gap became lower and lower while its position underwent a red shift because of the increased infiltration of silica species into the voids of the silica spheres, leading to the decrease of the refractive index contrast and the increase of effective refractive index. For sample VD-3, the peak almost became indistinguishable from the side fringes owning to the finite thickness of the film because its voids are fully filled with silica. However, a new sharp peak appeared after HF vapor etching, indicating that the interstice silica was successfully removed and the ordered structure of the self-assembled silica spheres was maintained. Obviously, the reflectance peaks underwent a blue-shift in comparison with that of sample VD-1 because of the reduction of the diameter of the silica spheres and the increase of the distance between the centers of the silica spheres.

It was experimentally observed that the amount of the silica precursor solution needed to fabricate crack-free CC film must be increased with the increase in the concentration of colloidal silica spheres. Figure 6.5 shows the relationship between the precursor solution volume, colloid concentration and the number of layers of CCs. With the increase of colloid concentration, the number of layers of the CC deposited on the substrate increases. Thus more silica is needed to fill up the voids between silica spheres and the amount of precursor solution increases.

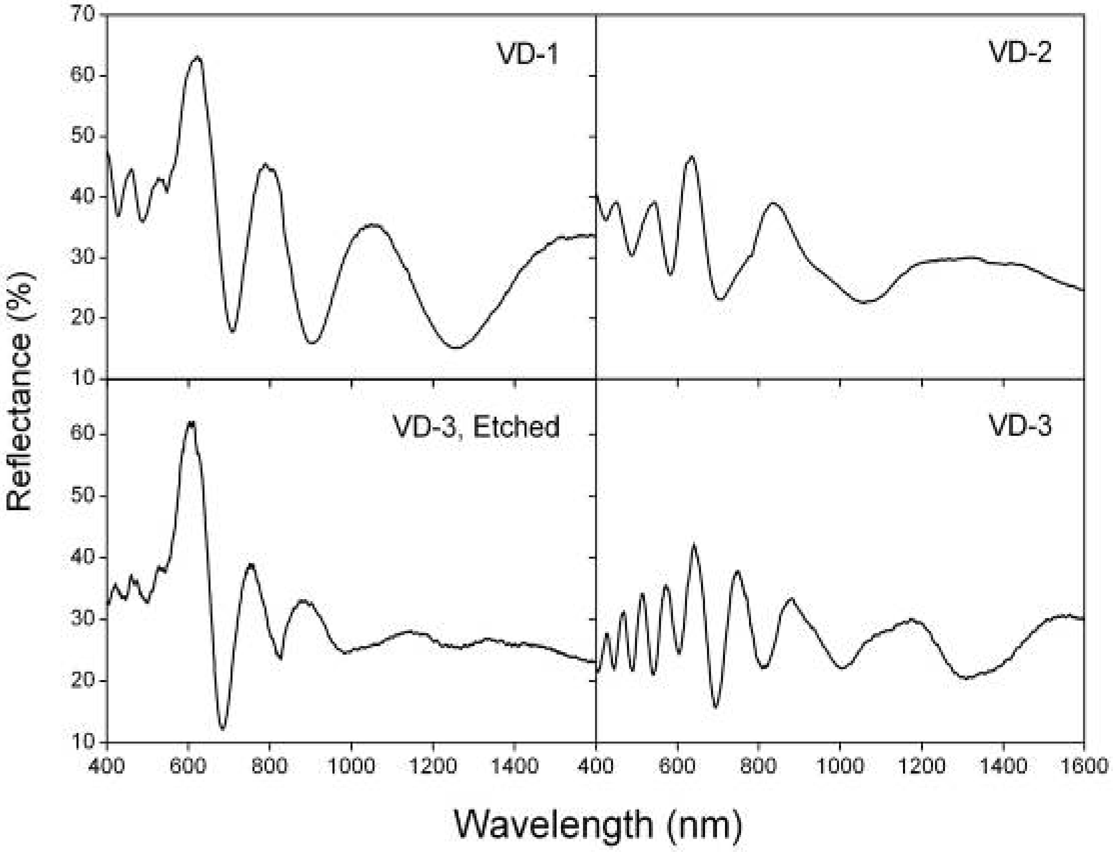

Figure 6.4. The reflectance spectra of the samples obtained from the VD experiments.

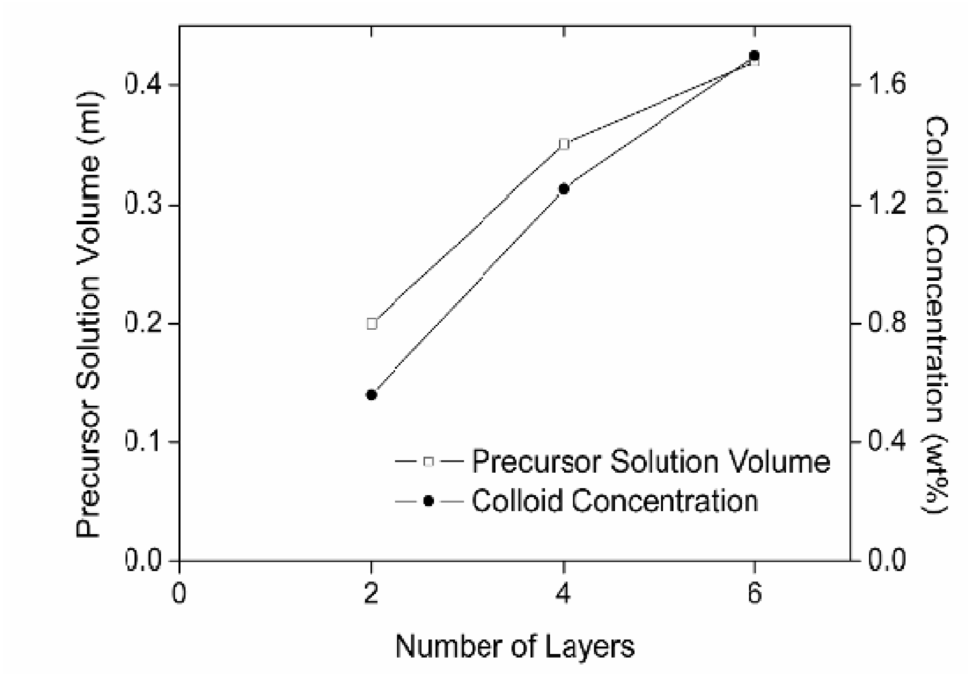

Figure 6.5 The relationship between the precursor solution volume, the colloid concentration and the number of the layers of the colloidal crystals.

6.3 Summary

A novel template-free approach to the fabrication of crack-free colloidal crystals was proposed in this thesis work. During this approach, a silica precursor solution is added to the colloid containing silica spheres. When the silica spheres self-assemble on a silicon substrate, additional silica is produced from hydrolysis of the precursor solution, filling up the voids between the silica spheres and forming a crack-free film. Interestingly, the silica in the interstices can be easily etched away by the vapor of hydrofluoric acid, leaving a crack-free non-close-packed colloidal crystal behind. The amount of the silica precursor solution needed to fabricate crack-free film increases with increasing number of the layers of colloidal crystals. Additionally, when excessive silica precursor solution is added in the VD process of producing silica sphere bilayer, the colloidal crystal film peels off partially from the substrate and leaves behind a large-area nano-bowl array.

Chapter 7

Fabrication of Free-Standing Non-Close-Packed Opal Films

7.1 Introduction

Self-assembly of colloidal microspheres (Xia, 2001) has been considered as a promising approach to the fabrication of photonic crystals (PhCs) (John, 1987; Yablonovitch, 1987). This process, however, usually produces a close-packed face-centered cubic (fcc) arrangement of the dielectric spheres, which itself does not exhibit a complete photonic band gap (PBG) (Zhang and Satpathy, 1990; Sozuer et al., 1992). While such self-assembled artificial opals (Xia et al., 2000; Norris and Vlasov, 2001; Lopez, 2003; Arsenault et al., 2004) can be employed as templates to fabricate PhCs with a complete PBG (Blanco et al., 2000; Vlasov et al., 2001), it has been shown that a structure templated by a non-close-packed opal (NCO) may have a wider PBG than that templated by a close-packed one (Doosje et al., 2000; Yethiraj and van Blaaderen, 2003; Chen et al., 2005).

Up to now, non-close-packed (NCP) architectures have been obtained by various methods. Yethiraj and van Blaaderen (2003) have achieved a NCP arrangement of polymer spheres in a stabilized colloidal suspension. NCP colloidal crystals have been obtained by means of binary layer-by-layer growth (Velikov et al., 2002) and colloidal epitaxy methods (Hoogenboom et al., 2003). NCP arrays of colloidal spheres have been immobilized in polymer matrix (Jiang and McFarland, 2004; Nakamura and Ishii, 2005) and hydrogel (Iwayama et al., 2003; Lawrence et al., 2005). Nanorobotic manipulation has been employed by García-Santamaría et al. (2002) to fabricate a NCP arrangement of spheres of the diamond architecture. Ozin and co-workers (Miguez et al., 2003) have demonstrated an approach to the fabrication of a NCP inverse opal (NCIO) by backfilling a close-packed inverse opal, which was further improved by Summers and co-workers (King et al., 2006). Fenollosa and Meseguer (2003; 2005) have described the fabrication of NCOs consisting of silica spheres connected by silica cylinders by chemically etching strongly annealed silica opals. The structure has subsequently been employed to fabricate two-dimensional structures of nanoshells interconnected by nanotubes (Meseguer and Fenollosa, 2005) Cho et al. (2005) demonstrated the fabrication of polystyrene (PS) NCOs through etching close-packed PS opals with hyperthermal neutral beam.

The work described in this chapter is regarding an approach to the fabrication of free-standing NCO films, which consist of an fcc lattice of PS spheres connected by PS cylinders with uniform structures in large domains by using silica-backfilled inverse opals as templates. The optical properties of the NCO films can be tuned by mechanical stretching (Iwayama et al., 2003; Lawrence et al., 2005; Nakamura and Ishii, 2005; Arsenault et al., 2006; Fudouzi and Sawada, 2006). The fabrication strategy is illustrated in Figure 7.1. First, a close-packed PS artificial opal was fabricated on a silicon substrate by using an inward-growing self-assembly technique (Yan et al., 2005). Second, after annealing, the synthetic opal was then infiltrated with a silica precursor by spin-coating (Matsuura et al., 2005), followed by drying at room temperature to allow the formation of a silica-infiltrated opal. Third, the PS beads were dissolved away in toluene to obtain an inverse opal. Fourth, by depositing a silica layer on the inner surface of the inverse opal using the chemical vapor deposition (CVD) method as described by Ozin and co-workers (Miguez et al., 2002), the size of the air spheres in the inverse opal was reduced. Thus, a structure consisting of NCP air spheres connected by air tubes, namely a NCIO, was obtained. Fifth, styrene monomer was infiltrated into the voids of the structure, followed by polymerization to allow the formation of PS in the voids of the NCIO (Jiang et al., 1999). Finally, the silica framework was removed with HF to leave behind a free-standing NCO film with a fcc lattice of PS spheres connected by PS cylinders, which separated from the silicon substrate automatically after complete removal of silica.

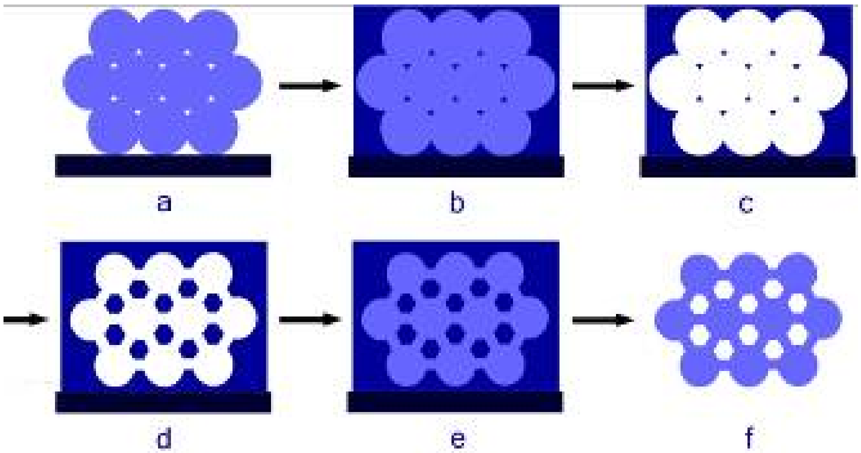

Figure 7.1 A scheme illustrating the steps of fabricating a NCO: (a) a PS opal fabricated by using an inward-growing self-assembly technique (Yan et al., 2005); (b) infiltration of the opal with silica by using a spin-coating method (Matsuura et al., 2005); (c) removal of the PS beads by toluene extraction; (d) CVD deposition of a silica layer on the inner surface of the inverse opal (Miguez et al., 2002); (e) infiltration of styrene monomer followed by polymerization (Jiang et al., 1999); (f) removal of silica by HF etching to obtain a free-standing NCO film.

7.2 The Fabrication of Non-Close Packed Inverse Opal

In this work, close-packed opals fabricated from 569-nm and 687-nm PS spheres were annealed at 110 °C for 20 and 30 min, respectively. The annealing step not only allowed the formation of connections between the PS spheres, which subsequently transformed into air pores connecting the air spheres in the inverse opals, but also improved the stability of the opal structures in the subsequent spin-coating process. It was also found that the spin-coating method is an effective method to control the morphology of the infiltrated silica. During the infiltration process, the inner surface of the PS opal was uniformly coated by a layer of silica while most of the protruding parts of the PS beads in the top layer were uncoated as suggested by the SEM image of the inverse opal structure (see Figure 7.2). This was probably because the silica precursor was attracted in the small voids among the PS beads driven by capillary forces. Such infiltrated silica morphology facilitated the subsequent processing steps, including removal of the PS beads, deposition of silica, and infiltration of styrene monomer. The silica was grown on the surface of the PS beads in a layer-by-layer manner during the infiltration process. In this work, three circles of infiltration were performed to enhance the infiltration.

After removal of the PS beads using the toluene extraction method, silica inverse opals, with air spheres interpenetrating each other, were formed. The diameters of the connections between the air spheres were measured to be 251 and 286 nm respectively in the inverse opals templated by the opals of 569-nm and 687-nm PS spheres. By depositing silica on the inner surfaces of the inverse opals, the thickness of the silica wall was increased at the expense of the diameter of the air spheres and the connection size. In the mean time, air tubes connecting the air spheres emerged. The length of the tubes doubled the thickness of the deposited silica layer approximately. The interpenetrating parts of the air spheres were reduced until the air spheres became tangent with each other. When further deposition of silica was performed, the air spheres became apart from each other to form a NCP arrangement (Miguez et al., 2003). Thus a NCP arrangement of air spheres connected by air tubes was obtained. By changing the deposited silica layer thickness, the size of the air spheres and the length of the air tubes can be controlled.

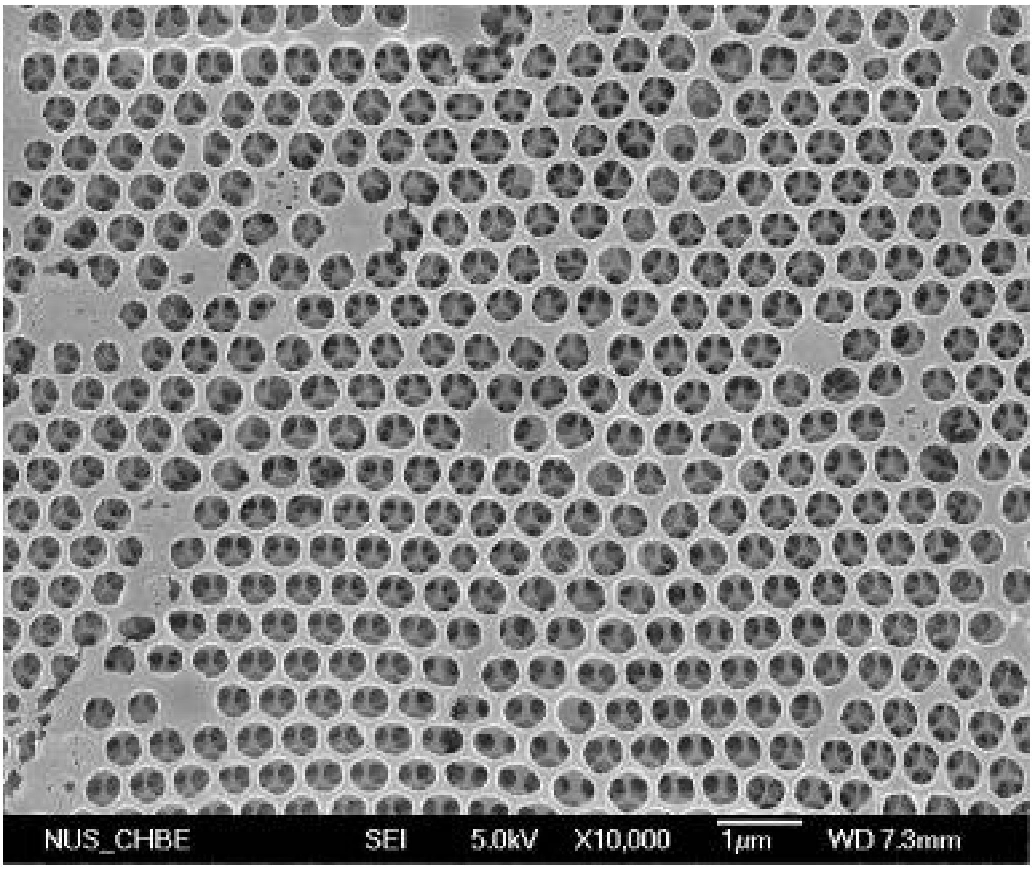

Figure 7.2 SEM top view of the inverse silica inverse opal replicated from a close-packed opal of 569-nm PS spheres.

Table 7.1 shows the samples involved in this work and their feature sizes. Among them the first three NCIO samples, namely NCIO-1, NCIO-2, and NCIO-3 were fabricated by depositing 28-nm, 59-nm, and 88-nm silica layer, respectively, on the surfaces of the silica inverse opals fabricated from close-packed opals of 569-nm PS spheres. After infiltration of styrene monomer, followed by polymerization and removal of the silica frameworks, three NCOs, namely, NCO-1, NCO-2, and NCO-3 were obtained from NCIO-1, NCIO-2, and NCIO-3, respectively. The other three NCOs, i.e., NCO-4, NCO-5, and NCO-6 were similarly fabricated from opals of 687-nm PS spheres.

Table 7.1 Feature sizes of the samples involved as obtained from SEM images

NCIO	Thickness of the backfilled silica layer (nm)	Connection size of the NCIO (nm)	Subsequent NCO	Diameter of PS spheres in NCO (nm)	Length of PS cylinders in NCO (nm)	Diameter of PS cylinders in NCO (nm)
NCIO-1	28	204	NCO-1	507	49	167
NCIO-2	59	126	NCO-2	438	94	88
NCIO-3	88	61	NCO-3	382	161	49
			NCO-4	630	20	216
			NCO-5	586	82	167
			NCO-6	550	130	136

Figure 7.3 shows the scanning electron microscope (SEM) images of samples NCIO-1, NCIO-2, and NCIO-3. The NCP air spheres separated by silica walls can be clearly seen. From samples NCIO-1 to NCIO-3, the silica wall thickness increased while the size of the air spheres and connections between the air spheres were decreased with the increase of the thickness of the deposited silica layer. The connection sizes between two adjacent air spheres were measured according to the SEM images and are reported in Table 1. It is seen that the decrease in the connection size is approximately double the thickness of the deposited silica, suggesting a uniform deposition of a silica layer on the surfaces of the air spheres and the air tubes connecting them.

Figure 7.4 shows the reflectance spectra of the inverse opal fabricated from 569-nm PS spheres and the subsequent NCIO samples. It can be seen that as the thickness of the deposited silica layer was increased, both the peaks in low- and high-energy regions underwent a red shift because of the increase of the effective refractive index of the films. The Fabry-Perot ripples around the main reflectance peaks are due to the interference of the light waves reflected at the top and bottom of the films with a finite thickness (Birner et al., 2001).

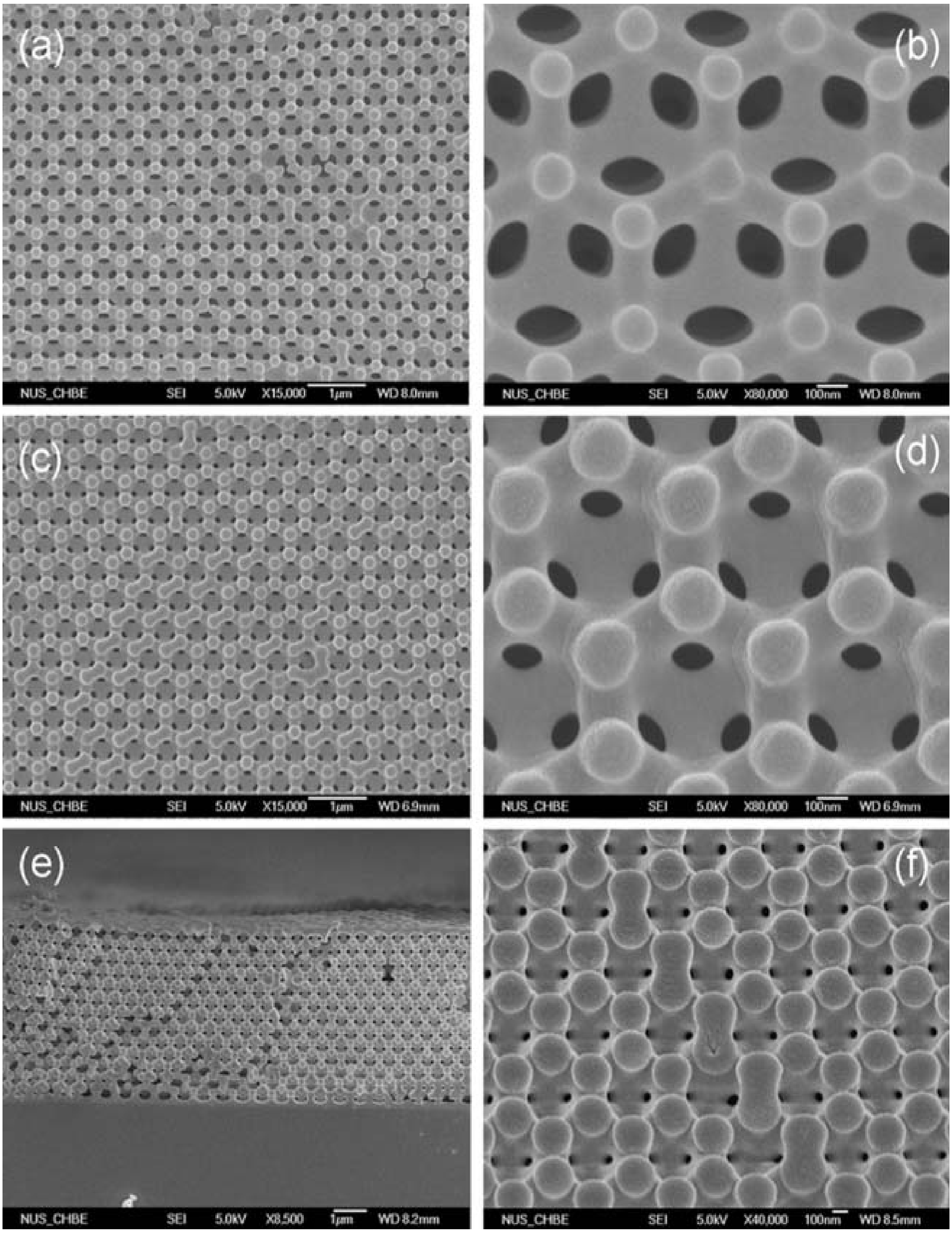

Figure 7.3 SEM images of NCIOs fabricated from close-packed opals of 569-nm PS spheres: (a, b) SEM images of NCIO-1 of different magnifications; (c, d) SEM images of NCIO-2 of different magnifications; and (e, f) cross-section views of NCIO-3 of different magnifications.

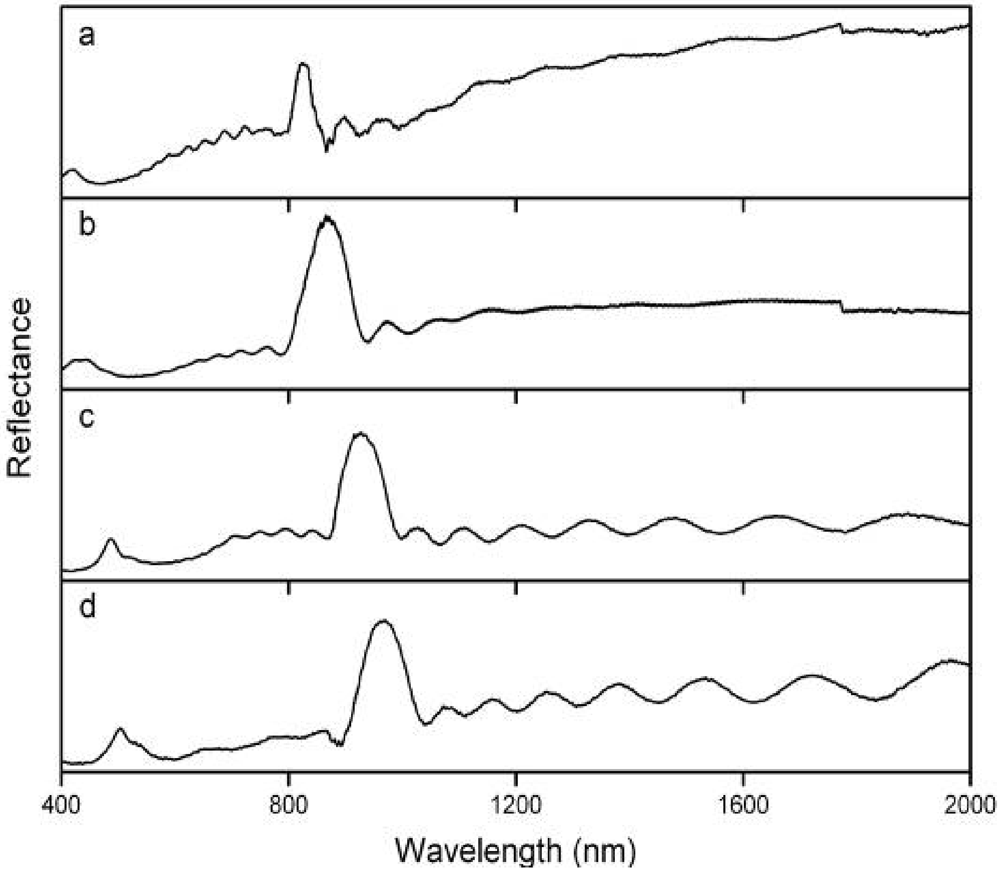

Figure 7.4 Reflectance spectra of (a) the inverse silica opal fabricated from the close-packed opal of 569-nm PS spheres, (b) NCIO-1, (c) NCIO-2, and (d) NCIO-3.

7.3 Fabrication of Non-Close Packed Opal

After infiltration of styrene monomer and polymerization followed by removal of the silica framework, free-standing NCO films replicating the voids of the NCIOs were obtained in large area (see Figure 7.5). The SEM images of samples NCO-1, NCO-2, and NCO-3 are shown in Figure 7.6. Uniform structures consisting of NCP PS spheres connected by PS cylinders can be seen for all samples. The shining color of the films and the SEM images in a smaller magnification (see Figure 7.5) showed that the structures are uniform in large domains. Because there was always some superfluous styrene accumulating between the surface of the NCIOs and the glass slide covering them during the infiltration of the styrene monomer, a solid PS layer (from 20 to 30 μm) formed on the surface of the NCO, which enhanced the strength of the films.

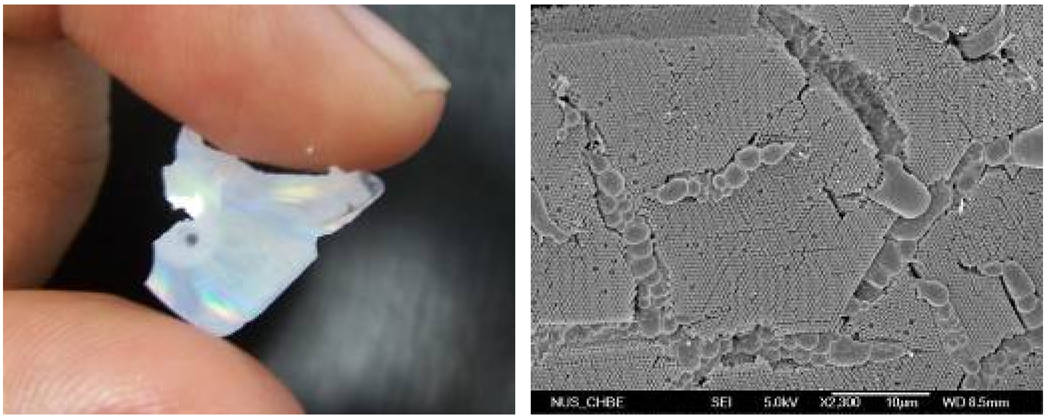

a **b**

Figure 7.5 (a, b) A photograph (taken with a Kodak DX7590) of NCPO-2 after being cut for characterization (the glass substrate was 2.2 × 2.2 cm^2).

From the data reported in Table 1, it can be concluded that the sizes of the PS spheres and cylinders can be precisely controlled by changing the thickness of the deposited silica layer. The decrease in the sphere size and the increase of the cylinder length also approximately doubled the thickness of the deposited silica layer. It is also seen that the sum of the sphere diameter and the cylinder length is smaller than the diameter of the original PS spheres. This is because the original PS spheres interpenetrated each other and contracted slightly during the annealing. Additionally, the diameters of the PS cylinders are smaller than that of the air tubes in the corresponding NCIOs due to the volume shrinkage of styrene upon polymerization (Jiang et al., 1999). The ratio of the cylinder length over the sphere size increases with the increase in the thickness of the deposited silica layer. In this work 687-nm PS beads were also used to fabricate close-packed opals as the starting templates. The inverse opals obtained from the 687-nm PS opals were backfilled with 18-, 49-, 70-nm silica layer and subsequent fabrications produced another three NCO structures, namely, NCO-4, NCO-5, and NCO-6 having 630-nm, 586-nm, and 550-nm PS spheres connected by 20-nm, 82-nm, and 130-nm cylinders respectively. The SEM image of NCO-4 is shown in Figure 7.6f.

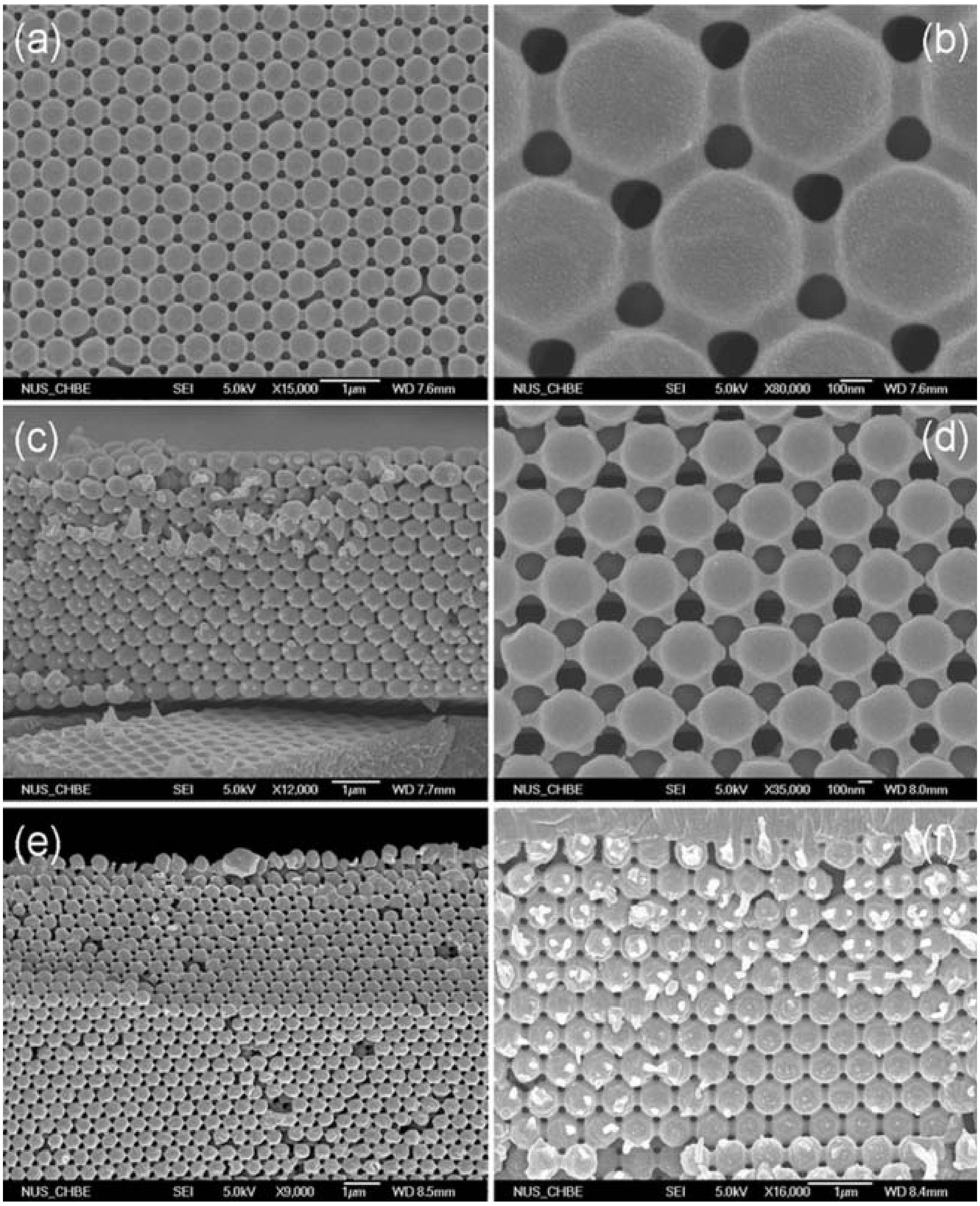

Figure 7.6 SEM images of NCO-1, NCO-2 and NCO-4: (a, b) top views of NCO-1 of different magnifications; (c) cross section view of NCO-1; (d-e) top view and perspective view of NCO-2, respectively; (f) cross section views of NCO-4.

The transmission spectra of the NCO samples are shown in Figure 7.7. It can be seen that with the decrease of the PS sphere size and the increase of the cylinder size a clear blue shift of the main transmittance valley occurred for both groups of NCO structures fabricated from 569-nm and 687-nm PS spheres. Fabry-Perot ripples are not obviously seen from most of the NCO samples, which is probably because of the influence of the solid PS layer and the difficulty of keeping the free-standing films highly flat during measuring the spectra.

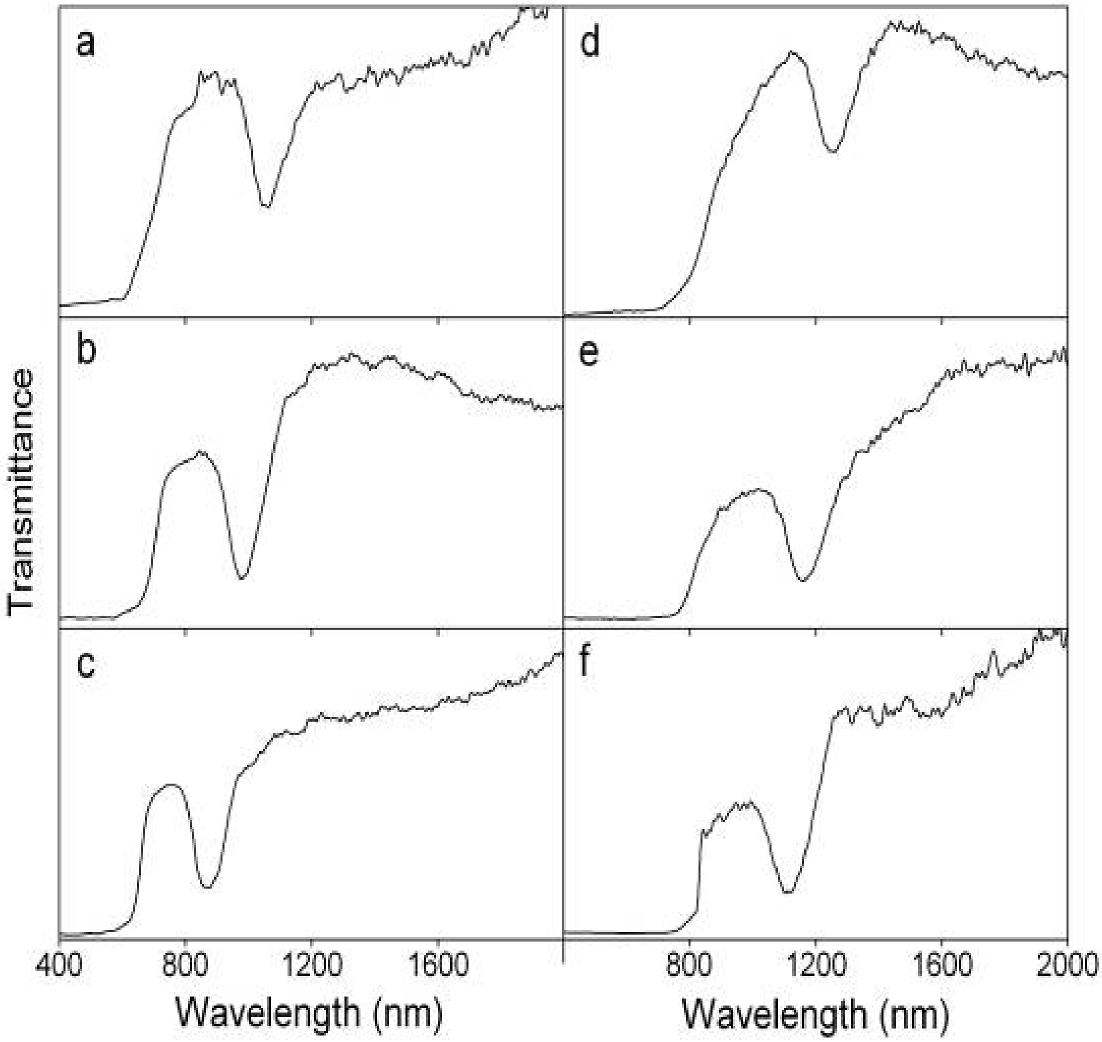

Figure 7.7 The transmission spectra of (a-c) NCO-1, NCO-2, and NCO-3, respectively; and (d-f) NCO-4, NCO-5, and NCO-6, respectively.

7.4 Tuning the Optical Properties of the Colloidal Crystals

Since the NCOs were obtained as free-standing films, the microstructures and the optical properties of the NCOs can be tuned simply by stretching the films. Figure 7.8 compares the transmission spectra of sample NCO-5 before and after stretching. It can be observed that the main transmittance valley moved toward the lower wavelength region upon stretching, most probably because of the elongation of the PS cylinders and the distortion of the PS spheres, resulting in an decrease in the dimensions of the PS spheres and cylinders along the direction vertical to the film surface, thus leading to the observed blue shift of the main transmittance valley.

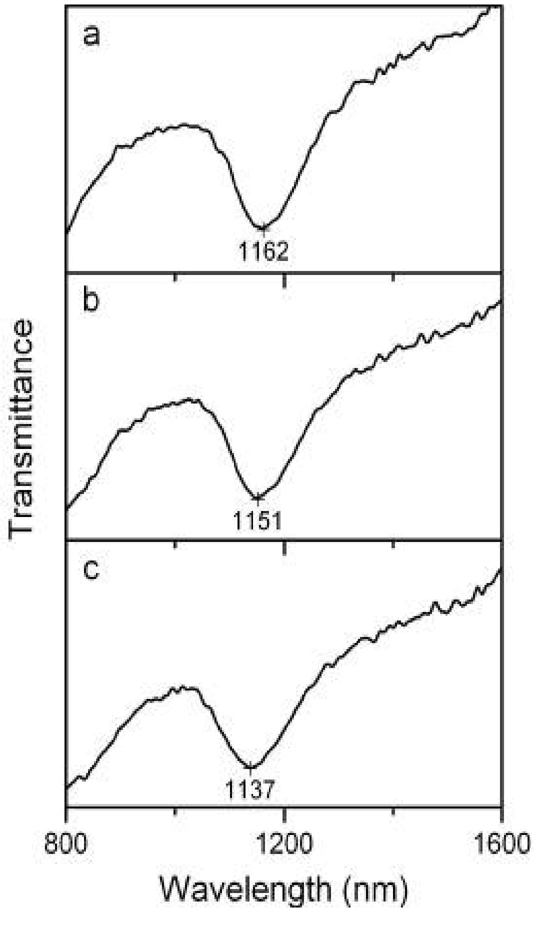

Figure 7.8 The transmission spectra of NCO-5 that was (a) not stretched, (b) stretched to 105% of its initial length, and (c) stretched to 110% of its initial length.

During annealing of the opals, the largest diameter of the connection area between two adjacent spheres that can be achieved is less than the radius of the sphere before all the pores are closed up (see Figure 7.9). Thus, in this method the largest thickness of silica layer that can be deposited on the silica inverse opal is less than half of the radius of the spheres forming the opal. This is similar to the approach to NCOs by etching strongly annealed silica opals (Fenollosa and Meseguer, 2003; Cho et al., 2005; Meseguer and Fenollosa, 2005), that the largest silica thickness that can be etched away is less than half of the radius of the initial silica beads before the structure collapses. Thus for both approaches, the smallest radius of the spheres in the NCO structures is larger than half of the radius of the initial spheres. Correspondingly, the largest cylinder length in the NCO structures that can be achieved is less than the difference between the length of O_1O_2 (the distance between the centers of two adjacent spheres, see Figure 7.9) and the radius of the initial spheres, and the ratio of the cylinder length over the sphere diameter in the NCO structure is less than 0.732. However, in our approach, the length of the PS cylinders can be adjusted by mechanical stretching. If elastomers, such as poly (dimethylsiloxane) (PDMS) (Fudouzi and Sawada, 2006), instead of PS, are used, elastic NCO structures can be realized. Thus, the ratio of the cylinder size to the sphere size can be highly tuned by mechanical forces, enabling the fabrication of various NCP structures.

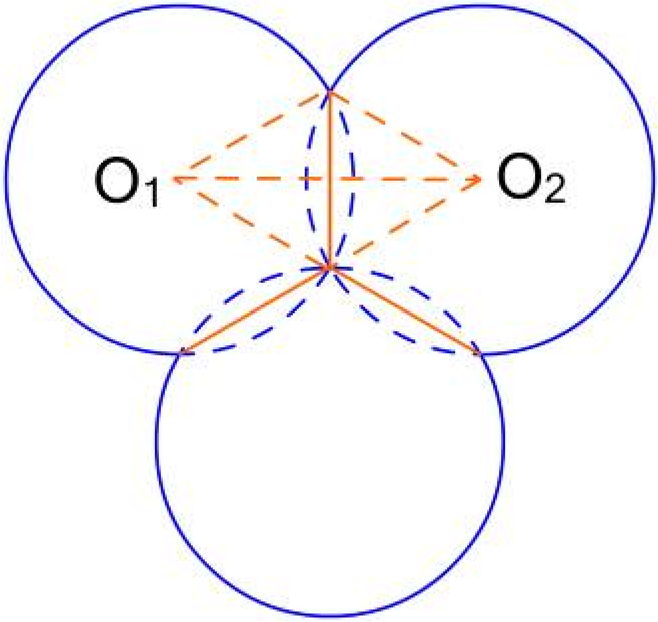

Figure 7.9. A scheme showing the largest possible connection size that can be achieved before the pore among three adjacent spheres is closed up.

7.5 Summary

In summary, this chapter has demonstrated an approach to the fabrication of non-close-packed opal films consisting of PS spheres connected by PS cylinders in large domains, of which the optical properties can be tuned by mechanical stretching. The chemical vapor deposition technique works well for deposition of silica layers on the surface of a silica inverse opal, producing uniform non-close-packed inverse opal structures. Upon infiltration of the non-closed-packed inverse opal with a polymer monomer (say styrene as demonstrated in this work), followed by polymerization and subsequent removal of the silica framework, a free standing non-closed-packed opal film can be obtained. Importantly, the optical properties of the non-closed-packed opal film can be tuned by mechanical stretching.

Chapter 8

The Fabrication of Binary Colloidal Crystals and Inverse Opals

8.1 Introduction

Fabrication of binary colloidal crystal has attracted a lot of interest in both theoretical study (Bartlett et al., 1990; Bartlett et al., 1992; Larsen and Grier, 1997) and applications (Garcia-Santamaria et al., 2002) since the discovery of binary superlattice in Brazilian opal (Sanders and Murray, 1978). Various types of binary nanoparticle superlattice have been synthesized through deliberate control of the electrical charges on the nanoparticles (Shevchenko et al., 2006; Shevchenko et al., 2006). Binary CCs have also been fabricated by layer-by-layer growth strategy (Jiang et al., 2001; Velikov et al., 2002; Wang and Mohwald, 2004), where monolayer of small spheres are deposited on the monolayer of large spheres. Co-deposition method was has been reported (Kitaev and Ozin, 2003; Cong and Cao, 2005) in the fabrication of binary CCs. However, in these reports, only surface structure was studied. Recently, co-deposition of binary (Wang et al., 2008) and trimodal (Wang et al., 2006) CCs and study of the inner structure were reported.

In this thesis work, binary CCs were fabricated and inverse CCs were prepared to determine the structure of the binary structure. Their optical properties were also investigated. Two different set of binary polystyrene (PS) spheres were employed.

Through the adjustment of the ratio of the number of the smaller spheres to the large spheres, the final structures of the binary CCs were successfully changed. The internal structures of the CCs were studied by imaging its cross-section and its inverse structures. The optical properties of the CCs and inverse CCs were studied with a UV-vis spectrometer.

8.2 The Fabrication of Binary Colloidal Crystals

The samples fabricated are listed in Table 8.1. It was found that horizontal deposition is an effective method of producing binary colloidal crystals. Iridescent colors could be clearly seen across the film after complete drying. Figure 8.1 shows the SEM images of sample B1 and B2. As enlisted in Table 1, B1 and B2 have the S/L size ratio of 0.154. The S/L particle number ratios are 4.1 and 8.1, respectively for B1 and B2.

Table 8.1 The binary colloids and the fabricated colloidal crystals samples

Sample	*Large Particles*		*Small Particles*		*Size ratio*	**Particle number**
	Size	VF	Size	VF	*(S/L)*	**ratio (S/L)**
B1	1000 nm	15.39%	154 nm	0.23%	0.154	4.1
B2	1000 nm	13.19%	154 nm	0.39%	0.154	8.1
B3	789 nm	8.59%	154 nm	0.16%	0.195	2.5
B4	789 nm	7.88%	154 nm	0.23%	0.195	3.9

It can be observed that the addition of small spheres in the colloid did not change the ordered arrangement of the large spheres. The arrangement of the small large spheres is ordered in the 3 fold interstitial voids among the large spheres on the crystal top surface in most of the areas. The increase of VF ratios of small and large spheres leads to the increased number of small spheres residing between the large spheres. The top layer structure of B1 shows that each large sphere is surrounded by 6 small particles, while B2 shows that each large sphere is surrounded by 15 small spheres. Both numbers are significantly larger than the averaged S/L particle number ratios, namely 4.1 and 8.1. It suggests that the small particles may not uniformly distribute throughout the binary crystals.

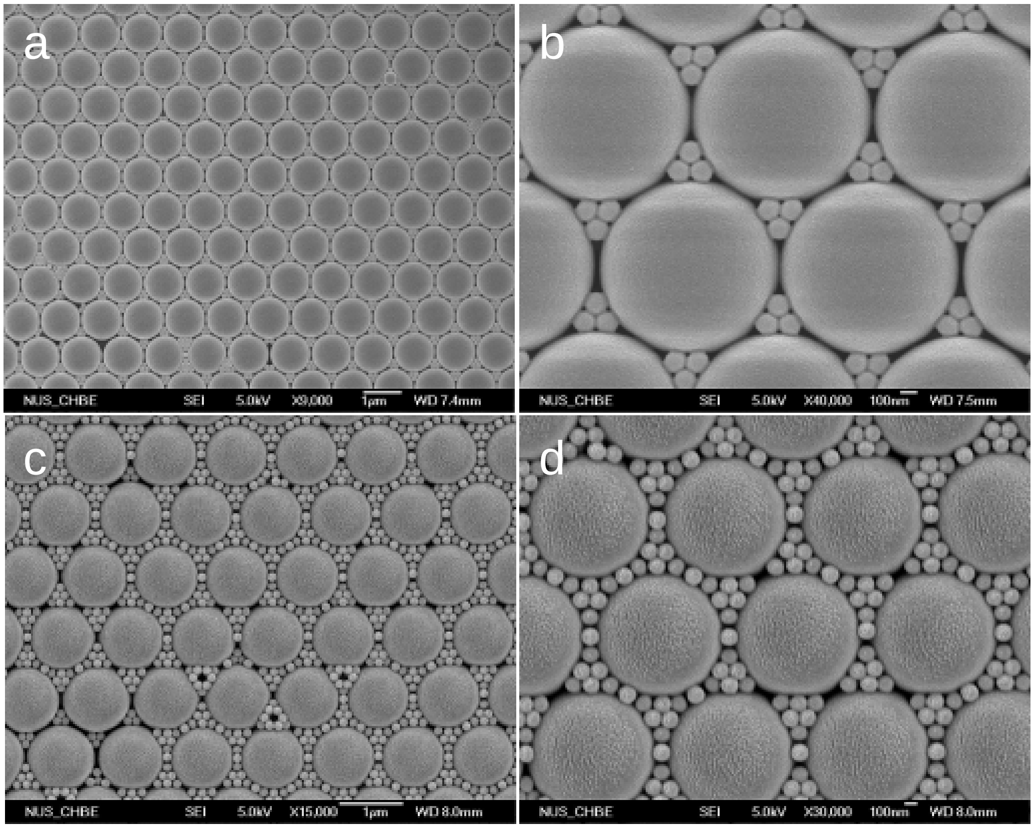

Figure 8.1 Top view SEM images of B1 (a, b) and B2 (c, d)

Figure 8.2 shows the structure of the binary CCs fabricated from B3 and B4. The patterns on the surfaces of the CCs are also largely uniform. Due to the increased S/L size ratio, 0.195, less small particles can be fitted into the interstitial voids among the large particles compared to B1 and B2. The top layer of B3 shows that most of the 3 fold voids are occupied by single small spheres while sporadically some voids accommodate 2 or 3 small particles. Sample B4 presents a large area of LS_6 binary crystal structure. Consistent with B1 and B2, this binary configuration is also greater than the averaged S/L particle number ratio, 3.9. To observe the distribution of the small spheres in the bulk of the CCs, the sample was broken into pieces and its cross-section view was taken by SEM. It was found that at the very bottom of the colloidal crystal, there is almost no presence of the small particles, and the distribution of the small spheres was not as uniform as on the top surface as shown in Figure 8.2b.

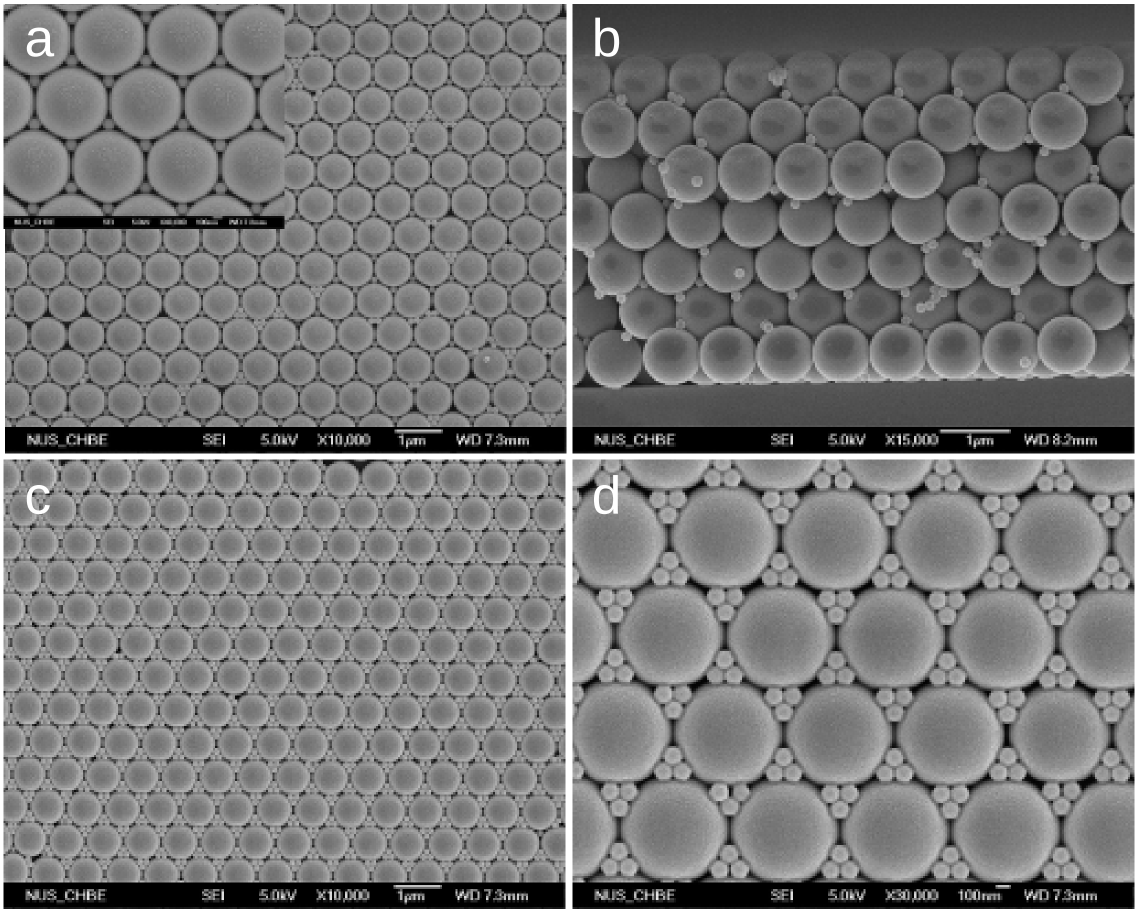

Figure 8.2 SEM images of B3 and B4. a) and b) are the top view and cross-section view of B3 respectively. c) and d) are the top view of B4.

After annealing, infiltration of silica and subsequent removal of PS spheres, their inverse structures were obtained, as shown in Figure 8.3. Besides the large and small pores originated from the templating large and small latex particles, on the SEM we can also observe large and small windows in the porous structure. The large windows are the result of original contact areas between the large particles, while the small windows reveal the original contract points between the large and small spheres. Therefore, even the top view SEM images of the inverse opals can offer some insight of the internal architecture. Figure 8.3a, 3b, 3c show the top view of the inverse B2, B3, B4. The large and small windows on the images demonstrate that the original large spheres were packed in fcc form and they are not separated apart by the small spheres, however the small spheres were not packed in a highly ordered fashion inside the colloidal crystal. The cross-section view of the inverse B4 also confirms the uneven distribution of the small spheres in the bulk CCs. It appears that the distribution of small spheres have a slight gradient with an increasing concentration towards the upper layers. .

From the above observation, a mechanism of the formation of the binary colloidal crystals is proposed as following: in the drying process of the colloidal suspension, the particles are equally dragged towards the edge of the substrate due to the higher evaporation rate at the 3 phase contact line and the consequent convective flow. The solvent evaporation first causes meniscus formed between the large spheres while the smaller ones are still immersed in the liquid existing as Brownian particles with a diffusion coefficient of $kT/6\pi ŋR$ (where k is the Boltzmann constant, T is the temperature, ŋ is the viscosity, and R is the particle radius). Thus the capillary force drives the ordered arrangement of the large spheres while the smaller spheres diffuse into the voids of the larger ones. Also because of the evaporation over the suspension surface, there is a minute upwards flow, which may be the cause of the slight gradient of the small sphere concentration from the bottom to the top layers of the colloidal crystal. On the top surface, the small spheres were controlled by the capillary force as well as the confinement of the voids between the large spheres, which probably resulted in the uniform arrangement. However, in the bulk the free movement of the small spheres is limited by the confinement of the interstices of the large spheres, therefore, under the conditions investigated in this study, they cannot be arranged evenly in the bulk.

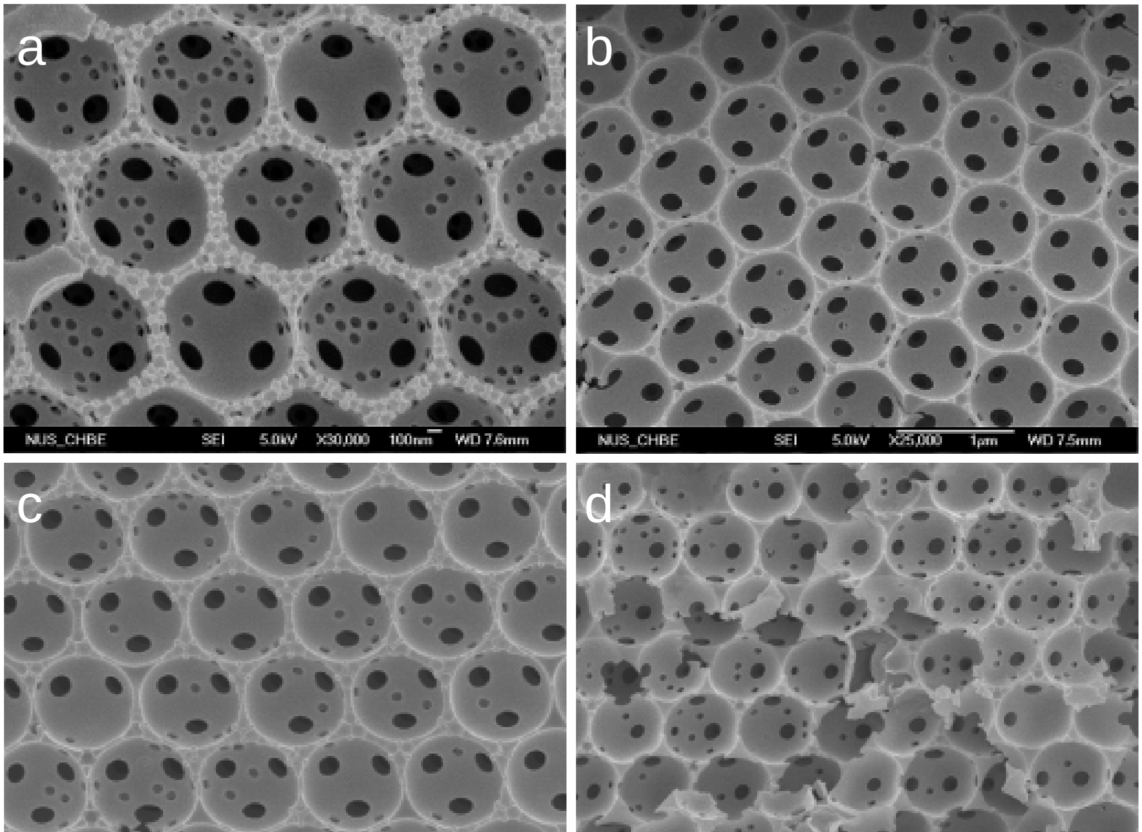

Figure 8.3 SEM images of inverse binary CCs: a) B2, b) B3, c) and d) are the top view and cross-section view of the sample B4.

The optical spectra of the samples were studied, as shown in Figure 8.4. The distinctive dips in the transmittance spectra confirm the ordered the structures of the binary opals and binary inverse opals. It was found that the main peak due to the pseudo-bandgap shifted to larger wavelength with the increase of the VF ratio of the small spheres to the large spheres. This is mainly because that the increase of the small spheres numbers in the binary CCs leads to larger effective refractive index, which leads to the red-shift of the main peak. However, in their inverse structures, a blue-shift happened when the VF ratio of the small spheres to the large spheres. This is due to the inverse influence of the increasing number of small spheres, which leads to the decrease of the effective refractive index of the inverse binary CCs.

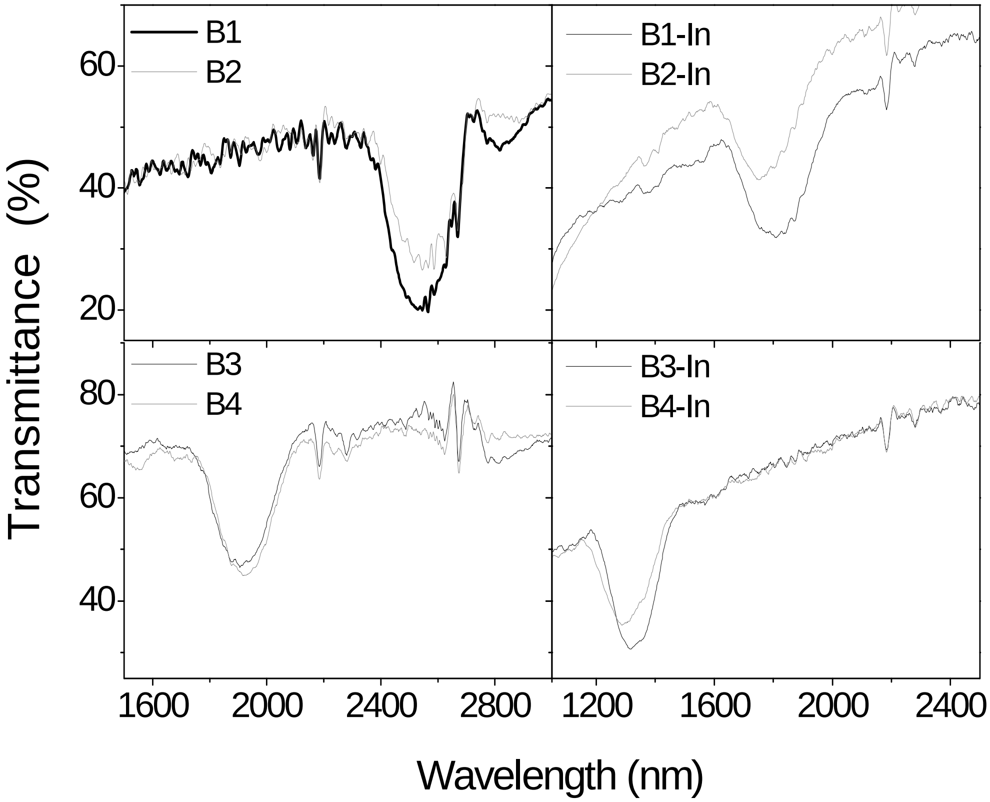

Figure 8.4 The spectra of the binary CCs and their inverse structures.

8.3 Summary

In this chapter the fabrication of binary colloidal crystal using a horizontal deposition method was demonstrated. Through the change of the volume fraction ratios of the small spheres to that of the large spheres, the structures of the binary colloidal crystals can be changed. It was found that the arrangement of the small spheres on the surface of the binary colloidal crystals can be ordered. However, in the bulk of the colloidal crystals the arrangement of the small spheres is not ordered because of the confinement effect of the large spheres. The optical spectra of the samples confirm the long-range order of the binary system, which originated from the large sphere packing.

Despite the less order of the small spheres in the binary crystal, the inverse structure possesses two sets of pores with defined sizes. Such a binary porous structure may find important applications in catalysis and separation. Equally importantly, the fabrication method presented in this study is simple and straightforward, with minimum equipment investment.

Chapter 9

Engineering Planar Defect in Colloidal Photonic Crystals

9.1 Introduction

Like the significance of doping in semiconductors, the introduction of well-defined defects into PCs is essential to harness their full potential in device application (Meade et al., 1991; Yablonovitch et al., 1991; Johnson and Joannopoulos, 2002). Recently, great efforts have been contributed to the incorporation of various defects into PCs. Linear defects have been fabricated by multi-photon polymerization (Lee et al., 2002; Jun et al., 2005), direct electron beam writing techniques (Ferrand et al., 2004), micromachining (Tetreault et al., 2003) and lithography patterning (Vekris et al., 2005; Yan et al., 2005; Yan et al., 2005). In addition, point defects have been created by using the layer-by-layer lithographic method (Ogawa et al., 2004; Qi et al., 2004), and direct electron beam writing (Ferrand et al., 2003; Ferrand et al., 2004). Very recently, we have demonstrated an approach by combining nanoimprinting lithography with self-assembly to incorporating point defects in PCs (Yan et al., 2005).

Planar defects have been successfully introduced into opals and inverse opals. Langmuir-Blodgett technique and the vertical deposition method have been employed to insert a layer of beads of different sizes into an opal (Wostyn et al., 2003; Zhao et al., 2003). Transferring printing has been used to embed a polyelectrolyte multilayer into opals, forming a tunable planar defect (Fleischhaker et al., 2005; Fleischhaker et al., 2005; Tetreault et al., 2005). Chemical vapor deposition (CVD) has also been used to create a defect layer in an inverse opal structure, which grew a solid silica layer onto the first multilayer of polystyrene (PS) opal infiltrated with silica before the growing of second multilayer of PS opal (Palacios-Lidon et al., 2004; Tetreault et al., 2004). Then after infiltrating the second PS multilayer with silica and removing the PS spheres in the whole structure, an inverse opal embedded with a solid silica layer was achieved.

In this chapter a facile method of fabricating colloidal crystals and inverse opals with a planar defect is reported. Through this method opals with a planar defect can be fabricated in a short period of time (as short as 5 hours). Inverse opals with planar defects can be obtained by direct inversion of the opals with planar defects. Only one time of infiltration process is needed and high-cost techniques such as lithography and CVD are not involved. As illustrated in Figure 9.1, our method is to fabricate PS multilayer embedded with a monolayer of silica beads, followed by infiltration of silica, and finally removal of the PS beads by calcinations to obtain an inverse silica structure while the silica bead layer becoming a solid defect layer embedded in the inverse structure. The growth of the PS layers was carried out by using an inward growing self-assembly method (Yan et al., 2005), while the silica-bead monolayer was introduced by using spin coating (Burmeister et al., 1998; Hulteen et al., 1999). Then an inverse opal with a planar defect can be obtained merely by using colloidal self assembly and wet chemistry methods without involving high-cost techniques such as lithography and CVD. Microscopy study showed the high structural quality of samples and optical spectra of the samples confirmed the existence of defect state. Different sizes of PS beads and silica beads were used in experiment, demonstrating the possibility of adjusting thickness of the defect layers and other parameters.

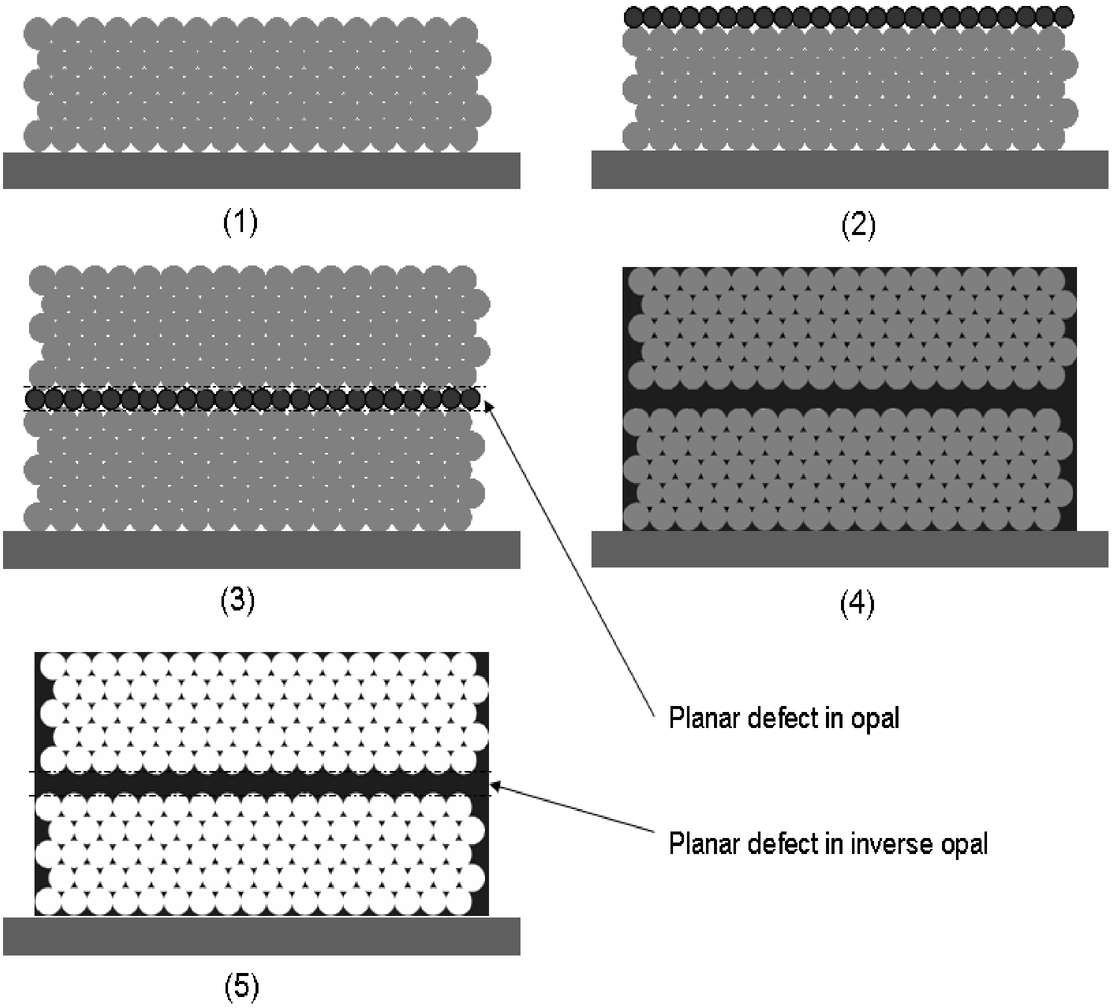

Figure 9.1 A scheme showing the steps of fabricating a planar defect embedded in an opal and inverse opal: (1) Growth of the first PS multilayer on a glass substrate by using an inward-growing self-assembly method (Yan et al., 2005); (2) Spin coating of a monolayer of silica beads on the surface of the PS colloidal crystal; (3) Growth of the second PS multilayer on the surface of the silica beads; (4) Infiltration with silica; (5) Removal of the PS particles by calcination.

9.2 The Insertion of Planar Defect

It was observed that the annealing step was essential to ensure the structural stability for the subsequent treatments. An alcoholic silica colloidal suspension was used during the spin-coating process because the surface of the PS beads became hydrophobic after drying.

Figure 9.2 shows the FESEM images of a sample consisting 20 layers of 560-nm PS particles embedded with a 225-nm silica bead layer and its inverted structure. The quality of PS colloidal crystal of both multilayers can be observed here. From the high-magnification image (Figure 9.2b) it can be seen clearly that a single-layer silica beads were successfully introduced into the PS colloidal crystal. Because of the uniformity of the silica layer, the quality of the second PS multilayer is as good as that of the first multilayer grown on a flat glass substrate. The quality of the crystal can also be revealed by the optical transmission spectra of the sample shown in Figure 9.3 (opal). The Fabry-Perot oscillations at both sides of main transmittance valley (mainly caused by the interference of light wave reflected by the top and bottom surfaces of the sample) indicate the uniformity of the sample thickness and similarity of long range crystal orientation (Wostyn et al., 2003).

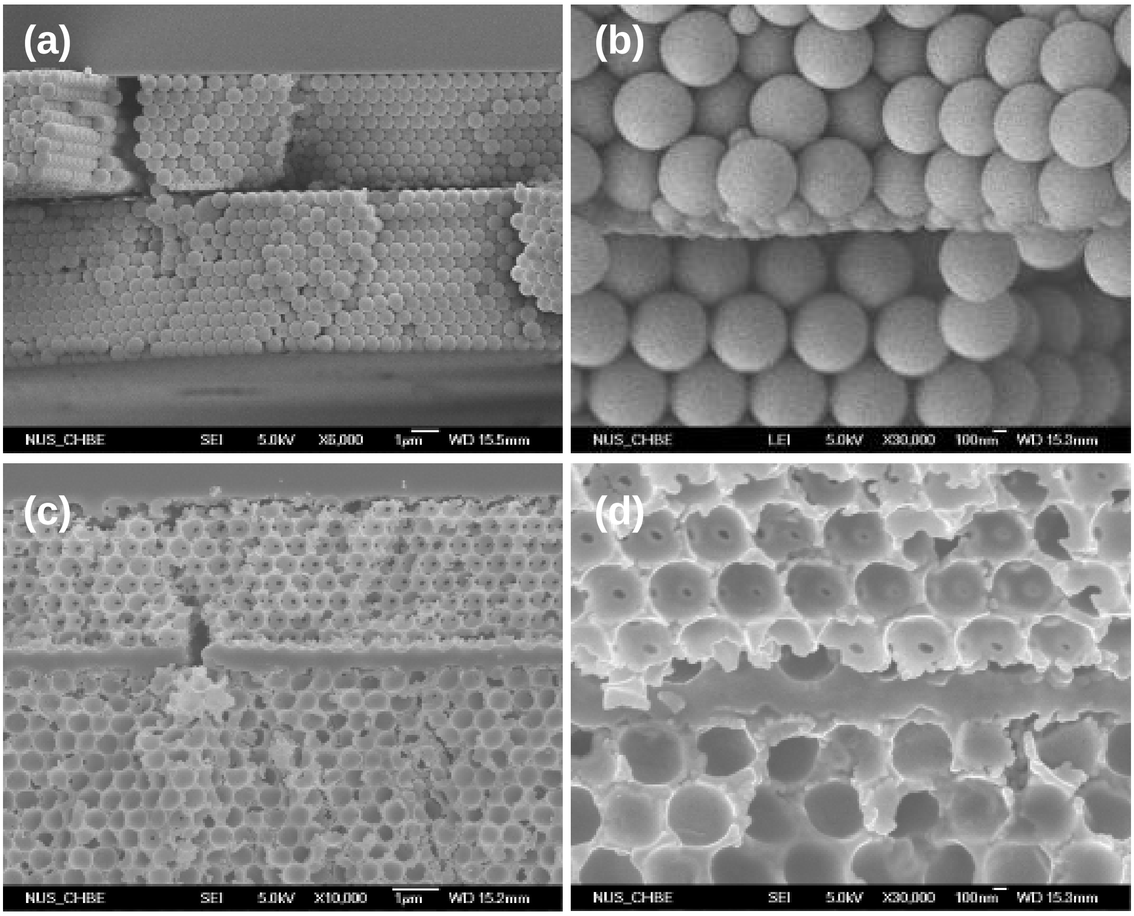

Figure 9.2 SEM images of an opal with planar defect and its inverted structure: (a, b) 20 layers of 560nm PS spheres embedded with a 225nm silica bead monolayer, low and high magnification; (c, d) the inverted opal sample, low and high magnification.

During the infiltration process the silica beads were connected together by the infiltrated silica to form a solid silica phase. After removal of the PS beads, the layer of the silica beads was left behind as a defect layer in the inverted opal structure. Figure 9.2 c and d show the microstructures of the inverted sample imaged using different magnifications. It can be observed that a homogenous silica layer was formed. The observed thickness, which was about 210 nm, is not exactly equal to the diameter of the silica beads (225nm) because the silica bead layer was corrugated by the PS layers. Besides calcination had led to a contraction of the silica beads. The diameter of spherical pores became 490 nm, smaller than the diameter of the PS spheres, because of contraction during calcination.

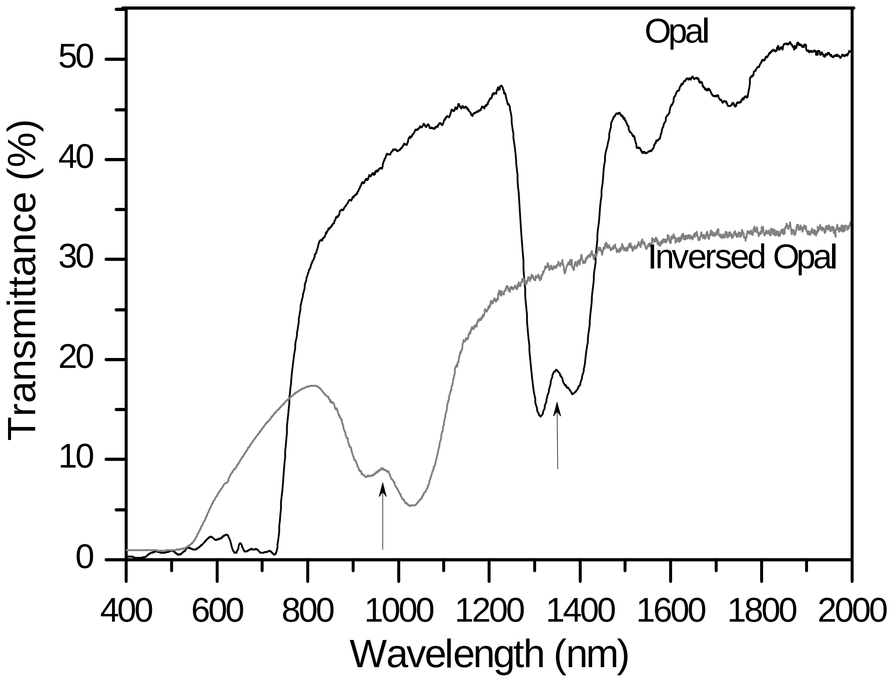

Figure 9.3 Optical transmittance spectra of an opal consisting of 20 layers of 560 nm PS particles embedded with a 225nm silica bead layer and its inverted structure.

The periodicity of dielectric constant was interrupted by the silica bead layer in the opal sample, and by the solid silica layer in the inverted structure. The interruption layer serves as a two-dimensional planar defect, introducing localized defect states into the band gap (Yablonovitch et al., 1991). The two arrows in Figure 9.3 indicate the position of the defect states. It is known that there are two kinds of defects: (1) reduced-index defect, introduced by removal of the material with a higher dielectric index or replacement of a material of a higher dielectric index with that of a lower dielectric index; (2) increased-index defect, produced by addition of the material with a higher dielectric index or replacement of the material of a lower dielectric index with that of a higher dielectric index (Johnson and Joannopoulos, 2002). The reduced-index defect induces acceptor modes originating from valence band while increased-index defect causes donor modes originating from conduction band. In the opal structure the dielectric index of silica (1.45) is lower than that of the surrounding PS beads (1.59) and the size of the silica spheres is smaller than that of the PS spheres. Then the silica layer serves as a reduced-index defect. However, in the inverted opal structure the PS beads are replaced by air. Silica becomes the material of a higher dielectric index, thus the silica layer change to behave as an increased-index defect.

Other PS spheres of 380 and 655 nm in diameter were also used together with the 225-nm silica spheres to fabricate sandwiched opal structures. The optical spectra of the sandwich opals are shown in Figure 9.4a, together with that of the previous sample. It can be seen that the position of the defect states moves towards the lower wavelength edge of the stop bands (conduction bands) with the increase of the diameter of the PS particles. This is because the defects are all of reduced-index nature, originating from the valence bands. Therefore the larger the PS particle diameters, the less the ratio of defect thickness to lattice parameter, and the larger the distance from defect states to the higher wavelength edge of the stop bands. This is consistent with results of previous reports (Tetreault et al., 2005; Yan et al., 2005).

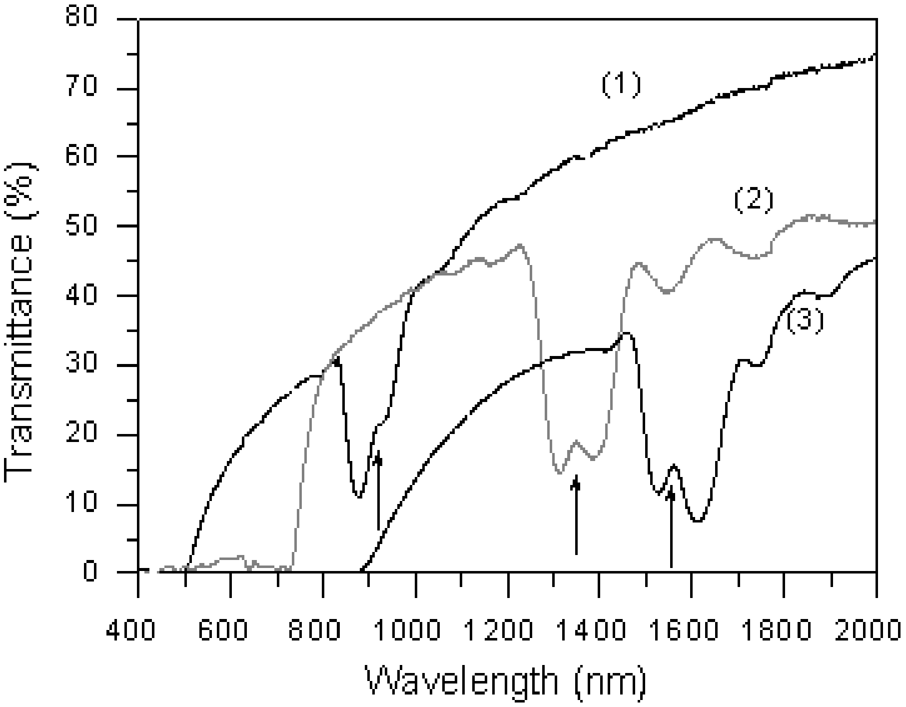

(a)

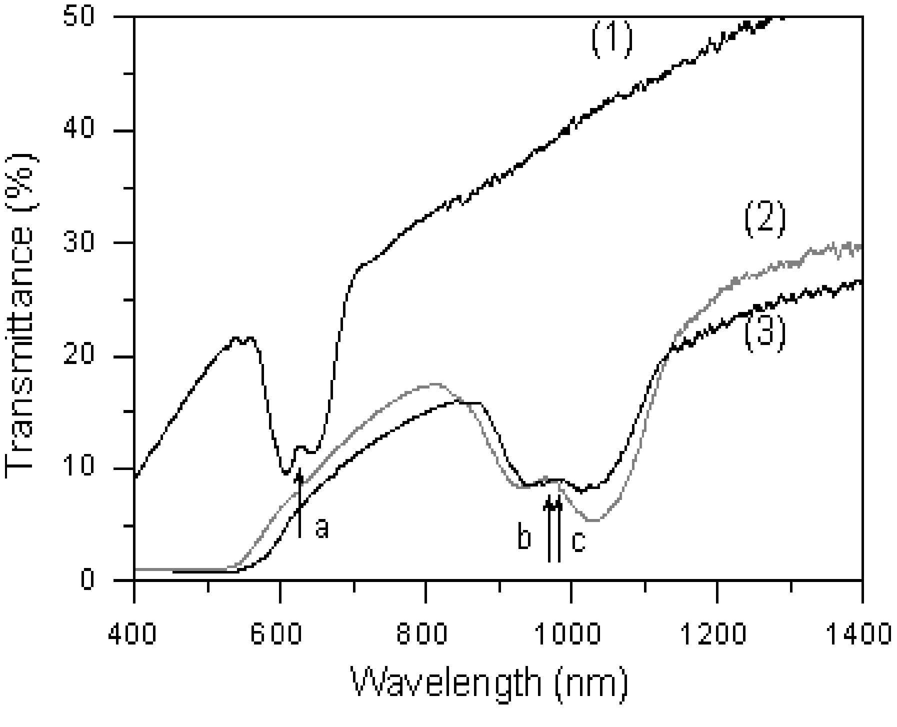

(b)

Figure 9.4 (a) Optical transmittance spectra of opals consisting of 225nm silica bead layer sandwiched by 20 layers of (1) 380nm, (2) 560nm and (3) 655nm PS particles; (b) Optical transmittance spectra of inverse opals fabricated using (1) 20 layers of 380-nm PS spheres embedded with a layer of 225-nm silica beads, (2) 20 layers of 560-nm PS spheres embedded with a layer of 225-nm silica beads and (3) 24 layers of 560-nm PS spheres embedded with a layer of 585-nm silica beads.

A comparison of the spectra of the inverse opals fabricated using 380- and 560-nm PS beads (see Figure 9.4b revealed that the position of the defect states moved towards the higher wavelength edge of the stop bands (valence bands) with the increase of lattice constant/defect thickness ratio.

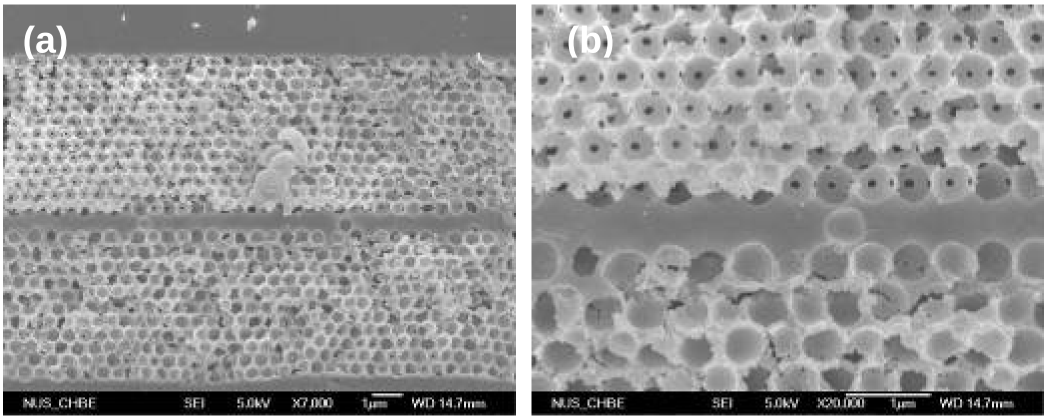

Figure 9.5 SEM images of inverse opals inverted from 24 layers of 560nm PS spheres embedded with 585nm silica bead layer (low and high magnification).

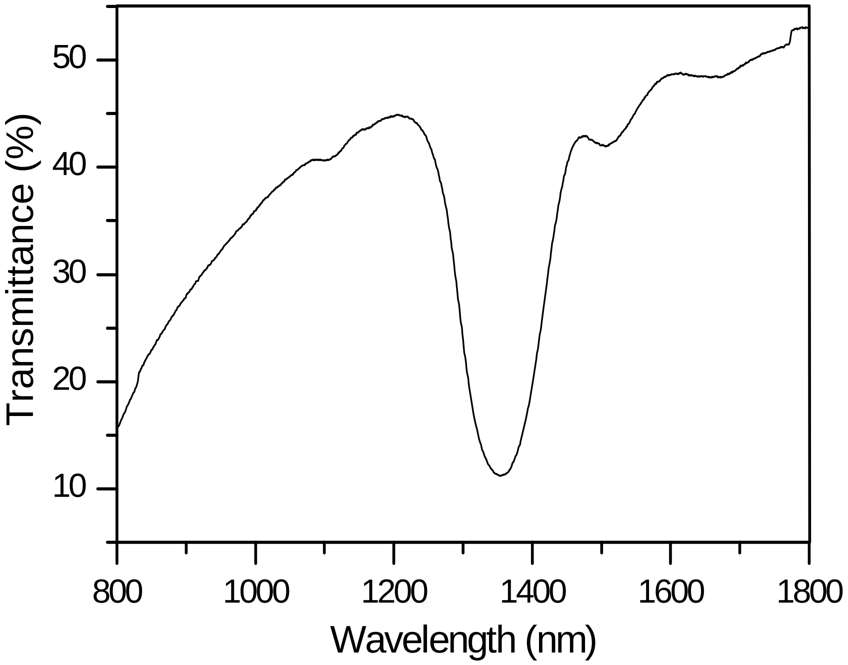

Figure 9.6 Optical transmittance spectra of opals consisting of 585nm silica bead layer sandwiched by 24 layers of 560nm PS particles

Through the change of the diameter of the silica beads embedded, the thickness of defect layer can be adjusted. In the present study, 585-nm silica beads were embedded into 560-nm PS multilayer. The spectrum of the opal structure did not show any defect state (see Figure 9.6), probably because the sizes and refractive indices of silica and PS beads are both very close to each other. After infiltration and calcination its inverted structure was obtained, and a 510nm solid defect layer was formed, as shown in Figure 9.5. The spectrum of inverted structure also clearly showed the defect state introduced, as indicated by the arrow c in Figure 9.4b.

9.3 Summary

This chapter illustrates a cost-effective way to fabricate opals with planar defect and successful conversion of them into inverse opals with planar defect. Through the combination of inward-growing self-assembly and spin-coating, a single layer of silica beads was inserted into PS opal. After infiltration of silica and removal of PS inverse opal structure with a homogeneous planar defect was obtained. The thickness of defect layer can be adjusted by changing the diameter of the silica beads. The fabrication method was proved to be efficient to achieve good crystal quality and defect layer uniformity. The existence of defect states induced by the planar defects was confirmed by transmission spectra of samples.

Chapter 10

Patterning Microsphere Surfaces and Fabrication of Nonspherical Particles

10.1 Introduction

Patterning of the surface of microspheres is of great interest because of its potential applications in directed self-assembly (Glotzer, 2004; Zhang and Glotzer, 2004; DeVries et al., 2007) and sensors (Perez et al., 2003). Various methods have been explored to fabricate Janus microspheres. The surfaces of colloidal spheres arranged in a monolayer were partially modified to produce Janus particles by using vapor deposition (Takei and Shimizu, 1997; Love et al., 2002; Correa-Duarte et al., 2005), Langmuir-Blodgett technique (Yokoyama et al., 2005), electroless deposition (Cui and Kretzschmar, 2006) and contact printing (Cayre et al., 2003). Janus spheres were also achieved by using membranes (Nagle and Fitzmaurice, 2003; Nagle et al., 2003), phase interface (Fujimoto et al., 1999; Petit et al., 2000; Paunov and Cayre, 2004) and substrate (Snyder et al., 2005) as protection. Microfluidic synthesis and nodule-protected modification of spheres (Perro et al., 2005) were found effective in relative large-scale production of Janus particles. Recently, more complex pattern has been achieved on the top-half of the spheres in the bottom layer of a colloidal crystal (CC) by using the top layers as masks to deposit Au on them (Zhang et al., 2005a;

2005b; Zhang et al., 2006). Nevertheless, most of these methods are suitable for the modification of the spheres arranged in a monolayer. Thus the modification is limited to one of hemispheres and the amount of the spheres produced is limited. It is still a challenge to pattern the whole surface of the spheres in large scale.

Most of the highly monodisperse non-spherical particles were fabricated by modification of spherical particles. Polymer multiplets were synthesized by seeded polymerization (Skjeltorp et al., 1986; H. R. Sheu, 1990; Kim et al., 2006; Mock et al., 2006). Ellipsoidal particles (Lu et al., 2001) and spheres with holes (Marczewski and Goedel, 2005; Yan et al., 2006) were fabricated by modifying microspheres. The fabrication of snow-man like particles (Koo et al., 2004), dimmers (Lu et al., 2003) and colloidal clusters (Velev et al., 2000; Cho et al., 2005) were also demonstrated. Hybrid nonspherical particles were synthesized by using functionalized silica spheres as seeds in a polymerization process (Reculusa et al., 2002; Reculusa et al., 2004; Reculusa et al., 2005) Complex particles were fabricated by colloidal lithography (Yang et al., 2006).

10.2 Patterning the Surface of Microspheres by 3D Colloidal Crystal Templating and Fabrication of Nonspherical Particles

In this chapter, we report, for the first time, the patterning of the surface of submicron spheres by three-dimensional (3D) colloidal crystal templating. A pattern with twelve dots distributed around the spherical surface can be formed on different particles. By using the patterned particles as seeds in the further regrowth process, three types of novel non-spherical particles were synthesized. This may serve as a general approach to the fabrication of submicron spheres with complex surface patterns and non-spherical particles in large amount.

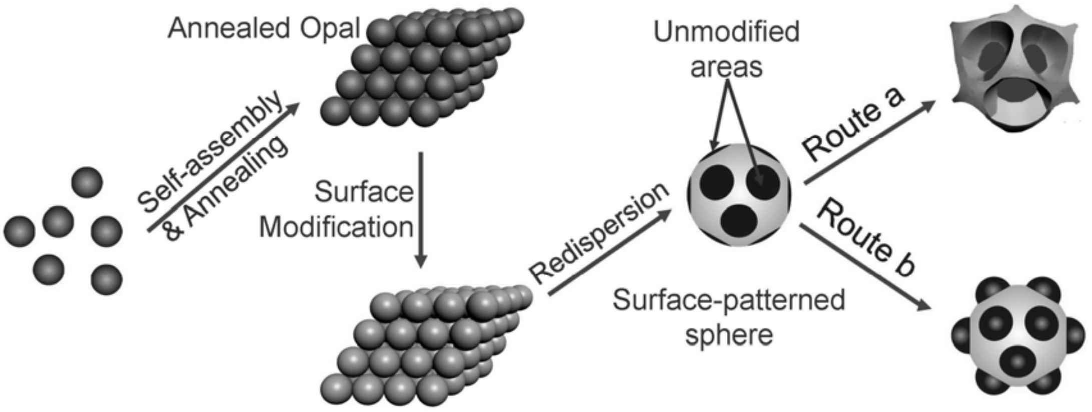

Figure 10.1 Schematic illustration of patterning microsphere surfaces and fabricating nonspherical particles using different strategies: a) a material is grown on the unmodified areas to obtain spheres with twelve nodules, b) seeded polymerization is used to obtain spheres with protruding edges, and c) a material is grown on the modified areas to achieve core-shell particles with holes on the shells (the holes on the equator are indicated by white dot lines).

The strategy of the patterning and the fabrication of non-spherical spheres are illustrated in Figure 10.1. First, monodisperse silica particles or polystyrene (PS) were allowed to self-assemble into a 3D CC, followed by annealing of the CC to form connection areas between adjacent spheres. Second, the CC was immersed into functionalizing solution to chemically modify the exposed areas of the sphere surface while the connection areas were shadowed by the adjacent spheres. Subsequently, after several times wash the functionalized CC was redispersed by ultrasonication. Thus, a colloid of spheres with twelve dots (transformed from the connection areas) pattern was obtained. Finally, by using these surface-patterned spheres as seeds, three novel types of non-spherical particles were fabricated through growing materials on different part of the surface pattern or seeded polymerization. Spheres with hemispheres connected to them can be formed when the material deposits only on the connection areas (Figure 10.1a), while core-shell spheres with holes on shells can be formed when the material grows on the exposed areas (Figure 10.1c). Particles with protruding edges can be achieved through a seeded polymerization process (Figure 10.1b).

10.2.1 Fabrication of Silica Nonspherical Particles

CCs of 41 5nm silica spheres were fabricated and calcinated at 750 °C to allow the formation of connections between adjacent spheres. Consequently the calcinated CCs were immersed into a solution containing MPS (3-(trimethoxysilyl)propyl methacrylate). Thus the exposed surfaces of the spheres in the CCs were grafted with MPS while the connection areas remained unmodified. After washing and redispersion, silica spheres with twelve dots patterned around the spherical surface were obtained. By using these surface-patterned spheres as seeds in a silica regrowth process (Giesche, 1994), spheres with twelve hemispheres connected to them were obtained as seen in Figure 10.2.

It is proved that the hemispheres grew from the connection areas by using some pieces of surface-modified CCs instead of well-redispersed spheres in the regrowth process (Figure 10.2c). This result, in return, proves the successful formation of a complex pattern on the silica spheres by 3D CC templating.

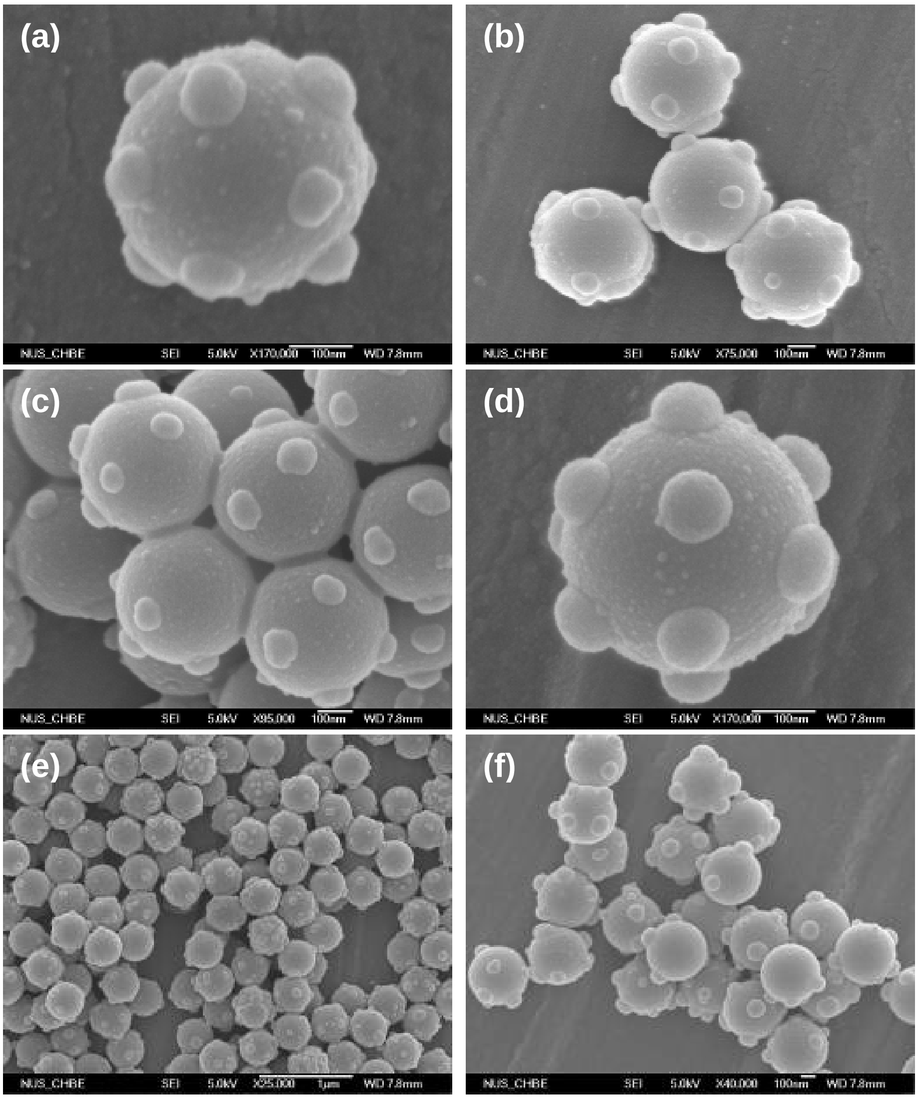

Figure 10.2 Scanning electron microscopy (SEM) images of the nonspherical silica particles: a, b) the particles resulted from an opal annealed for 5 h; c) the result of using a piece of MPS-modified CC in the regrowth process; d) the particle resulted from an opal annealed for 8 h. e) nonspherical silica particles obtained from a CC annealed for 5 h; f) nonspherical silica particles obtained from a CC annealed for 8 h.

Some of the spheres (see Figure 10.2 e and f) did not have 12 hemispheres connected to them, probably because that the size deviation of the beads made some of the spheres remain not connected with one or several of the 12 adjacent spheres after calcination. Figure 10.2d shows the result of the particle by prolonging the calcinations time from 5h (for Figure 10.2a) to 8h. The hemisphere diameter increased from 95nm to 115nm. This demonstrates that by adjusting the calcination time, the sizes of dots on the surface pattern could be tuned and so did the size of the hemispheres connected to the silica spheres.

In a close-packed CC of fcc (face-centered cubic) structure, every sphere, except those in the bottom or top layer, contacts 12 spheres around it. Thus the consequent patterned spheres and the nonspherical particles are limited to being 12-fold symmetry. However, through the change of the structure of the template CC, the number of spheres connecting to one sphere can be changed. For instance, if a CC with non-close-packed spheres in the same layers (a structure readily available as shown in Jiang and McFarland's article (Jiang and McFarland, 2004)) is employed, patterned spheres with 6-fold symmetry can be obtained, as illustrated in Figure 10.3a. Similarly, patterned particles with 7 chemical patches are expected to be achieved if a monolayer of close-packed CC is employed, as shown in Figure 10.3b. Additionally, in a binary CC composed of large and small spheres, the large sphere may be surrounded by more than 12 spheres, which might be used to fabricate particles with more than 12 patches or nodules.

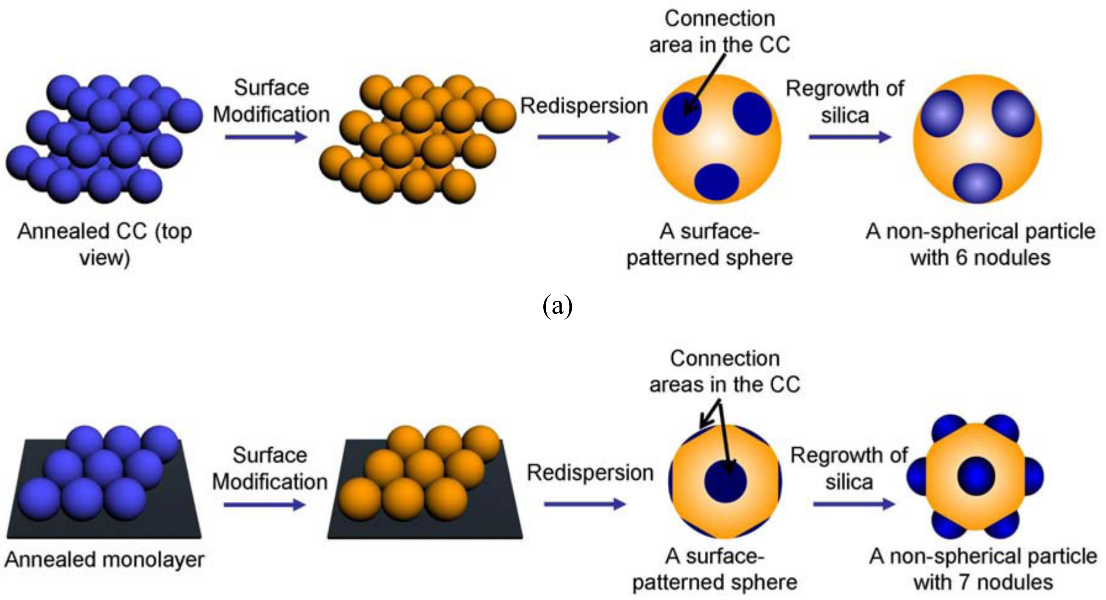

(a)

(b)

Figure 10.3 (a) Scheme of patterning sphere surfaces with 6 unmodified areas (another three are on the back side) and the fabricating of non-spherical with 6 nodules; (b) Scheme of patterning sphere surfaces with 7 unmodified areas and the fabricating of non-spherical with 7 nodules.

10.2.2 Fabrication of Polystyrene Nonspherical Particles

This method of patterning the surface of submicrometer spheres can also be applied to polymer beads. In our work, PS beads with a surface sulphonation pattern were obtained by sulphurizing PS CCs and redispersion of them. Contrary to the CCs before sulphonation treatment, CCs after sulphonation could be easily redispersed in water. To confirm the formation of surface pattern on the PS beads, these sulfurized PS spheres were re-grown in a seeded polymerization procedure. In this procedure, the mixture of 0.29g sulfurized 984nm PS spheres, 0.28ml styrene monomer and water was stirred for 60 min at 60°C. After addition of potassium persulfate and polymerization for 20 h, PS particles of 1.23μm with protruding edges, as illustrated in Figure 10.4, were obtained.

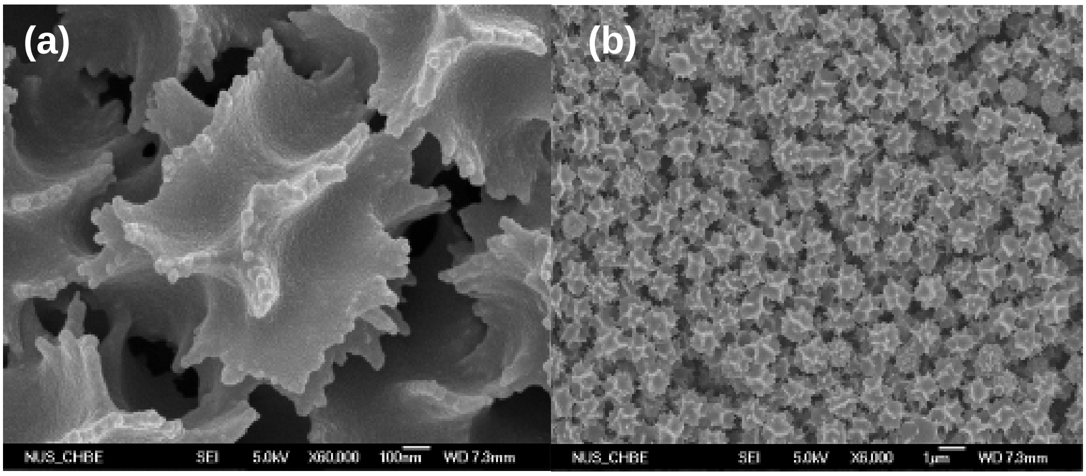

Figure 10.4 The SEM images of the nonspherical PS particles of different magnifications.

In the other two batches of seeded polymerization, which used untreated PS beads and completely sulphurized PS beads as seeds, the final particles were all spherical. This indicates that the formation of the protruding edges is due to the surface pattern on the PS seed particles. These PS particles with protruding edges were found still hydrophilic after complete drying.

Table 10.1 X-ray photoelectron spectroscopy (XPS) quantitative analyzing result of the PS particle surfaces

Mass Concentration (%) / *Samples Name*	*S*	*O*	**C**
Original PS beads	0.48	5.43	94.09
Sulphonated PS beads	10.46	29.38	60.16
Non-spherical PS particles	9.48	19.38	71.14

The XPS results in Table 10.1 show that the sulfur content increases greatly after sulphurnation. After seeded polymerization, the sulfur content on the surface decreases a little, but is still much larger than that in the surface of PS beads without sulphonation. Considering the shape and the surface composition of the beads, we propose a mechanism of the seeded polymerization process as following: after the addition of the initiator the free radicals generated by initiator react with styrene monomer in the aqueous phase to form oligomeric free radicals. Most of these oligomeric free radicals are captured by the existing PS beads and anchor preferentially on the hydrophilic part of their surface (Shim et al., 1999). The hydrophobic parts of the oligomeric radicals penetrate into the PS beads and react with styrene solubilized in the beads. Thus the polymerization mainly happens underneath the sulfurized part of the PS beads surface, leading to the formation of protruding edges on the particles.

Smaller PS beads of 400nm were also employed in this work to fabricate nonspherical particles. It was found that the final particles were with protruding arms rather than protruding edges (Figure 10.5). This morphology difference might be due to the small size of the beads, which caused that the thickness of the edges was so thin that they separated to form independent arms. Through the change of the monomer amount added in the regrowth process, the size of the final particles and the length of arms could be altered. From Figure 10.5, we can observe that the size of the beads increase from 490nm to 510nm and 650nm when the monomer amount increased from 0.1ml to 0.2ml and 0.4ml.

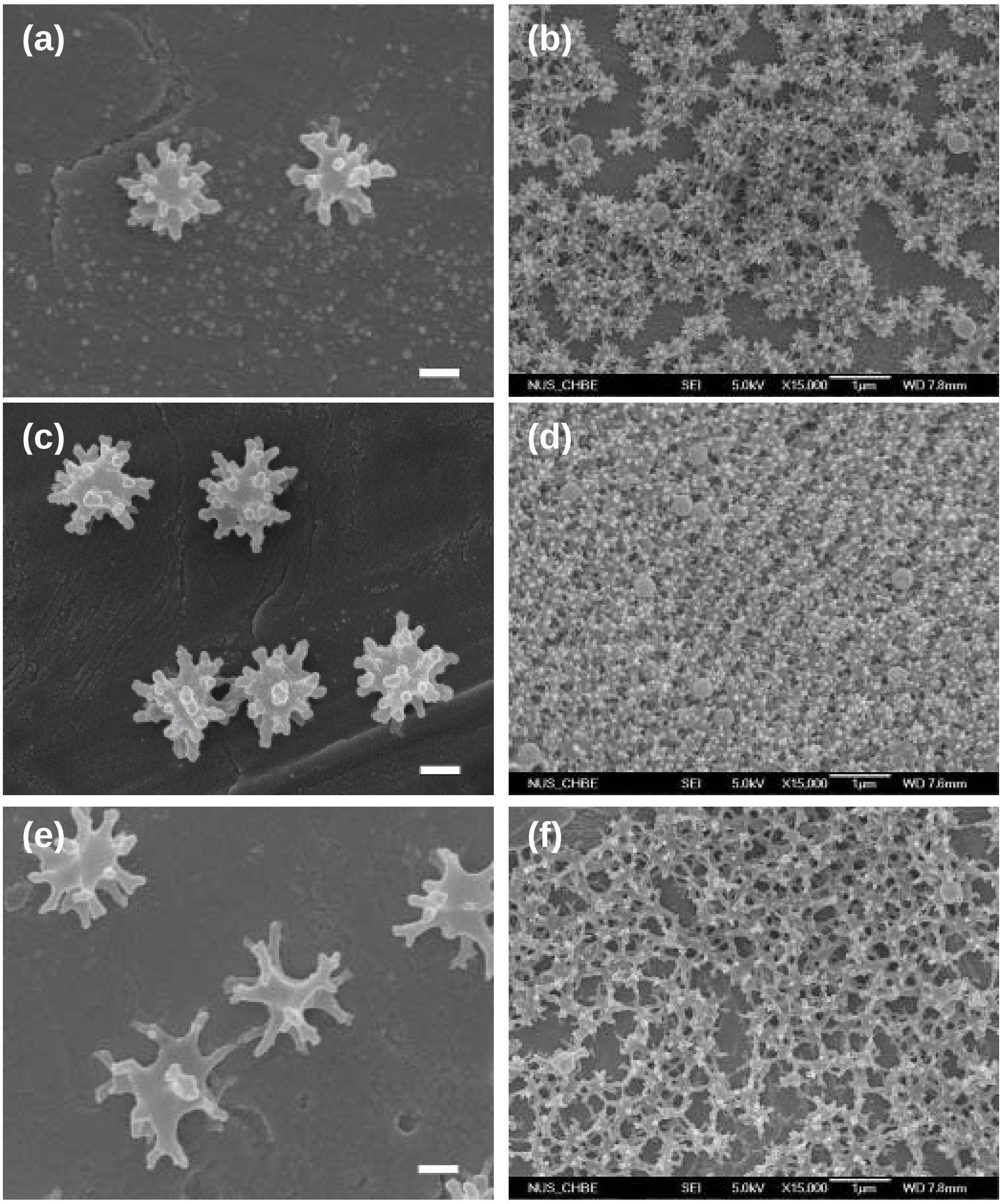

Figure 10.5 SEM images of nonspherical PS particles. (a, b) (c, d) (e, f) are the high and low magnification view of nonspherical particles fabricated from 400-nm PS beads, using 0.1 mL, 0.2 mL and 0.4 mL styrene in the seeded polymerization processes, respectively. The scale bars of image (a, c and e) are all 200 nm.

10.3 Drilling Nanoholes in PS Spheres

This chapter also demonstrated a very effective route to drilling nanohole in PS colloidal spheres, as schematically illustrated in Figure 10.6.

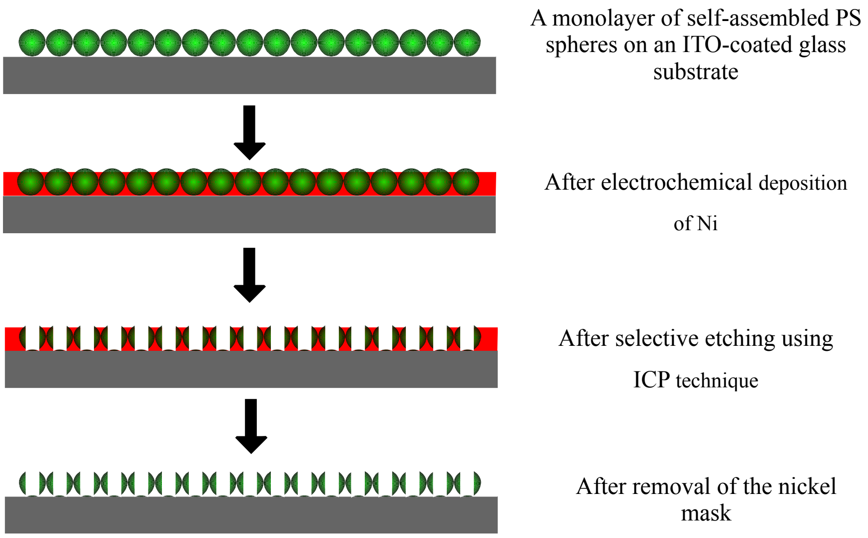

Figure 10.6 Schematic illustration of fabrication of an array of PS colloidal spheres with nanoholes.

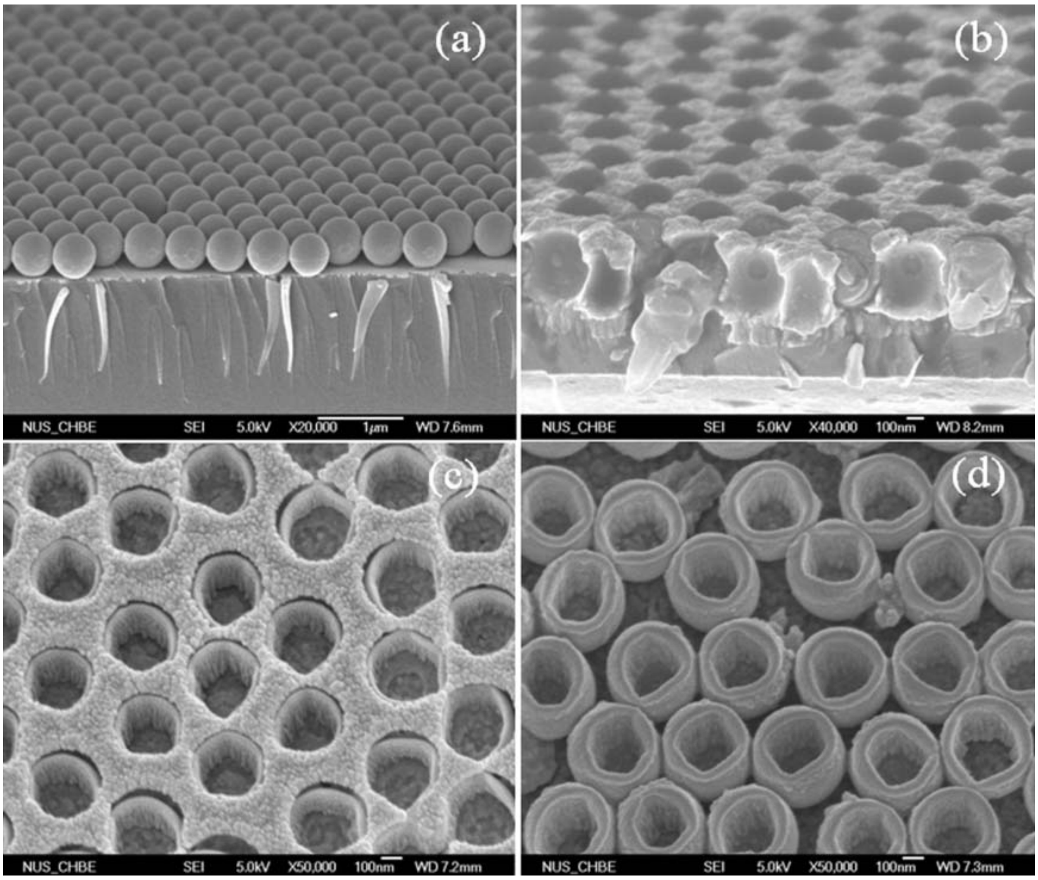

Figure 10.7 Scanning electron microscopy (SEM) images of (a) a colloidal monolayer of PS spheres of 450 nm in diameter self-assembled on an ITO-coated glass substrate, (b) an array of PS colloidal spheres partially embedded in a nickel layer, (c) after ICP etching for 3 min and 1.6 M HCl etching for another 3 min, and (d) an array of PS colloidal spheres with nanoholes.

The first step is the self assembly of a PS monolayer on a glass substrate coated with indium-tin-oxide (ITO). Subsequently, a layer of nickel was electrochemically deposited on the surface of the substrate, filling the interstice of the PS sphere monolayer. The thickness of the metal layer is carefully controlled to be larger than the radius but smaller than the diameter of the PS spheres. Thus, the PS colloidal spheres are partially covered by nickel and the upper hemispheres partially protrude from the metal layer. Consequently, in the following step of anisotropic dry etching using inductively coupled plasma (ICP), the deposited nickel acts as a mask, covering the equatorial parts while nanoholes are etched out through uncovered areas. Finally, a monolayer array of PS colloidal spheres with nanoholes is obtained after removal of the nickel by chemically etching with a diluted hydrochloric acid. The samples collected at different stages are characterized with a field-emission scanning electron microscope.

The hexagonally close-packed monolayer of PS spheres was fabricated by vertical depostion, as shown in Figure 10.7a. Through annealing, the monolayer formed a connection between adjacent spheres, which improved the stability of the structure during the following fabrication steps. Figure 10.7b shows a tilted cross-section view of the PS colloidal monolayer embedded in the nickel layer, obtained after the deposition of nickel. It can be clearly seen that the top surface of PS spheres partially protrude from the metal layer. Nickel was also found fully infiltrated into the interior space between the PS colloidal spheres and the nickel layer was quite uniform with a thickness of about 400 nm.

Figure 10.7c shows a tilted top view of the sample after being etched for 3 min. To obtain a better view of the etched PS spheres, here the etched sample was treated with a 1.6 M HCl solution for 3 min to thin the nickel layer. Because of the anisotropic nature of the ICP etching technique and the masking function of the Ni layer, it is seen that only the middle parts of the PS colloidal spheres were etched. Upon complete removal of the Ni layer, an array of PS colloidal spheres with nanoholes was obtained, as can be seen from Figure 10.7d. It should be noted that the order of the particle array was slightly distorted in comparison with that of the original PS monolayer, which was most probably caused by the wet chemical etching during the removal of the metal layer. A long-time annealing of the PS monolayer prior to electrochemical deposition may avoid such a structural distortion.

Electrochemical deposition of metals into the voids of a close-packed array of microspheres on conductive substrates has been used by many researchers to fabricate macroporous metal films (Jiang et al., 1999; Bartlett et al., 2000; Wijnhoven et al., 2000; Xu et al., 2000; Luo et al., 2001). The thickness of the metal film can be easily controlled through the time of electrochemical deposition due to the bottom-up-growth mechanism. This enables the fabrication of arrays of PS colloidal spheres with different nanohole sizes. The diameter of the nanoholes can be simply manipulated by the thickness of the deposited metal film according to a simple geometrical consideration: $r = [R^2 - (H - R)^2]^{1/2}$ (r is the radius of the holes, R is the radius of the PS spheres, and H is the thickness of the metal film). Thus, through manipulation of the thickness of the metal layer, the size of the nanohols can be controlled. For instance, if a nickel layer of

409 nm covers 450 nm PS spheres, the diameter of the nanoholes should be about 260 nm. The experimentally measured value from the cross-sectional SEM image shown in Figure 10.7d is in good agreement with the estimated value. Figure 10.8 a and b show the arrays of PS colloidal spheres covered with Ni metal layers of thicknesses of 421 and 309 nm leading to nanohole sizes of 220 and 306 nm, respectively.

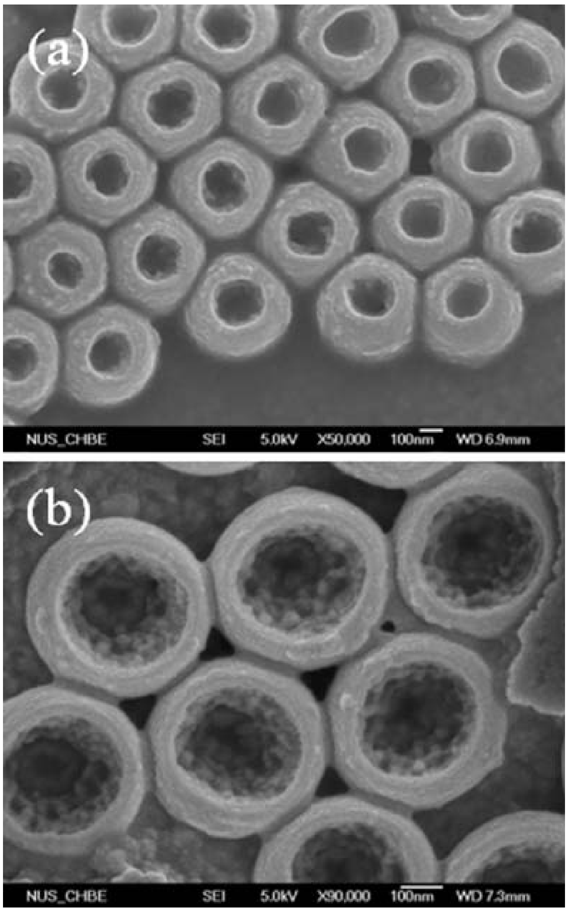

Figure 10.8 PS colloidal spheres with nanohole sizes of (a) 220 nm fabricated with a nickel mask layer of thickness of 421 nm, and (b) 306 nm fabricated with a nickel mask layer of thickness of 309 nm.

Additionally, the depth of the holes can also be tuned by controlling the ICP etching time. PS colloidal spheres with non-through holes could be produce by shorter etching time while a longer etching time resulted in PS spheres with through holes (see Figure 10.7d). The arrays of PS colloidal spheres with non-through pores have potential application as micro- and nano-vials for applications in chemical and biochemical microanalysis (Jiang, 2004; Jiang, 2005). Furthermore, the arrays are potentially applicable for selectively capturing particles smaller than the hole size (Xu et al., 2004).

10.4 Summary

In summary, this chapter illustrates a novel method to the fabrication of submicron spheres with chemically patterned surface through three-dimensional colloidal crystal templating. A pattern with dots distributed around the surface can be formed on spheres. This technique provides a general approach to patterning the whole surface of submicron spheres in large scale. By using these surface-patterned spheres as seeds, three new types of non-spherical particles are synthesized, which might find applications in directed self-assembly, the fabrication of superhydrophobic surface and drug delivery.

An effective approach to the fabrication of arrays of colloidal spheres with nanoholes was demonstrated by selectively etching of a colloidal monolayer partially embedded in an electrochemically deposited metal layer. Both the hole size and the hole depth can be controlled precisely. Since all the processes involved in this approach, fabrication of large-scale colloidal monolayer, electrochemical deposition of uniform metal layer, and dry etching, are quite mature, this approach enables the production of arrays of colloidal spheres with nanoholes in a simple and cost-effective manner. Colloidal spheres with nanoholes and their arrays might find potential applications in microanalysis, photonics and biology.

Chapter 11

Conclusion and Recommendations

11.1 Conclusions

While self-assembly of colloidal spheres has been considered to be a cost-effective way of producing photonic crystals, the application of this method is still limited by a number of fundamental issues, such as the unavailability of uniform colloidal particles with a desired refractive index, the presence of unwanted cracks in a self-assembled colloidal crystal, the difficulty in assembly of pre-designed crystalline structures other than the close-packed structures (fcc or bcc), and the challenge of incorporating engineered defects (wanted defects) into colloidal photonic crystals. This thesis work focused on solving some of the problems encountered in the self-assembly approach to the fabrication of photonic crystals.

In this thesis work, monodisperse silica and polystyrene spheres were synthesized. A seed-growth method was used to fabricate highly uniform silica spheres. The control of the final particle size was achieved by adjusting the seed size or the amount of TEOS added. According to the experimental data, the adding speed of TEOS must be controlled carefully to avoid the formation of secondary seeds, which will lead to the nonuniformity of the final bead sizes. The emulsifier-free emulsion polymerization technique was employed to synthesize polystyrene beads. The polystyrene bead size was found to increase with the amount of monomer and decrease with the addition of surfactant and divinylbenzene. In addition, silica/titania core-shell structures were synthesized by depositing titania on polycation modified silica sphere surface. Pt nanoparticles were also successfully incorporated within the titania shells. The preparation of graphitizable hollow carbon spheres (HCSs) with a single shell, deformed shell, double shell, and N-doped shell were also demonstrated by using silica spheres as templates via chemical vapor deposition (CVD) of benzene or acetonitrile.

A novel template-free approach to the fabrication of crack-free colloidal crystals was proposed and demonstrated. In this approach, the addition of a silica precursor solution into the colloid containing silica spheres provides an effective means of eliminating the formation cracks. When silica spheres crystallize on a silicon substrate, the precursor solution hydrolyzes to form additional silica species to fill in the interstices among the spheres in the colloidal crystal. The filled silica acts as a glue to stick the spheres firmly, thus avoiding the formation of cracks during the drying process. The hydrolyzed silica among the spheres can be easily etched away using hydrofluoric acid vapor to obtain a crack-free colloidal crystal, in which the spheres in the same layer do not touch each other while they touch with the spheres of the adjacent layers. The amount of the silica precursor solution needed to form crack-free film increases with increasing the number of the layers of colloidal crystals. Interestingly, when an excessive amount of silica precursor solution is introduced in the vertical deposition process of producing silica sphere bilayer, the colloidal crystal film peels off from the substrate, leaving behind a large-area nano-bowl array. This might provide a one-step cost-effective way of fabricating nano-bowl pattern in large areas.

A novel approach to the fabrication of non-close-packed colloidal crystal films consisting of spheres connected by cylinders in large domains has been demonstrated. In this approach, the chemical vapor deposition method is employed to deposit silica layers on the surface of a silica inverse opal, producing uniform inverse opal structures with non-close-packed air pores. Subsequent infiltration of the non-closed-packed inverse opal with styrene monomer followed by polymerization and removal of the silica framework yields a free standing non-closed-packed polystyrene opal film. The employment of chemical vapor deposition enables precise controlling of the final structure. The formation of free-standing polystyrene opal films allows tuning the optical properties of the films by mechanical stretching. If elastomer was used in the experiment, a highly tunable free-standing opal should be achieved.

Fabrication of binary colloidal crystals using the horizontal deposition method has been attempted in this thesis work. The significant advantages of this fabrication method lie in its simplicity and fast production rate (about 2 hours over an area of 2.2 × 2.2 cm^2). Through variations of the volume fraction ratio of small spheres over large ones, the structures of the binary colloidal crystals can be tuned. It has been found that the small spheres on the top surface of the binary colloidal crystals are embedded within the voids among large spheres in an ordered manner. However, studies of the internal structures have shown that in the bulk of the colloidal crystals the arrangement of the small spheres is not ordered, possibly due to the confinement effect within the interstitial pores among the large spheres, which restricts the motion of the small particles to self assemble themselves into an ordered fashion. Both structures of the binary colloidal crystal and inverse opals suggest an increasing gradient in the distribution density of small spheres in the direction from bottom to top perpendicular to the substrate. The spectra of all the samples confirm the long-range order of the binary system, which originated from the large sphere packing. The distinctive stop bands demonstrate that the pseudo bandgap property is not affected by the less-evenly distributed small particles in the system. The stop band positions also agree with the volumetric constitutions of the binary mixtures. The simple fabrication process, the ordered and gradient double pore system, as well as the optical property suggest that such binary colloidal crystals hold a great promise for applications beyond photonics, such as for catalysis, micro-reactors, and bio-sensing.

A pure wet chemistry method without involving lithography has been designed and demonstrated to fabricate colloidal crystals and their inverse structures with planar defects. A spin-coating technique has been shown to be quite useful to insert a defect layer into a colloidal crystal of polystyrene spheres. The defect layer can be transferred to the inverse structure of the colloidal crystal by infiltration of the void spaces of the colloidal crystal with silica followed by removal of the polystyrene spheres. The thickness of the defect layer can be controlled by changing the diameter of the silica beads or polystyrene beads. Optical spectra have confirmed the existence of defect states induced by the planar defects. The method demonstrated in this thesis work may provide a general approach to incorporating defect layers of controllable thickness in self-assembled colloidal photonic crystals.

An innovative method for chemical patterning of submicron spheres has succeeded in this thesis work. A pattern with round areas distributed around the surface can be formed on spheres through three-dimensional colloidal crystal templating. By using these surface-patterned spheres as seeds, three types of novel non-spherical particles can be fabricated. Such particles may find applications in directed self-assembly, creating of superhydrophobic surface, and drug delivery. This technique provides a general approach to patterning the whole surface of submicron spheres in a controllable manner in large scales.

11.2 Recommendations

In this thesis work, the formation of crack-free colloidal crystals was achieved by replacing the solvent layer with additional materials formed during the self-assembly. A precursor solution needs to be added in the colloid, which influences the property of the colloid. Thus, to obtain ordered colloidal crystals, the amount of the precursor solution that should be added is limited, and is the layer number of the colloidal crystals. An alternative approach of avoiding the formation of cracks is suggested to introduce the substrate contraction during the self-assembly process. For instance, if a polymer substrate with a hydrophilic surface, which can be swollen with organic solvent, is used in vertical deposition process using aqueous colloid, the release of the solvent from the substrate would lead to the contraction of the substrate. If the speed of the substrate contraction corresponds to that of the solvent evaporation, no formation of cracks is expected. The layer number of the colloidal crystals is also expected to be unlimited.

In the fabrication of non-close packed opals in this thesis work, the voids of the silica inverse opals are fully filled with polystyrene. If a chemical vapor deposition method is used to deposit a thin layer of material followed by removal of the silica inverse opal, an interesting structure consisting of hollow shells connected by air tubes can be obtained. In addition, an elastomer can be used to fabricate non-close packed opals instead of polystyrene. Thus, free-standing opal films with highly tunable optical properties are expected.

In patterning microsphere surface by colloidal crystal patterning, the change of the structure of the colloidal crystals will lead to the change of the surface pattern on the spheres. It is recommended that monolayer and non-close packed structure be used to produce micospheres with various surface patterns and various types of nonspherical particles.

References

Akahane, Y., Asano, T., Song, B. S. and Noda, S. High-Q photonic nanocavity in a two-dimensional photonic crystal. *Nature* **425** (6961): p944, 2003.

Allard, M. and Sargent, E. H. Impact of polydispersity on light propagation in colloidal photonic crystals. *Applied Physics Letters* **85** (24): p5887, 2004.

Aoki, K., Miyazaki, H. T., Hirayama, H., Inoshita, K., Baba, T., Sakoda, K., Shinya, N. and Aoyagi, Y. Microassembly of semiconductor three-dimensional photonic crystals. *Nature Materials* **2** (2): p117, 2003.

Arnal, P. M., Schuth, F. and Kleitz, F. A versatile method for the production of monodisperse spherical particles and hollow particles: Templating from binary core-shell structures. *Chemical Communications* (11): p1203, 2006.

Arsenault, A., Fournier-Bidoz, S. B., Hatton, B., Miguez, H., Tetrault, N., Vekris, E., Wong, S., Yang, S. M., Kitaev, V. and Ozin, G. A. Towards the synthetic all-optical computer: science fiction or reality? *Journal Of Materials Chemistry* **14** (5): p781, 2004.

Arsenault, A. C., Clark, T. J., Von Freymann, G., Cademartiri, L., Sapienza, R., Bertolotti, J., Vekris, E., Wong, S., Kitaev, V., Manners, I., Wang, R. Z., John, S., Wiersma, D. and Ozin, G. A. From colour fingerprinting to the control of photoluminescence in elastic photonic crystals. *Nature Materials* **5** (3): p179, 2006.

Arshady, R. Suspension, Emulsion, and Dispersion Polymerisation: a Methodological Survey. *Colloid and Polymer Science* **270**: p717, 1992.

Baek, K. H. and Gopinath, A. Self-assembled photonic crystal waveguides. *Ieee Photonics Technology Letters* **17** (2): p351, 2005.

Bartlett, P., Ottewill, R. H. and Pusey, P. N. Freezing of Binary-Mixtures of Colloidal Hard-Spheres. *Journal of Chemical Physics* **93** (2): p1299, 1990.

Bartlett, P., Ottewill, R. H. and Pusey, P. N. Superlattice Formation in Binary-Mixtures of Hard-Sphere Colloids. *Physical Review Letters* **68** (25): p3801, 1992.

Bartlett, P. N., Birkin, P. R. and Ghanem, M. A. Electrochemical deposition of macroporous platinum, palladium and cobalt films using polystyrene latex sphere templates. *Chemical Communications* (17): p1671, 2000.

Birner, A., Wehrspohn, R. B., Gosele, U. M. and Busch, K. Silicon-based photonic crystals. *Advanced Materials* **13** (6): p377, 2001.

Blanco, A., Chomski, E., Grabtchak, S., Ibisate, M., John, S., Leonard, S. W., Lopez, C., Meseguer, F., Míguez, H., Mondia, J. P., Ozin, G. A., Toader, O. and van Driel, H. M. Large-scale synthesis of a silicon photonic crystal with a complete three-dimensional bandgap near 1.5 micrometres. *Nature* **405** (6785): p437, 2000.

Bokros, J. C. *Chemistry and Physics of Carbon*. New York, Marcel Dekker, 1969

Braun, P. V. and Wiltzius, P. Microporous materials - Electrochemically grown photonic crystals. *Nature* **402** (6762): p603, 1999.

Breen, M. L., Dinsmore, A. D., Pink, R. H., Qadri, S. B. and Ratna, B. R. Sonochemically produced ZnS-coated polystyrene core-shell particles for use in photonic crystals. *Langmuir* **17** (3): p903, 2001.

Burmeister, F., Schafle, C., Keilhofer, B., Bechinger, C., Boneberg, J. and Leiderer, P. From mesoscopic to nanoscopic surface structures: Lithography with colloid monolayers. *Advanced Materials* **10** (6): p495, 1998.

Busch, K. and John, S. Photonic band gap formation in certain self-organizing systems. *Physical Review E* **58** (3): p3896, 1998.

Campbell, M., Sharp, D. N., Harrison, M. T., Denning, R. G. and Turberfield, A. J. Fabrication of photonic crystals for the visible spectrum by holographic lithography. *Nature* **404** (6773): p53, 2000.

Caruso, F. Nanoengineering of particle surfaces. *Advanced Materials* **13** (1): p11, 2001.

Caruso, F., Caruso, R. A. and Mohwald, H. Nanoengineering of inorganic and hybrid hollow spheres by colloidal templating. *Science* **282** (5391): p1111, 1998.

Caruso, F., Shi, X. Y., Caruso, R. A. and Susha, A. Hollow titania spheres from layered precursor deposition on sacrificial colloidal core particles. *Advanced Materials* **13** (10): p740, 2001a.

Caruso, F., Spasova, M., Saigueirino-Maceira, V. and Liz-Marzan, L. M. Multilayer assemblies of silica-encapsulated gold nanoparticles on decomposable colloid templates. *Advanced Materials* **13** (14): p1090, 2001b.

Caruso, R. A., Susha, A. and Caruso, F. Multilayered titania, silica, and Laponite nanoparticle coatings on polystyrene colloidal templates and resulting inorganic hollow spheres. *Chemistry of Materials* **13** (2): p400, 2001c.

Cayre, O., Paunov, V. N. and Velev, O. D. Fabrication of asymmetrically coated colloid particles by microcontact printing techniques. *Journal Of Materials Chemistry* **13** (10): p2445, 2003.

Cha, Y.-J. and Choe, S. Characterization of crosslinked polystyrene beads and their composite in SBR matrix. *Journal of Applied Polymer Science* **58**: p147, 1995.

Chabanov, A. A., Jun, Y. and Norris, D. J. Avoiding cracks in self-assembled photonic band-gap crystals. *Applied Physics Letters* **84** (18): p3573, 2004.

Chang, S. Y. and Ring, T. A. Map of Gel Times for 3 Phase Region Tetraethoxysilane, Ethanol and Water. *Journal of Non-Crystalline Solids* **147**: p56, 1992.

Chelnokov, A., Wang, K., Rowson, S., Garoche, P. and Lourtioz, J. M. Near-infrared Yablonovite-like photonic crystals by focused-ion-beam etching of macroporous silicon. *Applied Physics Letters* **77** (19): p2943, 2000.

Chen, H. B., Zhu, Y. Z., Cao, Y. L., Wang, Y. P. and Chi, Y. B. Photonic band gap in the face-centered cubic lattice of spherical shells connected by cylindrical tubes. *Physical Review B* **72** (11): p113113, 2005.

Chen, M., Wu, L. M., Zhou, S. X. and You, B. A method for the fabrication of monodisperse hollow silica spheres. *Advanced Materials* **18** (6): p801, 2006.

Cho, Y. S., Yi, G. R., Lim, J. M., Kim, S. H., Manoharan, V. N., Pine, D. J. and Yang, S. M. Self-organization of bidisperse colloids in water droplets. *Journal of the American Chemical Society* **127** (45): p15968, 2005a.

Cho, Y. S., Yi, G. R., Moon, J. H., Kim, D. C., Lee, B. J. and Yang, S. M. Connected open structures from close-packed colloidal crystals by hyperthermal neutral beam etching. *Langmuir* **21** (23): p10770, 2005b.

Chomski, E. and Ozin, G. A. Panoscopic silicon - A material for "all" length scales. *Advanced Materials* **12** (14): p1071, 2000.

Chung, Y. W., Leu, I. C., Lee, J. H. and Hon, M. H. Influence of humidity on the fabrication of high-quality colloidal crystals via a capillary-enhanced process. *Langmuir* **22** (14): p6454, 2006.

Cong, H. L. and Cao, W. X. Array patterns of binary colloidal crystals. *Journal Of Physical Chemistry B* **109** (5): p1695, 2005.

Correa-Duarte, M. A., Salgueirino-Maceira, V., Rodriguez-Gonzalez, B., Liz-Marzan, L. M., Kosiorek, A., Kandulski, W. and Giersig, M. Asymmetric functional colloids through selective hemisphere modification. *Advanced Materials* **17** (16): p2014, 2005.

Cui, J. Q. and Kretzschmar, I. Surface-anisotropic polystyrene spheres by electroless deposition. *Langmuir* **22** (20): p8281, 2006.

Cuisin, C., Chelnokov, A., Decanini, D., Peyrade, D., Chen, Y. and Lourtioz, J. M. Sub-micrometre dielectric and metallic yablonovite structures fabricated from resist templates. *Optical And Quantum Electronics* **34** (1-3): p13, 2002.

Dag, O., Ozin, G. A., Yang, H., Reber, C. and Bussiere, G. Photoluminescent silicon clusters in oriented hexagonal mesoporous silica film. *Advanced Materials* **11** (6): p474, 1999.

Deubel, M., Von Freymann, G., Wegener, M., Pereira, S., Busch, K. and Soukoulis, C. M. Direct laser writing of three-dimensional photonic-crystal templates for telecommunications. *Nature Materials* **3** (7): p444, 2004.

Deutsch, M., Vlasov, Y. A. and Norris, D. J. Conjugated-polymer photonic crystals. *Advanced Materials* **12** (16): p1176, 2000.

DeVries, G. A., Brunnbauer, M., Hu, Y., Jackson, A. M., Long, B., Neltner, B. T., Uzun, O., Wunsch, B. H. and Stellacci, F. Divalent metal nanoparticles. *Science* **315** (5810): p358, 2007.

Doosje, M., Hoenders, B. J. and Knoester, J. Photonic bandgap optimization in inverted fcc photonic crystals. *Journal Of The Optical Society Of America B-Optical Physics* **17** (4): p600, 2000.

Egen, M., Voss, R., Griesebock, B., Zentel, R., Romanov, S. and Torres, C. S. Heterostructures of polymer photonic crystal films. *Chemistry of Materials* **15** (20): p3786, 2003.

Fan, S. H., Villeneuve, P. R. and Joannopoulos, J. D. Channel drop tunneling through localized states. *Physical Review Letters* **80** (5): p960, 1998.

Feiertag, G., Ehrfeld, W., Freimuth, H., Kolle, H., Lehr, H., Schmidt, M., Sigalas, M. M., Soukoulis, C. M., Kiriakidis, G., Pedersen, T., Kuhl, J. and Koenig, W. Fabrication of photonic crystals by deep x-ray lithography. *Applied Physics Letters*

71 (11): p1441, 1997.

Feigel, A., Kotler, Z., Sfez, B., Arsh, A., Klebanov, M. and Lyubin, V. Chalcogenide glass-based three-dimensional photonic crystals. *Applied Physics Letters* **77** (20): p3221, 2000.

Fenollosa, R. and Meseguer, F. Non-close-packed artificial opals. *Advanced Materials* **15** (15): p1282, 2003.

Ferrand, P., Egen, M., Zentel, R., Seekamp, J., Romanov, S. G. and Torres, C. M. S. Structuring of self-assembled three-dimensional photonic crystals by direct electron-beam lithography. *Applied Physics Letters* **83** (25): p5289, 2003.

Ferrand, P., Seekamp, J., Egen, M., Zentel, R., Romanov, S. G. and Torres, C. M. S. Direct electron-beam lithography on opal films for deterministic defect fabrication in three-dimensional photonic crystals. *Microelectronic Engineering* **73-74**: p362, 2004.

Fleischhaker, F., Arsenault, A. C., Peiris, F. C., Kitaev, V., Manners, I., Zentel, R. and Ozin, G. A. DNA Designer Defects in Photonic Crystals: Optically Monitored Biochemistry. *Advanced Materials* **18** (18): p2387, 2006.

Fleischhaker, F., Arsenault, A. C., Wang, Z., Kitaev, V., Peiris, F. C., von Freymann, G., Manners, I., Zentel, R. and Ozin, G. A. Redox-tunable defects in colloidal photonic crystals. *Advanced Materials* **17** (20): p2455, 2005a.

Fleischhaker, F., Arsenault Andre, C., Kitaev, V., Peiris Frank, C., von Freymann, G., Manners, I., Zentel, R. and Ozin Geoffrey, A. Photochemically and thermally tunable planar defects in colloidal photonic crystals. *Journal of the American Chemical Society* **127** (26): p9318, 2005b.

Fleming, J. G., Lin, S. Y., El-Kady, I., Biswas, R. and Ho, K. M. All-metallic three-dimensional photonic crystals with a large infrared bandgap. *Nature* **417** (6884): p52, 2002.

Fudouzi, H. and Sawada, T. Photonic rubber sheets with tunable color by elastic deformation. *Langmuir* **22** (3): p1365, 2006.

Fujimoto, K., Nakahama, K., Shidara, M. and Kawaguchi, H. Preparation of unsymmetrical microspheres at the interfaces. *Langmuir* **15** (13): p4630, 1999.

Galli, M., Bajoni, D., Patrini, M., Guizzetti, G., Gerace, D., Andreani, L. C., Belotti, M. and Chen, Y. Single-mode versus multimode behavior in silicon photonic crystal waveguides measured by attenuated total reflectance. *Physical Review B* **72**

(12): p125322, 2005.

Garcia-Santamaria, F., Lopez, C., Meseguer, F., Lopez-Tejeira, F., Sanchez-Dehesa, J. and Miyazaki, H. T. Opal-like photonic crystal with diamond lattice. *Applied Physics Letters* **79** (15): p2309, 2001.

Garcia-Santamaria, F., Miyazaki, H. T., Urquia, A., Ibisate, M., Belmonte, M., Shinya, N., Meseguer, F. and Lopez, C. Nanorobotic manipulation of microspheres for on-chip diamond architectures. *Advanced Materials* **14** (16): p1144, 2002.

Gates, B. and Xia, Y. Photonic band-gap properties of opaline lattices of spherical colloids doped with various concentrations of smaller colloids. *Applied Physics Letters* **78** (21): p3178, 2001.

Gates, B., Yin, Y. D. and Xia, Y. N. Fabrication and characterization of porous membranes with highly ordered three-dimensional periodic structures. *Chemistry Of Materials* **11** (10): p2827, 1999.

Giesche, H. Synthesis of Monodispersed Silica Powders .1. Particle Properties and Reaction-Kinetics. *Journal of the European Ceramic Society* **14** (3): p189, 1994a.

Giesche, H. Synthesis of Monodispersed Silica Powders .2. Controlled Growth Reaction and Continuous Production Process. *Journal of the European Ceramic Society* **14** (3): p205, 1994b.

Glotzer, S. C. Some assembly required. *Science* **306** (5695): p419, 2004.

Graf, C. and van Blaaderen, A. Metallodielectric colloidal core-shell particles for photonic applications. *Langmuir* **18** (2): p524, 2002.

Griesebock, B., Egen, M. and Zentel, R. Large photonic films by crystallization on fluid substrates. *Chemistry of Materials* **14** (10): p4023, 2002.

Gu, Z. Z., Kubo, S., Qian, W. P., Einaga, Y., Tryk, D. A., Fujishima, A. and Sato, O. Varying the optical stop band of a three-dimensional photonic crystal by refractive index control. *Langmuir* **17** (22): p6751, 2001.

H. R. Sheu, M. S. E.-A. J. W. V. Uniform nonspherical latex particles as model interpenetrating polymer networks. *Journal of Polymer Science Part A: Polymer Chemistry* **28** (3): p653, 1990.

Herring, A. M., McKinnon, J. T., McCloskey, B. D., Filley, J., Gneshin, K. W., Pavelka, R. A., Kleebe, H. J. and Aldrich, D. J. A novel method for the templated synthesis of homogeneous samples of hollow carbon nanospheres from cellulose chars. *Journal of the American Chemical Society* **125** (33): p9916, 2003.

Ho, K. M., Chan, C. T., Soukoulis, C. M., Biswas, R. and Sigalas, M. Photonic Band-Gaps in 3-Dimensions - New Layer-by-Layer Periodic Structures. *Solid State Communications* **89** (5): p413, 1994.

Holgado, M., Garcia-Santamaria, F., Blanco, A., Ibisate, M., Cintas, A., Miguez, H., Serna, C. J., Molpeceres, C., Requena, J., Mifsud, A., Meseguer, F. and Lopez, C. Electrophoretic deposition to control artificial opal growth. *Langmuir* **15** (14): p4701, 1999.

Holland, B. T., Blanford, C. F., Do, T. and Stein, A. Synthesis of highly ordered, three-dimensional, macroporous structures of amorphous or crystalline inorganic oxides, phosphates, and hybrid composites. *Chemistry Of Materials* **11** (3): p795, 1999.

Hoogenboom, J. P., van Langen-Suurling, A. K., Romijn, J. and van Blaaderen, A. Hard-sphere crystals with hcp and non-close-packed structure grown by colloidal epitaxy. *Physical Review Letters* **90** (13): p138301, 2003.

Hulteen, J. C., Treichel, D. A., Smith, M. T., Duval, M. L., Jensen, T. R. and Van Duyne, R. P. Nanosphere lithography: Size-tunable silver nanoparticle and surface cluster arrays. *Journal of Physical Chemistry B* **103** (19): p3854, 1999.

Hunter, R. J. *Introduction to Modern Colloid Science*. Oxford, Oxford University Press, 1993

Im, S. H., Kim, M. H. and Park, O. O. Thickness control of colloidal crystals with a substrate dipped at a tilted angle into a colloidal suspension. *Chemistry Of Materials* **15** (9): p1797, 2003.

Im, S. H., Lim, Y. T., Suh, D. J. and Park, O. O. Three-dimensional self-assembly of colloids at a water-air interface: A novel technique for the fabrication of photonic bandgap crystals. *Advanced Materials* **14** (19): p1367, 2002.

Im, S. H. and Park, O. O. Effect of evaporation temperature on the quality of colloidal crystals at the water-air interface. *Langmuir* **18** (25): p9642, 2002.

Imada, M., Lee, L. H., Okano, M., Kawashima, S. and Noda, S. Development of three-dimensional photonic-crystal waveguides at optical-communication wavelengths. *Applied Physics Letters* **88** (17), 2006.

Istrate, E. and Sargent, E. H. Photonic crystal heterostructures - resonant tunnelling, waveguides and filters. *Journal Of Optics A-Pure And Applied Optics* **4** (6): pS242, 2002.

Iwayama, Y., Yamanaka, J., Takiguchi, Y., Takasaka, M., Ito, K., Shinohara, T., Sawada, T. and Yonese, M. Optically tunable gelled photonic crystal covering almost the entire visible light wavelength region. *Langmuir* **19** (4): p977, 2003.

Jang, J., Li, X. L. and Oh, J. H. Facile fabrication of polymer and carbon nanocapsules using polypyrrole core/shell nanomaterials. *Chemical Communications* (7): p794, 2004.

Jang, J. H., Ullal, C. K., Gorishnyy, T., Tsukruk, V. V. and Thomas, E. L. Mechanically tunable three-dimensional elastomeric network/air structures via interference lithography. *Nano Letters* **6** (4): p740, 2006.

Jiang, P. Surface-templated nanostructured films with two-dimensional ordered arrays of voids. *Angewandte Chemie-International Edition* **43** (42): p5625, 2004.

Jiang, P. Wafer-scale fabrication of periodic polymer attolitre microvial arrays. *Chemical Communications* (13): p1699, 2005.

Jiang, P., Bertone, J. F., Hwang, K. S. and Colvin, V. L. Single-crystal colloidal multilayers of controlled thickness. *Chemistry Of Materials* **11** (8): p2132, 1999a.

Jiang, P., Cizeron, J., Bertone, J. F. and Colvin, V. L. Preparation of macroporous metal films from colloidal crystals. *Journal of the American Chemical Society* **121** (34): p7957, 1999b.

Jiang, P., Hwang, K. S., Mittleman, D. M., Bertone, J. F. and Colvin, V. L. Template-directed preparation of macroporous polymers with oriented and crystalline arrays of voids. *Journal Of The American Chemical Society* **121** (50): p11630, 1999c.

Jiang, P. and McFarland, M. J. Large-scale fabrication of wafer-size colloidal crystals, macroporous polymers and nanocomposites by spin-coating. *Journal Of The American Chemical Society* **126** (42): p13778, 2004.

Jiang, P., Ostojic, G. N., Narat, R., Mittleman, D. M. and Colvin, V. L. The fabrication and bandgap engineering of photonic multilayers. *Advanced Materials* **13** (6): p389, 2001.

Jin, C., McLachlan, M. A., McComb, D. W., De La Rue, R. M. and Johnson, N. P. Template-Assisted Growth of Nominally Cubic (100)-Oriented Three-Dimensional Crack-Free Photonic Crystals. *Nano Letters* **5** (12): p2646, 2005a.

Jin, C. J., McLachlan, M. A., McComb, D. W., De La Rue, R. M. and Johnson, N. P. Template-assisted growth of nominally cubic (100)-oriented three-dimensional crack-free photonic crystals. *Nano Letters* **5** (12): p2646, 2005b.

Joannopoulos, J. D., Meade, R. D. and Winn, J. N. *Photonic Crystals: Molding the Flow of Light* Princeton University Press: Princeton, NJ, 1995

Joannopoulos, J. D., Villeneuve, P. R. and Fan, S. H. Photonic crystals: Putting a new twist on light. *Nature* **386** (6621): p143, 1997.

John, S. Strong Localization Of Photons In Certain Disordered Dielectric Superlattices. *Physical Review Letters* **58** (23): p2486, 1987.

John, S. and Busch, K. Photonic bandgap formation and tunability in certain self-organizing systems. *Journal Of Lightwave Technology* **17** (11): p1931, 1999.

Johnson, S. G. and Joannopoulos, J. D. *Photonic Crystals - The Road from Theory to Practice*. Boston, Kluwer, 2002

Jonsson, F., Torres, C. M. S., Seekamp, J., Schniedergers, M., Tiedemann, A., Ye, J. H. and Zentel, R. Artificially inscribed defects in opal photonic crystals. *Microelectronic Engineering* **78-79**: p429, 2005.

Juarez, B. H., Golmayo, D., Postigo, P. A. and Lopez, C. Selective formation of inverted opals by electron-beam lithography. *Advanced Materials* **16** (19): p1732, 2004.

Jun, Y., Leatherdale, C. A. and Norris, D. J. Tailoring air defects in self-assembled photonic bandgap crystals. *Advanced Materials (Weinheim, Germany)* **17** (15): p1908, 2005.

Kalinina, O. and Kumacheva, E. Polymeric nanocomposite material with a periodic structure. *Chemistry of Materials* **13** (1): p35, 2001.

Kawata, S., Sun, H. B., Tanaka, T. and Takada, K. Finer features for functional microdevices - Micromachines can be created with higher resolution using two-photon absorption. *Nature* **412** (6848): p697, 2001.

Kim, J. W., Larsen, R. J. and Weitz, D. A. Synthesis of Nonspherical Colloidal Particles with Anisotropic Properties. *J. Am. Chem. Soc.* **128** (44): p14374, 2006.

King, J. S., Gaillot, D. P., Graugnard, E. and Surnmers, C. J. Conformally back-filled, non-close-packed inverse-opal photonic crystals. *Advanced Materials* **18** (8): p1063, 2006.

Kitaev, V. and Ozin, G. A. Self-assembled surface patterns of binary colloidal crystals. *Advanced Materials* **15** (1): p75, 2003.

Koenderink, A. F., Johnson, P. M., Lopez, J. F. G. and Vos, W. L. Three-dimensional photonic crystals as a cage for light. *Comptes Rendus Physique* **3** (1): p67, 2002.

Koo, H. Y., Yi, D. K., Yoo, S. J. and Kim, D. Y. A snowman-like array of colloidal dimers for antireflecting surfaces. *Advanced Materials* **16** (3): p274, 2004.

Koumoto, K., Seo, S., Sugiyama, T., Seo, W. S. and Dressick, W. J. Micropatterning of titanium dioxide on self-assembled monolayers using a liquid-phase deposition process. *Chemistry of Materials* **11** (9): p2305, 1999.

Kuai, S. L., Hu, X. F., Hache, A. and Truong, V. V. High-quality colloidal photonic crystals obtained by optimizing growth parameters in a vertical deposition technique. *Journal Of Crystal Growth* **267** (1-2): p317, 2004.

Lai, N. D., Liang, W. P., Lin, J. H. and Hsu, C. C. Rapid fabrication of large-area periodic structures containing well-defined defects by combining holography and mask techniques. *Optics Express* **13** (14): p5331, 2005.

Lange, B., Zentel, R., Jhaveri, S. J. and Ober, C. K. 3D defect engineering in polymer opals. *Proceedings of SPIE-The International Society for Optical Engineering* **6182** (Photonic Crystal Materials and Devices III (i.e. V)): p61821W/1, 2006.

Larsen, A. E. and Grier, D. G. Like-charge attractions in metastable colloidal crystallites. *Nature* **385** (6613): p230, 1997.

Lawrence, J. R., Shim, G. H., Jiang, P., Han, M. G., Ying, Y. R. and Foulger, S. H. Dynamic tuning of photoluminescent dyes in crystalline colloidal arrays. *Advanced Materials* **17** (19): p2344, 2005.

Lee, K. T., Jung, Y. S. and Oh, S. M. Synthesis of tin-encapsulated spherical hollow carbon for anode material in lithium secondary batteries. *Journal of the American Chemical Society* **125** (19): p5652, 2003.

Lee, W. M., Pruzinsky, S. A. and Braun, P. V. Multi-photon polymerization of waveguide structures within three-dimensional photonic crystals. *Advanced Materials* **14** (4): p271, 2002.

Lellig, C., Hartl, W., Wagner, J. and Hempelmann, R. Immobilized highly charged colloidal crystals: A new route to three-dimensional mesoscale structured materials.

Angewandte Chemie-International Edition **41** (1): p102, 2002.

Li, H. L., Dong, W. T., Bongard, H. J. and Marlow, F. Improved controllability of opal film growth using capillaries for the deposition process. *Journal Of Physical Chemistry B* **109** (20): p9939, 2005a.

Li, J., Herman, P. R., Kitaev, V., Wong, S. and Ozin, G. A. F2-laser digital etching of colloidal photonic crystals. *Applied Physics Letters* **87** (14): p141106/1, 2005b.

Li, J. and Zeng, H. C. Preparation of monodisperse Au/TiO2 nanocatalysts via self-assembly. *Chemistry of Materials* **18** (18): p4270, 2006.

Li, W. H., Chen, L. X., Tang, D. H., Ding, W. Q. and Liu, S. T. Enhancement of available conversion efficiency of optical parametric amplifier in a cascaded photonic crystal structure. *Chinese Physics Letters* **22** (10): p2582, 2005c.

Li, Z. Y. and Zhang, Z. Q. Fragility of photonic band gaps in inverse-opal photonic crystals. *Physical Review B* **62** (3): p1516, 2000.

Li, Z. Y. and Zhang, Z. Q. Photonic bandgaps in disordered inverse-opal photonic crystals. *Advanced Materials* **13** (6): p433, 2001.

Lin, S. Y. and Fleming, J. G. A three-dimensional optical photonic crystal. *Journal Of Lightwave Technology* **17** (11): p1944, 1999.

Lin, S. Y., Ye, D. X., Lu, T. M., Bur, J., Kim, Y. S. and Ho, K. M. Achieving a photonic band edge near visible wavelengths by metallic coatings. *Journal Of Applied Physics* **99** (8): p083104, 2006.

Liu, B. and Zeng, H. C. Symmetric and asymmetric Ostwald ripening in the fabrication of homogeneous core-shell semiconductors. *Small* **1** (5): p566, 2005.

Lopez, C. Materials aspects of photonic crystals. *Advanced Materials* **15** (20): p1679, 2003.

Love, J. C., Gates, B. D., Wolfe, D. B., Paul, K. E. and Whitesides, G. M. Fabrication and wetting properties of metallic half-shells with submicron diameters. *Nano Letters* **2** (8): p891, 2002.

Lu, Y., Xiong, H., Jiang, X. C., Xia, Y. N., Prentiss, M. and Whitesides, G. M. Asymmetric dimers can be formed by dewetting half-shells of gold deposited on the surfaces of spherical oxide colloids. *Journal of the American Chemical Society* **125** (42): p12724, 2003.

Lu, Y., Yin, Y. D. and Xia, Y. N. Three-dimensional photonic crystals with non-spherical colloids as building blocks. *Advanced Materials* **13** (6): p415, 2001.

Lu, Y. F., Fan, H. Y., Stump, A., Ward, T. L., Rieker, T. and Brinker, C. J. Aerosol-assisted self-assembly of mesostructured spherical nanoparticles. *Nature* **398** (6724): p223, 1999.

Luo, G., Liu, Z. J., Li, L., Xie, S. H., Kong, J. L. and Zhao, D. Y. Creating highly ordered metal, alloy, and semiconductor macrostructures by electrodeposition, ion spraying, and laser spraying. *Advanced Materials* **13** (4): p286, 2001.

Maldovan, M. and Thomas, E. L. Diamond-structured photonic crystals. *Nature Materials* **3** (9): p593, 2004.

Marczewski, D. and Goedel, W. A. The preparation of submicrometer-sized rings by embedding and selective etching of spherical silica particles. *Nano Letters* **5** (2): p295, 2005.

Masse, P., Reculusa, S., Clays, K. and Ravaine, S. Tailoring planar defect in three-dimensional colloidal crystals. *Chemical Physics Letters* **422** (1-3): p251, 2006.

Matsuura, N., Yang, S., Sun, P. and Ruda, H. E. Development of highly-ordered, ferroelectric inverse opal films using sol-gel infiltration. *Applied Physics A-Materials Science & Processing* **81** (2): p379, 2005.

Matthias, S., Muller, F., Jamois, C., Wehrspohn, R. B. and Gosele, U. Large-area three-dimensional structuring by electrochemical etching and lithography. *Advanced Materials* **16** (23-24): p2166, 2004.

McLachlan, M. A., Johnson, N. P., De La Rue, R. M. and McComb, D. W. Thin film photonic crystals: synthesis and characterisation. *Journal Of Materials Chemistry* **14** (2): p144, 2004.

McLachlan, M. A., Johnson, N. P., De La Rue, R. M. and McComb, D. W. Domain size and thickness control of thin film photonic crystals. *Journal of Materials Chemistry* **15** (3): p369, 2005.

Meade, R. D., Brommer, K. D., Rappe, A. M. and Joannopoulos, J. D. Photonic Bound-States In Periodic Dielectric Materials. *Physical Review B* **44** (24): p13772, 1991.

Meseguer, F. and Fenollosa, R. Non-close packed colloidal crystals. *Journal Of Materials Chemistry* **15** (43): p4577, 2005.

Miguez, H., Chomski, E., Garcia-Santamaria, F., Ibisate, M., John, S., Lopez, C., Meseguer, F., Mondia, J. P., Ozin, G. A., Toader, O. and van Driel, H. M. Photonic bandgap engineering in germanium inverse opals by chemical vapor deposition. *Advanced Materials* **13** (21): p1634, 2001a.

Miguez, H., Meseguer, F., Lopez, C., Blanco, A., Moya, J. S., Requena, J., Mifsud, A. and Fornes, V. Control of the photonic crystal properties of fcc-packed submicrometer SiO2 spheres by sintering. *Advanced Materials* **10** (6): p480, 1998.

Miguez, H., Meseguer, F., Lopez, C., Lopez-Tejeira, F. and Sanchez-Dehesa, J. Synthesis and photonic bandgap characterization of polymer inverse opals. *Advanced Materials* **13** (6): p393, 2001b.

Miguez, H., Tetreault, N., Hatton, B., Yang, S. M., Perovic, D. and Ozin, G. A. Mechanical stability enhancement by pore size and connectivity control in colloidal crystals by layer-by-layer growth of oxide. *Chemical Communications* (22): p2736, 2002.

Miguez, H., Tetreault, N., Yang, S. M., Kitaev, V. and Ozin, G. A. A new synthetic approach to silicon colloidal photonic crystals with a novel topology and an omni-directional photonic bandgap: Micromolding in inverse silica opal (MISO). *Advanced Materials* **15** (7-8): p597, 2003.

Mihi, A., Ocana, M. and Miguez, H. Oriented colloidal-crystal thin films by spin-coating microspheres dispersed in volatile media. *Advanced Materials* **18** (17): p2244, 2006.

Mock, E. B., DeBruyn, H., Hawkett, B. S., Gilbert, R. G. and Zukoski, C. F. Synthesis of Anisotropic Nanoparticles by Seeded Emulsion Polymerization. *Langmuir* **22** (9): p4037, 2006.

Moon, J. H., Small, A., Yi, G. R., Lee, S. K., Chang, W. S., Pine, D. J. and Yang, S. M. Patterned polymer photonic crystals using soft lithography and holographic lithography. *Synthetic Metals* **148** (1): p99, 2005a.

Moon, J. H., Yang, S., Pine, D. J. and Yang, S. M. Translation of interference pattern by phase shift for diamond photonic crystals. *Optics Express* **13** (24): p9841, 2005b.

Muller, M., Zentel, R., Maka, T., Romanov, S. G. and Torres, C. M. S. Dye-containing polymer beads as photonic crystals. *Chemistry of Materials* **12** (8): p2508, 2000.

Nagle, L. and Fitzmaurice, D. Templated Nanowire Assembly on the Surface of a

Patterned Nanosphere. *Advanced Materials* **15** (11): p933, 2003.

Nagle, L., Ryan, D., Cobbe, S. and Fitzmaurice, D. Templated Nanoparticle Assembly on the Surface of a Patterned Nanosphere. *Nano Lett.* **3** (1): p51, 2003.

Nakamura, H. and Ishii, M. Effects of compression and shearing on the microstructure of polymer-immobilized non-close-packed colloidal crystalline arrays. *Langmuir* **21** (25): p11578, 2005.

Noda, S., Chutinan, A. and Imada, M. Trapping and emission of photons by a single defect in a photonic bandgap structure. *Nature* **407** (6804): p608, 2000a.

Noda, S., Tomoda, K., Yamamoto, N. and Chutinan, A. Full three-dimensional photonic bandgap crystals at near-infrared wavelengths. *Science* **289** (5479): p604, 2000b.

Noda, S., Yamamoto, N., Imada, M., Kobayashi, H. and Okano, M. Alignment and stacking of semiconductor photonic bandgaps by wafer-fusion. *Journal Of Lightwave Technology* **17** (11): p1948, 1999.

Noda, S., Yamamoto, N. and Sasaki, A. New realization method for three-dimensional photonic crystal in optical wavelength region. *Japanese Journal Of Applied Physics Part 2-Letters* **35** (7B): pL909, 1996.

Noguez, C. Surface Plasmons on Metal Nanoparticles: The Influence of Shape and Physical Environment. *J. Phys. Chem. C* **111** (10): p3806, 2007.

Norris, D. J., Arlinghaus, E. G., Meng, L. L., Heiny, R. and Scriven, L. E. Opaline photonic crystals: How does self-assembly work? *Advanced Materials* **16** (16): p1393, 2004.

Norris, D. J. and Vlasov, Y. A. Chemical approaches to three-dimensional semiconductor photonic crystals. *Advanced Materials* **13** (6): p371, 2001.

Ogawa, S. P., Imada, M., Yoshimoto, S., Okano, M. and Noda, S. Control of light emission by 3D photonic crystals. *Science* **305** (5681): p227, 2004.

Ozbay, E., Michel, E., Tuttle, G., Biswas, R., Ho, K. M., Bostak, J. and Bloom, D. M. Double-Etch Geometry For Millimeter-Wave Photonic Band-Gap Crystals. *Applied Physics Letters* **65** (13): p1617, 1994a.

Ozbay, E., Michel, E., Tuttle, G., Biswas, R., Sigalas, M. and Ho, K. M. Micromachined Millimeter-Wave Photonic Band-Gap Crystals. *Applied Physics Letters* **64** (16): p2059, 1994b.

Palacios-Lidon, E., Galisteo-Lopez, J. F., Juarez, B. H. and Lopez, C. Engineered planar defects embedded in opals. *Advanced Materials* **16** (4): p341, 2004.

Palacios-Lidon, E., Juarez, B. H., Castillo-Martinez, E. and Lopez, C. Optical and morphological study of disorder in opals. *Journal Of Applied Physics* **97** (6): p063502, 2005.

Park, S. H., Gates, B. and Xia, Y. N. A three-dimensional photonic crystal operating in the visible region. *Advanced Materials* **11** (6): p462, 1999.

Park, S. H. and Xia, Y. N. Fabrication of three-dimensional macroporous membranes with assemblies of microspheres as templates. *Chemistry of Materials* **10** (7): p1745, 1998.

Paunov, V. N. and Cayre, O. J. Supraparticles and "Janus" particles fabricated by replication of particle monolayers at liquid surfaces using a gel trapping technique. *Advanced Materials* **16** (9-10): p788, 2004.

Perez, J. M., Simeone, F. J., Saeki, Y., Josephson, L. and Weissleder, R. Viral-Induced Self-Assembly of Magnetic Nanoparticles Allows the Detection of Viral Particles in Biological Media. *J. Am. Chem. Soc.* **125** (34): p10192, 2003.

Perro, A., Reculusa, S., Pereira, F., Delville, M. H., Mingotaud, C., Duguet, E., Bourgeat-Lami, E. and Ravaine, S. Towards large amounts of Janus nanoparticles through a protection-deprotection route. *Chemical Communications* (44): p5542, 2005.

Petit, L., Sellier, E., Duguet, E., Ravaine, S. and Mingotaud, C. Dissymmetric silica nanospheres: a first step to difunctionalized nanomaterials. *Journal of Materials Chemistry* **10** (2): p253, 2000.

Pizem, H. and Sukenik, C. N. Effects of substrate surface functionality on solution-deposited titania films. *Chemistry of Materials* **14** (6): p2476, 2002.

Pozas, R., Mihi, A., Ocana, M. and Miguez, H. Building nanocrystalline planar defects within self-assembled photonic crystals by spin-coating. *Advanced Materials* **18** (9): p1183, 2006.

Pradhan, R. D., Tarhan, II and Watson, G. H. Impurity modes in the optical stop bands of doped colloidal crystals. *Physical Review B* **54** (19): p13721, 1996.

Pruzinsky, S. A. and Braun, P. V. Fabrication and characterization of two-photon polymerized features in colloidal crystals. *Advanced Functional Materials* **15** (12): p1995, 2005.

Qi, M. H., Lidorikis, E., Rakich, P. T., Johnson, S. G., Joannopoulos, J. D., Ippen, E. P. and Smith, H. I. A three-dimensional optical photonic crystal with designed point defects. *Nature* **429** (6991): p538, 2004.

Rana, R. K., Mastai, Y. and Gedanken, A. Acoustic cavitation leading to the morphosynthesis of mesoporous silica vesicles. *Advanced Materials* **14** (19): p1414, 2002.

Reculusa, S., Masse, P. and Ravaine, S. Three-dimensional colloidal crystals with a well-defined architecture. *Journal Of Colloid And Interface Science* **279** (2): p471, 2004.

Reculusa, S., Poncet-Legrand, C., Perro, A., Duguet, E., Bourgeat-Lami, E., Mingotaud, C. and Ravaine, S. Hybrid dissymmetrical colloidal particles. *Chemistry of Materials* **17** (13): p3338, 2005.

Reculusa, S., Poncet-Legrand, C., Ravaine, S., Mingotaud, C., Duguet, E. and Bourgeat-Lami, E. Syntheses of raspberrylike silica/polystyrene materials. *Chemistry of Materials* **14** (5): p2354, 2002.

Reculusa, S. and Ravaine, S. Synthesis of colloidal crystals of controllable thickness through the Langmuir-Blodgett technique. *Chemistry Of Materials* **15** (2): p598, 2003.

Reyes, Y. and Duda, Y. Modeling of drying in films of colloidal particles. *Langmuir* **21** (15): p7057, 2005.

Robbie, K. and Brett, M. J. Sculptured thin films and glancing angle deposition: Growth mechanics and applications. *Journal of Vacuum Science & Technology a-Vacuum Surfaces and Films* **15** (3): p1460, 1997.

Robbie, K., Sit, J. C. and Brett, M. J. Advanced techniques for glancing angle deposition. *Journal of Vacuum Science & Technology B* **16** (3): p1115, 1998.

Rogach, A. L., Kotov, N. A., Koktysh, D. S., Ostrander, J. W. and Ragoisha, G. A. Electrophoretic deposition of latex-based 3D colloidal photonic crystals: A technique for rapid production of high-quality opals. *Chemistry Of Materials* **12** (9): p2721, 2000.

Romanov, S. G., Ferrand, P., Egen, M., Zentel, R., Ahopelto, J., Gaponik, N., Eychmuller, A., Rogach, A. L. and Torres, C. M. S. Exploring integration prospects of opal-based photonic crystals. *Synthetic Metals* **139** (3): p701, 2003.

Sanders, J. V. and Murray, M. J. Ordered arrangements of spheres of two different sizes in opal. *Nature* **275**: p201, 1978.

Saravanamuttu, K., Blanford, C. F., Sharp, D. N., Dedman, E. R., Turberfield, A. J. and Denning, R. G. Sol-gel organic-inorganic composites for 3-D holographic lithography of photonic crystals with submicron periodicity. *Chemistry Of Materials* **15** (12): p2301, 2003.

Scrimgeour, J., Sharp, D. N., Blanford, C. F., Roche, O. M., Denning, R. G. and Turberfield, A. J. Three-dimensional optical lithography for photonic microstructures. *Advanced Materials* **18** (12): p1557, 2006.

Seet, K. K., Mizeikis, V., Matsuo, S., Juodkazis, S. and Misawa, H. Three-dimensional spiral-architecture photonic crystals obtained by direct laser writing. *Advanced Materials* **17** (5): p541, 2005.

Shevchenko, E. V., Talapin, D. V., Kotov, N. A., O'Brien, S. and Murray, C. B. Structural diversity in binary nanoparticle superlattices. *Nature* **439** (7072): p55, 2006a.

Shevchenko, E. V., Talapin, D. V., Murray, C. B. and O'Brien, S. Structural characterization of self-assembled multifunctional binary nanoparticle superlattices. *Journal of the American Chemical Society* **128** (11): p3620, 2006b.

Shim, S.-E., Cha, Y.-J., Byun, J.-M. and Choe, S. Size Control of Polystyrene Beads by Multistage Seeded Emulsion Polymerization. *J. Appl. Polym. Sci.* **71**: p2259, 1999a.

Shim, S. E., Cha, Y. J., Byun, J. M. and Choe, S. Size control of polystyrene beads by multistage seeded emulsion polymerization. *Journal of Applied Polymer Science* **71** (13): p2259, 1999b.

Skjeltorp, A. T., Ugelstad, J. and Ellingsen, T. Preparation of nonspherical, monodisperse polymer particles and their self-organization. *Journal of Colloid and Interface Science* **113** (2): p577, 1986.

Snyder, C. E., Yake, A. M., Feick, J. D. and Velegol, D. Nanoseale functionalization and site-specific assembly of colloids by particle lithography. *Langmuir* **21** (11): p4813, 2005.

Sozuer, H. S., Haus, J. W. and Inguva, R. Photonic Bands - Convergence Problems With The Plane-Wave Method. *Physical Review B* **45** (24): p13962, 1992.

Stachowiak, A. N., Bershteyn, A., Tzatzalos, E. and Irvine, D. J. Bioactive hydrogels with an ordered cellular structure combine interconnected macroporosity and robust mechanical properties. *Advanced Materials* **17** (4): p399, 2005.

Stein, A. Sphere templating methods for periodic porous solids. *Microporous And Mesoporous Materials* **44**: p227, 2001.

Stöber, W., Fink, A. and Bohn, E. Controlled Growth of Monodisperse Silica Spheres in Micron Size Range. *Journal of Colloid and Interface Science* **26** (1): p62, 1968.

Straub, M. and Gu, M. Near-infrared photonic crystals with higher-order bandgaps generated by two-photon photopolymerization. *Optics Letters* **27** (20): p1824, 2002.

Strohm, H. and Lobmann, P. Liquid-Phase Deposition of TiO₂ on Polystyrene Latex Particles Functionalized by the Adsorption of Polyelectrolytes. *Chem. Mater.* **17** (26): p6772, 2005.

Sugitatsu, A., Asano, T. and Noda, S. Line-defect-waveguide laser integrated with a point defect in a two-dimensional photonic crystal slab. *Applied Physics Letters* **86** (17): p171106, 2005.

Takei, H. and Shimizu, N. Gradient Sensitive Microscopic Probes Prepared by Gold Evaporation and Chemisorption on Latex Spheres. *Langmuir* **13** (7): p1865, 1997.

Tanaka, Y., Sugimoto, Y., Ikeda, N., Nakamura, H., Watanabe, Y., Asakawa, K. and Inoue, K. Guided modes of a width-reduced photonic-crystal slab-line-defect waveguide with asymmetric cladding. *Journal of Lightwave Technology* **23** (9): p2749, 2005.

Taton, T. A. and Norris, D. J. Device physics: Defective promise in photonics. *Nature* **416** (6882): p685, 2002.

Tetreault, N., Arsenault, A. C., Mihi, A., Wong, S., Kitaev, V., Manners, I., Miguez, H. and Ozin, G. A. Building tunable planar defects into photonic crystals using polyelectrolyte multilayers. *Advanced Materials* **17** (15): p1912, 2005.

Tetreault, N., Miguez, H., Yang, S. M., Kitaev, V. and Ozin, G. A. Refractive index patterns in silicon inverted colloidal photonic crystals. *Advanced Materials* **15** (14): p1167, 2003.

Tetreault, N., Mihi, A., Miguez, H., Rodriguez, I., Ozin, G. A., Meseguer, F. and Kitaev, V. Dielectric planar defects in colloidal photonic crystal films. *Advanced Materials* **16** (4): p346, 2004.

Tétreault, N., von Freymann, G., Deubel, M., Hermatschweiler, M., Pérez-Willard, F., John, S., Wegener, M. and Ozin, G. A. New route to three-dimensional photonic bandgap materials: Silicon double inversion of polymer templates. *Advanced Materials* **18** (4): p457, 2006a.

Tétreault, N., von Freymann, G., Deubel, M., Hermatschweiler, M., Pérez-Willard, F., John, S., Wegener, M. and Ozin, G. A. New Route to Three-Dimensional Photonic Bandgap Materials: Silicon Double Inversion of Polymer Templates. *Advanced Materials* **18** (4): p457, 2006b.

Tierno, P. and Goedel, W. A. Using electroless deposition for the preparation of micron sized polymer/metal core/shell particles and hollow metal spheres. *Journal Of Physical Chemistry B* **110** (7): p3043, 2006.

Tirumkudulu, M. S. and Russel, W. B. Role of capillary stresses in film formation. *Langmuir* **20** (7): p2947, 2004.

Tirumkudulu, M. S. and Russel, W. B. Cracking in drying latex films. *Langmuir* **21** (11): p4938, 2005.

Trau, M., Saville, D. A. and Aksay, I. A. Field-induced layering of colloidal crystals. *Science* **272** (5262): p706, 1996.

Trau, M., Saville, D. A. and Aksay, I. A. Assembly of colloidal crystals at electrode interfaces. *Langmuir* **13** (24): p6375, 1997.

Vekris, E., Kitaev, V., von Freymann, G., Perovic, D. D., Aitchison, J. S. and Ozin, G. A. Buried linear extrinsic defects in colloidal photonic crystals. *Advanced Materials* **17** (10): p1269, 2005.

Velev, O. D., Lenhoff, A. M. and Kaler, E. W. A class of microstructured particles through colloidal crystallization. *Science* **287** (5461): p2240, 2000.

Velikov, K. P., Christova, C. G., Dullens, R. P. A. and van Blaaderen, A. Layer-by-layer growth of binary colloidal crystals. *Science* **296** (5565): p106, 2002.

Velikov, K. P. and van Blaaderen, A. Synthesis and characterization of monodisperse core-shell colloidal spheres of zinc sulfide and silica. *Langmuir* **17** (16): p4779, 2001.

Vlasov, Y. A., Bo, X. Z., Sturm, J. C. and Norris, D. J. On-chip natural assembly of silicon photonic bandgap crystals. *Nature* **414** (6861): p289, 2001.

Wang, D. Y. and Mohwald, H. Rapid fabrication of binary colloidal crystals by stepwise spin-coating. *Advanced Materials* **16** (3): p244, 2004.

Wang, J., Ahl, S., Li, Q., Kreiter, M., Neumann, T., Burkert, K., Knoll, W. and Jonas, U. Structural and optical characterization of 3D binary colloidal crystal and inverse opal films prepared by direct co-deposition. *Journal of Materials Chemistry* **18** (9): p981, 2008.

Wang, J. J., Li, Q., Knoll, W. and Jonas, U. Preparation of multilayered trimodal colloid crystals and binary inverse opals. *Journal of the American Chemical Society* **128** (49): p15606, 2006a.

Wang, L. K., Yan, Q. F. and Zhao, X. S. From planar defect in opal to planar defect in inverse opal. *Langmuir* **22** (8): p3481, 2006b.

Wang, X. D., Yang, W. L., Tang, Y., Wang, Y. J., Fu, S. K. and Gao, Z. Fabrication of hollow zeolite spheres. *Chemical Communications* (21): p2161, 2000.

Wang, Y., Su, F. B., Lee, J. Y. and Zhao, X. S. Crystalline carbon hollow spheres, crystalline carbon-SnO2 hollow spheres, and crystalline SnO2 hollow spheres: Synthesis and performance in reversible Li-ion storage. *Chemistry of Materials* **18** (5): p1347, 2006c.

Wijnhoven, J., Zevenhuizen, S. J. M., Hendriks, M. A., Vanmaekelbergh, D., Kelly, J. J. and Vos, W. L. Electrochemical assembly of ordered macropores in gold. *Advanced Materials* **12** (12): p888, 2000.

Wong, S., Kitaev, V. and Ozin, G. A. Colloidal crystal films: Advances in universality and perfection. *Journal Of The American Chemical Society* **125** (50): p15589, 2003.

Woodcock, L. V. Entropy difference between the face-centred cubic and hexagonal close-packed crystal structures. *Nature* **385** (6612): p141, 1997.

Wostyn, K., Zhao, Y. X., de Schaetzen, G., Hellemans, L., Matsuda, N., Clays, K. and Persoons, A. Insertion of a two-dimensional cavity into a self-assembled colloidal crystal. *Langmuir* **19** (10): p4465, 2003.

Xia, Y. D. and Mokaya, R. Generalized and facile synthesis approach to N-doped highly graphitic mesoporous carbon materials. *Chemistry of Materials* **17** (6): p1553, 2005a.

Xia, Y. D. and Mokaya, R. Hollow spheres of crystalline porous metal oxides: A generalized synthesis route via nanocasting with mesoporous carbon hollow shells. *Journal of Materials Chemistry* **15** (30): p3126, 2005b.

Xia, Y. N. *A Special Issue on "Photonic Crystals", Adv. Mater.* **13**: p369, 2001.

Xia, Y. N., Gates, B. and Li, Z. Y. Self-assembly approaches to three-dimensional photonic crystals. *Advanced Materials* **13** (6): p409, 2001.

Xia, Y. N., Gates, B. and Park, S. H. Fabrication of three-dimensional photonic crystals for use in the spectral region from ultraviolet to near-infrared. *Journal Of Lightwave Technology* **17** (11): p1956, 1999.

Xia, Y. N., Gates, B., Yin, Y. D. and Lu, Y. Monodispersed colloidal spheres: Old materials with new applications. *Advanced Materials* **12** (10): p693, 2000.

Xie, R. G., Sekiguchi, T., Li, D. S., Yang, D. and Jiang, M. H. Precise fabrication of point defects in self-assembled three-dimensional macroporous photonic crystals. *Journal Of Physical Chemistry B* **110** (3): p1107, 2006.

Xu, D. W., Graugnard, E., King, J. S., Zhong, L. W. and Summers, C. J. Large-scale fabrication of ordered nanobowl arrays. *Nano Letters* **4** (11): p2223, 2004.

Xu, L. B., Zhou, W. L. L., Frommen, C., Baughman, R. H., Zakhidov, A. A., Malkinski, L., Wang, J. Q. and Wiley, J. B. Electrodeposited nickel and gold nanoscale metal meshes with potentially interesting photonic properties. *Chemical Communications* (12): p997, 2000.

Yablonovitch, E. Inhibited Spontaneous Emission In Solid-State Physics And Electronics. *Physical Review Letters* **58** (20): p2059, 1987.

Yablonovitch, E. Photonic Crystals: Semiconductors of Light. *Sci. Am.* **67**: p47, 2001.

Yablonovitch, E., Gmitter, T. J. and Leung, K. M. Photonic Band-Structure - The Face-Centered-Cubic Case Employing Nonspherical Atoms. *Physical Review Letters* **67** (17): p2295, 1991a.

Yablonovitch, E., Gmitter, T. J., Meade, R. D., Rappe, A. M., Brommer, K. D. and Joannopoulos, J. D. Donor And Acceptor Modes In Photonic Band-Structure. *Physical Review Letters* **67** (24): p3380, 1991b.

Yan, H. W., Blanford, C. F., Holland, B. T., Parent, M., Smyrl, W. H. and Stein, A. A chemical synthesis of periodic macroporous NiO and metallic Ni. *Advanced Materials* **11** (12): p1003, 1999.

Yan, H. W., Blanford, C. F., Holland, B. T., Smyrl, W. H. and Stein, A. General synthesis of periodic macroporous solids by templated salt precipitation and chemical conversion. *Chemistry Of Materials* **12** (4): p1134, 2000.

Yan, Q., Chen, A., Chua, S. J. and Zhao, X. S. Incorporation of point defects into self-assembled three-dimensional colloidal crystals. *Advanced Materials (Weinheim, Germany)* **17** (23): p2849, 2005a.

Yan, Q., Zhou, Z. and Zhao, X. S. Introduction of Three-Dimensional Extrinsic Defects into Colloidal Photonic Crystals. *Chemistry of Materials* **17** (12): p3069, 2005b.

Yan, Q., Zhou, Z., Zhao, X. S. and Chua, S. J. Line defects embedded in three-dimensional photonic crystals. *Advanced Materials (Weinheim, Germany)* **17** (15): p1917, 2005c.

Yan, Q. F., Liu, F., Wang, L. K., Lee, J. Y. and Zhao, X. S. Drilling nanoholes in colloidal spheres by selective etching. *Journal Of Materials Chemistry* **16** (22): p2132, 2006.

Yan, Q. F., Zhou, Z. C. and Zhao, X. S. Inward-growing self-assembly of colloidal crystal films on horizontal substrates. *Langmuir* **21** (7): p3158, 2005d.

Yang, H. W., Blanford, C. F., Lytle, J. C., Carter, C. B., Smyrl, W. H. and Stein, A. Influence of processing conditions on structures of 3D ordered macroporous metals prepared by colloidal crystal templating. *Chemistry of Materials* **13** (11): p4314, 2001.

Yang, M., Ma, J., Zhang, C. L., Yang, Z. Z. and Lu, Y. F. General synthetic route toward functional hollow spheres with double-shelled structures. *Angewandte Chemie-International Edition* **44** (41): p6727, 2005a.

Yang, Q. H., Xu, W. H., Tomita, A. and Kyotani, T. The template synthesis of double coaxial carbon nanotubes with nitrogen-doped and boron-doped multiwalls. *Journal of the American Chemical Society* **127** (25): p8956, 2005b.

Yang, S. M., Jang, S. G., Choi, D. G., Kim, S. and Yu, H. K. Nanomachining by colloidal lithography. *Small* **2** (4): p458, 2006.

Yang, S. M., Miguez, H. and Ozin, G. A. Opal circuits of light - Planarized microphotonic crystal chips. *Advanced Functional Materials* **12** (6-7): p425, 2002.

Yang, Z. Z., Niu, Z. W., Lu, Y. F., Hu, Z. B. and Han, C. C. Templated synthesis of inorganic hollow spheres with a tunable cavity size onto core-shell gel particles. *Angewandte Chemie-International Edition* **42** (17): p1943, 2003.

Yano, K. and Fukushima, Y. Particle size control of mono-dispersed super-microporous silica spheres. *Journal Of Materials Chemistry* **13** (10): p2577, 2003.

Yates, H. M., Pemble, M. E., Miguez, H., Blanco, A., Lopez, C., Meseguer, F. and Vazquez, L. Atmospheric pressure MOCVD growth of crystalline InP in opals. *Journal Of Crystal Growth* **193** (1-2): p9, 1998.

Ye, Y. H., Mayer, T. S., Khoo, I. C., Divliansky, I. B., Abrams, N. and Mallouk, T. E. Self-assembly of three-dimensional photonic-crystals with air-core line defects. *Journal Of Materials Chemistry* **12** (12): p3637, 2002.

Yethiraj, A. and van Blaaderen, A. A colloidal model system with an interaction tunable from hard sphere to soft and dipolar. *Nature* **421** (6922): p513, 2003.

Yokoyama, S., Nakahama, T., Mashiko, S., Nakao, M., Yamada, M., Nishio, K. and Masuda, H. Photonic crystal templates for organic solid-state lasers. *Applied Physics Letters* **87** (19), 2005.

Yu, A. M., Wang, Y. J., Barlow, E. and Caruso, F. Mesoporous silica particles as templates for preparing enzyme-loaded biocompatible microcapsules. *Advanced Materials* **17** (14): p1737, 2005.

Zeng, F., Sun, Z. W., Wang, C. Y., Ren, B. Y., Liu, X. X. and Tong, Z. Fabrication of inverse opal via ordered highly charged colloidal spheres. *Langmuir* **18** (24): p9116, 2002.

Zhang, G., Wang, D. Y. and Moehwald, H. Nanoembossment of Au patterns on microspheres. *Chemistry of Materials* **18** (17): p3985, 2006.

Zhang, G., Wang, D. Y. and Mohwald, H. Decoration of microspheres with gold nanodots-giving colloidal spheres valences. *Angewandte Chemie-International Edition* **44** (47): p7767, 2005a.

Zhang, G., Wang, D. Y. and Mohwald, H. Patterning microsphere surfaces by templating colloidal crystals. *Nano Letters* **5** (1): p143, 2005b.

Zhang, Z. and Satpathy, S. Electromagnetic-Wave Propagation In Periodic Structures - Bloch Wave Solution Of Maxwell Equations. *Physical Review Letters* **65** (21): p2650, 1990.

Zhang, Z. L. and Glotzer, S. C. Self-assembly of patchy particles. *Nano Letters* **4** (8): p1407, 2004.

Zhao, Y. X., Wostyn, K., de Schaetzen, G., Clays, K., Hellemans, L., Persoons, A., Szekeres, M. and Schoonheydt, R. A. The fabrication of photonic band gap materials with a two-dimensional defect. *Applied Physics Letters* **82** (21): p3764, 2003.

Zhou, Z. C., Li, Q. and Zhao, X. S. Evolution of interparticle capillary forces during drying of colloidal crystals. *Langmuir* **22** (8): p3692, 2006.

Zhou, Z. C., Yan, Q. F., Su, F. B. and Zhao, X. S. Replicating novel carbon nanostructures with 3D macroporous silica template. *Journal Of Materials Chemistry* **15** (26): p2569, 2005.

Zhou, Z. C. and Zhao, X. S. Flow-controlled vertical deposition method for the fabrication of photonic crystals. *Langmuir* **20** (4): p1524, 2004.

Zhu, J. X., Li, M., Rogers, R., Meyer, W., Ottewill, R. H., Russell, W. B. and Chaikin, P. M. Crystallization of hard-sphere colloids in microgravity. *Nature* **387** (6636): p883, 1997.

Zoldesi, C. I., van Walree, C. A. and Imhof, A. Deformable hollow hybrid silica/siloxane colloids by emulsion templating. *Langmuir* **22** (9): p4343, 2006.

Appendix

List of Publications Coming from This Thesis Work

- Patterning the surface of submicron spheres and fabrication of nonspherical particles. L. Wang, L. Xia, G. Li, X. S. Zhao, S. Ravaine, *Angew. Chem. Int. Ed.*2008, 47, 4725.

- Fabrication of crack-free colloidal crystals using a modified vertical deposition method. L. Wang, X. S. Zhao, *J. Phys. Chem. C* 2007, 111, 8538.

- Fabrication of free-standing non-close-packed opal films. L. Wang, Q. Yan, X. S. Zhao, *J. Mat. Chem.* 2006, 16, 4598.

- From planar defect in opal to planar defect in inverse opal. L. Wang, Q. Yan, X. S. Zhao, *Langmuir* 2006, 22, 3481.

- Artificial defect engineering in three-dimensional colloidal photonic crystals. Q. Yan, L. Wang, X. S. Zhao, *Adv. Funct. Mater. 2*007, 17, 3695.

- Drilling nanoholes in colloidal spheres by selective etching. Q. Yan, F. Liu, L. Wang, J. Y. Lee, X. S. Zhao, *J. Mat. Chem.* 2006, 16, 2132.

- Hollow carbon spheres with a controllable shell structure. F. Su, X. S. Zhao, Y. Wang, L. Wang, J. Y. Lee, *J. Mat. Chem.* 2006, 16, 4413.

- Copolymer-controlled homogeneous precipitation for the synthesis of porous microfibers of alumina. P. Bai, F. Su, P. Wu, L. Wang, F. Lee, L. Lv, Z. Yan, X. S. Zhao, *Langmuir* 2007, 23, 4599.

- Preparation and characterization of SiO2/TiO2-Pt core/shell nanostructures and evaluation of their photocatalytic activity. G. Li, L. Wang, L. Lv, X. S. Zhao, *J. Nanosci. Nanotechnol.* In press.